Shallow Water Tuned Liquid Dampers

Modeling, simulation and experiments

Krabbenhøft, Jørgen; Georgakis, Christos T.; Santos, Ilmar; Poulsen, Peter Noe

Publication date:
2011

Document Version
Publisher's PDF, also known as Version of record

Shallow Water Tuned Liquid Dampers

Modeling, simulation and experiments

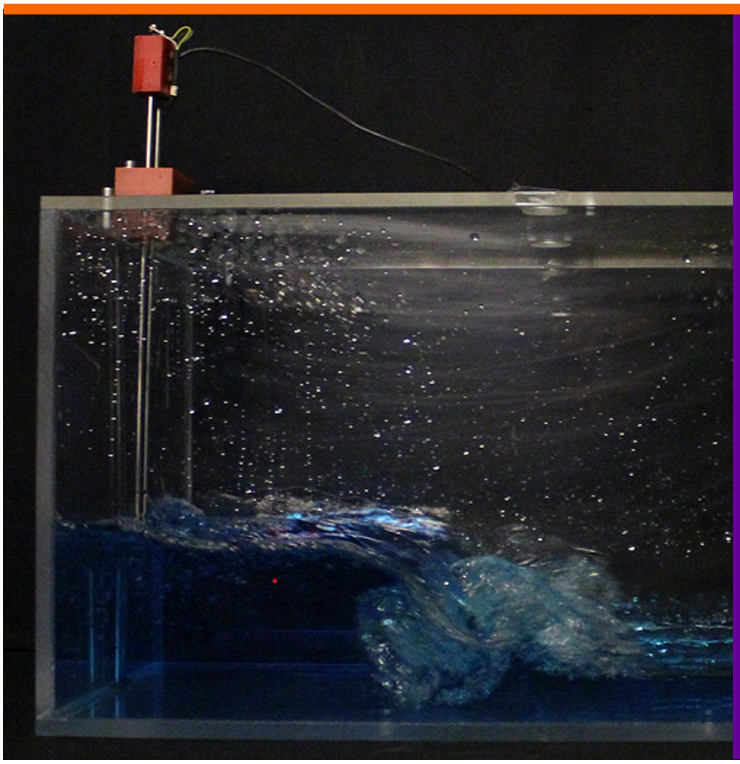

Jørgen Krabbenhøft

PhD Thesis

Department of Civil Engineering

2011

DTU Civil Engineering Report R-234 (UK)
March 2011

DTU Civil Engineering
Department of Civil Engineering

Shallow Water Tuned Liquid Dampers

Modeling, simulation and experiments

Jørgen Krabbenhøft

Ph.D. Thesis

Department of Civil Engineering
Technical University of Denmark

2010

Shallow Water Tuned Liquid Dampers
Modeling, simulation and experiments

Printed by DTU-Tryk
Department of Civil Engineering
Technical University of Denmark
9788778773142
1601-2917

To Heidi

Preface

This thesis is submitted as a partial fulfilment of the requirements for the Danish Ph.d. degree. The work has been carried out at the Department of Civil Engineering at the Technical University of Denmark, with Associate Professor Christos Georgakis as main supervisor and Peter Noe Poulsen, also from The Department of Civil Engineering, and Ilmar Santos from the The Department of Mechanical Engineering, as co-supervisors. I want to thank Associate Professor Christos Georgakis, for making this research study possible and for the encouragement and support I received throughout the study.

From the Department of Mechanical Engineering I would like to express my appreciation to Professor Per Madsen, Associate Professor Harry Bingham, Assistant Professor Allan Engsig-Karup for their valuable comments and advice. Finally I want to express my sincere gratitude to Assistant Professor Henrik Bredmose for sharing his experience and knowledge in fluid dynamics and for his sincere interest and encouragement.

During the winter 2008-2009 I spent four months at the Laboratory of Applied Mathematics at the University of Trento, Italy. Here I gained great insight in the world of numerical fluid dynamics and spent four inspiring and unforgettable months. I am deeply indebted to Professor Eleuterio Toro and Associate Professor Michael Dumbser and thank them for their kindness and openness.

A large part of the work was of experimental character and from the technical staff at the Department of Civil Engineering I would like to thank Martin Dandanell, Keld Plougmann, Christian Rasmussen and Jonathan Schwartz. Your help was much appreciated. Also thanks to Jimmie Beckerlee and Uffe Lind from Force Technology for their help with wave gages, accelerometers and other pieces of equipment borrowed during this study.

Also I would like to thank my close PhD colleagues Einar Ingolfsson, Henrik Gjelstrup, Jens Henrik Nielsen, Jacob Schmidt and Benjamin Riisgaard for their support and friendship.

Finally, I would like to thank my family and close friends for their support, understanding, continuous encouragement and guidance. Thank you to my brother Kristian Krabbenøft for helping out with proof reading and for support and advice when ever it was needed. During the study my son Holger was born who helped set things in perspective, especially in periods with low tide. However, this work would not have been possible without the endless support and love from my partner in life and best friend, Heidi, to whom this thesis is dedicated.

Abstract

The use of sloshing liquid as a passive means of suppressing the rolling motion of ships was proposed already in the late 19th century. Some hundred years later the use of liquid sloshing devices, often termed Tuned Liquid Dampers (TLD), began to find use in the civil engineering community.

The TLDs studied in this thesis essentially consist of a rectangular container partially filled with liquid in the form of plain tap water. The frequency of the liquid sloshing motion, which is adjusted by varying the length of the tank and the depth of the water, is tuned to the structural frequency of interest. When, due to various disturbances, the structure starts vibrating, the liquid motion or sloshing is initiated due to the frequency tuning and sloshing forces are imposed on the structure. The main focus of the present work has been the development of a mathematic model capable of predicting the interaction between a structure and fluid sloshing forces.

A mathematical model describing liquid sloshing in shallow water is formulated by simplifying the full Navier-Stokes equations expressed in a moving frame of reference. The resulting set of equations are known as the Nonlinear Shallow Water (NSW) equations, or the St. Venant equations, named after the originator who derived the set of equations in 1871. The set of equations are developed with the purpose of describing sloshing in tanks with relatively large base amplitudes which result in the formation of moving hydraulic jumps or bores, by some researchers on TLDs termed wave breaking. A large part of the energy dissipation in the fluid is anticipated to stem from the turbulence in the vicinity of the moving hydraulic jump, and in order to verify this supposition the effect of bottom friction is included in the mathematical model. Studies reveal that for realistic roughness parameters the bottom friction has very limited effect on the liquid sloshing behavior and can be neglected. Herby the postulate is verified.

Based on the mathematical model three dimensionless parameters are derived showing that the response of the damper depends solely on ratio of the base amplitude and tank length, A/L, on the frequency ratio of the forcing frequency and sloshing frequency, Ω/ω_w, and finally on a friction parameter γ. These dimensionless parameters have been postulated by several researches in the field of TLDs but has not been derived rigorously as in the present thesis.

In the derivation of the dimensionless parameters it is assumed that the proposed mathematical model captures the relevant physical processes in the problem. The model is based on a shallow water assumption and an extensive measurement campaign is carried out to establish an appropriate upper limit for the filling or depth defined by the ratio of the water depth and tank length, h/L, for which the mathematical model is valid. Moreover, the experiments are used to determine the effects of the forcing ratio A/L and

frequency ratio Ω/ω_w on the sloshing behavior. The current study is novel in its rigorous approach and brings valuable information on the range of application for the proposed mathematical model.

In order to solve the mathematical model an extensive amount of work has been invested in computational fluid dynamics. Other similar reported studies of the NSW equations in connection with sloshing has used cumbersome, computationally expensive and somewhat outdated numerical solution schemes. We compare a state of the art, high order, shock capturing method with a simpler low order scheme and find that the simple scheme is adequate for simulating shallow water sloshing.

The interaction between a shallow water TLD and a structure, the main focus of the work, is analyzed experimentally and by simulation. The mathematical sloshing model is coupled to a simple Single-Degree-Of-Freedom (SDOF) system in a general framework and a time integration scheme is proposed. A number of interaction experiments are performed where TLDs are coupled to an elastic structure. The elastic structure is given an initial horizontal displacement and then released. The mathematical interaction model captures the transient free surface behavior of liquid sloshing as well as the position of the hydraulic jump very well. By coupling the shallow water TLD to the structure, the total structural damping is increased and the increased damping is estimated precisely by the model. The mathematical model is further verified using experimental results from the literature on the interaction of shallow water TLDs and elastic structures. The interaction model predicts the structural amplitude satisfactorily but introduces a small error in the frequency location of the maximum structural amplitude.

Resumé

Anvendelsen af væskers frie overflade til begrænsning af rulning af skibe blev fremsat allerede i slutningen af det nittende århundrede. Godt og vel hundrede år senere begyndte lignede anordninger, ofte benævnt væske dæmpere, at finde anvendelse i bygnings konstruktioner. Væskedæmperne studeret i denne afhandling består i al sin enkelthed at en rektangulær tank delvist fyldt med væske i form a vandhanevand. Frekvens a væskens skvulpebevægelse, som kan justeres ved at variere tank længden og væske dybden, er tunet således at skvulpefrekvensen er sammenfaldende med den pågældende konstruktions egenfrekvens. Når strukturen begynder at svinge som følge af eksterne påvirkninger, begynder væsken at skvulp på grund af frekvenstuningen og hydrodynamisk kræfter påføres konstruktionen. Det har været hoved formålet med nærværende afhandling at opstille en matematisk model til at estimere interaktionen mellem en struktur og hydrodynamiske kræfter fra skvulpebevægelser. En matematisk model til beskrivelse af bevægelsen af frie væskers overflade i lavt vand er formuleret ved en simplificering af de fulde Navier-Stokes ligninger opskrevet i et henførelsessytem. De udledte ligninger er kendt som de ikkelineære fladvands ligninger, eller St. Venant ligninger, opkaldt efter udvikleren som udledte ligningerne i 1871. Ligninger udledes med hensigt på at beskrive skvulpebevægelser i kar udsat for relativt store vandrette bevægelser som resulterer i dannelsen af rejsende hydrauliske spring, refereret til som brydende bølger af visse forskere indenfor væskedæmpere. En stor del af energidissipationen forventes at stamme fra turbulens i det hydrauliske spring og for at verificere dette postulat medtages effekt af bundfriktion i den matematiske model. Nye studier viser at for realistiske ruhedder har bund friktionen en meget begrænset effekt på væskebevægelsen og kan negligeres. Hermed kan det konkluderes at hovedparten af energidissipationen i væsken stammer fra det hydrauliske spring. Ud fra den matematiske model udledes tre dimensionsløse parameter der viser at den frie overflade af væske alene er styret af forholdet mellem den vandrette flytning af tanken og længden af tanken A/L, af forholdet mellem belastningsfrekvens og skvulpefrekvensen og endelig af en friktionsparameter. Disse dimensionsløse parametre er tidligere blevet postuleret af forskere i væskedæmpere men er ikke blevet udledt rigoristisk som i den nuværende afhandling. Ved udledningen af de dimensionsløse parametre er det forudsat at den matematiske model kan anvendes og er i stand til at beskrive de relevante fysiske processer tilstede i problemet. Modellen er baseret på en lavvandsantagelse og en omfattende forsøgsmatrix udføres for a fastlægge en fornuftig øvre grænse for dybdeforholdet defineret som forholdet mellem væske dybden og tank længden h/L, for hviket den matematiske model kan anvendes. Ydermere bruges eksperimenterne til at fastlægge effekten af flytningsforholdet A/L og frekvensforholdet Ω/ω_w. På trods af at lignende forsøg har være udført føri forbindelse med beskrivelse af væskedæmpere, så er nærværende studie unik i form af sin ritoristiske

tilgang og tilføjer vigtig viden til hvornår den forslåede matematiske model kan anvendes. For at løse den matematiske model er et omfattende mængde arbejde blevet investeret i numerisk fluid mekanik. Andre lignende rapporterede studier af St. Venant ligninger i forbindelse med skvulpning, har anvendt komplicerede, beregningstunge og i en vis grad gammeldags, numeriske metoder. Vi sammenligner en moderne, højere ordens metode men en simplere lav ordens metode og finder at den simple metode er tilstrækkelig til beskrivelse af de undersøgte fænomen. Resultat er nyt og meget brugbart for ingeniører med en interesse i lavvands væskedæmpere men med en begrænset indsigt i numerisk fluiddynamik. Interaktion mellem en lavvands væskedæmper og struktur, hovedfokus for nærværende arbejde, analyseres eksperimentelt og ved simuleringer. Den matematiske model til beskrivelse af frie væskers overflade kobles til et simpelt ét frihedsgradsystem in en generel ramme, og en tidsintegrationsprocedure fremsættes. Et antal interaktionseksperimenter udføres hvor væskedæmpere kobles til en elastisk struktur. Den elastiske struktur gives en initial vandret udbøjning og slippes herefter. Dem matematiske interaktionsmodel fanger det transiente forløb af den frie væskeoverflade samt placeringen af det hydrauliske spring meget overbevisende. Ved at koble lavvands dæmperen til strukturen øges dæmpning af systemet og den forøgede dæmpning estimeres præcist af modellen. For store vibrationsamplituder er modellens estimater af dæmpningen bedre end for lave vibrationsamplituder. Den matematiske model verificeres yderligere ved hjælp af resultater fra litteraturen omhandlende interaktionen mellem lavvands væskedæmpere og elastiks strukturer udsat for harmonisk belastninger. Interaktionsmodellen estimerer størrelsen af strukturens udbøjning tilfredsstillende men introducerer en lille afvigelse i frekvensen hvor den største udbøjning af strukturen forekommer.

Table of Contents

Paper IV

"Simulation of tuned liquid dampers using a momentum conserving nonlinear shallow water model: theory, computations and experimental verification",
J. Krabbenhøft & B. Lazarov.
Published in: *Proceedings of the 3rd Int. Conf. on Structural Engineering, Mechanics and Computations, Cape Town, South Africa, 10-12 Sept. 2007* 193

Part I

Summary

Chapter 1

Introduction

All tall and slender structures such as chimneys, telecommunication towers, cables etc. are characterized by having a relatively low natural frequency as well as a low structural damping. This makes the structures especially vulnerable to dynamic loads such as buffeting wind loads and aero-elastic loads from vortex shedding and galloping. The dynamical response of a structure is a function of structural damping and the magnitude and frequency of the applied load. Thus, in order to reduce the dynamic response of a structure, one is forced either to alter the loading or increase the damping. This thesis is concerned with the latter aspect, namely methods for increasing the structural damping.

It appears that the most popular means of increasing damping in chimney, cables, telecommunication towers etc is by installing so-called Tuned Mass Dampers (TMDs). However, in the last 10-20 years Tuned Liquid Dampers (TLDs) have become increasingly popular and are now being routinely used, for example by a number of Danish chimney manufacturers. It is easy to understand their popularity considering the simplicity of a TLD which in essence is nothing more than a tank partially filled with water added an anti freezing substance. Such a device obviously requires very little maintenance compared to a mechanical device such as a TMD. The popularity of TLD's seem to be limited by the fact that their description is far more complex than a simple spring-mass system like a TMD, making them difficult to design, and equally important from a deign point of view, difficult to predict.

Though TLD's have been researched rater extensively the main focus has been on the application of TLDs in connection with the serviceability limit states (SLS), such as occupant discomfort in residential buildings and airport control towers. Vibrations in connection with SLS studies are characterized by having a relatively small vibration amplitude with an allowable root mean square (RMS) value typically in the order of 10 milli-g or 0.1m/s^{-2}. Assuming a structural frequency of 0.5Hz, this corresponding to RMS displacements in the order of 10 mm. By comparison the allowable displacements for a chimney is easily 4-6 times higher and for cables even as much as 10 times higher. Since the present work is concerned with TLD's for the latter type of structures the case of TLDs exposed to high vibration levels must be considered.

When dealing with TLD's one inevitable has to deal with sloshing. The phenomenon of sloshing is defined as the movement of the free surface of liquids contained in close tanks. The sloshing motion of the contained liquid generates hydrodynamic loads on the

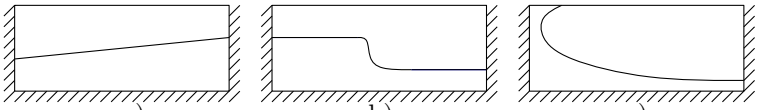

Figure 1.1: *Three different sloshing patterns:a) Planer sloshing, b) Wave breaking or formation of moving hydraulic jump. Surface profile discontinuous c) Smooth continuous surface profile impacting tank ceiling*

tank walls, and the prediction of these loads is in general the main challenge for engineers working with liquid sloshing. Besides being relevant for TLD's, sloshing is of great concern in aerospace, nuclear, naval and civil engineering. Hence, an abundant literature on the subject can be found. Thus, recently Ibrahim (2005) made an intensive review on liquid sloshing collecting thousands of references.

The description of TLDs obviously requires a description of the interaction between the liquid sloshing forces and the structure to which the device is attached. The most complicated part in this equation is by far the description of the sloshing forces. For this reason a large part of this thesis has been devoted entirely to sloshing and on the derivation and solution of mathematical models used to simulate sloshing. This strategy has been chosen, partly based on the fact that having established an accurate sloshing model the interaction between the sloshing forces and structure is relatively straight forward and partly by the belief that in order to understand TLDs one needs to dive down deeper in the phenomenon of sloshing.

The remaining part of the introduction is organized as follows. First a short introduction and a review of TLDs is presented followed by a description of various strategies for simulating liquid sloshing in general. We then proceed with a more detailed description of sloshing in rectangular tanks, which has been the sole focus of the present work. Finally the motivation and organization of the thesis is summed up.

1.1 Slosh Dampers

A tank, partially filled with liquid, given a disturbance will result in a motion of the free liquid surface. This motion of free surface, Figure 1.1, may be everything from simple planar to discontinuous to violent and chaotic depending on the character of the disturbance but also, and as importantly, on the geometry of the container together with the physical properties of the liquid. A civil engineer may experience sloshing behavior in this entire range, and depending on the application, the sloshing may be regarded as a positive or negative phenomenon. Figure 1.2 shows a sketch of a water tower which typically consists of a concrete tower suspending a large liquid tank. If the structure is excited by for example an earthquake the presence of the liquid in the tank may generate large hydrodynamics forces, increasing the design loads, which in this case have to be taken into account when designing the tower structure. On the other hand, it is possible to take advantage of the sloshing loads which is utilized in TLD's. The basic and primary function of a TLD is to generate a feedback force to the structure to which the device is attached. Regarding the position of the device on the structure, generally it can be said that the closer the TLD is placed to the maximum deflection point of the structural

vibration mode of interest, the higher the efficiency. This rules applies to all vibration damping devices. The efficiency of the TLD naturally depends on the magnitude of the generated sloshing force, but equally important, on the phase of the sloshing force relative to the motion of structure, to which it is fed back. Thus in order to describe a TLD satisfactorily one must establish a mathematical model that provide a description of the magnitude of the sloshing forces as well as the phase of the sloshing forces relative to the structural response.

1.1.1 Anti-roll devices

In naval engineering a device for suppressing the roll motion of ships was first introduced at the end of the nineteenth century by Watts (1885) and simply consisted of a liquid tank placed onboard the ship thereby creating a counter balancing moment when the ship oscillated in roll at its resonance frequency. Later Frahm (1909) introduced U-tube shaped tanks, which are fundamentally different from the free surface tank proposed by Waters, in the sense that the effect of the free surface vanishes i U-tube and the problem is essentially reduced to that of describing an internal fluid flow in the tube. Frahm's U-tubed tanks, often termed Tuned Liquid Column Dampers (TLCD) or Liquid Column Vibration Absorbers (LCVA), have been investigated quite extensively recently by several authors for use in civil engineering structures with promising results Yalla and Kareem (2000); Hochrainer (2005). However, these devices are by construction primarily limited to unidirectional use.

1.1.2 Tuned Liquid Dampers

Since Watts's and Frahm's inventions, several applications of utilizing liquid motion as vibration control devices has been reported in the literature. Since the early 1960'ties TLD's have been applied as damping devices to reduce the oscillations of space satellites

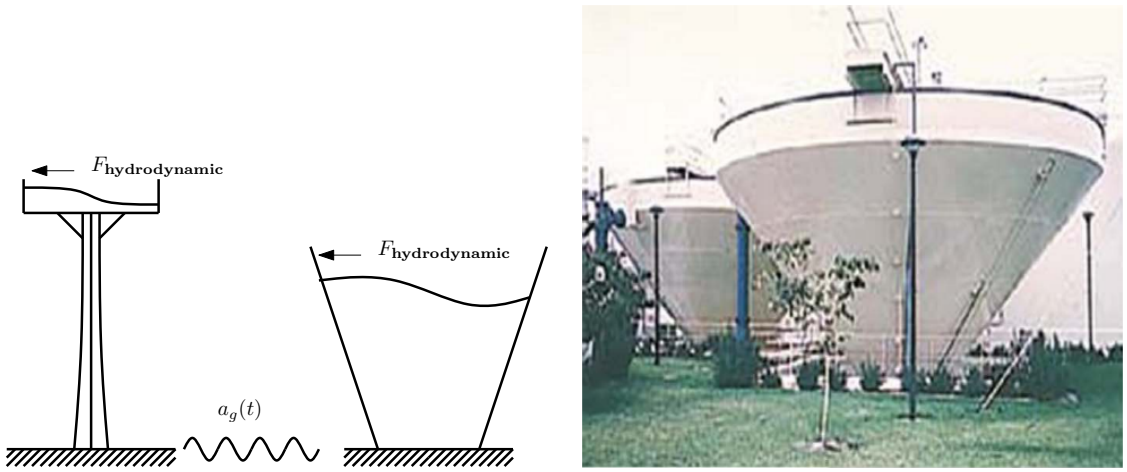

(a) Sketch of water towers (b) Conical water tower

Figure 1.2: *a) Sketch of two different types of water tower exposed to a ground acceleration $a_g(t)$ from an earthquake. b) Picture of conical water tower.*

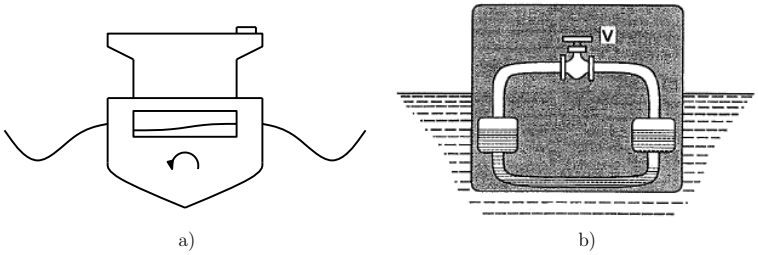

Figure 1.3: *Anti roll devices used in naval engineering. a) Device proposed by Watts utilizing free surface sloshing of liquid in a container b) Frahm's anti-rolling device comprised of two liquid filled compartments attached with a tube.*

Fujino et al. (1988). They are typically used for for controlling the librational motion (i.e. oscillating motion of orbiting bodies relative to each other) of satellites where the period may range from 90 minutes to as long as 24 hours Seto and Modi (1997). The idea of applying TLD's to reduce vibrations in civil engineering structures emerged in the 1980'ties and it seems to be generally acknowledged Fujino et al. (1988); Tait (2004) that the early pioneers were Bauer (1984) together with Modi and Welt (1987) and Kareem and Sun (1987). Numerous articles have been written on TLDs in the last 20 years. In the late 1980'ties a group led by Fujino, Fujino et al. (1988, 1992); Fujino and Sun (1993) and including Sun et al. (1989); Sun (1991); Sun et al. (1992); Sun and Fujino (1994), Pacheco and Chaiseri, investigated TLDs experimentally and numerically. This work was followed up by Tamura et al. (1992, 1995, 1996), Wakahara et al. (1992) and Koh et al. (1994, 1995) in a number of articles more concerned with practical applications of TLDs. One of the pioneers, Modi and Welt (1987); Modi et al. (1995); Modi and Seto (1997, 1998); Modi and Akinturk (2002) together with Welt and Modi (1992b,a) contributed significantly with the use of TLDs in connection with wind induced vibrations. Another important contribution is from Reed et al. (1998) and Gardarsson (1997); Gardarsson and Yeh (2001) and Yu et al. (1999), who focused on the more fundamental aspects of sloshing as well on TLDs and derived simplistic design models to be used by engineers. The present work has to a great extent been inspired by the work of Gardarsson (1997). Kareem and Sun (1987); Kareem (1990) and Yalla also contributed significantly however the majority of their work focused on applying Tuned Liquid Column Dampers where as aforementioned the liquid free surface is not important. Finally The group of El Damatty and Tait et al. (2002, 2004a,b, 2005b,a, 2007, 2008) did a rather extensive research on TLDs both numerically and experimentally. There entire work was based on deep water TLD's in connection with SLS studies and hence relatively low amplitude applications.

All the above mentioned references concerned with TLDs took a small wave amplitude assumption as point of departure, except for the work by Gardarsson (1997) and Reed et al. (1998) who assumed large wave amplitudes. The models based on small waves amplitude simply break down when the wave amplitudes become large. Different strategies to overcome this problem has been propose. Fujino et. al. added empirical damping terms to the fluid equations to get a proper fit with experiments and Tait et. al. added porous screens in the liquid, thereby introducing a large amount of internal damping which reduced the wave amplitudes to an acceptable limit for the model point

of view. Gardarsson (1997) took a large wave amplitude as point of departure and used a complete different set of equations than Fujino et. al. that are capable of describing wave breaking. These equations were derived by the brilliant French mechanician and mathematician Adhémar Jean Claude Barré de Saint-Venant in 1871 for studying open channel flows. The equations, known as the St. Venant equations or the Nonlinear Shallow Water (NSW) equations, were analyzed briefly in Gardarsson (1997) and later by Reed et al. (1998).

1.2 Modelling Sloshing

As mentioned earlier the main problem in sloshing is the prediction of the hydrodynamic forces acting on the tank. The local pressure distribution in the liquid, typically near a wall, may be extremely complex and impossible to model accurately and one may be forced to conduct an experimental investigation. Over the last fifty years or so, several researchers and engineers have modelled sloshing using many different methods, depending on the assumptions made, the computational cost and the accuracy.

1.2.1 Mechanical analogies

The fastest, but not necessarily the simplest, way to model sloshing forces consists of defining an analogous mechanical system. Many different system have been chosen from simple linear mass-spring systems to more complex nonlinear pendulum systems. In an early paper by Graham and Rodriguez (1952) linear mechanical systems were derived to describe the response of fuel in a rectangular tank with prescribed harmonic motions in translation, pitching and yawing. The derived system for translational motion is depicted in figure 1.4 and as the figure indicates the sloshing behavior can be described by an infinite number modes each defined by simple spring-mass systems with a unique mass, stiffness and damping. In the original investigation by Graham et. al. the mass for each mode was found as Graham and Rodriguez (1952):

$$\frac{m_n}{m_w} = \frac{8\tanh((2n+1)\pi h/L)}{(2n+1)^3 h/L}, \quad n = 0, 1, 2, ... \tag{1.1}$$

where m_w is the total mass of water contained in the system. The expression (1.1) is shown in figure 1.4 and it is clear that the first mode is by far the dominating. Also it is interesting to note that in a linearized theory the participating mass of the first sloshing mode converges, for a decreasing liquid depth, to a maximum value of 81% of the total water mass. Later H.N. (1966) in an extensive NASA report described a large variety of models which recently was updated by Dodge (2000). In Dodge (2000) he describes the program SLOSH, which computes the properties of an analogue mechanical system given a certain tank geometry. On http://sloshcentral.bbbeard.org/ the mentioned references, and many others, are shared online.

1.2.2 Potential theory

More complicated models of sloshing loads can be deduced from the potential theory, i.e. the fluid equations describing the motion of irrotational and inviscid flow. In the linearized

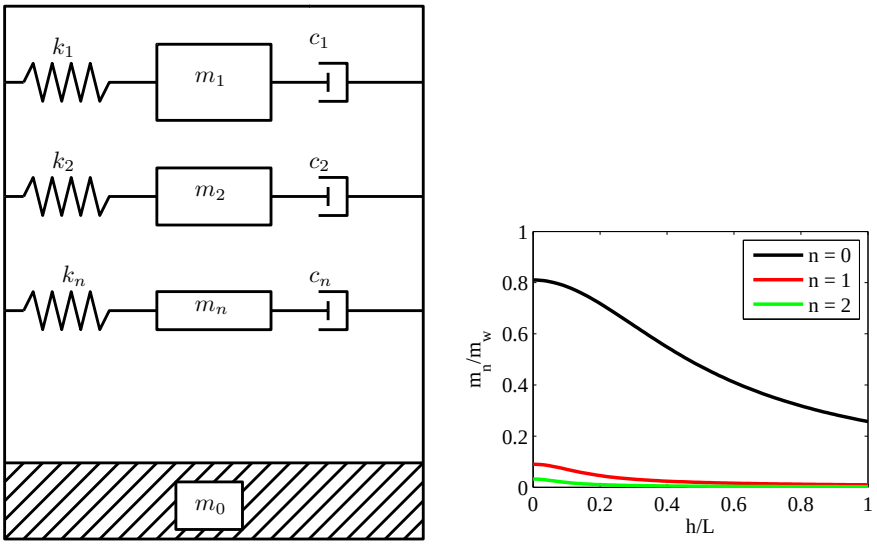

(a) Sketch of water towers (b) Conical water tower

Figure 1.4: *Mechanical analogy of rectangular tank in translational motion. a) Mechanical system b) Participating mass*

form these equations were used by Graham and Rodriguez (1952), just mentioned, to derive analogous mechanical systems. Faltinsen proposed a truncated modal theory by decomposing the free surface into a sum of modes, and included nonlinearities up to third order, Faltinsen (1974). Later Faltinsen et al. (2000) extended the modal theory and derived an infinite system of ordinary differential equations, each describing the amplitude of a given mode, and solved the truncated system numerically, typically using in the order of 10-20 modes, with very little computational cost. While the method developed by Faltinsen et. al. provide fast results they fail when the base motion amplitude is large or when the liquid is shallow. Moreover the models are limited to certain tank geometries, they cannot handle breaking waves and dissipation must be introduced with the use empirical correction factors obtained from experiments.

1.2.3 Full Navier Stokes solvers

When the flow is characterized by breaking, impacting on the tank ceiling and other extreme situations, one may resort to solving the full Navier-Stokes (N-S) equations directly. As the efficiency and speed of computers grow this approach is becoming more relevant and popular for many engineering disciplines. The methods are especially relevant for situations where local fluid behavior is of interest, e.g. slamming loads locally on a wall.

When handling free surface flows an additional nonlinear equation arises from the free surface description which complicates the numerical procedures substantially. The complication lies in the fact that the computational domain is no longer fixed in space due to the free surface boundary. In general the problem can be solved using either grid methods or meshless methods. For the grid methods the most popular techniques for capturing the free surface are Marker and Cell (MAC) technique, Level Set (LS) technique and the Volume of Fluid (VOF) method. Common for all the methods is that the mesh

must be updated in every time step which requires the use of a stabilization technique. The so-called meshless methods, also called gridless methods or particle methods, are based on a Lagrangian formulation consisting in dividing the fluid domain into particles each with advective fluid properties. Among these methods the Smooth Particle Hydrodynamics (SPH) method is particularly popular. Despite growing computer power, the method is still relatively time consuming, and as reported in the recent paper by Marsh et al. (2010), who studied 2D sloshing in a rectangular tank, the CPU time varied between approximately 1 day to 2 weeks, depending on the water depth, for a 20 second simulation time.

1.2.4 Shallow water theory

In the area of coastal hydrodynamics, concerned with modelling of flows in rivers, channels, estuaries etc, shallow water approximations of the incompressible Navier-Stokes equations are often used. The most popular model equations for studying near-shore hydrodynamics, Brocchini et al. (2001), and in general free surface flows in shallow water, are the Nonlinear Shallow Water Equations (NSW equations) also known as de Saint-Venant equations together with a large class of so-called Boussinesq-type equations (BT equations). A comprehensive overview and review of BT equations is given in Madsen (1999). In the shallow water models the momentum and mass conservation equations are depth-integrated resulting in a reduction of variables by one compared to the full problem described earlier. But more importantly, by substituting the nonlinear kinematic boundary condition into the depth integrated mass and momentum equations, the full nonlinear description of the free surface is retained *exactly* leaving only, for the 3D case, two equations for the conservation of momentum and one equation for the conservation of mass. The variable describing the free surface enters into the mass conservation equation and thus requires no special treatment.

While these simplified models fail to give a detailed description of the local fluid behavior, a natural consequence of the averaging, they are very well suited for providing a description of the over all fluid behavior. The models though are by construction limited to the shallow water case which might be a serious limitation. However, and imperative for use in connection with describing TLDs, the models are often very fast to solve.

1.3 Sloshing in rectangular tanks

As aforementioned, the present work is limited to studying sloshing in rectangular tanks. From a practical point of view rectangular containers are often used, and from a modelling point of view this restriction simplifies the mathematical formulation considerably. Moreover only horizontal motion of the tank is consider which is clearly the dominating motion in connection civil engineering structures.

The function describing the free surface height in a rectangular container partially filled with liquid, $\eta(x, y)$, can be described by an infinite Fourier series with a circular frequency for each mode given by

$$\omega_{w,ij} = \sqrt{g k_{ij} \tanh(k_{ij} h)}, \quad k_{ij} = \pi \sqrt{(i/L_1)^2 + (j/L_2)^2}, \quad i + j \neq 0 \tag{1.2}$$

where g is the gravitational constant, k_{ij} the wave number, L_1 and L_2 the horizontal dimension of the tank in the two directions and h the liquid depth. The corresponding surface profiles are described by

$$\eta(x,y) = \cos[i\pi(x+\frac{1}{2}L_1)/L_1]\cos[j\pi(y+\frac{1}{2}L_2)/L_2], \quad i,j \geq 0 \tag{1.3}$$

For the 2D case $L_2 = \infty$ and (1.2) is further simplified by

$$\omega_{w,i} = \sqrt{gk_i \tanh(k_i)}, \quad k_i = \pi i/L_1 \tag{1.4}$$

For the shallow water case, defined by $h/L \ll 1$ on may use the following approximation of (1.4):

$$\omega_{w,i}^{\text{shallow}} = k_i\sqrt{gh} \tag{1.5}$$

where $c = \sqrt{gh}$ is the well known expression for the propagation speed of waves in shallow water. An estimate of the error on the sloshing frequency when using (1.5) is easily derived using a Taylor series expansion of tanh as

$$\frac{\tilde{\omega}_w}{\tilde{\omega}_w^{\text{shallow}}} = 1 - \tfrac{1}{6}(kh)^2 + O((kh)^4) \tag{1.6}$$

Thus for $h/L = 0.1$ the error on the frequency using the simplified expression is 1.6% while for $h/L = 0.05$ the error is 0.4%.

1.3.1 Critical depth and jump frequency

When considering linear potential theory, described just previously, the response of the fluid is identical to that of a classic linear oscillator, i.e. the frequency response curve describing the relation between forcing frequency and magnitude of the steady state response, has a unique peak at the resonance frequency. When considering the nonlinear fluid equations the steady state response does not present a single amplitude for a given frequency, but instead different steady states solution exist depending on wether the given frequency is approached with an increasing or decreasing forcing frequency as shown in figure 1.5. Ockendon and Ockendon (1973) showed that the frequency response curve changes from a hardening type (increasing amplitude with increasing forcing frequency) to a softening type behavior (decreasing amplitude with increasing forcing frequency) as the depth passes through a certain critical value. Waterhouse (1994) showed that this depth, often referred to as the critical depth, is given by $h_0/L = 0.34$. The steady state curves showing this behavior is depicted in figure 1.5. Looking at the frequency response curves one could be tempted to select fluid depth equal to the critical depth. However the solution for this water depth is unstable and might result in swirling motion of the liquid Faltinsen et al. (2003). Also in figure 1.5 the so called jump frequency is shown. The presence of a single jump frequency has been experimentally verified by many authors including the present one Krabbenhoft et al. (2010a). Recently Gardarsson (2007) presented experimental results for a oscillating tank showing the presence of two jump frequencies i.e. a different jump frequency for increased and decreased forcing frequency

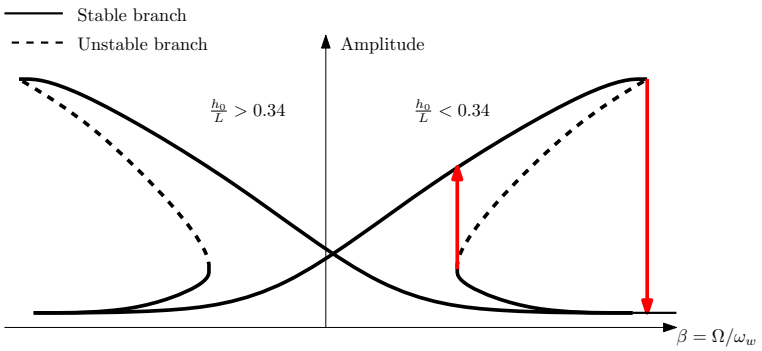

Figure 1.5: *Frequency response functions illustrating the hardening and softening behavior for fillings ratios below and above the critical depth, respectively. Also shown is the stable and unstable branches together with two jump frequencies.*

as shown in the presented figure. Finally it must be emphasized that the frequency response curves shown in figure 1.5 is a very crude simplification of the real physics. The stability diagram for liquid sloshing in a rectangular tank is extremely complex and is a function also of forcing ratio, forcing direction and liquid properties Faltinsen et al. (2000, 2005).

1.3.2 Breaking waves

When the depth ratio h/L becomes small experimental studies shown for relatively low forcing values A/L, so-called bores, also sometimes referred to as traveling hydraulic jumps, appear for forcing frequencies near the lowest sloshing frequency. The bores introduce a a high internal liquid dissipation and as a consequence the motion of the liquid in the tank is rapidly periodic at the forcing frequency. The mathematical modelling of such phenomena requires a careful selection of method. An obvious method would be the SPH method described earlier and used by Marsh et al. (2010). However, as mentioned this method is extremely CPU demanding. Another much simpler, cheaper and elegant approach is to use the NSW equations which conserves momentum and mass and are capable of capturing discontinuous surface profiles and the *associated energy loss*. This is the main reason for the popularity of the NSW equations in the area of coastal engineering where the model is useful for modelling phenomena as run-up on beaches or simulation of tsunamis were wave breaking is present for both cases.

1.4 Motivation and organization of thesis

Simulation of liquid sloshing is an enormous field and many different strategies can be used depending on the shape of the liquid tank, the depth ratio h/L and the magnitude of the forcing term A/L. The geometry has already been chosen as rectangular so the two parameters that will decide on the modelling strategy is the magnitude of the depth ratio and forcing ratio.

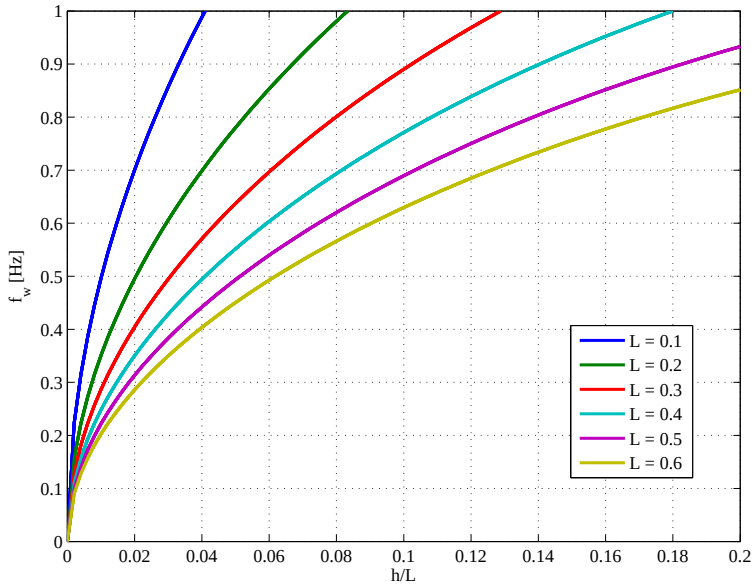

Figure 1.6: *Sloshing frequency f_w as function of filling ratio h/L for discrete tank lengths L.*

1.4.1 Shallow or deep water TLD's and forcing ratio

As stated in equation (1.4) the sloshing frequency is a function of liquid depth h and tank length L. Notice from the equation that a given sloshing frequency ω_w can be constructed using many different h/L ratios, see figure 1.6 In the present thesis we are primarily interested in slender structures such as structural cables, chimneys, telecommunication towers etc. The mentioned structures all have the common feature of having a low natural frequency, typically well below 1 Hz, and a relative small horizontal dimension, the latter resulting in an often limited installation space, i.e. a limited horizontal TLD length. If we again return to figure 1.6 the sloshing frequencies for six different tank lengths between 10 and 60cm is shown as function of the filling ratio. It is clear that for structural frequencies in the range, say $0 < f_w < 0.7$ Hz, the filling ratio hardly exceeds $h/L = 0.1$ and in fact stays well below for $L < 40$ cm. This very simple study clearly shows the motivation for using shallow water TLD's with $h/L < 0.1$.

Another important parameter is the forcing ratio A/L, A in this context being the structural amplitude at the installation point of the damper. The allowable maximum displacement varies for different structures, but an acceptable peak amplitude of 2-5 cm is not unusual, resulting in a forcing ratio for a 40 cm tank in the range $0.05 < A/L < 0.12$. Experimental results show that forcing ratios of this magnitude will result in the formation of bores, i.e. breaking waves.

1.4.2 Scope of thesis

The main aim of the present work is to establish a mathematical model for simulating rectangular shallow water TLD's attached to elastic structures. Based on the previous discussion we decided to model liquid sloshing using a mathematical model that conserves momentum and mass but captures energy dissipation in breaking waves. This feature is

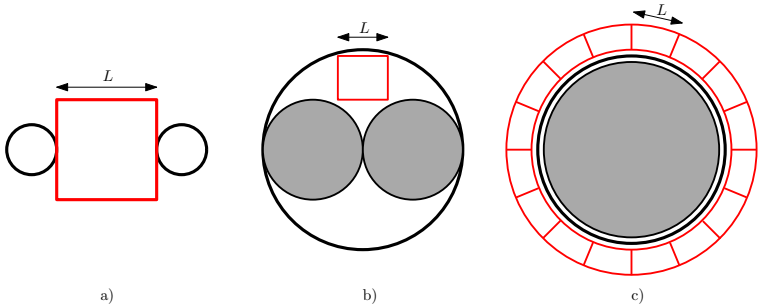

Figure 1.7: *Different examples of rectangular TLD installation (TLD showed as red boxes): a) placed between to cable hangers or smoke stacks b) Placed inside a chimney c) Placed on the outer perimeter of a steel stack.*

found in the NSW equations which are derived from the full N-S equations formulated in a non-inertial coordinate system. The same equations have been studied by several researchers in connection with sloshing, Dillingham (1981); Armenio and Rocca (1996); Gardarsson (1997) ,however the present study has several improvements and additions.

The present research includes the following:

- The NSW equations are derived from the full viscous N-S equations and the importance of bottom friction is studied.
- The equations are formulated in a non-inertial system incorporating the effect of tank movements elegantly and easily. In fact the equations are derived for a general moving and rotating tank for use in future studies.
- Dimensionless parameters defining the liquid sloshing behavior will be derived. These are useful for gaining insight in the problem and for construction eventual design procedures for shallow water TLD's.
- The equations are solved suing state of the are methods numerical methods and the simplest method possible for solving the fluid equations is found.Moreover in this connection the numerical treatment is done rigorously with an extensive convergence study performed for verification of the numerical implementation. Methods used earlier for studying sloshing in connection with NSW equations are too complex to be used by non expert engineers in fluid dynamics.
- An extensive measurement campaign is carried out in order to determine the range of applicability of the proposed mathematical model. To the authors knowledge this data is nonexistent.
- A mathematical model describing the interaction of liquid sloshing and elastic structures will be formulated and tested in transient decay experiments as well as for force steady state experiments.

The thesis is divided into two main parts: First an extensive summary supplemented with previously unpublished material, covering the main theory and typical results is presented.

This part is then followed by three journal papers and a single conference paper covering the material of the thesis. The thesis, or extended summary, is organized as follows:

In chapter 2 the mathematical sloshing model is derived with an in depth discussion on choice of formulation. In chapter 3 the numerical methods for solving the fluid model are derived and discussed. Chapter 4 presents a comparison study of experimental and simulated results and the range of application is discussed. Chapter 5 is devoted to the description and discussion of a proposed mathematical model for simulating the interaction of TLD's and structures. Final remarks, conclusions, discussion and future work is presented in the final chapter 6.

Chapter 2

Mathematical fluid models

When developing, or choosing, a mathematical model one must base the selection on at least the following criteria:

Relevant physics: The mathematical model should be able to describe the relevant physics of the investigated problem. In this connection it is important to emphasize the word relevant since this is where the art of engineering judgement often enters the modelling process.

Accuracy: Having decided on which physics the mathematical model should capture one must also pose the question on what accuracy is needed. Often a linear model may be sufficient and provide the required accuracy and for other cases a pertubation of the nonlinear system, including only a few nonlinear terms may be sufficient.

Computational cost: Having chosen a mathematical model, that we suspect, or at least hope, will describe the physics of the problem at hand, the mathematical model must be solved. Often the mathematical model is too complex for an analytical solution to be derived and a numerical method has to be applied. In this context accuracy again enters, however in a different meaning than accuracy form a model point of view. If the mathematical model is not accurate one can use any high order, state of the art, numerical method to solve the equations but the results will still be inaccurate. On the other hand if the mathematical model is accurate and relevant a poor numerical method may provide inaccurate results leaving the precise mathematical model useless. In either case it is simply paramount that the chosen numerical method is able to solve the mathematical model satisfactorily so the engineer can decide wether the *mathematical model* is sufficient or not

Regarding the first point discussed above regarding the relevant physics, we may ask which physical quantities or variables describes liquid sloshing in a closed container. It turn out, that the variables are in fact the same that enter all free surface flow problems, namely: the particle velocity in in the three orthogonal directions x, y and z denoted $u(x, y, z, t)$, $v(x, y, z, t)$ and $w(x, y, z, t)$ which are all function of space and time, the pressure in fluid and at the boundaries $p(x, y, z, t)$, and finally the position or motion of the free surface describe by the function $z = \eta(x, y, t)$. Thus the complete sloshing problem is described by the five independent variables u, v, w, p and η. For an incompressible fluid, which as a very good approximations is considered her, two material properties are needed, namely a density ρ and a viscosity μ. Depending on the material behavior of the fluid

different mathematical models must be used to describe the viscous effects.

In sloshing problems, and in general free surface flow problems, the Navier-Stokes (N-S) equations together with kinematic and dynamic boundary conditions is the most complex and complete mathematical model. Neglecting viscosity and assuming an initial irrotational flow the N-S equations can be further simplified into the Euler equations. Removing all nonlinearities in the equations lead to a relatively simple set of linear equations which for some very simple cases can be solved analytically and for other cases a numerical solution must be performed.

2.1 Full 3D Navier-Stokes equations

The governing equations describing three dimensional flows of a constant density and incompressible fluid are the well know N-S equations which express the conservation of momentum and mass Casulli and Zanolli (2002):

$$u_t + (uu)_x + (uv)_y + (uw)_z = -p_x/\rho + (\nu u_x)_x + (\nu u_y)_y + (\nu u_z)_z \tag{2.1}$$

$$v_t + (vu)_x + (vv)_y + (vw)_z = -p_y/\rho + (\nu v_x)_x + (\nu v_y)_y + (\nu v_z)_z \tag{2.2}$$

$$w_t + (wu)_x + (wv)_y + (ww)_z = -p_z/\rho + (\nu w_x)_x + (\nu w_y)_y + (\nu w_z)_z - g \tag{2.3}$$

$$u_x + v_y + w_z = 0 \tag{2.4}$$

where $u(x, y, z, t)$, $v(x, y, z, t)$ and $w(x, y, z, t)$ are the velocity components in the horizontal x, y direction and vertical z direction, $p(x, y, z, t)$ is the pressure, g is the gravitational constant, ρ the constant fluid density and $\nu = \mu/\rho$ a viscosity coefficient which must be determined from a relevant materia, and/or turbulence model, and is in general a function of space and time. We have chosen to use the subscript notation for partial derivatives, i.e.

$$()_x = \frac{\partial()}{\partial x}, \quad ()_t = \frac{\partial()}{\partial t} \tag{2.5}$$

When possible this notation will be used. The first three equations (2.1)-(2.3) express the conservation of momentum in the x, y and z direction respectively, while (2.4) express the conservation of mass.

2.1.1 Boundary conditions for free surface flows

The N-S equations given in (2.1)-(2.4) apply to all flows and not only free surface flows. In order to describe a free surface flow an additional variable is introduced defined by $z = \eta(x, y, t)$. This function is assumed to be single valued and therefor cannot describe e.g. collapsing flows such as plunging breakers. The kinematic surface condition is expressed as Vreugdenhil (1994)

$$\eta_t + u^s\eta_x + v^s\eta_y = w^s \tag{2.6}$$

where the superscript s refers to surface. The above equation, in popular terms, express that fluid particles must not leave the free surface. A similar condition is applied at the bottom and assuming the bottom topography can be expressed also by a single valued function $z = h(x, y)$, the kinematic bottom condition is

$$u^b h_x + v^b h_y + w^b = 0 \tag{2.7}$$

where superscript b refers to bottom. The condition states that the velocity component perpendicular to the bottom must vanish.

At the free surface a an additional boundary condition relating to the pressure is needed, termed a dynamic boundary condition, and is given by the following

$$p(x, y, \eta, t) = p_e(x, y, t) \tag{2.8}$$

where the subscript e refers to excess pressure. For situations where no external pressure is actively applies the excess pressure will be constant and equal to the atmospheric pressure.

For the non-viscous case the above boundary conditions completely define the free surface problem and closes the system equations an the system is said to be well-posed. For the viscous case four additional equations are needed: two for the free surface and two for the bottom, specifying the tangential stress condition. For the free surface we get Vreugdenhil (1994)

$$\nu(u_z + u_x\eta_x - u_y\eta_y)^s = \tau_x^s \tag{2.9}$$
$$\nu(v_z + v_x\eta_x - v_y\eta_y)^s = \tau_y^s \tag{2.10}$$

where τ_x^s and τ_y^s are applied tangential surfaces stresses in the x and y direction respectively. Similarly conditions can be stated for the bottom

$$\nu(u_z + u_x h_x + u_y h_y)^b = \tau_x^b \tag{2.11}$$
$$\nu(v_z + v_x h_x + v_y h_y)^b = \tau_y^b \tag{2.12}$$

where τ_x^b and τ_y^b are tangential surfaces stresses in the x and y direction respectively.

2.1.2 Evaluation of boundary shear stresses

The surface shear stresses in practice arise in environmental flows as a consequence of wind stresses Vreugdenhil (1994) and are a function of the external wind velocity near the surface and a shape factor. For the case of sloshing in a closed container one can as a very good approximation set $\tau_x^s = \tau_y^s = 0$. As for the shear stress at the bottom the situation is more complex. The size and direction of the shear stresses at the bottom is a complex function of surface roughness, Reynolds number, flow stationarity etc. and is an active area of research. Because of this complexity many researchers and engineers choose to describe the bottom stress using empirical formulas. A very popular formulation is the so-called Manning formula Madsen et al. (2005)

$$\tau_b^x = \gamma_B u_b \quad \gamma_B \tau_b^y = v_b \tag{2.13}$$

with

$$\gamma_B = \frac{g}{M^2(h+\eta)^{1/3}}\sqrt{u_b^2 + v_b^2} \tag{2.14}$$

where M is the manning number with the dimension $\mathrm{m}^{1/3}/\mathrm{s}$ (the inverse of the also commonly used Manning's n) and g is the gravitational constant . The assumption in (2.13) that the bottom stress is proportional to the square of the horizontal velocity

is valid only for stationary or near-stationary flows such as long period shallow water flows, where shear stresses and horizontal fluid velocity are in phase Vreugdenhil (1994). More explicitly it can be shown that the approximation is valid as long as the relation $h^2/\nu < 0.1T$ is fulfilled, where h is the water depth, ν the viscosity and T the period of the oscillating flow. An estimate of the eddy viscosity is $\nu \simeq 0.1$ m^2/s and $h_0 \simeq 0.1$ m giving a period $T > 1$ s which is valid for all our experiments. The friction coefficient (2.14) is seen to be inverse proportional to the total local water depth, and thus can be expected to have increasingly strong effects as the depth decreases. It must be stressed that the above discussion is based on some quite coarse simplifications. The boundary layer behavior for the sloshing problems considered in this context are very complex and include laminar and turbulent regions and transition regions between the two. Evaluating shear stresses based on the assumption of turbulent flow is conservative, i.e. turbulent wall shear stresses are much larger the laminar stresses Faltinsen and Timokha (2009), and can thus be used as a good starting point for evaluating the importance of bottom friction.

2.2 Governing equations in a non-inertial tank fixed coordinate system

The N-S equations given in (2.1)-(2.3), expressing conservation of momentum, are derived using Newton's second law which is well known only to be valid in an inertial system which is defined as system, or frame of reference, in which an object moves with a constant velocity unless acted on by external forces. The earth is a very good approximation of an inertial system for our case, however when considering e.g. tidal waves or atmospheric flows the earth can no longer be regarded as an inertial system but must instead be treated as a non-inertial system or a moving frame of reference.

For our case we want to study the fluid behavior relative to the tank motion and this is done most appropriately by introducing a tank fixed coordinate system from which all flow variables can be described locally. By choosing a non-inertial frame of reference we need to transform each variable from the original globally fixed, or inertial system, to the tank fixed coordinate system. The spatial derivatives are invariant, i.e. not affected by transformations, however the time derivatives are affected and have to be altered Faltinsen and Timokha (2009).

Let the translation and the angular velocity of the tank-fixed coordinate system be described by the following vector functions

$$\mathbf{R}(t)^{\mathrm{T}} = [X(t), Y(t), Z(t)] \quad \boldsymbol{\Omega}(\mathbf{t})^{\mathrm{T}} = [\dot{\theta}_1(t), \dot{\theta}_2(t), \dot{\theta}_3(t)] \tag{2.15}$$

and let the position and fluid velocity vector *relative* to the tank-fixed coordinate system be defined by

$$\mathbf{v}^{\mathrm{T}} = [u, v, w] \quad \mathbf{r}^{\mathrm{T}} = [x, y, z] \tag{2.16}$$

Then the absolute acceleration $\mathbf{V}_t$ of a particle is given by

$$\mathbf{V}_t = \ddot{\mathbf{R}} + \dot{\boldsymbol{\Omega}} \times \mathbf{r} + \boldsymbol{\Omega} \times (\boldsymbol{\Omega} \times \mathbf{r}) + \frac{\mathrm{D}\mathbf{v}}{\mathrm{D}t} + 2\boldsymbol{\Omega} \times \mathbf{v} \tag{2.17}$$

where we have used the notation $\dot{()} = \mathrm{d}()/\mathrm{d}t$ and the notation $\mathrm{D}\mathbf{v}/\mathrm{D}t$ to emphasize that it is the particle or material derivative. In (2.17) $\mathbf{v}$ is the non-inertial velocity, i.e. the velocity measured relative to the tank-fixed coordinate system, and the time derivatives (and convective terms naturally) in (2.1)-(2.3), must be replaced by the whole righthand side of (2.17) in order to describe the fluid motion in the tank-fixed coordinate system. Also the gravitational constant should be rotated according to Faltinsen and Timokha (2009):

$$g_1 = g\sin\theta_2, g_2 = -g\cos\theta_2\sin\theta_1, g_3 = -g\cos\theta_2\cos\theta_1 \tag{2.18}$$

It is obvious that rotation around the vertical z-axis θ_3 does not alter g. Finally the N-S equations expressed in a tank-fixed coordinate system are

$$u_t + (uu)_x + (uv)_y + (uw)_z = -p_x/\rho + (\nu u_x)_x + (\nu u_y)_y + (\nu u_z)_z + B_1 \tag{2.19}$$
$$v_t + (vu)_x + (vv)_y + (vw)_z = -p_y/\rho + (\nu v_x)_x + (\nu v_y)_y + (\nu v_z)_z + B_2 \tag{2.20}$$
$$w_t + (wu)_x + (wv)_y + (ww)_z = -p_z/\rho + (\nu w_x)_x + (\nu w_y)_y + (\nu w_z)_z + B_3 \tag{2.21}$$
$$u_x + v_y + w_z = 0 \tag{2.22}$$

with

$$\mathbf{B} = \begin{bmatrix} B_1 \\ B_2 \\ B_3 \end{bmatrix} = \begin{bmatrix} g\sin\theta_2 \\ -g\cos\theta_2\sin\theta_1 \\ -g\cos\theta_2\cos\theta_1 \end{bmatrix} - \ddot{\mathbf{R}} - \dot{\mathbf{\Omega}}\times\mathbf{r} - \mathbf{\Omega}\times(\mathbf{\Omega}\times\mathbf{r}) - 2\mathbf{\Omega}\times\mathbf{v} \tag{2.23}$$

2.2.1 Pure translation of non-inertial system

For a pure translational non-inertial system we have $\mathbf{\Omega} = \mathbf{0}$ and the $\mathbf{B}$ is simply

$$\mathbf{B} = \begin{bmatrix} B_1 \\ B_2 \\ B_3 \end{bmatrix} = \begin{bmatrix} 0 \\ 0 \\ -g \end{bmatrix} - \begin{bmatrix} \ddot{X}(t) \\ \ddot{Y}(t) \\ \ddot{Z}(t) \end{bmatrix} \tag{2.24}$$

2.2.2 Translation and rotation of 2D non-inertial system

Next consider the 2D case for translation and rotation, i.e. $\mathbf{R}^{\mathrm{T}} = [X, 0, Z]$ and $\mathbf{\Omega}^{\mathrm{T}} = [0, \dot{\theta}_2, 0]$. This results in the following additional terms

$$\mathbf{B} = \begin{bmatrix} B_1 \\ B_2 \\ B_3 \end{bmatrix} = \begin{bmatrix} g\sin\theta_2 \\ 0 \\ -g\cos\theta_2 \end{bmatrix} - \begin{bmatrix} \ddot{X}(t) + \ddot{\theta}_2 z + \dot{\theta}_2{}^2 x \\ 0 \\ \ddot{Z}(t) - \ddot{\theta}_2 x + \dot{\theta}_2{}^2 z - 2\dot{\theta}_2 u \end{bmatrix} \tag{2.25}$$

2.3 Shallow water theory

In the area of coastal engineering, concerned with areas such as modelling of flows in harbors, channels estuaries and rivers, a large variety of different possible wave conditions, bottom topographies etc. usually have to be analyzed for a given problem. For these problems a mathematical model should be able to at least account for nonlinear effects, and possibly also, depending on wether breaking occur or not, to account for frequency

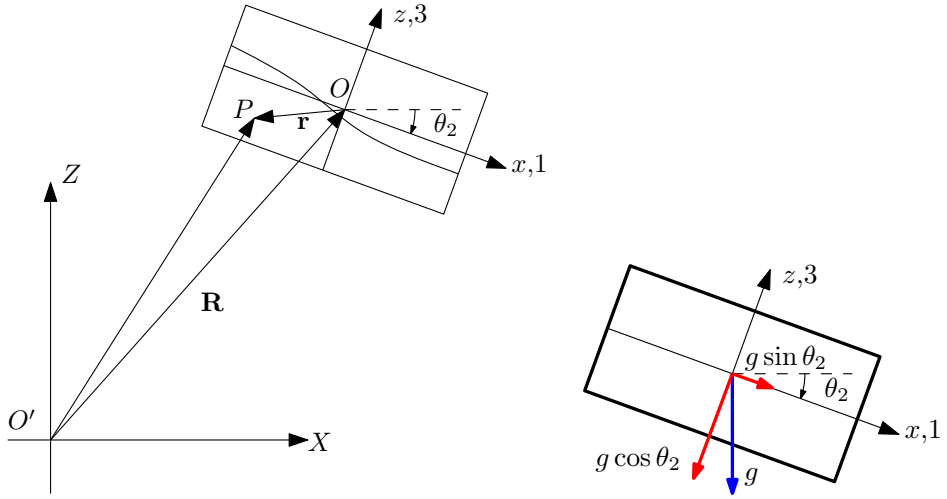

(a) Translation and rotation of non-inertial system

(b) Projection of g along the direction of local coordinate x and z axis.

Figure 2.1: *Translation and rotation of non-inertial frame of reference.*

dispersion effects, i.e. the effect that the wave celerity, or wave speed, depends on the wave length. The incompressible Navier-Stokes equations (2.1)-(2.4) would certainly provide a very accurate mathematical model for all these mentioned problems however the numerical solution of a problem would involve a three-dimensional spatial domain with a complex free surface boundary condition (2.6). The price, measured in CPU time, of solving such a model is very high and would for many practical applications require the use of a large computer cluster, and for other large problem it might simply be impossible to solve. For this reason more simple mathematical models have been developed by coastal engineers that reduces the number of equations involved but retains the most important physics of the problem. In practice the simplified mathematical models utilizes the shallow-water nature of these coastal near-shore problems, by averaging the Navier-Stokes equations through the depth reducing the order of the spatial dimension by one. But equally important, by averaging the continuity equation (2.4), the nonlinear free surface boundary condition is absorbed into this equation, thus requiring no special solution strategies for the complex free surface. Remember, as mentioned in the introduction, that capturing the free surface in the full N-S equations is by far trivial and a large number of methods have accordingly been developed with a sole purpose of handling this problem. The very natural question then of course arises: When can the water be treated as shallow?

2.3.1 Long wave theory - amplitude and frequency dispersion

Instead of the term shallow water the word long wave theory is often used instead as a general classification of waves with long wave lengths compared to the water depth. More precisely, according to the classical paper by Peregrine, the ratio of water depth h to wave length λ, i.e.

$$\sigma = \frac{h}{\lambda} \tag{2.26}$$

must satisfy $\sigma \ll 1$ for all long wave theories. However to finalize the classification of the wave a second parameter is needed expressing the ratio of wave height H to wavelength

$$\epsilon = \frac{H}{\lambda} \tag{2.27}$$

Before continuing with the classification two important definitions are introduced namely

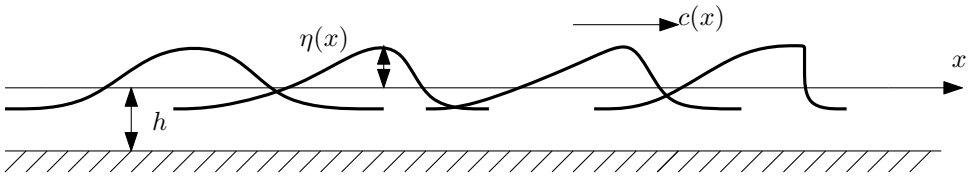

(a) Amplitude dispersion

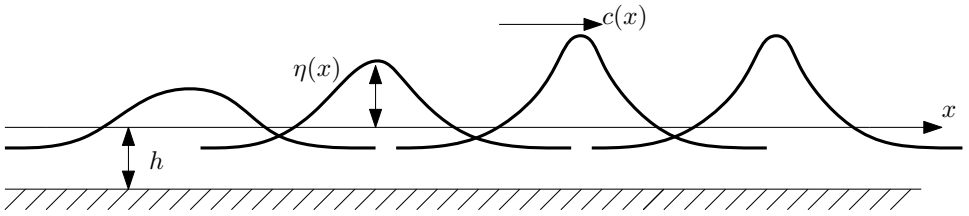

(b) Amplitude and frequency dispersion

Figure 2.2: *Illustration of amplitude and frequency dispersion.*

amplitude dispersion and frequency dispersion. The two definitions relate to how waves disperse or propagate. From linear shallow water theory it is well known that waves propagate with a celerity given by $c = \sqrt{gh}$ where h is the undisturbed water depth. Mathematically this is expressed as a constant value in the advection term in the wave equation, i.e. the u_x term. Imagine now that the advection is a function of the local fluid velocity, i.e. a nonlinear advection term of the form uu_x, then as u increases the celerity also increases. Nonlinear advection terms give rise to amplitude dispersion since $c(x) = \sqrt{g(h + \eta(x))}$, i.e. the deeper the total water depth the faster celerity. This phenomenon is illustrated in figure 2.2(a) showing that amplitude dispersion finally leads to a breaking wave characterized by a vertical front or a shock. The importance of amplitude dispersion is governed by the term ϵ, i.e. by the magnitude of the wave amplitude H compared to the wave length. A consequence of amplitude dispersion is that the wave will *always* break independent of the initial conditions. Of course from real life experience we know that this is certainly not the case. By adding a so-called dispersion term to the equations they now become what is called frequency dispersive. In general in literature the term dispersion is related to frequency dispersion, and simply implies that the propagation speed of the wave depended on the wave number, i.e. the wave length. Notice for case of pure amplitude dispersion that the celerity is independent of the wave length, i.e. they contain no frequency dispersion. By including frequency dispersion the classical soliton waves are produced as shown in 2.2(b) where the wave gathers in to a hump of water. This hump will never break which certainly is not true either since we know that for a certain steep front eventually the wave will break. But breaking never occurs due to an equilibrium between the nonlinear advection term and the dispersion terms. The

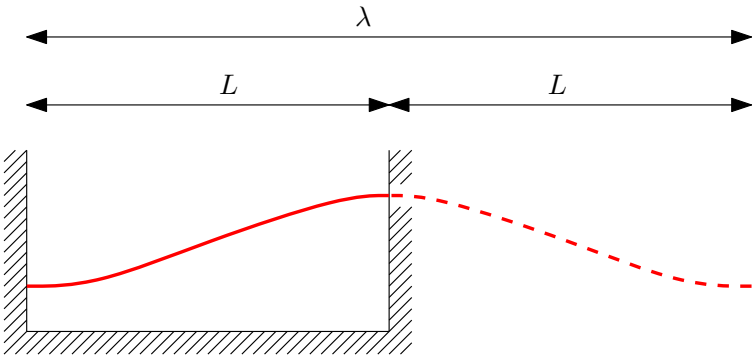

Figure 2.3

importance of frequency dispersion is determined from the magnitude of σ, i.e. the depth ratio h/λ.

Using the above two parameters there are three cases that can be considered Svendsen (1994): **Case 1:** $\epsilon \ll \sigma^2$

The situation corresponds to the case of very small wave amplitudes and linear theory can be used. Frequency dispersion should be included

Case 2: $\epsilon = \sigma^2$

This is the case studied by Peregrine Peregrine (1967) and is the case where nonlinear effects, i.e. amplitude dispersion, is of the same order of magnitude as the frequency dispersion. The derived equations are termed the Boussinesq equations. In the derivation the vertical velocity is approximated by a linear variation leading to a non-hydrostatic pressure distribution.

Case 3: $\epsilon \gg \sigma^2$

This corresponds to the case where the amplitude dispersion dominates the problem. Amplitude dispersion simply means that the wave celerity depends on the wave amplitude. As a result of this an initially smooth wave will eventually steepen or break as the particles at the highest point of the wave moves faster than particles below. This behavior is described by the so-called Nonlinear Shallow Water equations (NSW equations) or St. Venant equations. The equations have no frequency dispersion in the sense that the wave celerity is independent of the wavelength as as aforementioned only depend on the amplitude of the wave. The vertical velocity is assumed negligible leading to a hydrostatic pressure distribution.

Now returning to the question posed before entering this discussion on long wave theory on when to use shallow water or not? Based on the previous discussion a more relevant question is: When can we assume shallow water, and if in fact we can assume shallow water should frequency dispersion be included or not? It turns out that the two questions can not be entirely separated. Thus for flows classified by Case 2, i.e. where frequency and amplitude dispersion are of same order, the theory requires $h/\lambda < 0.1$ Le Méhauté (1976). For case 3, i.e. for flows with steepening waves, it turns out that $h/\lambda < 0.05$. Two important notes should be made here. First of all the given limits are only guiding and should be treated as such. Secondly the limits given here are based on waves in open waters and therefor may not apply to sloshing problems. As show in figure 2.3 the first sloshing mode in a rectangular tank has a wave length twice the tank length

$\lambda = 2L$. Thus for the above classifications to apply for sloshing one might assume that for case 2 we would require $h/L < 0.2$ and for case 3 $h/L < 0.1$, i.e. more favorable restrictions.

Regarding the question on wether to include frequency dispersion or not it is the motivation of this work to describe sloshing for relatively large base amplitudes which by experimental verification is known to lead to breaking waves. For this reason we concentrate on the NSW equations and leave the frequency dispersive Boussinesq equations.

2.4 The NSW equations in a non-inertial system

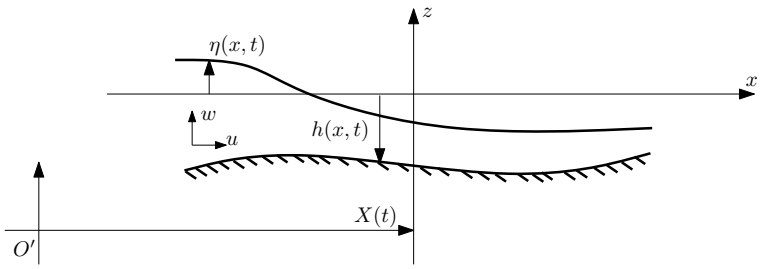

Figure 2.4: *Sketch of flow domain*

In the following the nonlinear shallow water equations, NSW equations, for a newtonian fluid in a non-inertial frame are derived. The various simplifications performed in the derivation will be addressed and discussed. The shown derivation follows Casulli (2007); Pinder (1977), but is however extended by formulating the fluid equations in a pure horizontally translational coordinate system, i.e. $\mathbf{B}^{\mathrm{T}} = [\ddot{X}(t), \ddot{Y}(t), -g]$.

The derivation of the NSW equations in essence consist of first simplifying the vertical momentum equation (2.21), then integrating the horizontal momentum equations (2.19)-(2.20) as well at the continuity equation (2.22), and in the process utilizing the boundary conditions (2.6)-(2.7) together with the shear stresses (2.9)-(2.12) to simplify the integrated expressions. The derivation is most naturally started with integration of the continuity equation since no assumptions are made in this part.

2.4.1 Integration of the continuity equation

Integrating the continuity equation (2.22) over the depth, i.e. from $-h$ to η yields

$$\int_{-h}^{\eta} u_x dz + \int_{-h}^{\eta} v_y dz + \int_{-h}^{\eta} w_z dz \tag{2.28}$$

We are looking for terms expressing the average particle velocity i.e.

$$U(x,y,t) = \frac{1}{H}\int_{-h}^{\eta} u(x,y,z,t)dz \quad V(x,y,t) = \frac{1}{H}\int_{-h}^{\eta} v(x,y,z,t)dz \tag{2.29}$$

where the total depth H is defined as

$$H(x,y,t) = h(x,y) + \eta(x,y,t) \tag{2.30}$$

Thus, (2.28) must be manipulated such that the integration and differentiation operator switch positions. For this the Leibniz integral rule can be used, expressing

$$\int_{a(x)}^{b(x)} \frac{\partial f(x,z)}{\partial x} dz = \frac{\partial}{\partial x} \int_a^b f dz + \frac{\partial a}{\partial x} f(x,a) - \frac{\partial b}{\partial x} f(x,b) \tag{2.31}$$

i.e. the differentiation operator is moved outside the integral by adding two additional terms including the differentiation of the lower and upper integration limit. Using this result (2.28) is rewritten as

$$\begin{aligned} &\frac{\partial}{\partial x} \int_{-h}^{\eta} u dz - u^s \eta_x + u^b (-h)_x + \\ &\frac{\partial}{\partial y} \int_{-h}^{\eta} v dz - v^s \eta_y + v^b (-h)_y + w^s - w^b = 0 \end{aligned}$$

Applying the boundary conditions (2.6)-(2.7) yields the depth integrated continuity equation

$$\eta_t + \frac{\partial}{\partial x} \int_{-h}^{\eta} u dz + \frac{\partial}{\partial y} \int_{-h}^{\eta} v dz = 0 \tag{2.32}$$

The equation is rewritten using (2.29) as

$$H_t + (HU)_x + (HV)_y = 0 \tag{2.33}$$

Here it is also utilized that the bottom variation function of space only, and therefor η can be replaced by H under the time differentiation. Some authors define the two variables Madsen et al. (2005)

$$Q = HU, \quad P = HV \tag{2.34}$$

which inserted in (2.33) gives

$$H_t + Q_x + P_y = 0 \tag{2.35}$$

It is quite remarkable that the nonlinear surface and bottom boundary conditions have been absorbed in the continuity equation and that the final partial differential equation reduces to a simple linear 2D advection equation.

2.4.2 Assumptions on the vertical momentum equation

In flows where the horizontal length scales are large compared to vertical scales one can assume that the vertical acceleration of the fluid, as well as the vertical viscous forces are small compared to the acceleration of gravity and to the pressure gradient in the vertical direction Casulli and Cheng (1992). Consequently, by neglecting the acceleration and viscous terms in the vertical momentum equation the following equation for pressure results

$$p_z = B_3 = -\rho g \tag{2.36}$$

The pressure equation readily yields the pressure distribution in the depth by integration

$$p(x,z,t) = p_e(x,t) + \rho g\left(\eta(x,t) - z\right) \tag{2.37}$$

where $p_e(x,t) = p_0$ is the excess pressure. The pressure distribution is clearly seen to be hydrostatic which is a consequence of neglecting inertia and viscous forces in the vertical direction. Substituting the pressure expression (2.37) into the horizontal momentum equations yields the following two dimensional model equations

$$u_t + (uu)_x + (uv)_y + (uw)_z = -g\eta_x + (\nu u_x)_x + (\nu u_y)_y + (\nu u_z)_z + B_1 \tag{2.38}$$

$$v_t + (uv)_x + (vv)_y + (vw)_z = -g\eta_y + (\nu v_x)_x + (\nu v_y)_y + (\nu v_z)_z + B_2 \tag{2.39}$$

$$H_t + (HU)_x + (HV)_y = 0 \tag{2.40}$$

The above three equations contain four unknowns u, v, w and η, so in order to close the system an additional fourth equation is needed or one of the variables have to be eliminated. It turns out that by integrating the horizontal momentum equations the vertical particle velocity can be eliminated using the kinematic surface bottom boundary conditions, thereby closing the system of equations.

2.4.3 Integration of horizontal momentum equations

To keep a sense of perspective in these somewhat tedious manipulations, we split the procedure up into four parts: first the left hand side of the momentum equation, i.e. the advection terms, is integrated, secondly the pressure term on the right hand side is treated, thirdly the inhomogeneous source term which arise as a consequence on the non-inertial system description is integrated and finally the viscous terms are integrated.

Advection terms

Vertical integration of the left hand side of equation (2.38) from bottom to top yields:

$$\begin{aligned}
&\int_{-h}^{\eta} [u_t + (uu)_x + (uv)_y + (uw)_z] dz \\
= \;& \frac{\partial}{\partial t}\int_{-h}^{\eta} u dz + \frac{\partial}{\partial x}\int_{-h}^{\eta} uu dz + n\frac{\partial}{\partial y}\int_{-h}^{\eta} uv dz \\
- \;& u^s[\eta_t + u^s\eta_x + v^s\eta_y - w^s] + u^b[u^b(-h)_x + v^b(-h)_y - w^b] \\
= \;& (HU)_t + (HUU)_x + (HUV)_y \qquad (2.41) \\
+ \;& \frac{\partial}{\partial x}\int_{-h}^{\eta} (u-U)^2 dz + \frac{\partial}{\partial y}\int_{-h}^{\eta} (u-U)(v-V) dz \qquad (2.42)
\end{aligned}$$

Pressure term

Integrating the pressure term yields

$$\int_{-h}^{\eta} g\eta_x dz = Hg\eta_x \tag{2.43}$$

The integrated result is slightly rewritten in order to use H, and not η, as a variable

$$Hg\eta_x = gH(\eta + h)_x - gHh_x = (\tfrac{1}{2}gH^2)_x - gHh_x \tag{2.44}$$

Non-inertial term

Integration of the inhomogeneous term from the non-inertial description needs to be performed. Here caution should be shown since B_1 is in general a function of $\mathbf{r}$ and hence can not in general be multiplied by the depth as for the pressure term (2.43). However for the case of pure translational motion the result is

$$\int_{-h}^{\eta} B_1 dz = -H\ddot{X}(t) \tag{2.45}$$

where $X(t)$ is a known function of time.

2.4.4 Viscous terms

Integration of the viscous terms on the right side of (2.38) yields

$$\begin{aligned} & \int_{-h}^{\eta} [(\nu u_x)_x + (\nu u_y)_y + (\nu u_z)_z] dz \\ = \; & \frac{\partial}{\partial x} \int_{-h}^{\eta} \nu u_x dz + \frac{\partial}{\partial y} \int_{-h}^{\eta} \nu u_y dz \\ - \; & \nu(u_x \eta_x + u_y \eta_y - u_z)|_{z=\eta} + \nu(u_x(-h)_x + u_y(-h)_y - u_z)|_{z=-h} \end{aligned}$$

The last two terms in the above equation are seen to equal the shear stresses in the x-direction at the surface and bottom, τ_x^s and τ_x^b respectively, as expressed by (2.9) and (2.11). The two first advection terms in the above equation can not directly be evaluated. How ever, by adding and subtracting both of the following integrals $\int_{-h}^{\eta} \nu U_x dz$ and $\int_{-h}^{\eta} \nu V_x dz$, yields the following

$$\begin{aligned} & \frac{\partial}{\partial x} \int_{-h}^{\eta} \nu U_x dz + \frac{\partial}{\partial y} \nu U_y dz + \tau_s^x - \tau_b^y \\ + \; & \frac{\partial}{\partial x} \int_{-h}^{\eta} \nu (u-U)_x dz + \frac{\partial}{\partial y} \int_{-h}^{\eta} (u-U)_y dz \\ = \; & (\bar{\nu} H U_x)_x + (\bar{\nu} H U_y)_y + \tau_x^s - \gamma_B U \qquad (2.46) \\ + \; & \frac{\partial}{\partial x} \int_{-h}^{\eta} \nu (u-U)_x dz + \frac{\partial}{\partial y} \int_{-h}^{\eta} (u-U)_y dz - \gamma_B (u^b - U) \qquad (2.47) \end{aligned}$$

where the vertically averaged viscosity coefficient $\bar{\nu}$ is defined as

$$\bar{\nu} = \frac{1}{H} \int_{-h}^{\eta} \nu dz \tag{2.48}$$

2.5 The final equations

In the previous, the momentum equation in the x-direction was integrated vertically and the exact same steps follow for the momentum equation in the y-direction. If u and v are assumed independent of z, i.e. the vertical variation of the horizonal particle velocities is

assumed small, then the terms in (2.42) and (2.47) disappear and the full depth averaged equations are

$$(HU)_t + (HUU + \tfrac{1}{2}gH^2)_x + (HUV)_y = gHh_x - H\ddot{X}$$
$$+(\bar{\nu}HU_x)_x + (\bar{\nu}HU_y)_y - \gamma_B U \tag{2.49}$$
$$(HV)_t + (HUV)_x + (HVV + \tfrac{1}{2}gH^2)_y = gHh_y - -H\ddot{Y}$$
$$+(\bar{\nu}HV_x)_x + (\bar{\nu}HV_y)_y - \gamma_B V \tag{2.50}$$
$$H_t + (HU)_x + (HV)_y = 0 \tag{2.51}$$

Here the surface stresses have been neglected i.e. $\tau_x^s = \tau_y^s = 0$. These three coupled PDEs are the complete depth averaged NSW equations, including viscosity, for a non-inertial system, which have to be solved for the three unknown function $U(x, y, y)$, $V(x, y, t)$ and $H(x, y, t)$. Numerical methods for solving the equations will be discussed in the next chapter.

2.5.1 Discussion of viscosity and bottom topography

The depth averaged momentum equations (2.49) and (2.50) each contain three terms accounting for viscous effects. The first two terms in each equation account for viscous effects in the fluid bulk and the last terms for bottom friction. In the foregoing analysis the viscosity term ν has not been addressed detailed and has as such been regarded as a known function in space and time. To establish a function would either require extensive experimental measurements or detailed CFD analysis, both which are out of scope with the present work. Instead we choose to neglect the two terms for the bulk viscosity and focus only the the bottom friction term. As discussed earlier, the physical processes in the bottom boundary layer are complex, and we have already chosen the well known engineering approach as discussed in e.g. Brocchini et al. (2001) or Madsen et al. (2005) to approximate the friction components using the Manning formula 2.13. Also in this light it seems excessive to include further complicated viscosity terms.

As regards the inhomogeneous terms describing the effect of bottom topography it is seen that the terms enter the equations as a constant defined by the slope of the bottom multiplied with the water depth. In the following a flat bottom is assumed and the bottom terms disappear. The final set of equations can now be written as

$$(HU)_t + (HUU + \tfrac{1}{2}gH^2)_x + (HUV)_y = -H\ddot{X}(t) - \gamma_B U \tag{2.52}$$
$$(HV)_t + (HUV)_x + (HVV + \tfrac{1}{2}gH^2)_y = -H\ddot{Y}(t) - \gamma_B V \tag{2.53}$$
$$H_t + (HU)_x + (HV)_y = 0 \tag{2.54}$$

2.6 Flux or velocity formulation

As discussed earlier the formation of breaking waves are expected in the solution due to relative large base motion amplitudes. In the NSW equations a breaking wave appears in the solution as a moving hydraulic jump often termed a bore in coastal engineering. Mathematically a moving hydraulic jump, which in essence is a discontinuity, is called a shock. To handle shocks correctly one should show show extra care in choosing the

correct mathematical formulation as this turns out to be crucial for the behavior of the solution. In the following two apparently identical formulations, but with quite different behavior, are presented and discussed.

First we put the derived equations (2.52)-(2.54) on matrix vector form as

$$\mathbf{U}_t + \mathbf{F}(\mathbf{U}) + \mathbf{G}\mathbf{U} = \mathbf{S}(\mathbf{U}) \tag{2.55}$$

where the *conserved* vector of variables is

$$\mathbf{U} = \begin{bmatrix} H \\ HU \\ HV \end{bmatrix} \tag{2.56}$$

and

$$\mathbf{F}(\mathbf{U}) = \begin{bmatrix} HU \\ HUU + \frac{1}{2}gH^2 \\ HUV \end{bmatrix} \quad \mathbf{G}(\mathbf{U}) = \begin{bmatrix} HV \\ HUV \\ HVV + \frac{1}{2}gH^2 \end{bmatrix} \tag{2.57}$$

$$\mathbf{S}(\mathbf{U}) = \begin{bmatrix} 0 \\ -H\ddot{X}(t) - \gamma_B U \\ -H\ddot{Y}(t) - \gamma_B V \end{bmatrix} \tag{2.58}$$

The formulation given here is the so-called flux formulation which conserves the variables given in $\mathbf{U}$ which are mass H, and momentum in the two horizontal directions HU and HV respectively. These variables are often referred to as physical variables since they conserve the physical quantities of mass and momentum Toro (Apr 2009). It is remarkable fact that these equations *implicitly* describe the energy dissipation that is well known to occur across a bore or hydraulic jump. This is a very strong motivation for using the equations for complex sloshing problems involving wave breaking and is in fact probably the only simplified fluid model capable of this. Certainly the Boussinesq type equations discussed previously can not capture this effect.

Many researchers often formulate the NSW equations in another set of variables, known as mathematical variables, which are the particle velocities in the two directions, i.e. U and V, and the mass H is left unchanged. This formulation is known as the velocity formulation and is easily derived by expanding the derivatives in (2.52) and (2.53):

$$U_t + UU_x + VU_y = -H\ddot{X}(t) - \gamma_B U \tag{2.59}$$
$$V_t + UV_x + VV_y = -H\ddot{Y}(t) - \gamma_B V \tag{2.60}$$
$$H_t + (HU)_x + (HV)_y = 0 \tag{2.61}$$

For the 2D case, i.e. for $V = \mathbf{G} = 0$, the matrix vector form of the equations are

$$\mathbf{U} = \begin{bmatrix} H \\ U \end{bmatrix} \tag{2.62}$$

$$\mathbf{F}(\mathbf{U}) = \begin{bmatrix} HU \\ \frac{1}{2}UU + gh \end{bmatrix} \quad \mathbf{S}(\mathbf{U}) = \begin{bmatrix} 0 \\ -H\ddot{X}(t) - \gamma_B U \end{bmatrix} \tag{2.63}$$

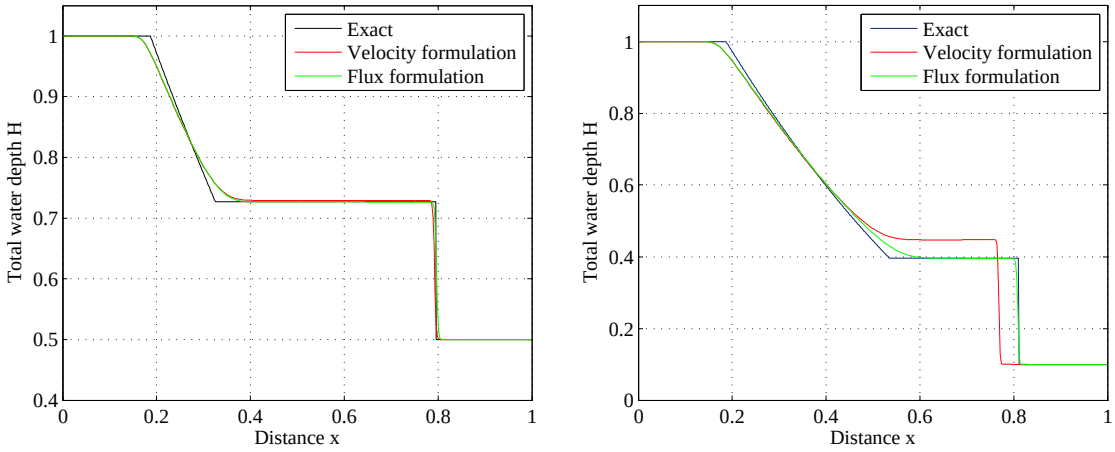

(a) $H_R/H_L = 0.5$ (b) $H_R/H_L = 0.1$

Figure 2.5: *Dam-break problem using a momentum conserving and velocity conserving formulation*

Even though the flux formulation (2.52)-(2.54) and (2.59)-(2.61) may seem identical they are far from it. In Krabbenhoft et al. (2010a) the two formulations were investigated and it was found that for strong shocks, i.e. large discontinuities in the water depth, the velocity formulation failed to converge to the exact solution, while the flux formulation clearly converged, see figure 2.5. For weaker shocks the discrepancy between the two methods became less pronounced. However as there is no difference in the complexity of the solution procedure of the two formulations one should always use the flux formulation thereby guaranteeing conservation of momentum.

2.7 Important sloshing parameters - the 2D case

It is convenient to rewrite the NSW equations on non-dimensional form to extract governing dimensionless parameters. In papers concerning TLD's the base motion amplitude to tank length ratio A/L has been used Reed et al. (1998); Yu et al. (1999) to characterize the dampers, but the used ratio has not been justified on a theoretical basis. Also no other parameters for characterizing the a TLD exists. In this section all dimensional variables are starred unless otherwise stated. Furthermore, without any loss of generality, we consider only the 2D case of (2.55)-(2.58) by setting $V = 0$.

2.7.1 Nondimensionalization

In the following the bottom is assumed to be flat, i.e. $h = h_0$. Assuming the base motion as being sinusoidal the horizontal acceleration of the tank is given by

$$\ddot{X}^*(t^*) = -A^*\Omega^{*2}\sin(\Omega^* t^*) \tag{2.64}$$

The scaling parameters are chosen as follows:

$$x^* = x/k^*, t^* = t/\omega_w^*, H^* = Hh_0^*, U^* = \sqrt{gh_0^*}U \tag{2.65}$$

where $k^* = \pi/L^*$, L^* is the tank length, $\omega_w^* = k^*\sqrt{gh_0}^*$ the lowest linear sloshing frequency of the water using a shallow water assumption, h_0^* the *mean* still water level (in general $h = h(x)$) and g the acceleration of gravity. The following identities are obtained using the chainrule and 2.65

$$\frac{\partial()}{\partial t^*} = \frac{\partial()}{\partial t}k^*\sqrt{gh_0^*} \qquad \frac{\partial()}{\partial x^*} = \frac{\partial()}{\partial x}k^* \tag{2.66}$$

Combining (2.64)-(2.66) with (2.55)-(2.58) the nondimensionalized set of mass and momentum conserving equations are derived

$$\mathbf{U}_t + \mathbf{F}(\mathbf{U})_x = \mathbf{S}(\mathbf{U}, x, t) \tag{2.67}$$

$$\mathbf{U} = \begin{pmatrix} H \\ HU \end{pmatrix}, \mathbf{F} = \begin{pmatrix} HU \\ HU^2 + \frac{1}{2}H^2 \end{pmatrix}, \mathbf{S} = \begin{pmatrix} 0 \\ -\gamma\frac{|U|U}{H^{1/3}} + H\Lambda\Omega^2\sin(\Omega t) \end{pmatrix} \tag{2.68}$$

$$\begin{array}{lll} \text{I.C.} & : & H(x,0) = 1,\ U(x,0) = 0 \\ \text{B.C.} & : & U(\frac{\pi}{2},t) = U(\frac{\pi}{2},t) = 0 \end{array} \tag{2.69}$$

with the dimensionless parameters

$$\beta = \frac{\Omega^*}{\omega_w^*} \qquad \Lambda = A^*k^* = \pi\frac{A^*}{L^*} \qquad \gamma = \frac{g}{\mu M^{*2}h_0^{*1/3}} \tag{2.70}$$

where the depth ratio μ has been defined as

$$\mu = h_0^*k^* = \pi\frac{h_0^*}{L^*} \tag{2.71}$$

The depth parameter is only relevant as long as friction term is present. From the nondimensionalization we can conclude that the sloshing problem in shallow water is alone governed by the three dimensionless parameters in (2.70): a frequency parameter β, an amplitude parameter Λ and finally a friction parameter γ. It should be emphasized that the analysis is based on the NSW equations, and the parameters are as such only meaningful from a practical point of view as long as the NSW equations captures the relevant physics involved in given problem. As mentioned in the introduction it is the objective of the current work to clarify this.

The magnitude of the forcing term from the base motion of the tank is seen to be a product of the amplitude parameter Λ, as stated by previous researchers Reed et al. (1998); Yu et al. (1999), and the frequency ratio squared β^2. At resonance, which is the working area of interest, the forcing frequency is approximately equal to the linear sloshing frequency $\Omega^* \simeq \omega_w^*$ resulting in $\beta \simeq 1$, leaving as an approximation Λ as the only relevant parameter with respect to the forcing term. Further more, neglecting the bottom friction and sloping bottom the depth term and friction parameter vanishes leaving Λ as the only relevant parameter. This is a very strong results and shows the motivation for establishing the parameter range for which the NSW equations are valid. Returning to the first term

on the right side of (2.68) the strength of the friction term depend, not surprisingly, on the inverse of the depth parameter μ. This is in agreement with e.g. Brocchini et al. (2001), but also from a physical argumentation it seems reasonable based on the fact that the dissipating bottom boundary layer extends relatively over a larger part of the total water depth for shallow water. A parameter study in Krabbenhoft et al. (2010a) showed that the effect of bottom friction, for realistic depth ratios and surface roughness has little effect on the liquid sloshing response. The result confirms the supposition that the majority of dissipation stems from turbulence in the moving hydraulic jump.

2.7.2 Non dimensional sloshing force and energy dissipation

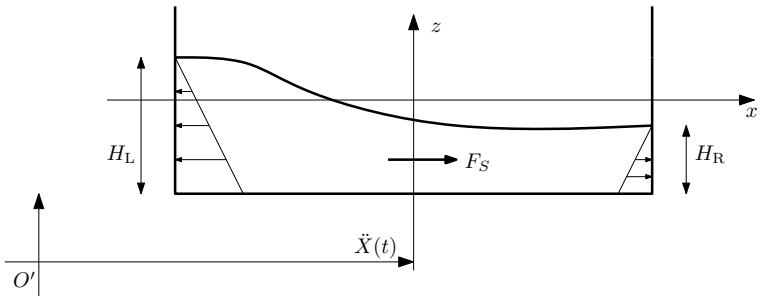

Figure 2.6: *Definition of horizontal sloshing force F_S using a hydrostatic pressure assumption*

For the shallow water case the sloshing force, i.e. the force containing both the inertial and dynamic contribution Krabbenhoft et al. (2010a,b), is calculated using the hydrostatic pressure assumption as the difference between the integrated pressure on the right and left tank wall

$$F_S^* = \tfrac{1}{2}\rho^* g({H_R^*}^2 - {H_L^*}^2) \tag{2.72}$$

The sloshing force is nondimensionalized with the maximum inertial force of the water treated as a solid mass

$$F_S = \frac{F_S^*}{m_w^* A^* {\Omega^*}^2} = \frac{1}{2\pi\Lambda\beta^2}(H_L^2 - H_R^2) \tag{2.73}$$

where m_w^* is the total mass of water pr. tank width. Another important quantity is the work done by the sloshing force pr. forcing period defined as

$$\Delta E^* = \int_T^* F_S^* dX^*(t^*) \tag{2.74}$$

With respect to TLD's (2.74) is a measure of structural energy being dissipated pr. cycle by the sloshing force. For this reason we refer in the following to ΔE^* as the dissipated energy pr. cycle. ΔE^* is nondimensionalized as follows

$$\Delta E = \frac{\Delta E^*}{\frac{1}{2}m_w^*(A^*\Omega^*)^2} = \frac{2}{\Lambda}\int_T F_S dX(t) \tag{2.75}$$

The factor $\frac{1}{2}m_w^*(A^*\Omega^*)^2$ is not the energy of liquid motion but simply a reference value.

2.8 Summary and conclusion

Solving the full Navier-Stokes equations for simulating Tuned Liquid Dampers is too excessive for several pragmatic reasons. The first, and foremost reason, is the CPU time required for solving the set of equations. A simulation time of seconds can easily require hour, days or even weeks of CPU time. In the future with growing computer power this approach may become attractive. Second, constructing numerical schemes for capturing the complex discontinuous surface profile, as we expect to be present, is a rather complicated problem and requires specialized methods which rely on empirical tuning parameters for guaranteeing stability of the free surface.

The following conclusions can be drawn:

- By assuming long wave theory and vertical particle velocities to be unimportant the full N-S equations can be approximated by the so called Nonlinear Shallow Water equations or St. Venant equations. The dimension of the problem is hereby reduced by 1, and the description of the free surface is treated exactly and much easier than for the full 3D problem.

- The NSW equations are amplitude dispersive and are capable of describing wave breaking. For the base amplitudes A and tank lengths L considered, breaking waves will indeed be present for the majority of practical cases of interest. For lower base amplitudes the generated wave amplitudes will become smaller and for this case a Boussinesq type formulation, including frequency dispersion, should be used. The Boussinesq equations conserve energy and thus empirical constants must be added to account for dissipation in the boundary layers and surface Keulegan (1959); Miles (1967); Vandorn (1966); Lepelletier and Raichlen (1988).

- The NSW equations can be formulated with two different sets of conserved variables, namely mass and momentum, known as the flux formulation, and mass and particle velocity, known as the velocity formulation. It is important to use the correct formulation, given by the flux formulation, in order to estimate the correct speed of the bore known as the shock speed. If the flux formulation is used the equations implicity capture the energy dissipation across the bore and no empirical constants are required.

- The effect of bottom friction is found to have little effect on the liquid sloshing for relevant tank parameters.

- By performing a nondimensionalization it is found that the shallow water sloshing can be described by only three dimensionless parameters and only two for the non-viscous case. The depth enters the equations as a pure scaling parameter and thus does not alter the behavior of the solution. In other words, if the NSW equations provide a applicable model for the sloshing behavior, then the engineer in a design situation should pay no special attention to the depth but solely focus on the A/L-ratio. This will make the deign process of the TLD much simpler.

With respect to the last point the fundamental question then naturally arises: do the NSW equations in fact constitute an usable model, and if yes for which depth ratios h/L,

amplitude ratios A/L and frequency ratios β does the model perform well. In order to answer these questions a strategy for solving the NSW equations must be established which is the topic of the following chapter.

Chapter 3

Numerical methods

Having established a mathematical model the equations must be solved to provide a solution. Analytical solutions are always preferred, however establishing analytical solutions to nonlinear partial differential equations is extremely difficult, time consuming and often impossible. Instead the equations must be solved *approximately* using a numerical method.

Having constructed and implemented a numerical methods it is essential to verify that the method gives reliably results, i.e. solves the mathematical problem with an acceptable accuracy. The only way to verify this is by testing the numerical method on problems where an analytic solution exists. If an analytical solution does not exist then one must be constructed.

This chapter focuses on the choice, development and verification of numerical methods.

3.1 Mathematical models - classification

In the present research the numerical work has almost entirely been focused on the solution of the mathematical fluid models. The solution of linear structural systems is far more simple and the description of a coupled TLD-structure model is presented in Krabbenhoft et al. (2010c) where solution strategies for the structural model is addressed. In the following the focus is on mathematical models of the type:

$$\mathbf{U}_t + \mathbf{F}(\mathbf{U}) + \mathbf{G}(\mathbf{U}) = \mathbf{S}(\mathbf{U}) \tag{3.1}$$

Here $\mathbf{U}$ is a vector of conserved variables and $\mathbf{F}$ and $\mathbf{G}$ are, in general, nonlinear vector functions of $\mathbf{U}$ and $\mathbf{S}$ is a source term vector. The system of Partial Differential Equations (PDEs) in (3.1) is by mathematicians referred to as a first order hyperbolic system of partial differential equations. A subclass of hyperbolic equations are the so-called System of Balance Laws, or SBL in short, to which the equation in (3.1) belongs. If the source terms is omitted, i.e. only the homogeneous part is considered, the equations are often called a System of Conservation Laws, or SCL in short LeVeque (2002). The term conservation stems form the fact that in certain volume quantities are conserved and can change only due to disturbances along the volume boundary.

Elliptic equations, and thus SBL's and SCL's, can be characterized as being wave-like. This means that disturbances in a certain point in a domain is felt only locally and

from the disturbance position propagates with a finite speed out into the domain along certain routes know as *characteristics*. This local character of the equations makes the use of explicit methods very attractive. The behavior of hyperbolic equations is thus qualitatively fundamentally different from e.g. parabolic equations, such as heat flow, where a disturbance on the boundary immediately is felt in the complete domain.

It is well know that the hyperbolic systems of equations given by the NSW equations will develop discontinuous solutions, also know as shocks, even when given smooth initial conditions. Handling of shocks or discontinuous solutions is in general very difficult to treat numerically and is an important parameter when choosing a numerical methods.

The source term in (2.55) constitute another possible difficulty. We showed in (2.14) that the term describing bottom friction may become very large for shallow water depths. Such source terms are commonly classified as being *stiff* and are notoriously difficult to treat numerically.

3.2 Choice of numerical method

In theory, and practice, many different numerical method can be used for solving System of Balance Laws as (3.1), and in-fact many different methods are being used. The choice of method relies on many different factors where an important one is without doubt based on tradition. The most popular methods for solving SCL's and SBL's, though, seem to be the Finite Volume (FV) method, followed by the Finite Difference (FD) method and Finite Element (FE) method, where the last mentioned seems to be growing in popularity. A methods which is receiving much attention is the so called Discontinuous Galerkin (DG) method, which is a hybrid of standard Galerkin FE and the FV method. In the area of gas dynamics, the Euler equations of gas dynamics, or just the compressible Euler Equations, take the form given by (3.1). Gas dynamics is an that has been researched extensively during the last century and he FV method has been used widely in this research which has matured it significantly. Also, as discussed earlier, the nature of the NSW equations eventaully lead to discontinuities in the solution in the shape of bores or shocks, and this is naturally described in a FV context, as opposed to e.g. a FD method where derivatives are approximated by finite differences which can be expected to break down near discontinuities.

During the period of this PhD study all methods, except the standard FE method, were examined and tested, and we found that the FV method suited our specific needs the best.

3.3 The Finite Volume Method

One of the main differences of the FV method, compared to e.g. FD or FE methods, is that the domain of interest is broken down into grid *cells* or volumes, rather than into grid points. Each grid cell is defined by its boundaries or volume and a point, typically chosen in the barycenter (center of mass) of the volume, at which the *average* of the variable of interest is defined. I.e the discrete approximate solution is represented by averaged values at the barycenter of the discrete cells rather than approximations of the solution at single points.

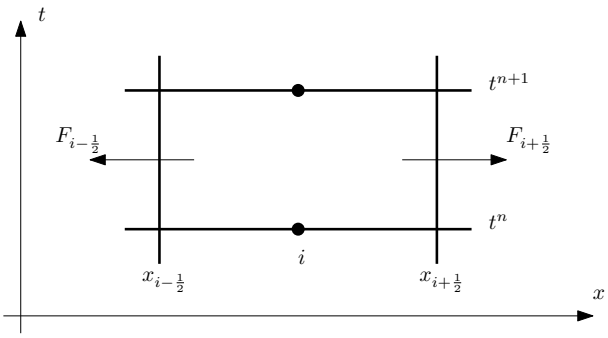

Figure 3.1: *Control volume V_i in space and time.*

Without any significant loss of generality we start out by considering the 2D SCL given by

$$\mathbf{U}_t + \mathbf{F}(\mathbf{U}) = \mathbf{S}(\mathbf{U}) \tag{3.2}$$

with

$$\mathbf{U} = \begin{bmatrix} H \\ Q \end{bmatrix} \quad \mathbf{F}(\mathbf{U}) = \begin{bmatrix} Q \\ Q^2/H + \frac{1}{2}gH^2 \end{bmatrix} \tag{3.3}$$

where the momentum Q is defined by $Q = HU$. The above system of PDEs corresponds to the homogeneous 2D case of the NSW equations given in (2.55)-(2.58). The equation stated in e.g. (3.2) is called the differential form a SCL and is valid only for the case of smooth solutions. A more general form of the equation is the integral form which is derived by integrating (3.2) along the boundary of the domain, i.e.

$$\oint [\mathbf{U}_t + \mathbf{F}(\mathbf{U})_x] ds = \mathbf{0} \tag{3.4}$$

Choosing a quadrilateral control volume in the $x - t$ plane with the dimensions

$$V_i = [x_{i-\frac{1}{2}}, x_{i+\frac{1}{2}}] \times [t^n, t^{n+1}] \tag{3.5}$$

he following integral form of the balance law is derived

$$\mathbf{U}_i^{n+1} = \mathbf{U}_i^n - \frac{\Delta t}{\Delta x_i}[\mathbf{F}_{i+\frac{1}{2}} - \mathbf{F}_{i-\frac{1}{2}}] \tag{3.6}$$

where the average value of the solution in the element $Q_i =]x_{i-\frac{1}{2}}, x_{i+\frac{1}{2}}[$ is given by

$$\mathbf{U}_i^n = \frac{1}{\Delta x_i} \int_{x_{i-\frac{1}{2}}}^{x_{i+\frac{1}{2}}} \mathbf{U}(x, t^n) dx \tag{3.7}$$

and

$$\mathbf{F}_{i+\frac{1}{2}} = \frac{1}{\Delta t} \int_{t^n}^{t^{n+1}} \mathbf{F}(\mathbf{U}(x_{i+\frac{1}{2}}, t)) dt \tag{3.8}$$

In the above the element size Δx and time increment $\Delta t$is defined by

$$\Delta x_i = x_{i+\frac{1}{2}} - x_{i-\frac{1}{2}} \quad , \quad \Delta t = t^{n+1} - t^n \tag{3.9}$$

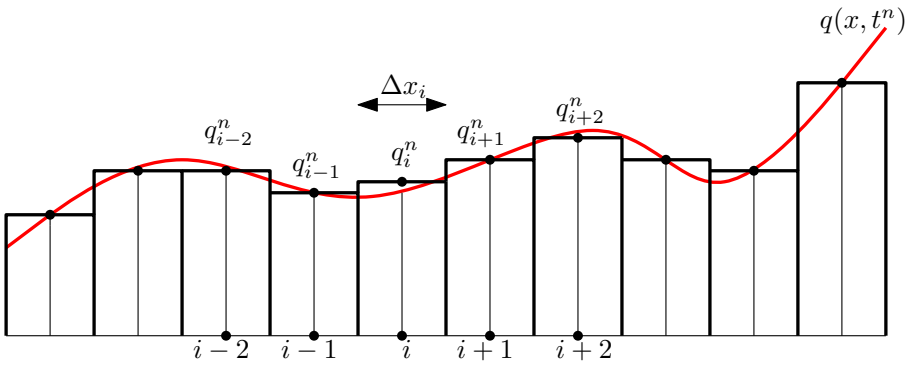

Figure 3.2: *Averaged smooth solution*

The equation stated in (3.6) is *exact*, and is the integral form of of the SCL defined on differential form in (3.2). The main point here is that the derived integral form of the equations have no limitations regarding discontinuities, and hence notice that no differential operators appear in (3.6)-(3.8) but rather only integral operators are present. In fact we want to use the form (3.6) directly as a numerical scheme and in order to do so, the numerical fluxes $\mathbf{F}_{i\pm\frac{1}{2}}$ must be approximated in some way. The Russian mathematician Sergei Godunov proposed a method for this purpose and thereby gave birth to a whole class of methods known as Godunov methods.

3.4 Godunov method

The idea proposed by Godunov is in fact very simple and relies on the physics of the considered problem. Godunov utilized the fact that when a smooth solution $q(x,t)$ is discretized by averages as shown in figure 3.2 then the interface between each cell is in in fact characterized by a so-called Riemann problem. The Riemann problem is defined by the following initial value problem

$$\left.\begin{aligned} \mathbf{U}_t + \mathbf{F}(\mathbf{U}) &= \mathbf{0} \\ \mathbf{U}(x,0) &= \begin{cases} \mathbf{U}_L \\ \mathbf{U}_R \end{cases} \end{aligned}\right\} \tag{3.10}$$

The initial value problem is sketched in figure 3.3 at the initial time and the depth and velocity are shown beneath the initial state at a later time $t = t_*$. This problem shows two characteristic wave patterns that also were observed in the performed sloshing experiments. A shock wave, or compression wave, travels from left to the right. The shock moves from high depth to shallow depth with a certain speed. To the left a so-called rarefraction wave, or a depression wave is present which is not characterized, as the shock, by a *single* front but instead by a head and a tail front and a smooth behavior in between. The wave patterns in $x-t$ space is depicted at the lowest graph. Here the shock is seen to be describe by a single line in $x-t$-space, called a characteristic, which gives the position and speed of the shock. To the left the rarefraction wave is described by a so-called *fan* of characteristics with a clear head and tail. What is extremely interesting about the wave pattern is that in the region $x/t = 0$ the solution is constant for all t. This is simply the nature of the Riemann problem and it can be shown that the solution,

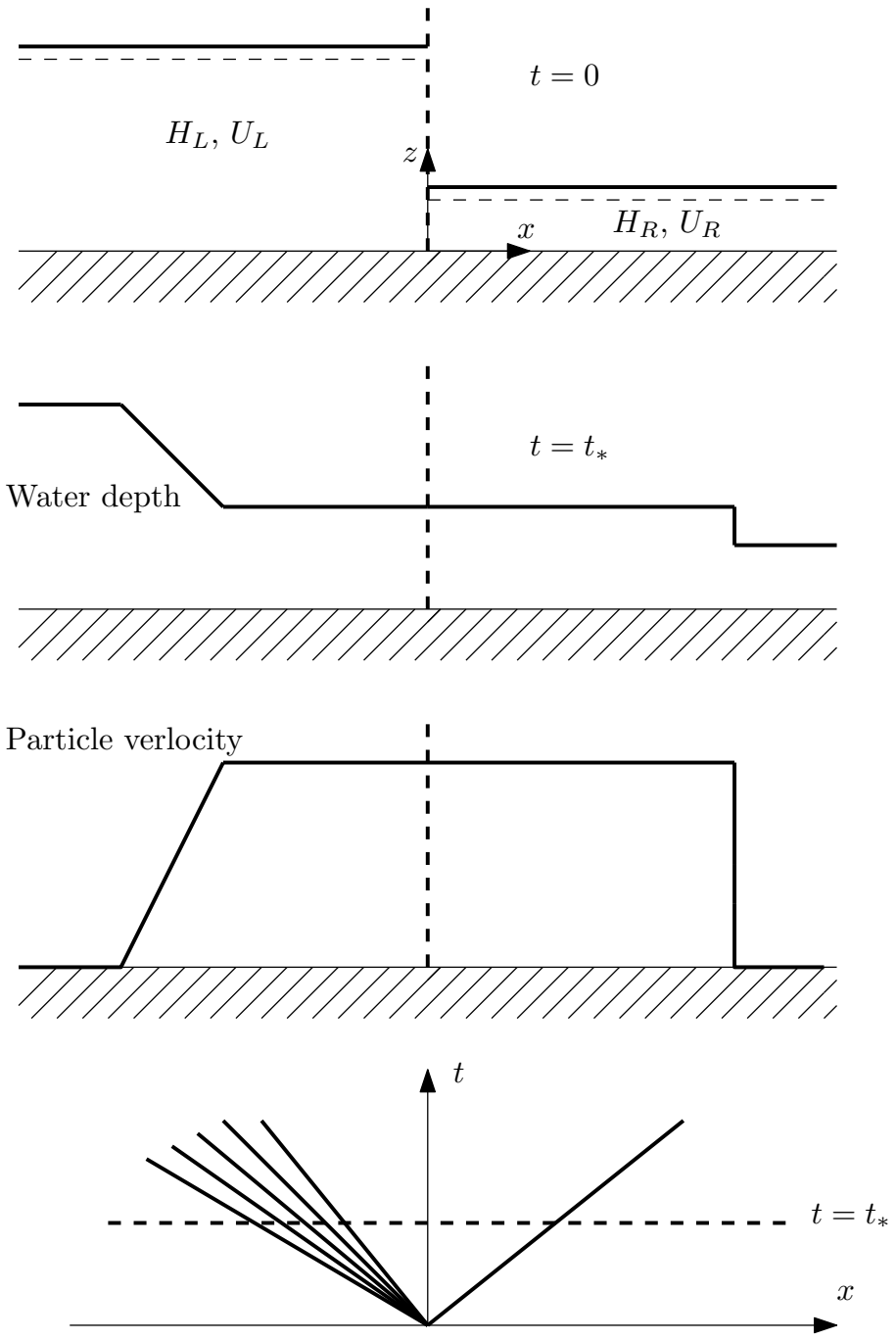

Figure 3.3: *Riemann problem*

depending on the initial conditions, can be described by a total of ten different wave patters of the kind shown at the bottom of figure 3.3 Toro (April 2001). All solution bare the property with a constant solution in time at $x/t = 0$. Recall that the the numerical flux function, that we are after, is defined by the following integral

$$F_{i+\frac{1}{2}} = \frac{1}{\Delta t} \int_{t^n}^{t^{n+1}} \mathbf{F}(\mathbf{U}(x_{i+\frac{1}{2}}, t))dt \tag{3.11}$$

i.e. the integral evaluated in time at an element boundary. It has just been shown that the solution at the edge is constant in time so the numerical flux can simply be evaluated as

$$F_{i+\frac{1}{2}} = \mathbf{F}(\mathbf{U}_{i+\frac{1}{2}}(0)) \tag{3.12}$$

where the solution vector along the line $x/t = 0$ is $\mathbf{U}_{i+\frac{1}{2}}(x/t = 0)$. Having evaluated the numerical fluxes along the boundaries the solution can be updated suing (3.6) which ends the description of Gudonov methods. Of course there are some unanswered questions: how is the solution at the interface along the line $x/t = 0$ actually found and what about time stepping restrictions.

3.4.1 Time stepping

The time stepping restriction is very simple. We demand that each of the Riemann problems at all the interfaces of the domain do not interact. Thus if the fastest wave speed in the entire domain is say $S_{\max}$ and the smallest element length is Δx, then the restriction of the time step is simply

$$\Delta t < \mathrm{CFL}\frac{\Delta x}{S_{\max}} \tag{3.13}$$

The CFL number, or courant number, should in general be chosen between 0 and 1 to guarantee stability. Often CFL = 0.9 is chosen in practice. The maximum wave speed $S_{\max}$ can be estimated using the following formula

$$S^n_{\max} = \max_i \left\{ |U^n_i| + \sqrt{gH^n_i} \right\} \tag{3.14}$$

3.4.2 Acquiring solution along $x/t = 0$

Given the Riemann problem (3.10) it is actually possible to derive the exact solution. The complete solution of the Riemann problem is described in Toro (April 2001). The group of solver that use the exact solution of the Riemann problem to find the solution along all the element interface are know as exact Riemman solvers. The exact Riemann solvers are quite slow since the process of finding the solution along the element boundary requires all ten wave patterns to be looked through, also known as the sampling process, and is very time consuming. The so-called Random Choice Method, or Glimm's methods, relies on the exact solution of the Riemann problem. Alternatively the Riemann problem can be solve approximately which has given name to a very popular class of solvers known as approximate Riemann solvers.

3.5 Approximate Riemann solvers

An exhaustive collection of approximate Riemann solver is given by Toro in the Toro (April 2001,A). The most popular approximate Riemann solvers are the HLL method, developed by Harten, Lax and Van Leer, the method of Roe and finally the Rusanov method. The complexity of the methods vary from a derivation point of view but from an implementation point of view they are quite similar.

In general the computation of a flux at a given element interface, say at location $x_{i+\frac{1}{2}}$ requires information of the states on each side of the interface, i.e. $\mathbf{U}_i$ and $\mathbf{U}_{i+1}$ for the right boundary on element i. Thus the computation of the numerical flux can be written as

$$\mathbf{F}_{i+\frac{1}{2}} = \mathbf{F}_h(\mathbf{U}_L, \mathbf{U}_R) \tag{3.15}$$

where $\mathbf{F}_h$ is some function based on an approximative solution of the Riemann problem. The subscript L and R refer to left and right state, respectively. For the the flux at the right boundary in (3.15) $\mathbf{U}_L = \mathbf{U}_i$ and $\mathbf{U}_R = \mathbf{U}_{i+1}$. We choose to use the Rusanov scheme, with the following flux function:

$$\mathbf{F}^{Rus}_{i+\frac{1}{2}} = \frac{1}{2}(\mathbf{F}(\mathbf{U}^n_L) + \mathbf{F}(\mathbf{U}^n_R)) - \frac{1}{2}S^+\Delta t(\mathbf{U}^n_R - \mathbf{U}^n_L) \tag{3.16}$$

where

$$S^+ = \max\{|U_L| + a_L, |U_R| + a_R\}, a_L = \sqrt{gH_L} \tag{3.17}$$

3.6 Source terms

Source terms potentially constitute a difficulty for the case of stiff source terms. However non stiff source terms are in general more easy to treat using a splitting procedure. Including a source term the update formula (3.6) is simply augmented with an additional term

$$\mathbf{U}^{n+1}_i = \mathbf{U}^n_i - \frac{\Delta t}{\Delta x_i}[\mathbf{F}_{i+\frac{1}{2}} - \mathbf{F}_{i-\frac{1}{2}}] + \Delta t\mathbf{S}_i \tag{3.18}$$

with

$$\mathbf{S} = \frac{1}{\Delta t}\frac{1}{\Delta x_i}\int_{x_{i-\frac{1}{2}}}^{x_{i+\frac{1}{2}}}\int_{t_n}^{t_{n+1}} \mathbf{S}(\mathbf{U}, x, t)dxdt \tag{3.19}$$

In general we find that using a simple forward Euler integration in space and time works well, i.e.

$$\mathbf{S}_i \simeq \mathbf{S}(\mathbf{U}^n_i, x_i, t^n) \tag{3.20}$$

3.7 High order methods

The methods mentioned so far have all been first order methods, i.e. the approximation error is of order Δx. The methods are relatively simple to implement, stabile and monotone, but have the rather big disadvantage of being very dissipative. This is essentially what guarantees their stability. As our focus is analyzing sloshing behavior in tanks, and a very important part of the problem is estimating the internal fluid damping, it is important that the estimated energy dissipation stems from the physics and not from the numerical methods. This was our main motivation for implementing a high order method. Another motivation is that certain high order methods can treat stiff source terms very efficiently which may become important when including bottom friction for very shallow water depths.

To start the discussion once aging we return to the *exact* update formula given in (3.6). The accuracy of the method simply depends on the accuracy of the numerical fluxes $\mathbf{F}_{i\pm\frac{1}{2}}$

and the accuracy of the state vector $\mathbf{U}_i$, expressing the averaged value of the state within element i. Thus in order to increase the accuracy, or order of the method, the order of the spatial discretization must be increased but also the temporal elapse of the state vector must be established in order to compute the numerical flux (3.8) with a higher degree of accuracy.

3.7.1 Spatial discretization - reconstruction

When using the FV method one always operates on average cell values. This is simply in the structure of the method as seen when deriving the integral form of the conservation law. Consider an initially smooth function at time n, $q(x, t^n)$, depicted in figure 3.2 and approximate this smooth function by cell averages as shown with the black staircases. Then the order of the proposed method will naturally depend on the accuracy of which these cell averages represent the solution. The simplest 1. order method simply approximates the initial smooth solution with the averages

$$q_i^n = \frac{1}{\Delta x_i} \int_{i-\frac{1}{2}}^{i+\frac{1}{2}} q(x, t^n) dx \tag{3.21}$$

Even though the integral in (3.21) is done *exactly* the variation of solution $q(x, t)$ is now represented as a staircase function and therefor the approximate solution is of order $O(\Delta x)$.

Given the exact averages, which can always be computed using any high order Gaussian quadrature, it is however possible to *reconstruct* the initial smooth solution. Thus using average values a variables does not prohibit a higher order spatial discretization of the solution and thereby a higher order method. Often the local solution is reconstructed using polynomials: a first order method reconstructs using a polynomium of order 0, i.e. a constant value, a second order methods reconstructs the solution using a first order polynomium, i.e. s straight line, and so on.

There is however quite a substantial aber dabei when increasing the method to a higher order which is concerned with the smoothness or monotonicity of the solution. In connection with his PhD work Godunov derived a theorem directly related to construction of higher order methods. The theorem states that:*all linear schemes of accuracy greater than one will produce spurious oscillations in the vicinity of discontinuities* Toro (April 2001). Linear in this context is essentially linked to the reconstruction operator, i.e. how the reconstruction is performed. The theorem is analogous of saying that any linear scheme having the property of providing non-oscillatory, i.e. monotone, solutions can at most have 1. order accuracy. For this reason it was not until Van Leer in the early nineteen seventies were able to develop a second order scheme without spurious oscillations Toro (April 2001).

As a result of Godunov's theorem an extensive research has been done, and is still very active, on reconstructions techniques that provide a non-oscillatory solution. The most popular are the Total Variational Deminishing (TVD) schemes for second order accuracy and Essential Non Oscillatory (ENO) and Weighted Essential Non Oscillatory (WNEO) reconstruction schemes, for higher order accuracy Dumbser et al. (2008). Common for all three methods is that they provide a *nonlinear* reconstruction of the solution across

the element and thus circumvent Godunovs first theorem and provide non-oscillatory solutions. There are many ways of performing the ENO or WENO reconstruction Liu et al. (1994); Jiang and Shu (1996); Hu and Shu (1999), where the WENO approach suggested in Dumbser et al. (2008), has been used in the present work.

We start by defining the new relative space variable ξ

$$x = x_{i-\frac{1}{2}} + \xi \Delta x \quad , \xi \in [0, 1] \tag{3.22}$$

Given the cell averaged data $\bar{q}_j^n$ (in the following a bar is used to emphasize that this is an average value) in all elements Q_j we want to construct a spatial polynomial in element Q_i, based on cell averaged data at time t^n, of the form

$$w_i(\xi, t^n) = \sum_{l=0}^{M} \Psi_l(\xi) \hat{w}_l(t^n) \tag{3.23}$$

where $\Psi(\xi)$ are re-scaled Legendre polynomials that form an orthogonal basis on the interval $I = [0, 1]$. Thus, coefficients $\hat{w}(t^n)$ needs to be computed. For the method to be conservative the reconstructed polynomial should conserve the initial averaged data for element Q_i *and* the surrounding elements Q_j, i.e.

$$\int_{Q_j} w_i(\xi, t^n) d\xi = \sum_{l=0}^{M} \int_{Q_j} \Psi_l(\xi) d\xi \ \hat{w}_l(t^n) = \bar{q}_j^n \tag{3.24}$$

This integral conservation laws enables os to compute the coefficients but first a number of stencils, i.e. a collection of elements, must be defined. The reconstruction is performed for every element, and for each element a number of stencils must defined where the size of the stencil defines the order of the reconstruction. Define the stencils S_i^s, for element i by

$$S_i^s = \bigcup_{j=i+s-k}^{i+s+k} \tag{3.25}$$

where s is the stencil shift, i the element for which the reconstruction is performed and k the length of the stencil. For our case three stencils are used for each element: a central stencil S_i^0, left stencil S_i^{-k} and a right stencil S_i^k. Choosing a reconstruction polynomial of order $M = 2$, i.e. a third order method, results in a stencil with spatial extension $k = 1$ Dumbser et al. (2008). The three stencils for this case are shown in figure 3.4. Using (3.24) and (3.25) a linear system of equations can be used to find the coefficients $\hat{w}_l$, i.e.

$$A_{jl} \cdot \hat{w}_l^{(i,s)} = \bar{q}_j^n \tag{3.26}$$

where standard tensor notation is used. Notice that the system of equations in (3.26) must be solved for each stencil. The linear reconstruction process will for $k = 1$ provide three reconstructed polynomials $w_i^{-k}(\xi, t)$, $w_i^0(\xi, t)$ and $w_i^k(\xi, t)$ but only one is needed. In order to obtain the final non-oscillatory reconstruction polynomial for element Q_i the, altogether nine, coefficients obtained from (3.26) will be combined into three values by

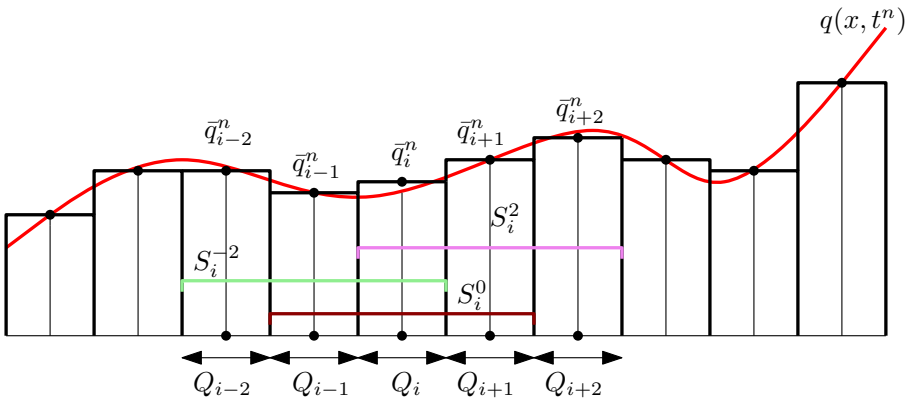

Figure 3.4: *Left, centered and right stencil for Q_i with $k = 1$.*

weighting these with nonlinear weights obtained from the averaged values. The final polynomial is

$$w_i(\xi, t^n) = \hat{w}_l^i(t^n)\Psi_l(\xi) \tag{3.27}$$

with

$$\hat{w}_l^i(t^n) = \omega_0 \hat{w}_l^{(i,0)}(t^n) + \omega_{-k}\hat{w}_l^{(i,-k)}(t^n) + \omega_k \hat{w}_l^{(i,k)}(t^n) \tag{3.28}$$

The nonlinear weights are computed as

$$\omega_s = \frac{\tilde{\omega}_s}{\omega_0 + \omega_{-k} + \omega_k}, \quad \tilde{\omega} = \frac{\lambda_s}{(\sigma_s + \varepsilon)^r} \tag{3.29}$$

The oscillation indicator σ_s is defined by

$$\sigma_s = \Xi_{lm}\hat{w}_l^s \hat{w}_m^s, \qquad \Xi_{lm} = \sum_{\alpha=1}^{M} \int_0^1 \frac{\partial^\alpha \Psi_l(\xi)}{\partial \xi^\alpha} \frac{\partial^\alpha \Psi_m(\xi)}{\partial \xi^\alpha} d\xi \tag{3.30}$$

where M is the degree of the reconstruction polynomial. Note that the so-called oscillation indicator matrix Ξ_{lm} is is independent of the mesh and of the problem and is thus universal. The parameters ε and r are constant and we choose $\varepsilon 10^{-14}$ and $r = 12$. The linear weights λ_s are chosen as $\lambda_1 = \lambda_{-1} = 1$ and a large central weight $\lambda_0 = 10^5$ Dumbser et al. (2008). Using these weights, which are empirical and, then by experience the reconstructed polynomial will be monotone. Using the above nonlinear weights the central stencil is used in regions with a smooth solution and for shocks, which occur very locally, the left or right stencils will automatically be preferred.

3.7.2 Local space-time representation

Having established a higher order spatial reconstruction polynomial the last thing we need to take care of, in order to construct a high order method, is the time integration. The lowest order of the space or temporal discretization will decide the order of the complete scheme. In many WENO methods the spatial reconstruction shown just earlier is combined with a Runge-Kutta integration scheme for the time integration. This mean that in each of the Runge-Kutta steps the reconstruction procedure must be performed and furthermore the limits on the time step are often very restrictive with CFL conditions

of the type $\Delta t = O(\Delta x^2)$ Dumbser et al. (2008). Another route, and the one chosen here, is the so-called local space-time DG method proposed by Dumbser et al. (2008). The idea is to construct a local space-time representation of the solution and then integrate the numerical fluxes (3.8) in time and use the standard updating formula (3.6). This will result in scheme with a time step restriction of the type $\Delta t = O(\Delta x)$ and furthermore the reconstruction needs to be performed only once per time step. Instead a space-time representation must be constructed and then a numerical integration of the fluxes, and eventual source terms, must be performed. In the following a detailed description of the method is performed. The derivation is performed for a scalar nonlinear Balance Law but the procedure follows exactly the same steps for a System of Balance Laws Dumbser et al. (2008). Thus, consider the scalar nonlinear Balance Law:

$$u_t + f(u)_x = s(u) \tag{3.31}$$

It is convenient to make a change of variables in space and time defined by

$$x = x_{i-\frac{1}{2}} + \Delta x_i \xi \quad t = t^n + \tau \Delta t \quad 0 \leq \tau, \xi \leq 0 \tag{3.32}$$

Using (3.32) in (3.31) yields

$$u_\tau + \frac{\Delta t}{\Delta x} f(u)_\xi = \Delta t s(u) \quad , u = u(\xi, \tau) \tag{3.33}$$

where the constants on the flux and source term arises from the coordinate transformation The computational domain is covered by spatial elements $Q_i =]x_{i-\frac{1}{2}}, x_{i+\frac{1}{2}}[$ and cell average of $u(\xi, \tau)$ within Q_i at time t^n is defined by

$$\bar{u}_i^n = \int_0^1 u(\xi, 0) d\xi \tag{3.34}$$

Integrating (3.33) in dimensionless space ξ and time τ leads to the well know update formula (3.6)

$$\bar{u}_i^{n+1} = \bar{u}_i^n - \frac{\Delta t}{\Delta x_i}(f_{i+\frac{1}{2}} - f_{i-\frac{1}{2}}) + \Delta t S_i \tag{3.35}$$

with

$$f_{i-\frac{1}{2}} = \int_0^1 f(u_i(0, \tau)) d\tau \quad S_i = \int_0^1 \int_0^1 s(u_i(\xi, \tau)) \tag{3.36}$$

As discussed in 3.5 the computation of the numerical flux in general requires the states on either side of the given interface. I.e. considering the interface at position $x_{i+\frac{1}{2}}$, or $\xi = 1$, requires the use of $u_i(1, \tau)$ and $u_{i+1}(0, \tau)$ in the computation of the numerical flux $f_{i+\frac{1}{2}}$. The solution in space and time is approximated by the following sum

$$u_i(\xi, \tau) \simeq \sum_{l=1}^{N} \Phi_l(\xi, \tau) \cdot \hat{u}_l^i := \Phi_l(\xi, \tau) \hat{u}_l^i \tag{3.37}$$

where the sum is expressed using classical summation convention in tensor calculus, i.e. summation over all indexes that appear twice. The space-time test functions $\Phi_l(\xi, \tau)$ are constructed using Lagrange polynomials in space and time $\Psi(\xi)$ and $\Psi(\tau)$ as

$$\Phi_k(\xi, \tau) = \Psi_i(\xi) \cdot \Psi_j(\tau) \tag{3.38}$$

j \ i	0	1	2
0	1	2	3
1	4	5	6
2	7	8	9

Figure 3.5: *Mono-index k for given values of i and j.*

where k is so-called mono-index ranging from 1 to the number of degrees of freedom $N = (M+1)^2$, where M is the order of the polynomials used. For the current work we have used $M = 2$, i.e. polynomials of 2. order and thus the mono-index ranges from 1 to 9. Now the governing PDE (3.33) is multiplied with the test functions (3.38) and integrated over the element in space and time

$$\left\langle \Phi_k, \frac{\partial}{\partial \tau} u_i \right\rangle + \frac{\Delta t}{\Delta x} \left\langle \Phi_k, \frac{\partial}{\partial \xi} f(u_i) \right\rangle = \Delta t \left\langle \Phi_k, s(u_i) \right\rangle \rangle \tag{3.39}$$

where the space-time operator is defined by

$$\langle f, g \rangle = \int_0^1 \int_0^1 f(\xi, \tau) g(\xi, \tau) d\xi d\tau \tag{3.40}$$

In a standard Discontinuous Galerkin (DG) scheme one would apply integration by parts thereby first moving the derivative onto the test function and secondly introducing information about the neighbor elements. How ever in the present context we are only interested in a local formulation and thus do not integrate by parts in space. The integration by parts is performed only in the temporal part which yields

$$[\Phi_k, u_i]_1 - [\Phi_k, w_i]_0 - \left\langle \frac{\partial}{\partial \tau} \Phi_k, u_i \right\rangle + \frac{\Delta t}{\Delta x} \left\langle \Phi_k, \frac{\partial}{\partial \xi} f(u_i) \right\rangle = \langle \Phi_k, s(u_i) \rangle \tag{3.41}$$

where the spatial integration operator has been defined by

$$[f, g]_\tau = \int_0^1 f(\xi, \tau) g(\xi, \tau) d\xi \tag{3.42}$$

Note that the temporal differentiation is removed and for $\tau = 0$ the state is effectively defined by the reconstruction polynomial $w_i = \Psi_m(\xi) \hat{w}_m^i(t^n)$, as discussed earlier. At time $\tau = 1$ we consider the solution inside the element and thus by introducing the ansatz (3.37) and the reconstruction polynomial at time t^n into (3.41) yields

$$\begin{aligned} &\left([\Phi_k, \Phi_l]_1 - \left\langle \frac{\partial}{\partial \tau} \Phi_k, \Phi_l \right\rangle \right) \hat{u}_l^i \\ &- [\Phi_k, \Psi_m]_0 \hat{w}_m^i(t^n) + \frac{\Delta t}{\Delta x_i} \left\langle \Phi_k, \frac{\partial}{\partial \xi} f(u_i) \right\rangle - \Delta t \left\langle \Phi_k, S(\Phi_l \hat{u}_l^i) \right\rangle = 0 \end{aligned} \tag{3.43}$$

The numerical flux can approximated by

$$f(u_i) \simeq \Phi_k f(\hat{u}_l^i) \tag{3.44}$$

which results in the final nonlinear system of equations for the unknown $\hat{u}_l^i$:

$$\left([\Phi_k, \Phi_l]_1 - \left\langle \frac{\partial}{\partial \tau} \Phi_k, \Phi_l \right\rangle \right) \hat{u}_l^i$$
$$-[\Phi_k, \Psi_m]_0 \hat{w}_m^i(t^n) + \frac{\Delta t}{\Delta x_i} \left\langle \Phi_k, \frac{\partial}{\partial \xi} \Phi_k \right\rangle f(\hat{u}_l^i) - \Delta t \left\langle \Phi_k, S(\Phi_l \hat{u}_l^i) \right\rangle = 0 \quad (3.45)$$

The system of equations can be written in a more compact format as

$$\left(F_{kl}^1 - K_{kl}^\tau \right) \hat{u}_l^i - F_{km}^0 \hat{w}_m^i + \frac{\Delta t}{\Delta x_i} K_{kl}^\xi f(\hat{u}_l^i) - \Delta t S_l = 0 \quad (3.46)$$

In practice the nonlinear system of equations (3.46) is solved by constructing an initial guess $\hat{u}_l^{(i,1)}$ using the reconstruction coefficients $\hat{w}_m^i$, which is know for local time $\tau = 0$, and solving

$$u_l^{(i,2)} = \left(F_{kl}^1 - K_{kl}^\tau \right)^{-1} \left(\Delta t S_l - \frac{\Delta t}{\Delta x_i} K_{kl}^\xi f(\hat{u}_l^{(i,1)}) + F_{km}^0 \hat{w}_m^i \right) \quad (3.47)$$

Using $\hat{u}_l^{(i,2)}$ new fluxes and source terms are computed and a new value $\hat{u}_l^{(i,3)}$ is computed. The procedure converges very quickly and the mentioned procedure is approximately three times for the solution to converge.

3.7.3 Summing up

We can now summarize the described method and the steps needed in order to solve general nonlinear Balance Laws. For *each* element the following steps should be performed:

I Compute the reconstruction polynomials $\hat{w}_m^i(t^n)$ at time t^n given the cell averages $\bar{u}_i^n$ using (3.28).

II Compute the local space-time solution $\hat{u}_l^i$ by solving the system of nonlinear equations in (3.46).

III Use the solution $u_i(\xi, \tau)$ to compute the source and numerical fluxes in (3.36) using a gaussian quadrature and update the solution using (3.35).

Its quite clear from the the previous that the derived method is extremely complex compared to the first order approximate Riemann solvers discussed earlier. Not only is the price in implementation increased substantially but also the CPU time is increased quite dramatically. The reason for the large increase in CPU time is mainly due to the solution of the nonlinear system of equations (3.47) but also by the fact that the Gaussian quadrature is performed when evaluating the source terms and numerical fluxes.

In the implementation polynomials of 2. degree are used corresponding to a third order method. This results in a source vector S_l with nine elements. Each element in the source vector has the form

$$S_l = \left\langle \Phi_k, S(\Phi_l \hat{u}_l^i) \right\rangle = \int_0^1 \int_0^1 \Psi_i(\xi) \Psi_j(\tau) S(\xi, \tau) d\xi d\tau \quad (3.48)$$

Table 3.1: *Initial values used for the dam-break problem*

H_L $[m]$	U_L $[m/s]$	H_R $[m]$	U_R $[m/s]$	x_c $[m]$	t_{end} $[s]$
1.0	0.0	0.5	0.0	0.5	0.1

Using second order polynomials thus results in an integrand of minimum fourth order, depending on the order of the source term. The Gaussian quadrature very quickly grows in size and for our case we found it necessary to use three points in space *and* time resulting in 9 terms to be evaluated for each element in the source term matrix S_l, i.e. a total of 81 evaluation for *each* element.

The price is certainly high, but in return the scheme is extremely robust, third order accurate and able to handle stiff source terms which may be relevant when studying friction terms in very shallow water.

3.8 Numerical tests

The purposes of performing the numerical test is fist and foremost to establish a solid foundation for determining what numerical scheme to use. I.e. is a low order scheme sufficient or should a high order method be used. We have implemented the first order Godunov scheme and the third order scheme discussed in 3.7. Both schemes have been tested a reported in Krabbenhoft et al. (2010a) and in the following we discuss the results. In all tests the 2D NSW equations (3.2), with and with out source terms, are treated.

If implemented correctly it is without any doubt that the high order scheme will outperform a lower order scheme. On the other hand, the implementation cost and CPU time, is much greater for a high order scheme so we would rather use a simple, and efficient low order scheme. The method should be able to capture shocks, handle source terms, and have low numerical dissipation, compared to physical dissipation. These three points are discussed in the following sections

3.8.1 Shocks

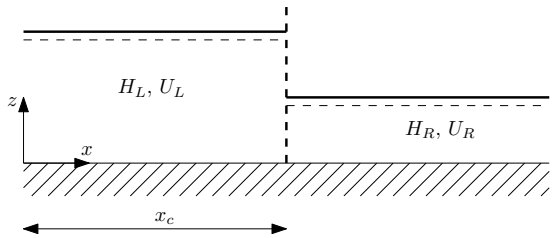

Figure 3.6: *Dam-break problem. Initial depth profile at time* $t = 0$

The dam break problem is a classical test case for verifying shock capturing capabilities of a method. The vertical wall at position $x_c$is remove at time $t = 0$ and the water depth and particle velocities are computed at a later time $t_end = 0.1s$. The problem corresponds to a classical Riemann problem as discussed in 3.4 and contains a right moving *shock*, or

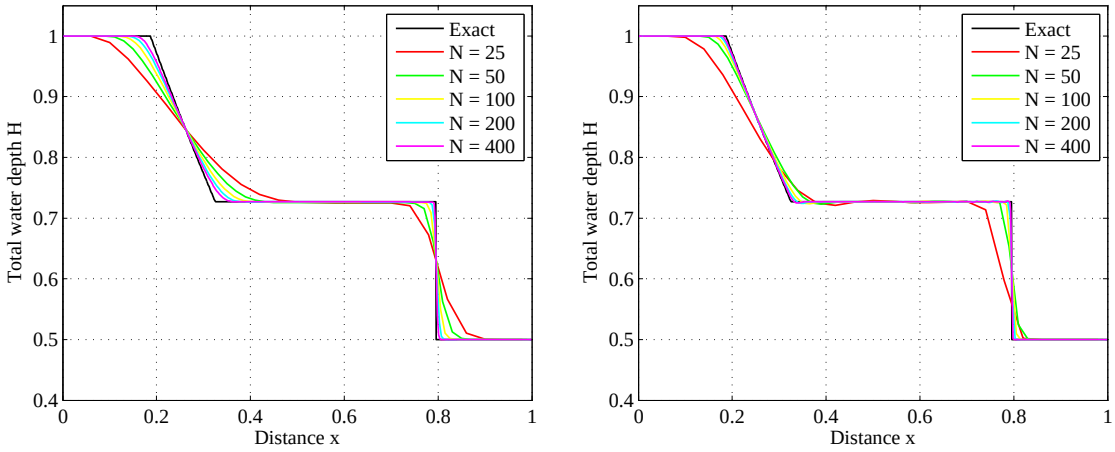

(a) 1. order (b) 3. order

Figure 3.7: *Dam-break problem grid convergence study for 1. order and 3. order methods. CFL = 0.9*

compression, wave and a left moving rarefraction, or depression wave. The results in figure 3.7 clearly show that the 1. and 3. order method both converge to the exact solution for increasing mesh density and more important the methods capture the position of the right moving shock wave. Also in Krabbenhoft et al. (2010a) the convergence is proven by computing the convergence rates.

3.8.2 Source terms

To test how well the implemented methods handle source terms an exact reference solution is constructed as discussed in Krabbenhoft et al. (2010a). A convergence study verifies that both the 1. order and 3. order methods converge with rates of approximately 1 and 3, respectively, and it is thus concluded that the implementation is correct. While the 3. order method certainly converges with a much higher rate and with very impressive low error norms the CPU time is also large compared to the 1. order method.

3.8.3 Sloshing simulation

Having established that both methods are capable of capturing shocks as well as treating source terms the methods are ready to be tested on a sloshing problem given on non-dimensional form in (2.68). We consider a 2D tank with length $L = 0.59$ m with a water depth of $h = 0.0295$ m. This corresponds to a shallow water sloshing frequency of

$$\_w = \frac{\sqrt{gh}}{2L} = 0.456\text{Hz} \Rightarrow \omega_w = 2\pi f_w = 2.865\text{rad/s} \tag{3.49}$$

The tank is given a sinusoidal horizontal base motion described by the function

$$X(t) = A\sin(\Omega t) \tag{3.50}$$

with $\Omega = \omega_f$, i.e. the excitation frequency is set equal to the linear sloshing frequency corresponding to $\beta = 1.0$, and $A = 0.1$ m. Using a time stepping restriction of CFL=0.9

Table 3.2: *Tank dimension and forcing values.*

L	h_0	A	Ω	g	A/L	β	γ
[m]	[m]	[m]	[rad/s]	m/s^2	[-]	[-]	[-]
0.590	0.0295	0.059	2.865	9.81	0.1	1.0	0.0

Table 3.3: *Parameters for sloshing simulation*

and 128 elements the water depth at the left tank wall, the total horizontal sloshing force and the hysteresis loop is shown in figure 3.8, computed using a 1. order and 3. order method. It is clear from the figure that for the specific test case the 3. order method brings limited extra information to the results. A very important parameters is the computed energy using the hysteresis loop. This parameter is a measure of the interaction between the sloshing force and the base to which the liquid container is fixed. In Krabbenhoft et al. (2010a) the energy is computed using the 1. and 3. order method and it i shown that the difference in the computed energy between the two methods is less than 1% when using 256 elements or more.

3.9 Summary and conclusion

The numerical treatment of systems of nonlinear inhomogeneous hyperbolic partial differential equations known as System of Balance Laws has been treated in detail. The equations are complicated in treating primarily due the presence of shocks. We have implemented and tested two different approximate Riemann solvers of 1. and 3. order. The following conclusions can be drawn:

- The implementation of the 1. order method is simple compared to the complex 3. order method derived.
- The 1. and 3. order approximate Riemann solver using a numerical Rusanov flux is capable of capturing shocks very well.
- Source terms are generally not simple to handle. We have tested the 1. and 3. order methods on a test case with a constructed source term showing that both methods converge.
- In a sloshing simulation, using realistic physical values, the 1. and 3. order methods are compared showing that they produce almost identical results. When Using more than 256 elements the the computation of the energy in the hysteresis loops differ with less than 1%.

Summing up the main conclusions it is clear that 1. order methods is sufficient for treating sloshing simulations based on the NSW equations.

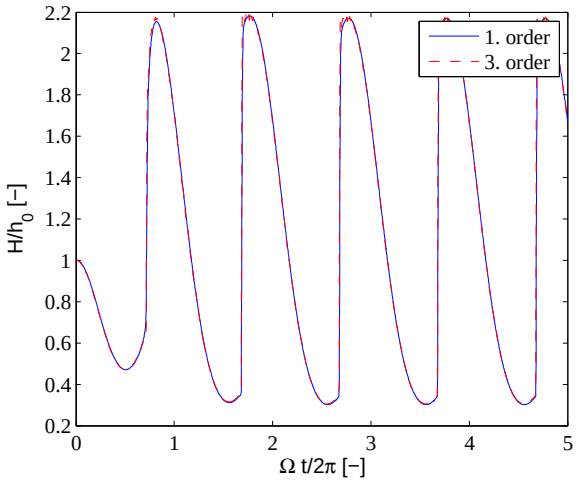

(a) Time variation of dimensionless total height

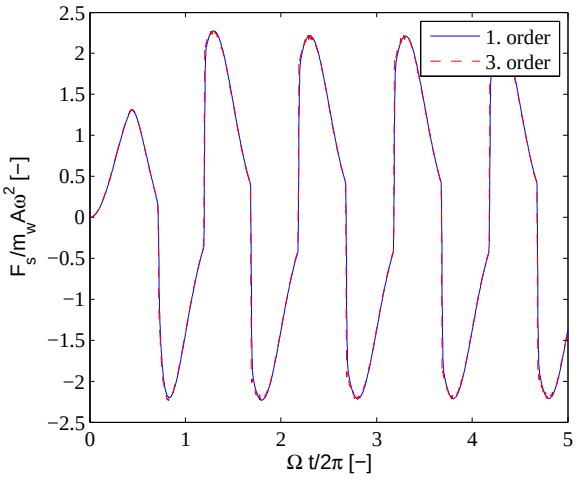

(b) Time variation of dimensionless shear force

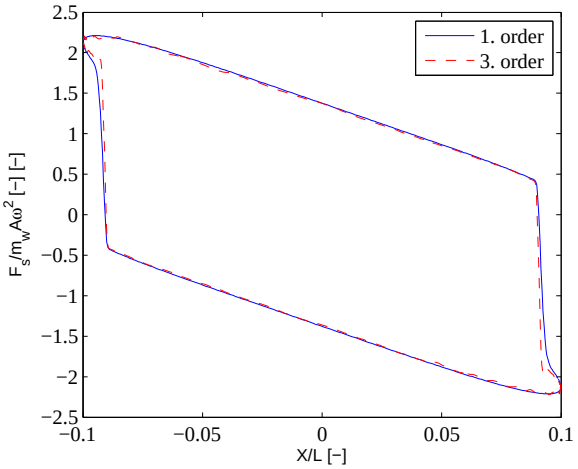

(c) Dimensionless hysteresis loop

Figure 3.8: *Sloshing simulations using 1.order and 3. order methods*

Chapter 4

Shaking table experiments and verification

In the present study two different types of experiments were performed, namely shaking table experiments where the tank was enforced a prescribed horizontal sinusoidal base motion and experiments where the interaction between the TLD and a SDOF structure was examined. Finally with respect to the TLD-structure interaction experiments results from experiments performed by Sun Sun (1991) were used in the verification of a proposed TLD-strcuture interaction model Krabbenhoft et al. (2010c) In this chapter the results from the shaking table experiments with a prescribed motion is discussed.

4.1 Objectives

The derived mathematical model consisting of the NSW equations formulated in a non-inertial frame of reference, was investigated in detail in chapter 2. By nondimensionalizing the governing equations it was shown that the liquid behavior depends on three dimensionless parameters and that the depth is a simple scaling parameter. It is clear that for some depth ratios h/L the mathematical model is bound to break down. As the depth increases the vertical particle velocity increases in importance and the hydrostatic pressure assumption becomes invalid. The second parameter of interest is the forcing ratio A/L. For low forcing we expect that the mathematical model will be inadequate since for low wave amplitudes dispersion becomes increasingly important as argued in 2.3.1. For very high forcing ratios we also expect the mathematical model to break down. The third parameter of interest is the frequency ratio $\beta = \Omega/\omega_w$. Finally the fourth parameter is the effect of bottom friction. It was shown in the theoretical paper Krabbenhoft et al. (2010a) that for realistic Manning numbers (describing the friction of the bottom) the bottom friction was with little effect on the results. For this reason we initially simply neglect the bottom friction in the following. To sum up the experimental results should be used to establish a working range for the mathematical model and more specifically clarify the following points

- How does h/L-ratios affect the sloshing behavior?
- How does A/L-ratios affect the sloshing behavior?

- How does the frequency ratio β affect the solution?
- Should bottom friction be included in the mathematical model?

4.2 Presented variables

In all the performed experiments we measured the horizontal displacement and acceleration of the shaking table $X(t)$ and $\ddot{X}(t)$, the wave height at the left and right tank wall H_L and H_R, and the total base shear force F_x in the direction of the shaking motion. Based on the measured signals the following quantities were derived:

Dimensionless forcing frequency

The horizontal motion of the shaking table is prescribed according to

$$X(t) = A\sin(\Omega t) \tag{4.1}$$

We define the dimensionless forcing frequency β by

$$\beta = \frac{\Omega}{\omega_w} \tag{4.2}$$

where ω_w is the linear shallow water sloshing frequency given in (1.5).

Dimensionless water depth

The dimensionless water depth at the tank end walls is defined by

$$H'_L(t) = \frac{H_L(t)}{h} \qquad H'_R(t) = \frac{H_R(t)}{h} \tag{4.3}$$

For displaying the variation of water depth in time the above definition is sufficient. For a certain time series we also want to show the water depth as function of forcing frequency, i.e. frequency response curves or functions. In figure 4.1 a general response signal y is shown representing $H(t)$ with the excitation period indicated at the top. Based on the measured time series the local maximum and minimum values inside equidistant time windows, defined by the forcing period, are found and the maximum value is defined as the *mean value* of N collected local maximum values.

$$y^{\text{mean}} = \frac{1}{N}\sum_{i=1}^{N} y_i^{\max} \tag{4.4}$$

The same definition applies to the minimum values. Likewise the standard deviation may be computed as

$$y^{\text{rms}} = \frac{1}{N}\sum_{i=1}^{N} (y_i^{\max} - y^{\text{mean}})^2 \tag{4.5}$$

When plotting frequency response curves the above definitions are used.

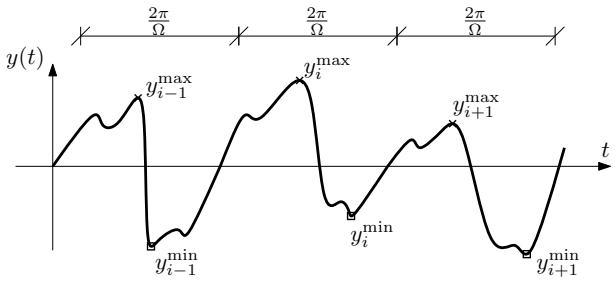

Figure 4.1: *Definition of maximum and minimum values*

Dimensionless sloshing force

The sloshing force include the inertial force from "frozen liquid" F_S is nondimensionalized according to Krabbenhoft et al. (2010b)

$$F'_S(t) = \frac{F_S(t)}{m_w \Omega^2 A} \tag{4.6}$$

where the base motion is defined by (4.1) and m_w is the mass of frozen water $m_w = \rho LWh$.

The sloshing force will have the same magnitude in either direction and therefor we do not need to define a maximum and a minimum as for the case of the water depth. However we still use the definitions (4.4) and (4.5) when plotting the sloshing force as function of excitation frequency.

Dimensionless energy

The definition of mechanical work is given by the following path integral

$$W_C = \int_C \mathbf{F} \cdot \mathrm{d}\mathbf{x} \tag{4.7}$$

where in general force and displacement is combined using the dot product. If we want to compute the amount of mechanical work done by sloshing force pr. excitation period the result is

$$\Delta E = \int_{t_0}^{t_0+T_e} F_S(t) dX(t) \tag{4.8}$$

where $T_e = 2\pi/\Omega$. The dot product has been omitted since the direction of sloshing force is parallel to the displacement vector. It is important to emphasize that the above equation (4.8) is an expression for the work done by the sloshing pr. cycle and not the energy dissipated inside the liquid. To convince one self that this is in fact the case on might think of the simple case of an undamped mass-spring system placed on a moving base. For a base motion frequency equal to the natural frequency of the spring-mass system, the integral (4.8) will grow towards infinity since the force grows to infinity *and* is in phase with $\dot{X}$. Thus the size of ΔE depends on both the magnitude of the force and on the phase difference between the. We choose in the following, maybe a bit misleadingly, to name the quantity ΔE the energy dissipation pr. cycle. The quantity is nondimensionalized using the mechanical energy of the "frozen liquid", i.e.

$$\Delta E' = \frac{\Delta E}{\frac{1}{2} m_w (A\Omega)^2} \tag{4.9}$$

Dimensionless phase

In all the shaking table experiments we consider steady state response of the sloshing motion by fixing the excitation frequency Ω for a period of 120 seconds pr. chosen value. The liquid response will be nonlinear and a spectral analysis will show that the signals, wether it be the water depth variation or sloshing force, contains the fundamental sloshing frequency $\omega_1 = \omega_w$, together with odd numbers of the fundament frequency i.e. $\omega_1, 3\omega_1, 5\omega_1, ...$ and so on. The reason for the odd frequencies is naturally that thy correspond to the unsymmetrical sloshing modes.

It is interesting to perform a spectral analysis of the liquid response to quantify the number of higher harmonic involved in the sloshing motion but also to gain insight in the phase between the sloshing modes and the shaking table displacement $X(t)$.

The one-sided cross power spectral density (CPSD) S_{xy} between two signals x and y is defined by

$$S_{xy}(\omega) = \sum_{0}^{\infty} R_{xy} e^{-i\omega\tau} d\tau \tag{4.10}$$

where $R_{xy}(\tau)$ is the correlation function given by

$$R_{xy}(\tau) = \lim_{T\to\infty} \int_{-T/2}^{T/2} x(t)y(t+\tau)dt \tag{4.11}$$

The phase spectrum $\Phi_{xy}(\omega)$ defining the phase between the spectral components of x and y is defined by

$$\phi_{xy}(\omega) = \tan^{-1} \frac{\mathrm{Im}[S_{xy}]}{\mathrm{Re}[S_{xy}]} \quad , \Phi_{xy}(\omega) \in]-\pi, \pi[\tag{4.12}$$

The phase spectrum ϕ_{xy} will contain phase information about all spectral components of x and y independent of the energy contained at the respective frequencies. To extract only the relevant phase components multiply (4.12) with the normalized CPSD:

$$\phi'_{xy}(\omega) = \frac{\phi_{xy}(\omega)}{\pi} \frac{S_{xy}(\omega)}{\max(S_{xy}(\omega))} \tag{4.13}$$

such that only phase information for relevant frequencies are presented. Thus for $\phi'_{xy} = \frac{1}{2}$ there is a 90 degrees phase between the base amplitude and sloshing force. By setting $x(t) = X(t)$ and $y(t) = F_s(t)$ the spectra S_X, S_{F_s} and S_{XF_s} and the phase ϕ' can be computed using the shown formula.

4.3 TLD subjected to horizontal base motion

An extensive measurement campaign was carried out as shown in table 4.1. We used the same container for all experiments with horizontal dimension $LxW = 590$.

4.3.1 Effect of forcing ratio A/L

In figure 4.2 three snap shots show the free liquid surface for different forcing ratios. It is clear from the pictures that the character of the free surface changes quite dramatically

File id [-]	h [mm]	h/L [-]	ω_w [rad/s]	f_w [Hz]
h20a05 - h20a60	20	0.034	2.360	0.376
h30a05 - h30a60	30	0.051	2.890	0.460
h40a05 - h40a60	40	0.067	3.337	0.531
h50a05 - h50a60	50	0.085	3.731	0.594
h60a05 - h60a60	60	0.102	4.087	0.651

Table 4.1: *Measurement campaign*

for the shown forcing ratios. Thus for $A/L = 0.009$ the surface is smooth and more than a single wave mode is present in the solution, while for $A/L = 0.034$ a discontinuity has been formed that travels back and forth and for $A/L = 0.1$ a clear bore is present with the free surface close to horizontal on either side of the discontinuity. In Krabbenhoft et al. (2010b) a similar analysis was performed with a more detailed description.

Figure 4.3 presents the measured and computed sloshing force for a period of 60 seconds. First note that the mathematical model captures the sloshing forces remarkably well and with the model giving better results for larger A/L values. It seems that the numerical model underestimates the magnitude of the sloshing forces compared to the measured values. The bottom friction is not included in the simulation and from the shown comparison study it seems certain that friction should not be included as this will result in a further decrease of the simulated sloshing force.

Next it is noted that the magnitude of the sloshing force decreases dramatically for increased forcing ratios which must be explained by an increase in internal fluid damping for higher A/L-values. This is not surprising considering the behavior of the free surface as shown in figure 4.2 where certainly more energy is dissipated when a bore is present compared to the situation with a smooth free surface. This will later turn out to be a major weakness of shallow water TLDs namely that the internal damping simply becomes too large for large A/L-ratios. For the lowest forcing ratio $A/L = 0.009$ higher harmonics are clearly present in the solution which is not described by the NSW equations.

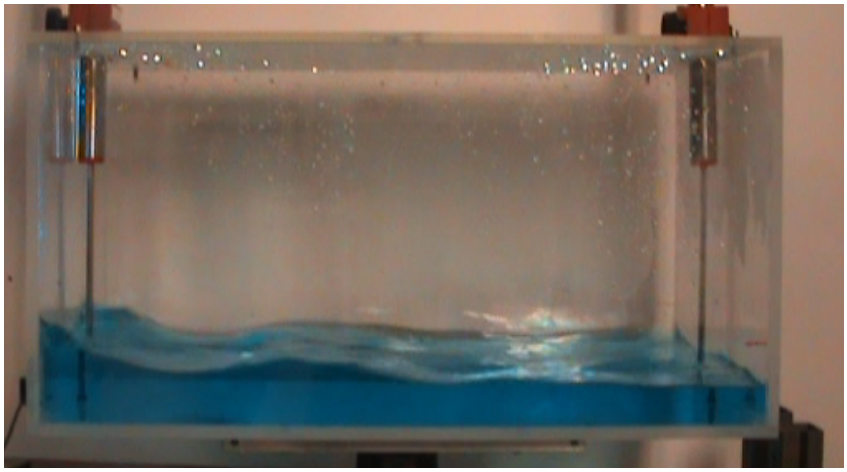

(a) $A/L = 0.009$

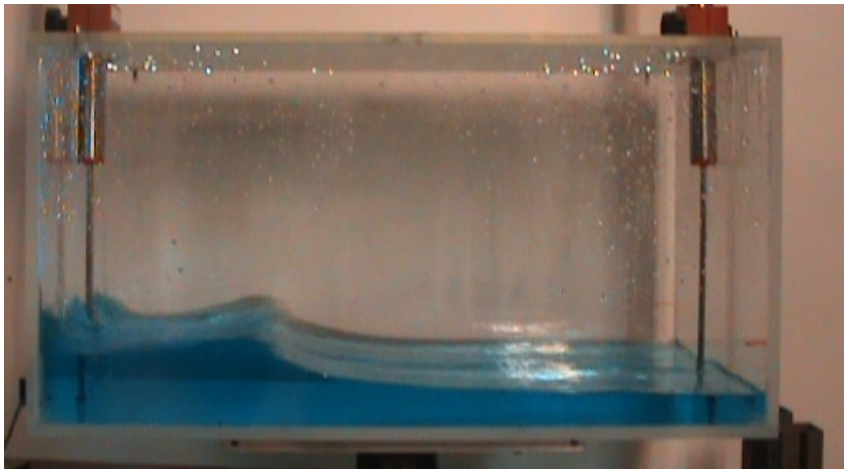

(b) $A/L = 0.034$

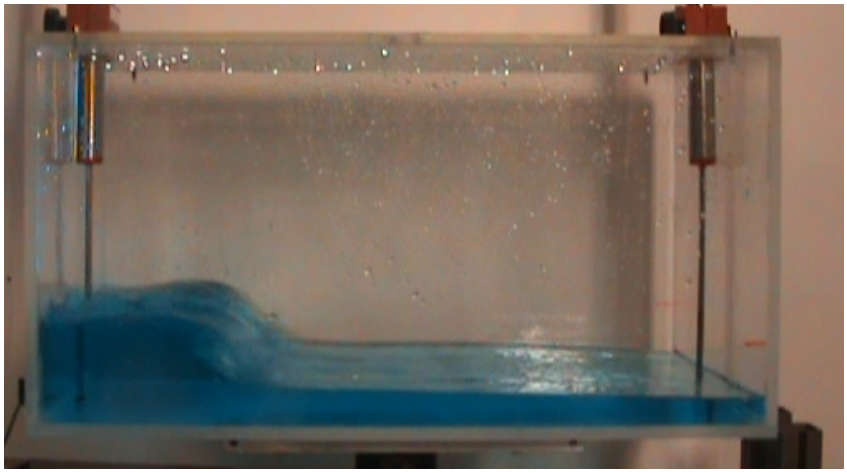

(c) $A/L = 0.10$

Figure 4.2: *Surface profiles for fixed forcing frequency* $\beta = 1.0$ *and amplitude* $A = 5, 20$ *and 60 mm corresponding to* $A/L = 0.009, 0.034$ *and 0.10. Water depth* $h = 40$ *mm.*

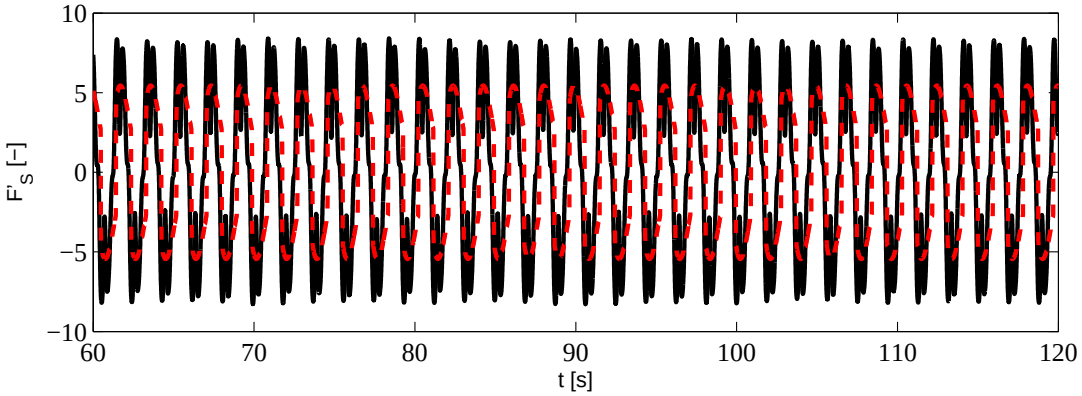

(a) $A/L = 0.009$

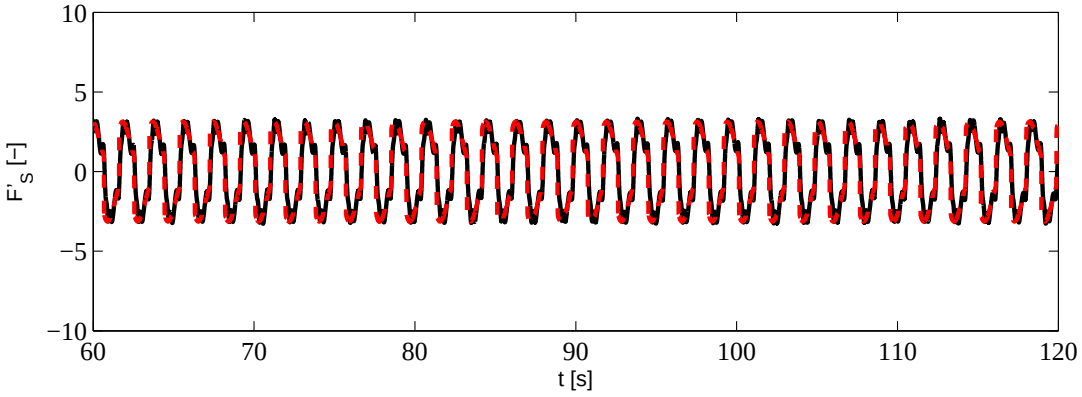

(b) $A/L = 0.034$

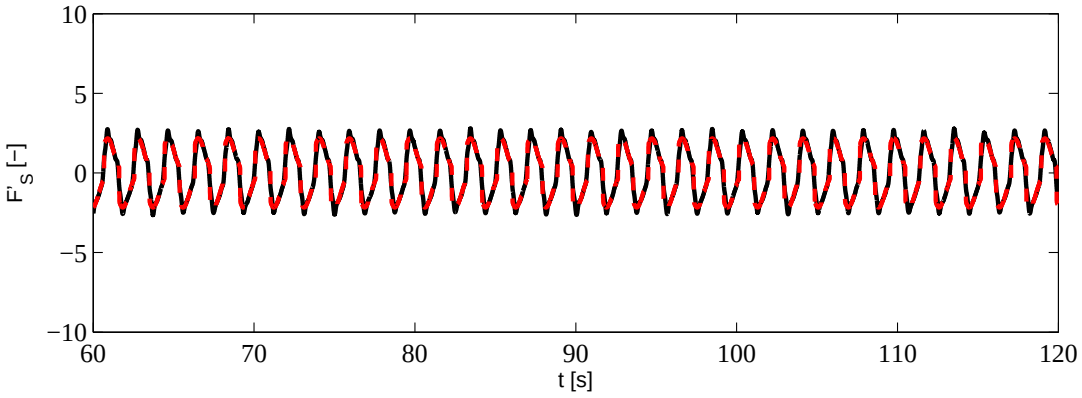

(c) $A/L = 0.10$

Figure 4.3: *Experimental and computed dimensionless sloshing force F'_S for $\beta = 1$ and $h = 40$ mm. Experiments: ——, simulations: - - -*

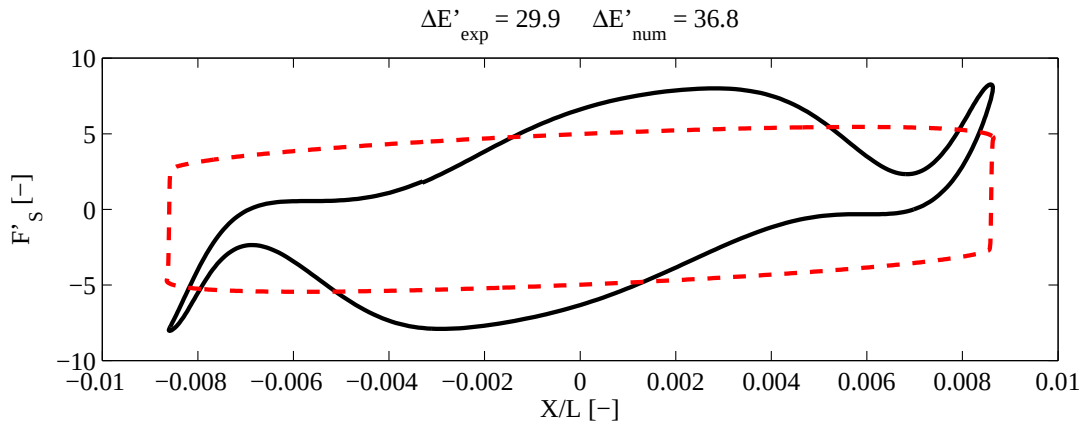

(a) $A/L = 0.009$

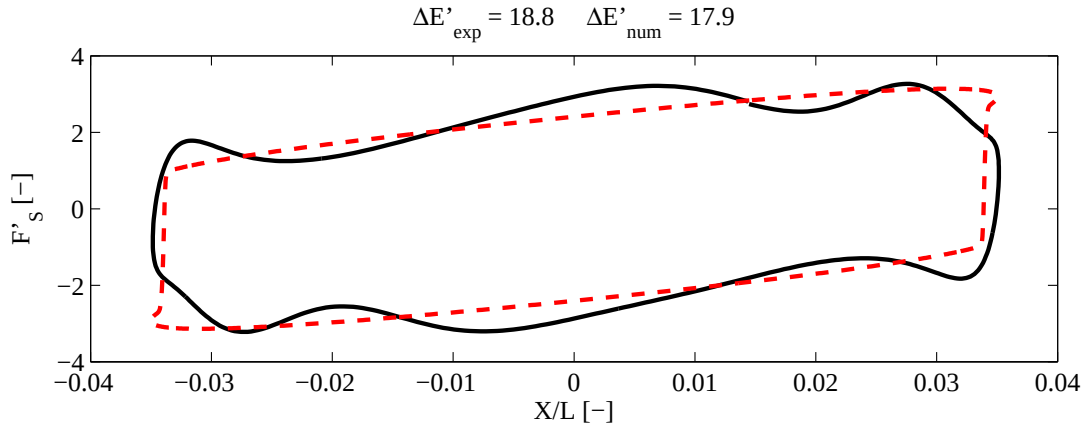

(b) $A/L = 0.034$

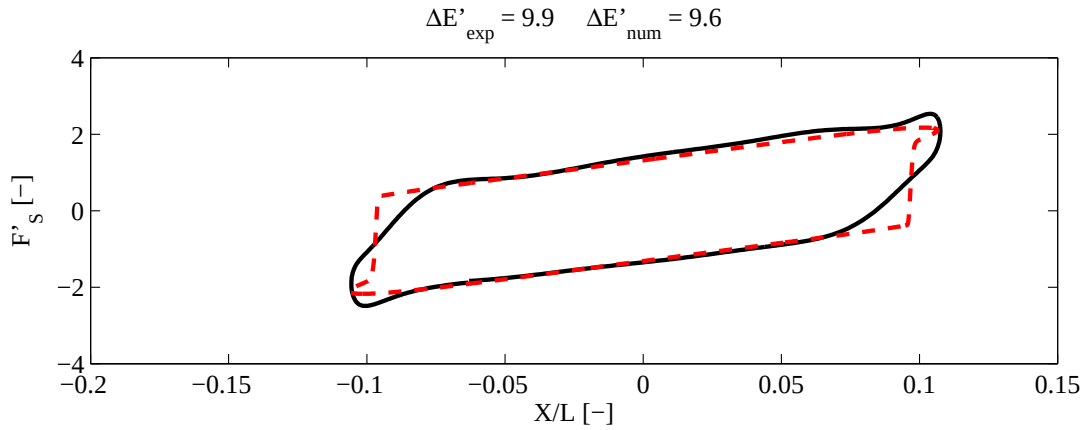

(c) $A/L = 0.10$

Figure 4.4: *Experimental and computed hysteresis loops for $\beta = 1$ and $h = 40$ mm. Experiments: ——, simulations: - - -*

4.3.2 Effect of depth ratio h/L

Presented in figures 4.5-4.5 are surface profiles for three different water depths for three different forcing ratios. In all figures the frequency ratio is constant at $\beta = 1.0$. In figure 4.5 the lowest forcing ratio of $A/L = 0.009$ is considered for water depths of $h = 20, 40$ and 60 mm. For the water depths the surface profiles, visually, all seem smooth and no breaking occurs. Also for the highest depth ratio a single soliton is visible traveling back and forth in the tank, see Krabbenhoft et al. (2010b) for further visual data, while for lower depth ratios it seems that more wave modes are present. In figure 4.6 the forcing ratio is increased to $A/L = 0.034$ while the same three water depths are considered. The free surface is now no longer smooth and all profiles have a clear discontinuity in the form of breaking region traveling back and forth. Finally, for the forcing ratio of $A/L = 0.10$ the discontinuity is now even clearer. For the lowest depth ratio the discontinuity appears as turbulent rather flat region. For higher dept ratios the discontinuity is seen to be represented by spilling breaker or by a clear roller.

In figures 4.8-4.10 the elapse of the sloshing force and hysteresis loops, corresponding to the previously shown snap shots, are presented for a time period of 20 seconds. For the lowest forcing ratio $A/L = 0.009$ the aforementioned trend of higher wave harmonics appearing for shallower water is clear from the time variation of the sloshing force in figure (4.8)(a-b). Even though higher harmonics are clearly present their contribution to the dissipated energy $\Delta E'$ is negligible which can be concluded by comparing the dissipated energy from experiment with that form the simulation. Increasing the depth ratio to 0.068 seems to remove one of wave modes and hence reducing the dissipated energy. The simulation curves, do not vary for the different water depths, however as seen in the dissipated energy ΔE_{sum} there are small variations. The reason for this is as follows. For each experiments the displacement time series of the shaking table is fitted to a harmonic function as described in Krabbenhoft et al. (2010b). This fitted function is passed on to the numerical routine. As a consequence there may be small variations in the forcing ratio A/L for each experiment which leads to small variations in the dissipated energy from the simulations. Finally for the largest depth ratio of 0.1 the sloshing force time series is represented by a signal, clearly nonlinear, with a single peak for each maxima and minima. Observe to the right in figure 4.8(f) that the measured sloshing force is almost in phase with the base motion displacement and thus the hysteresis loop hardly opened up. This results in a very poor energy dissipation. From a TLD perspective this results is very important and shows that using a large filling ratio, even though the frequency ratio is 1, results in a sloshing force that dissipates very little mechanical energy.

Increasing the forcing amplitude, figure 4.9 and 4.10 results in near perfect fits between experiments and simulations. Clearly the agreement is better for low depth ratios but even for, what must in the current context be considered as, large depth ratios of 0.1 the agreement is extremely well. Again one should bear in mind that the mathematica model is based on solid physical argumentation and that no empirical constants are used, and when considering the extreme complex fluid behavior shown in the previous snap shots, the agreement is even more impressive.

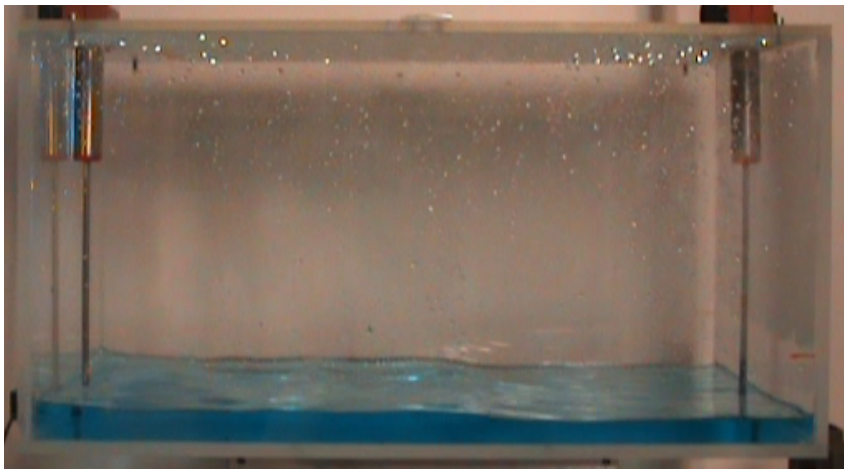

(a) $h/L = 0.034$

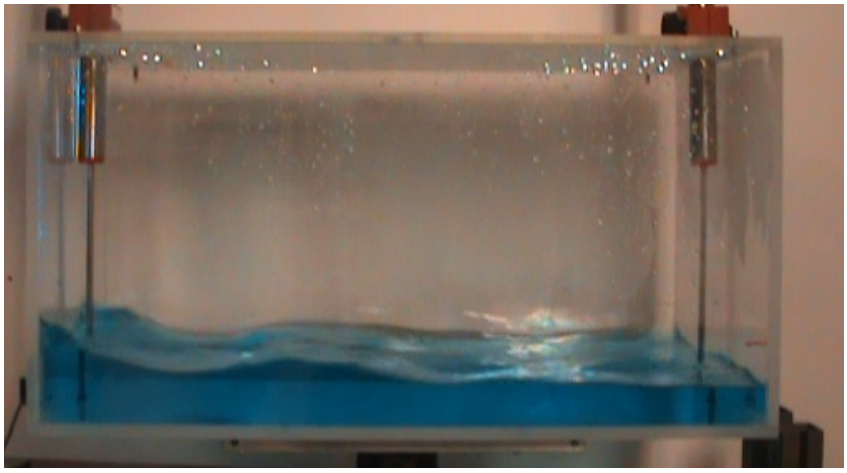

(b) $h/L = 0.068$

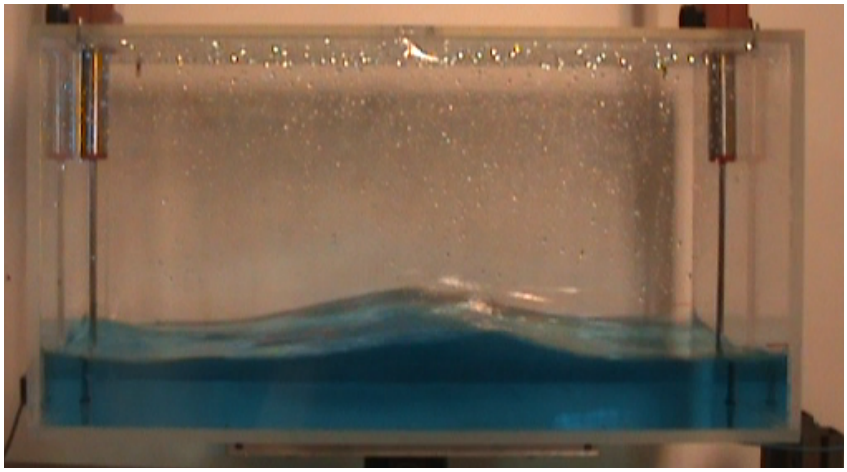

(c) $h/L = 0.10$

Figure 4.5: *Surface profiles for fixed forcing frequency* $\beta = 1.0$ *and amplitude* $A = 5$ *mm corresponding to* $A/L = 0.009$*. Water depth* $h = 20, 40$ *and 60 mm.*

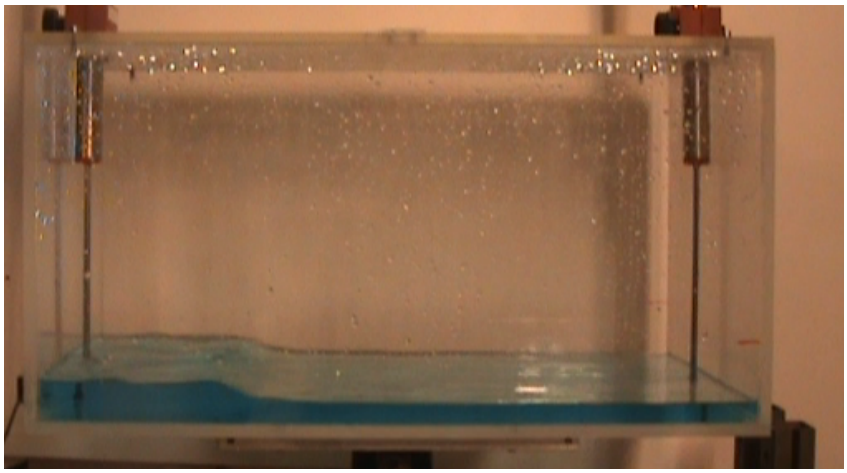

(a) $h/L = 0.034$

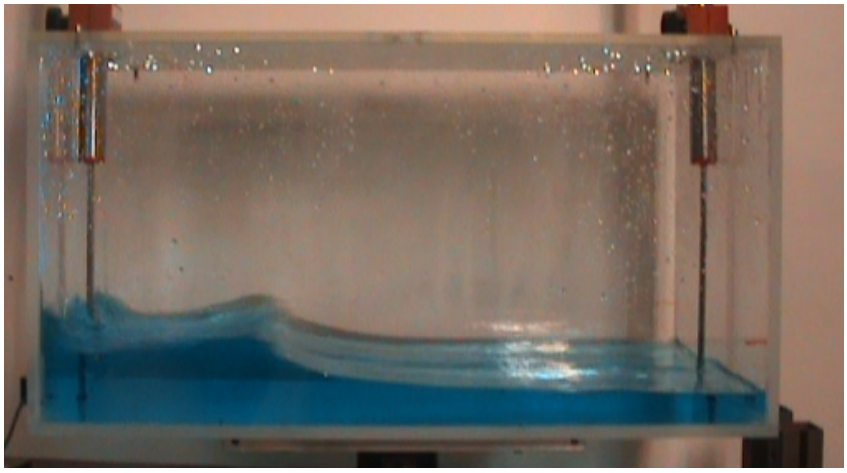

(b) $h/L = 0.068$

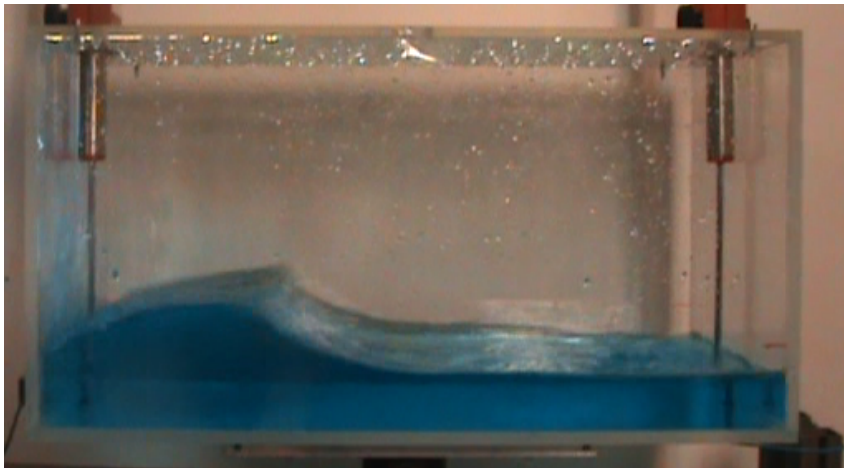

(c) $h/L = 0.10$

Figure 4.6: *Surface profiles for fixed forcing frequency* $\beta = 1.0$ *and amplitude* $A = 20$ *mm corresponding to* $A/L = 0.034$*. Water depth* $h = 20, 40$ *and 60 mm.*

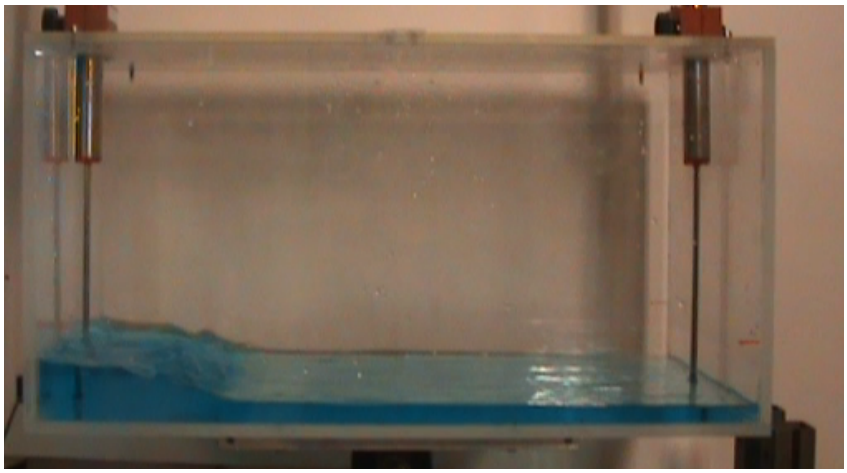

(a) $h/L = 0.034$

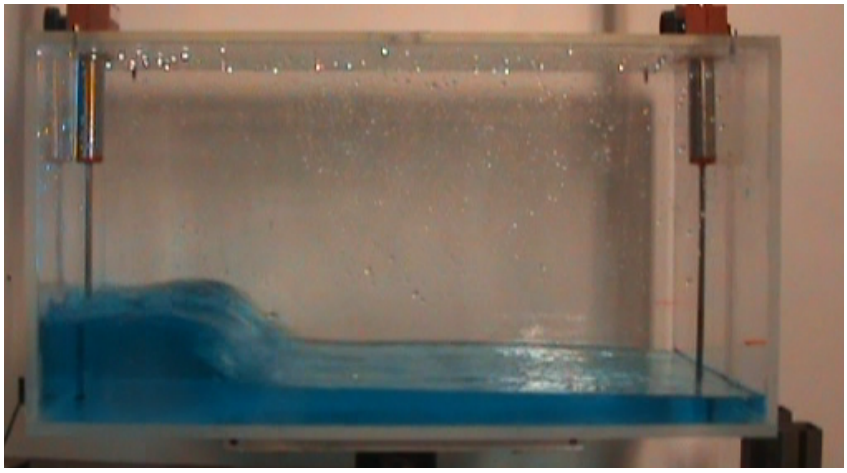

(b) $h/L = 0.068$

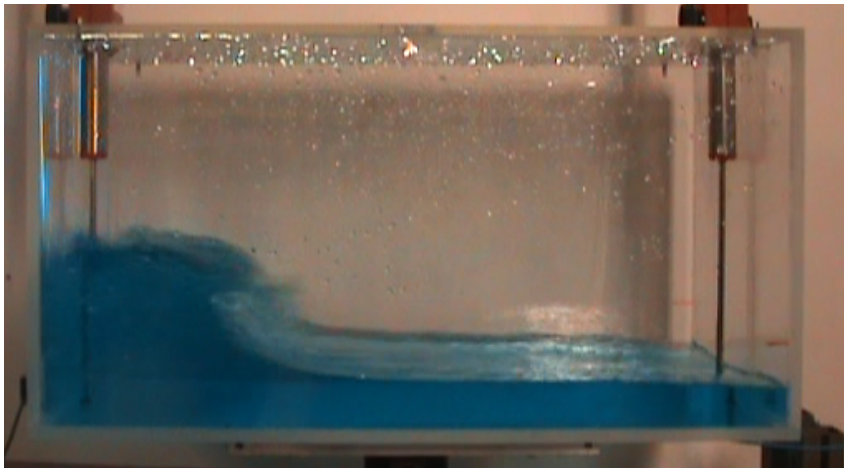

(c) $h/L = 0.10$

Figure 4.7: *Surface profiles for fixed forcing frequency* $\beta = 1.0$ *and amplitude* $A = 60$ *mm corresponding to* $A/L = 0.10$. *Water depth* $h = 20, 40$ *and 60 mm.*

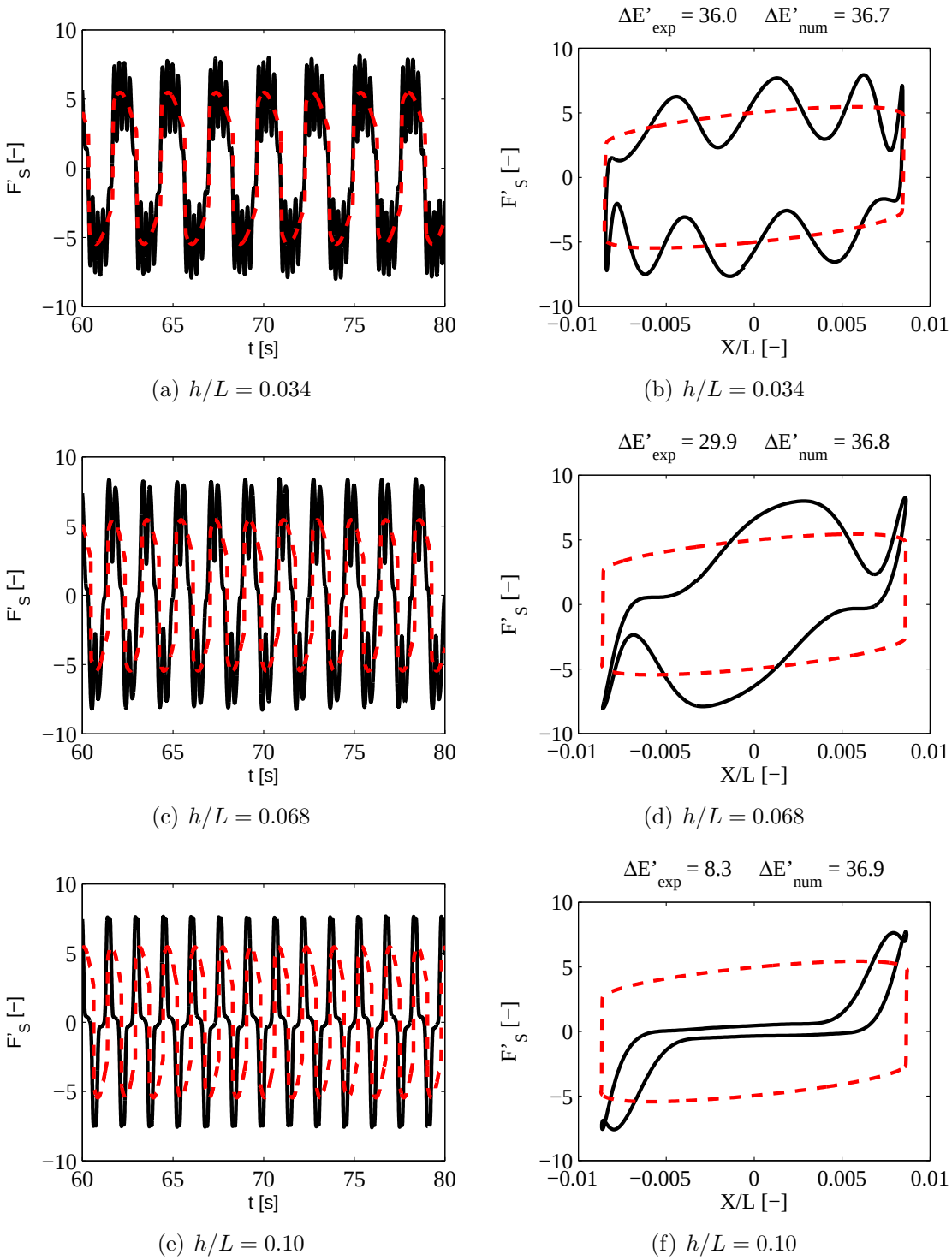

(a) $h/L = 0.034$ (b) $h/L = 0.034$

(c) $h/L = 0.068$ (d) $h/L = 0.068$

(e) $h/L = 0.10$ (f) $h/L = 0.10$

Figure 4.8: *Dimensionless sloshing force and hysteresis loops for* $\beta = 1.0$ *and amplitude* $A = 5$ *mm corresponding to* $A/L = 0.009$. *Water depth* $h = 20, 40$ *and 60 mm. Experiments:* ——, *simulations:* - - -

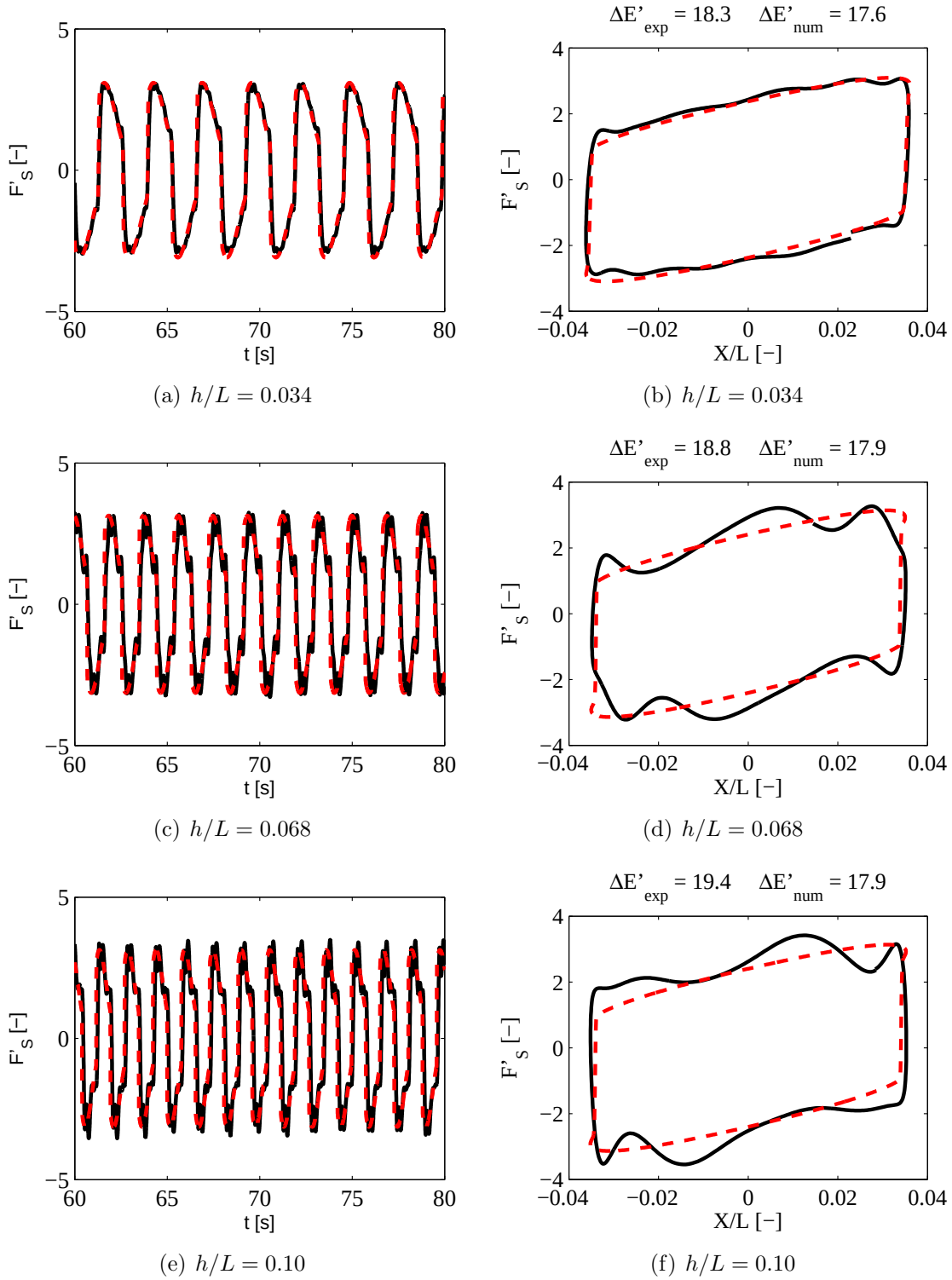

(a) $h/L = 0.034$ (b) $h/L = 0.034$

(c) $h/L = 0.068$ (d) $h/L = 0.068$

(e) $h/L = 0.10$ (f) $h/L = 0.10$

Figure 4.9: *Dimensionless sloshing force and hysteresis loops for* $\beta = 1.0$ *and amplitude* $A = 20$ *mm corresponding to* $A/L = 0.034$. *Water depth* $h = 20, 40$ *and 60 mm. Experiments:* ——, *simulations:* - - -

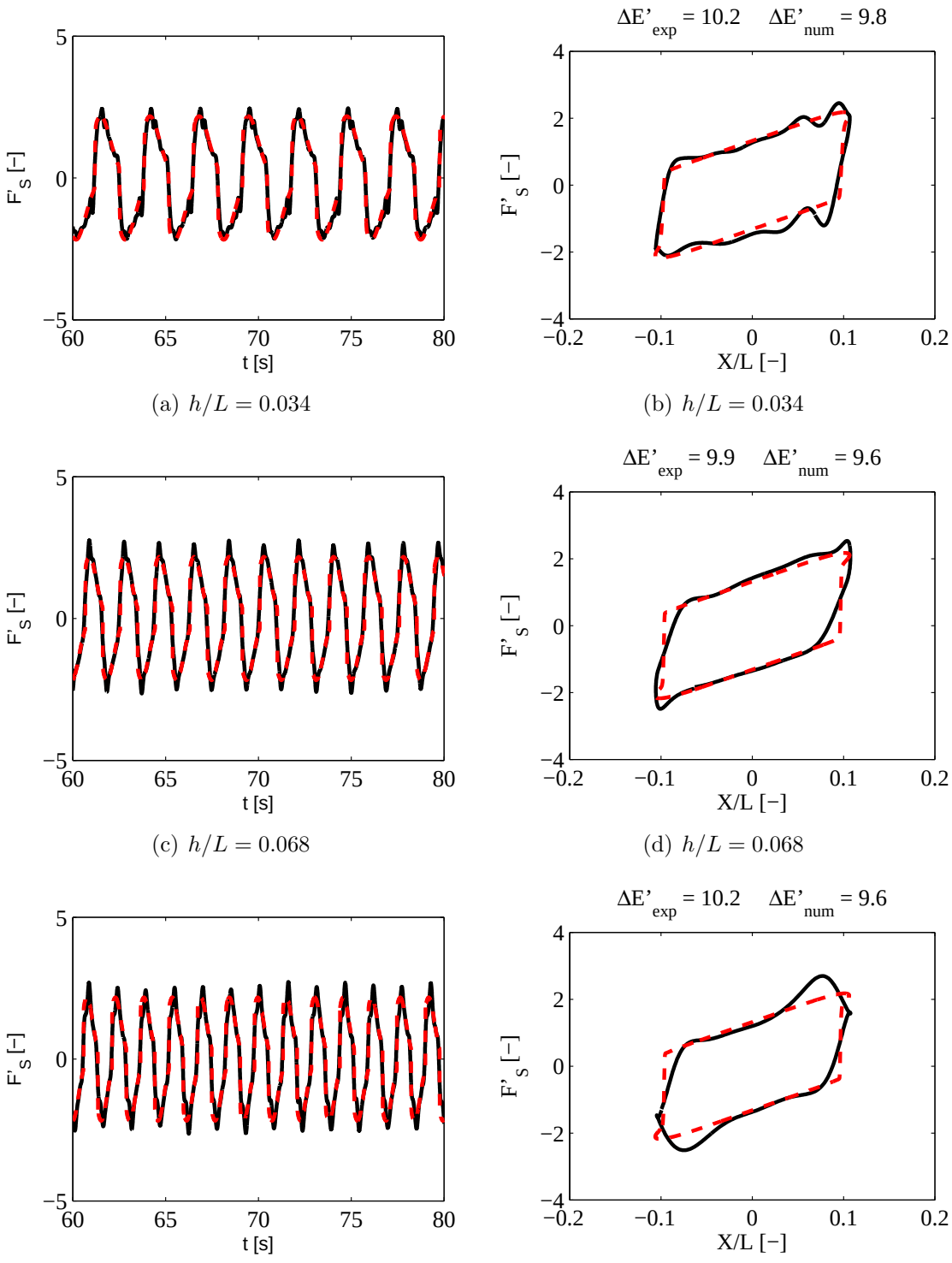

(a) $h/L = 0.034$ (b) $h/L = 0.034$

(c) $h/L = 0.068$ (d) $h/L = 0.068$

(e) $h/L = 0.10$ (f) $h/L = 0.10$

Figure 4.10: *Dimensionless sloshing force and hysteresis loops for $\beta = 1.0$ and amplitude $A = 60$ mm corresponding to $A/L = 0.10$. Water depth $h = 20, 40$ and 60 mm. Experiments: ——, simulations: - - -*

4.3.3 Effect of frequency ratio β

In the previous section we considered the variation of the sloshing force and hysteresis loops for fixed frequency ratios of $\beta = 1$. As the frequency is varied the sloshing behavior will alter its characteristics which will be described in the following.

Again three different water depths are investigated namely $h = 20, 40$ and 60 mm and the forcing ratio is set to a constant value of $A/L = 0.034$ corresponding to $A = 20$ mm. In figure 4.9 we considered these three cases for $\beta = 1$. Presented in figure 4.11 are the frequency response curves for the dimensionless forcing frequency and dissipated energy, i.e. the variation of the quantities as function of the frequency ratio β. We present both experimental and simulated results, with the experimental results defined by mean values (4.4) together with standard deviation (4.5) shown with green error lines in the figures.

First the width of the frequency response curves are noticed. There seem to be quite a large region in the vicinity of $\beta = 1$ where the sloshing force and energy dissipation is almost constant. The tendency though is clear that the curves peak at a frequency slightly larger than $\beta = 1$ which is characteristic for hardening type systems as a shallow water sloshing system is typically characterized as Krabbenhoft et al. (2010a,b).

The simulation captures the frequency response curve for the sloshing force very well, and even better for the dissipated energy. According to our mathematical model each of the computed curves in 4.11 are identical for a fixed forcing ratio and variable depth ratio, i.e. they are independent of the water depth. The experimental curves are clearly affected by changing depth ratios noticed by the frequency position of the sudden drop, know as the jump frequency. For the lowest depth ratio the experimental sloshing forces experiences a sudden drop, or jump, for $\beta \simeq 1.4$ while for a depth ratio of 0.1 the drop happens at $\beta \simeq 1.2$. This jump is clearly not captured by the mathematical model which results in a much smoother frequency response curve for the sloshing force and dissipated energy.

To further clarify the effect of the depth ration on the experiment result the dimensionless sloshing force, dissipated energy and water depth at the left tank wall, are presented for the three different water depths $h = 20, 40$ and 60 mm, in figure 4.12-4.14. The effect of depth ratio now becomes clearer. In general the sloshing force is captured well in the frequency region of say $0.7 < \beta < 1.2$, except for low forcing ratios. This is as expected from the previous analysis in section 4.3.1. For $\beta > 1.2$ the mathematical model over estimates the experimental results and should not be used in this frequency region for estimating the sloshing force. In figure 4.13 the dissipated energy is presented and the results are much more convincing with an over all better agreement between experiments and simulations. However still the frequency region of applicability is still limited to $0.7 < \beta < 1.2$. For low depth ratios the energy dissipation is actually captured quite well and the agreement is much better here than for the sloshing force. The explanation lies in the fact that the plotted sloshing force contains a lot of higher harmonics that do not contribute so significantly to the dissipated energy which must be a consequence of a non optimal phase shift. Finally in figure 4.14 the water depth at the left wall is presented. The agreement is quite poor except for the lowest depth ratio and is, like just aforementioned, a consequence of a significant amount of higher wave harmonics in the solution which are not present in the mathematical model.

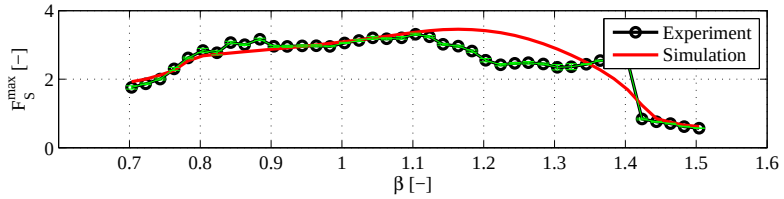

(a) $h/L = 0.034$

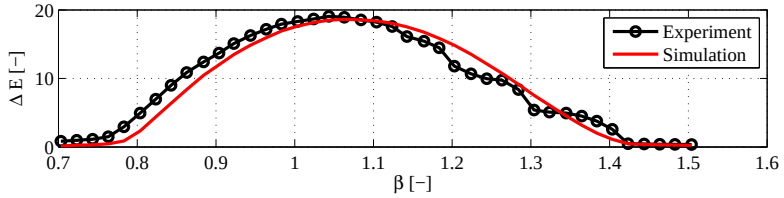

(b) $h/L = 0.034$

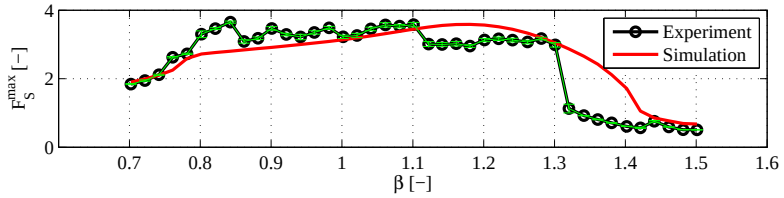

(c) $h/L = 0.068$

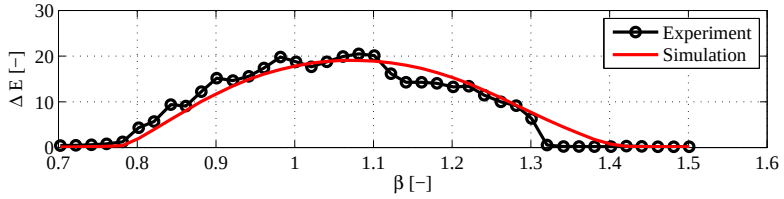

(d) $h/L = 0.068$

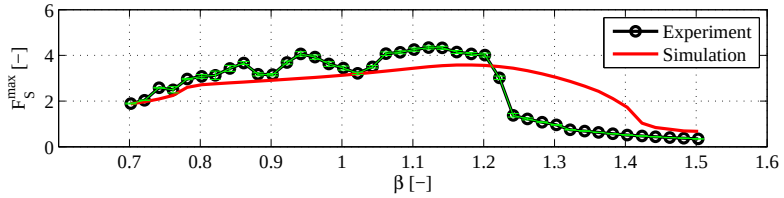

(e) $h/L = 0.10$

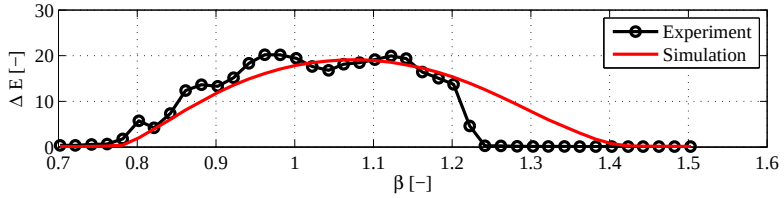

(f) $h/L = 0.10$

Figure 4.11: *Dimensionless sloshing force and dissipated energy for a fixed amplitude $A = 20$ mm corresponding to $A/L = 0.034$. Water depth $h = 20, 40$ and 60 mm. Experimental mean value: ——, Experimental $\pm\sigma$: ——, simulations: ——*

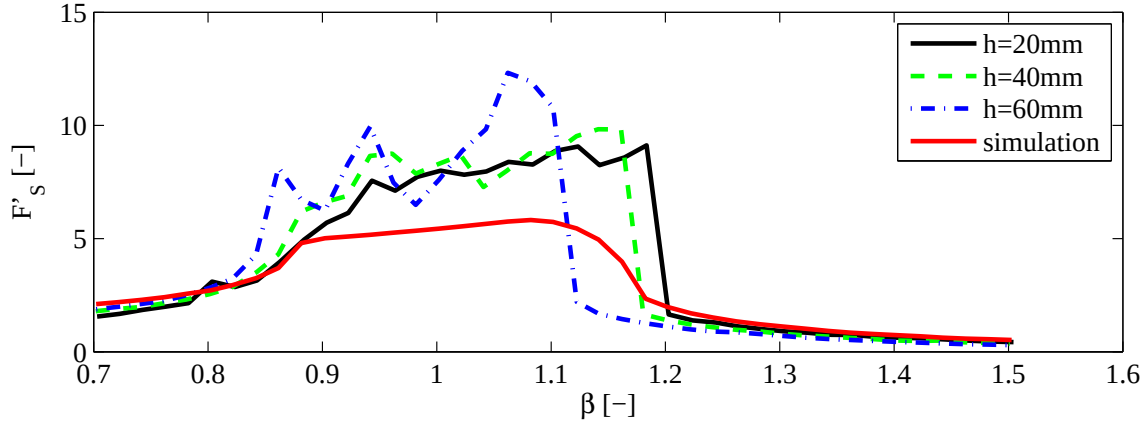

(a) $A = 5$ mm

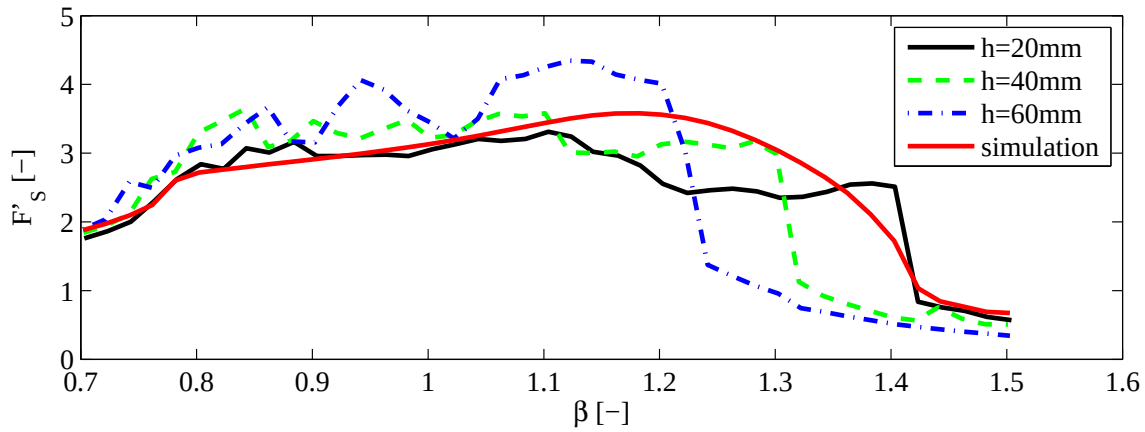

(b) $A = 20$ mm

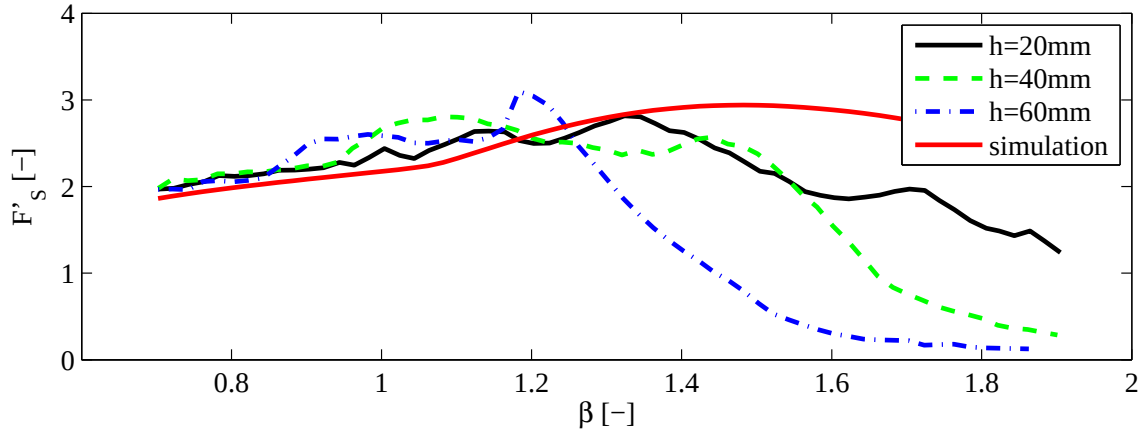

(c) $A = 60$ mm

Figure 4.12: *Frequency response curves for maximum sloshing force.*

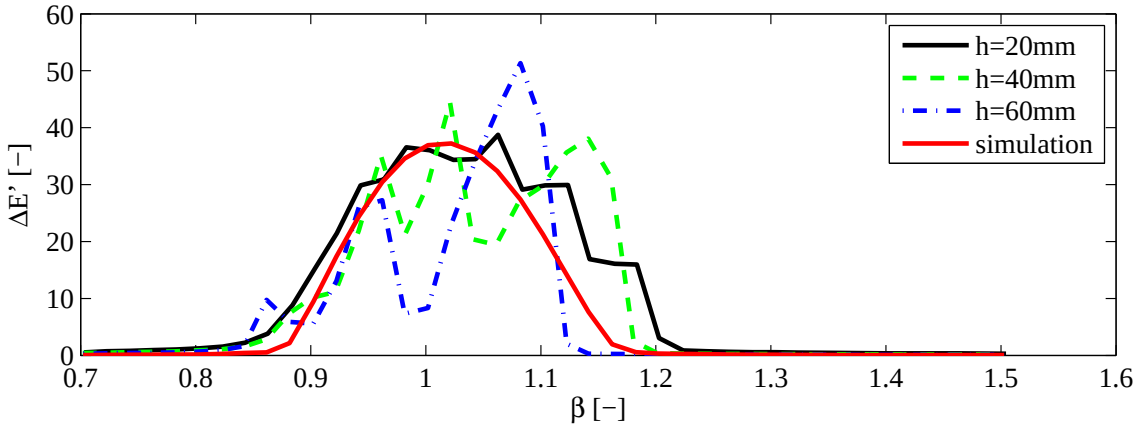

(a) $A = 5$ mm

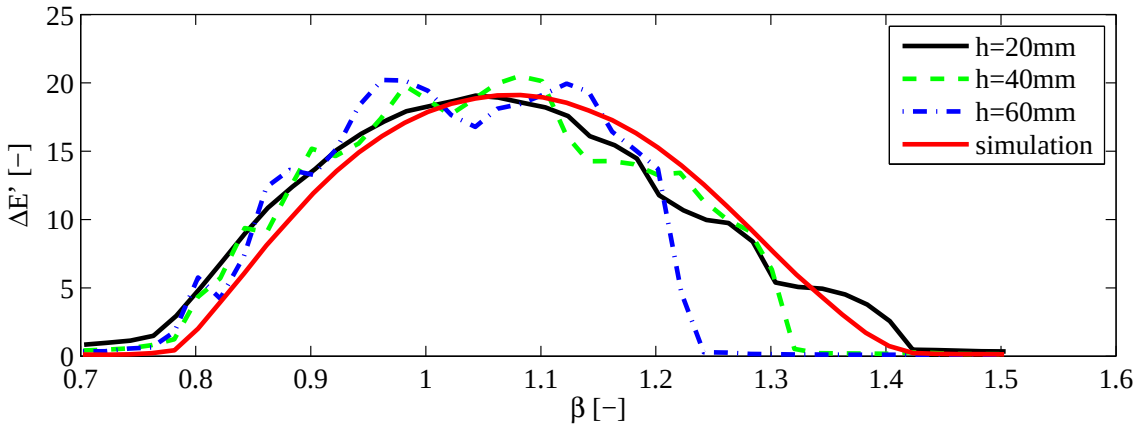

(b) $A = 20$ mm

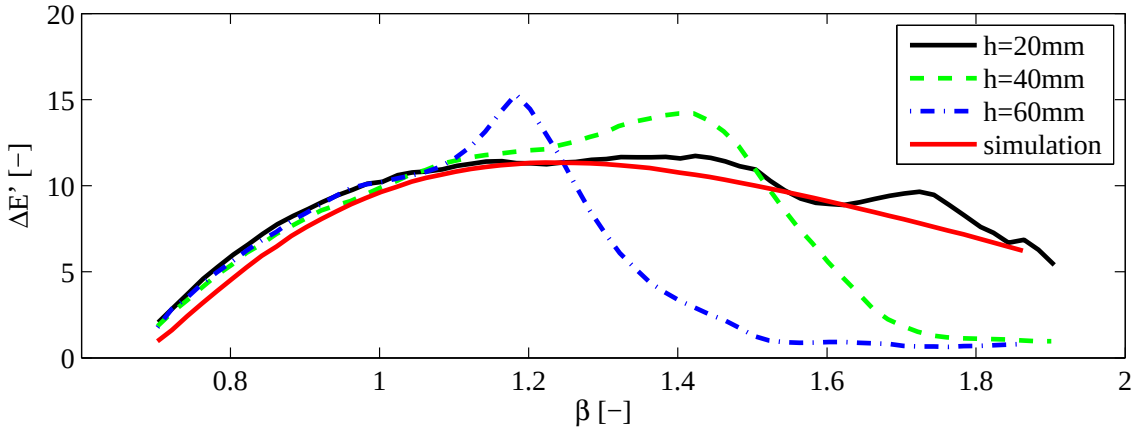

(c) $A = 60$ mm

Figure 4.13: *Frequency response curves for dissipated energy per. cycle.*

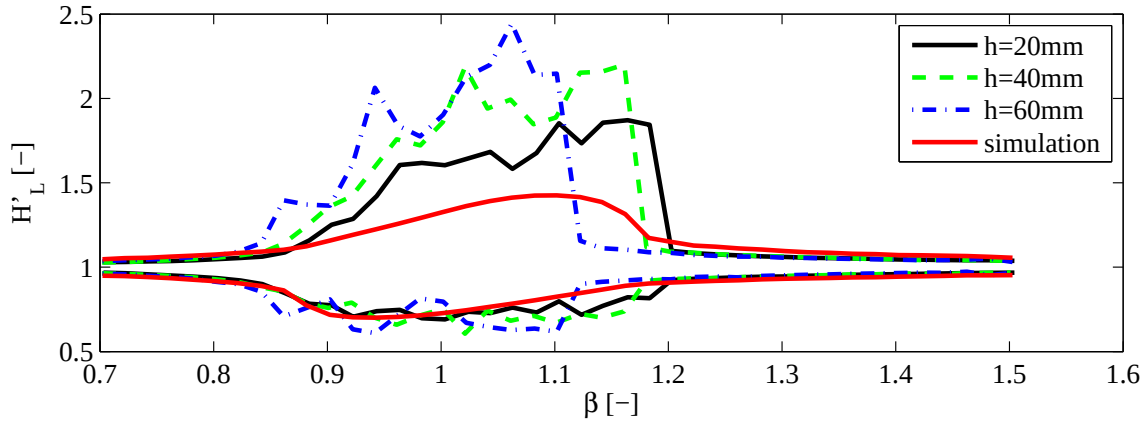

(a) $A = 5$ mm

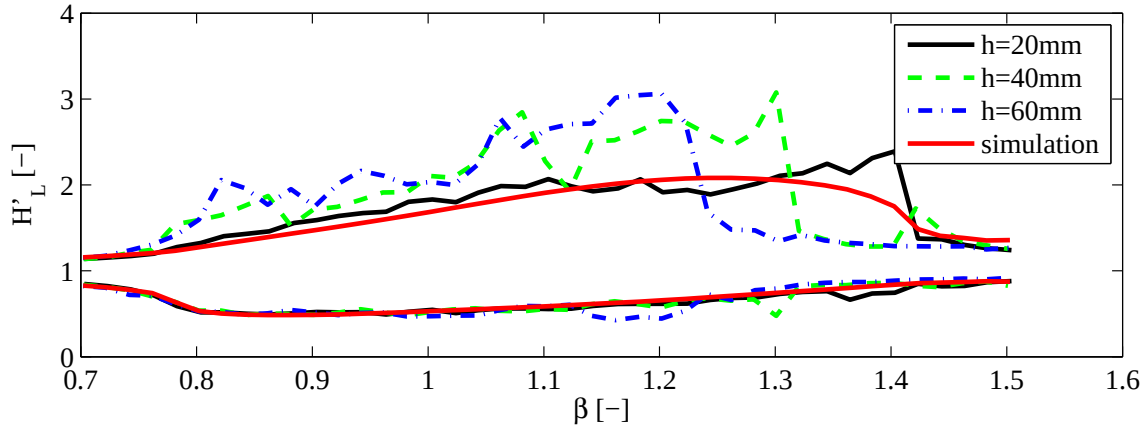

(b) $A = 20$ mm

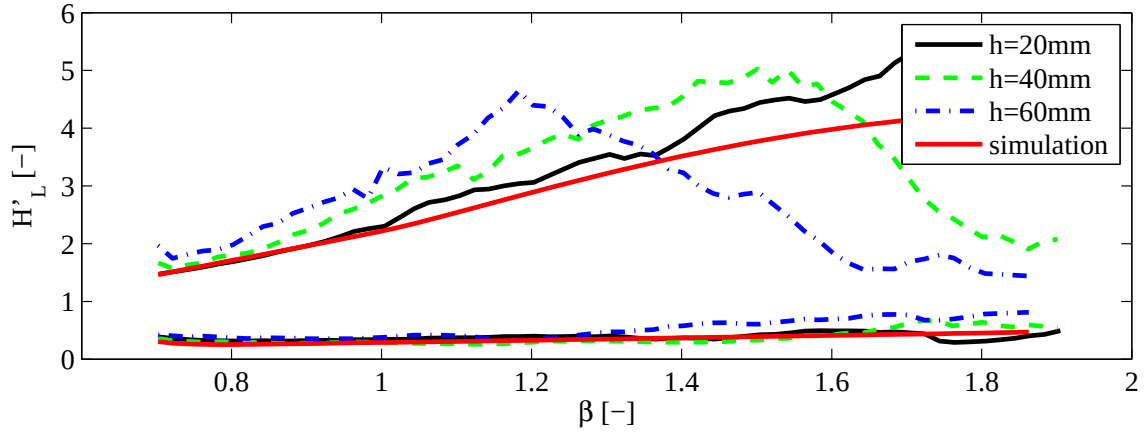

(c) $A = 60$ mm

Figure 4.14: *Frequency response curves for maximum and minimum water depth at left wall.*

4.4 Phase lag and sloshing force amplitudes

The computation of the dissipated energy using the integral (4.8) is a measure of the mechanical energy being dissipated by the sloshing force, as discussed earlier. The magnitude of the dissipated energy depends on the magnitude of the sloshing force as well as the phase difference between the sloshing force and base amplitude. Thus if the sloshing force is, say, in phase with the base amplitude the dissipated energy will be zero.

To investigate the phase between the sloshing force and base amplitude spectral analysis of the sloshing force is performed as described in 4.2. We consider the case with a forcing ratio of $A/L = 0.039$, i.e. a base amplitude of 20 mm, and three different depth depths of $h = 20, 40$ and 60 mm. The results from the analysis is presented in figure 4.15. To the left standard deviation of the 1 harmonic is shown together with the standard deviation of the full signal, i.e. the signal including all harmonics. To the right the dimensionless phase between the first harmonic of the sloshing force and the base amplitude is plotted. Form the figures to the left it is noted that the first harmonic contains by far the largest amount of the signal however for larger water depths the higher harmonics seem to become more dominating. The phase lag is seen to have an almost linear variation with the optimal value of $\phi \simeq 0.5$ occurring for larger values of β as the forcing ratio increases. The mathematical model captures the sloshing force amplitude as well as the phase rather convincingly.

4.5 Summary and conclusion

An in depth analysis of the sloshing behavior of water in a rectangular tank with an enforced sinusoidal horizontal motion, has been investigated in depth. All the presented graphs together with additional graphs not presented in the chapter can be found in the appendix.

The following main conclusions can be drawn:

- In all the simulations the bottom friction has been omitted indicating that this term is not important for the studied cases. This agrees with the analytical and numerical investigation of the friction term in Krabbenhoft et al. (2010a).

- The forcing ratio A/L should in general be larger than 0.03 when using the NSW equations for modelling sloshing in a rectangular container. For very low depth ratios the mathematical model may provide reasonable results for a lower forcing ratios.

- Increasing the forcing ratio A/L decreases the dimensionless sloshing force and dissipated energy as a result of increased energy dissipation internally in the fluid. Thus one might expect the internal liquid damping to result in a non-optimal damper.

- The water depth ratio h/L has a significant influence on the sloshing behavior. Especially a combination of low forcing ratio and high depth ratio is difficult for the mathematical model to handle. On the other hand the proposed model handles large depth ratios surprisingly well for high forcing ratios. The upper limit proposed

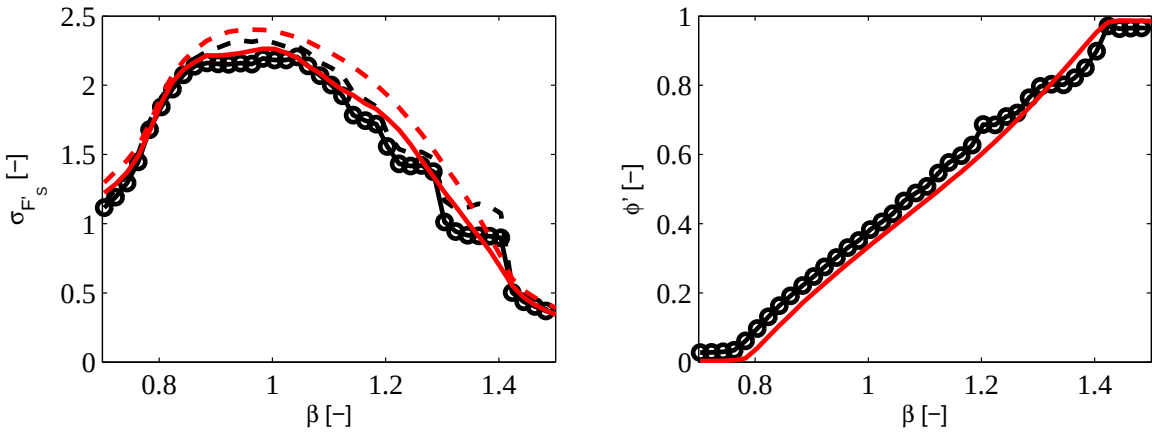

(a) $A = 20$ mm, $h = 20$ mm.

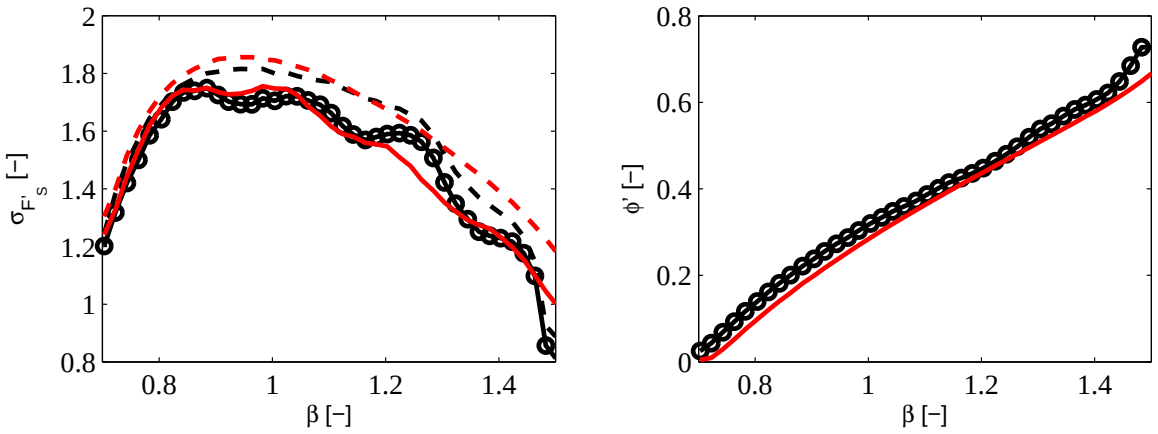

(b) $A = 20$ mm, $h = 40$ mm.

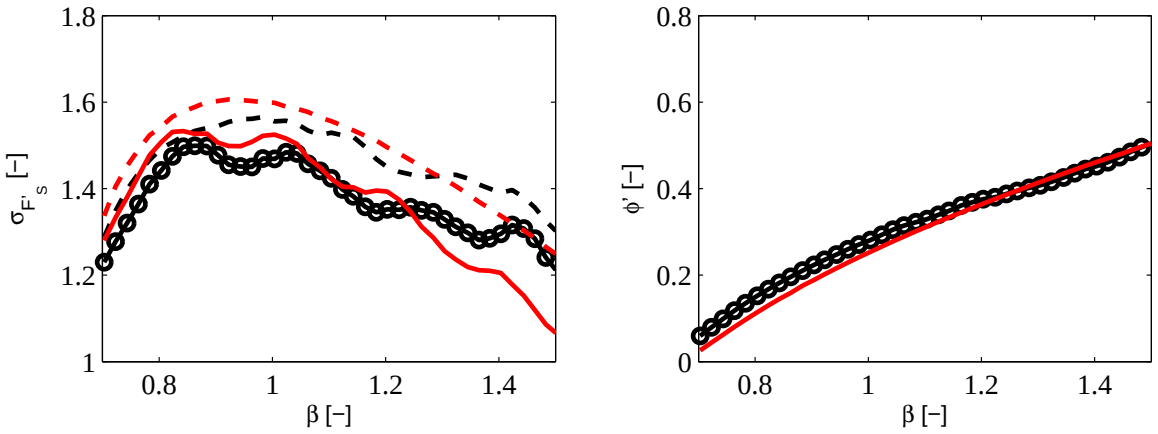

(c) $A = 20$ mm, $h = 60$ mm.

Figure 4.15: *Amplitude of sloshing force and phase. ——: experimental first harmonic, – – –: experimental all harmonics, ——: simulation first harmonic, – – –: simulation all harmonics.*

in chapter 2 of $h/L = 0.1$ seems to be a reasonable choice. However the present results indicate that one may increase this limit for larger forcing ratios.

- The fact that the depth ratio has no significant influence on the sloshing behavior in a qualitatively sense can be useful for establishing deign charts for dampers or for developing simpler analogous mechanical sloshing models.
- The frequency ratio β should in general be in the range $0.7 < \beta < 1.2$ for the mathematical model to capture the sloshing force and dissipated energy. For large forcing and water ratios a larger frequency ratio than $\beta = 1.2$ should not be used, however for smaller depth ratios of $h/L < 0.05$ the mathematical model may be used up to $\beta = 1.4$.
- The free surface elevation at the tank walls is not capture very well by the model. The higher wave harmonics an substantial "run-up" effects cause the experimental signals to differ from the simulated signals. The effect of the higher harmonics, however, is less pronounced for the sloshing forces and even less for the dissipated energy.
- A frequency analysis sows that the majority of information is contained in the first harmonic. Additionally the phase between the first harmonic of the sloshing force and the base amplitude follow a very simple almost linear trend.

Chapter 5

TLD-structure interaction

Instead of imposing a prescribed motion of the tank, as done in chapter 4, it is possible to analyze the coupled motion, or the interaction of the liquid in the tank and an external, typical, elastic structure. TLD-structure interaction analysis is relevant for determining the amount of increased damping of the structure as a result of the coupling.

The coupling between sloshing flows and elastic systems has been studied in the past for several different applications using analytical and numerical models to describe the fluid motion. Modelling the interaction of liquid sloshing and elastic structures using mechanical analogies for the liquid system was being used already in the early sixties in connection with propellant sloshing in aeronautical engineering Bauer (1963). Later Dillingham Dillingham (1981), in a completely different field, studied the motion of ship vessels with water on deck. In his study he coupled the NSW equations in a rectangular tank, which he solve using the Random Choice Method, or Glimm's method, with a simple two degree of freedom system. The study was purely numerical. Sayer and Baumgarten Sayar and Baumgarten (1982) studied the coupling between spherical slosh dampers and elastic systems using a nonlinear pendulum analogy for describing the fluid sloshing. A couple of years later Bauer Bauer (1984) analyzed the coupling motion between a rectangular liquid container and an excited structure. The analytical derived expressions were compared to experimental results. In Chaiseri et al. (1989) a Boussinesq type fluid model, later referenced quite extensively by Fujino Fujino et al. (1992); Fujino and Sun (1993) and Sun Sun (1991); Sun et al. (1989, 1992); Sun and Fujino (1994), was coupled to an elastic structure excited with a harmonic force. Kareem in Kareem (1990) made an analytical study of fluid slosh dampers. Kaneko et. al. coupled Peregrine's Peregrine (1967) Boussinesq equations to a pylon structure to investigate the added damping effects. They used deep water dampers with a filling ratio of $h/L = 0.18$ and considered low forcing ratios of approximately $A/L = 0.001$. To increase the effect of the damper they added internal damping screens which they also included in their mathematical model. This model was later used by Tait et. al. in an extensive study Tait et al. (2004a, 2005b,a, 2007).

There exist a very limited amount of published data concerned with the interaction between shallow water TLDs, modelled using the NSW equations, and elastic structures. In Yu et al. (1999) the authors concluded: *Although the use of numerical simulation of the sloshing motion under large amplitude excitation using the shallow water wave equations*

has been successfully accomplished,Reed D. A. (1996a,b), this model does not provide an effective design tool in its present form. Instead the authors tried to develop a mechanical analogy using experimental data.

In the paper Krabbenhoft et al. (2010c) we pursued the idea of coupling the NSW equations with an elastic structure to determine how well the interaction model handles transient effects as well as forced state state situations. This chapter describes the work done in this paper.

5.1 Experimental setup

In order to verify the proposed mathematical interaction model, discussed in the next section, experiments are conducted. The test rig was constructed in such a way that it could be used both for prescribed motion experiments as well as interaction experiments. Regarding the latter we initially wanted to perform both free decay as well as forced experiments, but due to technical difficulties the forced experiments could not be conducted within the time frame of this study. Instead we chose to borrow experimental data from the work of Sun Sun (1991) who conducted a total of four forced response experiments in connection with his PhD work. The two first experiments were low amplitude experiments with $A/L \simeq 0.004 - 0.01$ and the last two with larger amplitudes of $A/L \simeq 0.025 - 0.05$. We only compared the last two experiments as reported in Krabbenhoft et al. (2010c)

5.1.1 Free decay experiments

(a) (b)

Figure 5.1: *Photograph of simple release mechanism.*

For conducting the free decay experiments a simple release mechanism, depicted in figure 5.1, was constructed. The table, suspended by four wires and attached with four horizontal springs, was given a horizontal initial displacement of approximately 60 mm and was secured using the hinge as depicted in figure 5.1. After the water had come to a rest the hinge was knocked out of its position, i.e. released, and the liquid response together with the table response were recorded using LabView and National Instrument equipment.

Exp. name [-]	L [mm]	W [mm]	h [m]	m_w [kg]	h/L [-]	f_w [Hz]	f_w/f_s [-]	m_w/m_s [-]
Case1a	590	335	58	11.5	0.098	0.640	1.08	2.29
Case1b	590	335	50	9.88	0.085	0.594	1.01	1.98
Case1c	590	335	45	8.89	0.076	0.563	0.96	1.78
Case1d	590	335	40	7.91	0.068	0.531	0.90	1.58
Case2a	400	200	28	2.24	0.070	0.655	1.11	0.45
Case2b	400	200	25	1.98	0.062	0.617	1.05	0.40
Case2c	400	200	22	1.79	0.056	0.586	0.99	0.36
Case2d	400	200	19	1.54	0.048	0.543	0.92	0.31

Table 5.1: *Different tank configurations for the free decay tests.*

In the free decay experiments, two TLD's with different dimensions were tested. The TLD data is given in table 5.1. The reason for testing the two different sized containers was simply to verify that the scaling effects are captured by the mathematical model.

5.1.2 Forced experiments

In the work by Sun Sun (1991) interaction experiments were conducted where the elastic structure was enforced with a harmonic load. A container with a length of 390 mm and width of 220 cm was filled with 30 mm of water corresponding to a sloshing frequency of $f_w = 0.696$ Hz. The mass ratio of TLD to structure was 1.05% and the structural frequency and damping of the structure was measured to $f_s = 0.689$ Hz and $\delta_s = 0.32$ %, respectively. Two different loading cases were considered: one where the structural response at resonance experienced a maximum value of $X_{\max} = 50$ mm and another with $X_{\max} = 100$ mm.

5.2 Mathematical model

A mathematical model coupling the liquid sloshing with a SDOF system was derived in Krabbenhoft et al. (2010c):

$$\dot{\mathbf{z}} = \mathbf{A}(\mathbf{z}) + \mathbf{F} \tag{5.1}$$

with

$$\mathbf{A}(\mathbf{z}) = \begin{bmatrix} V \\ -(2\zeta_s\omega_s v + \omega_s^2)/M \\ -\mathbf{F}(\mathbf{U})_x) \end{bmatrix} \quad , \quad \mathbf{F} = \begin{bmatrix} 0 \\ (F_e + F_S(H))/M \\ \mathbf{S}(H, \ddot{X}) \end{bmatrix} \tag{5.2}$$

The coupled nonlinear system in (5.1) is integrated in time using an explicit approach as discussed in Krabbenhoft et al. (2010c).

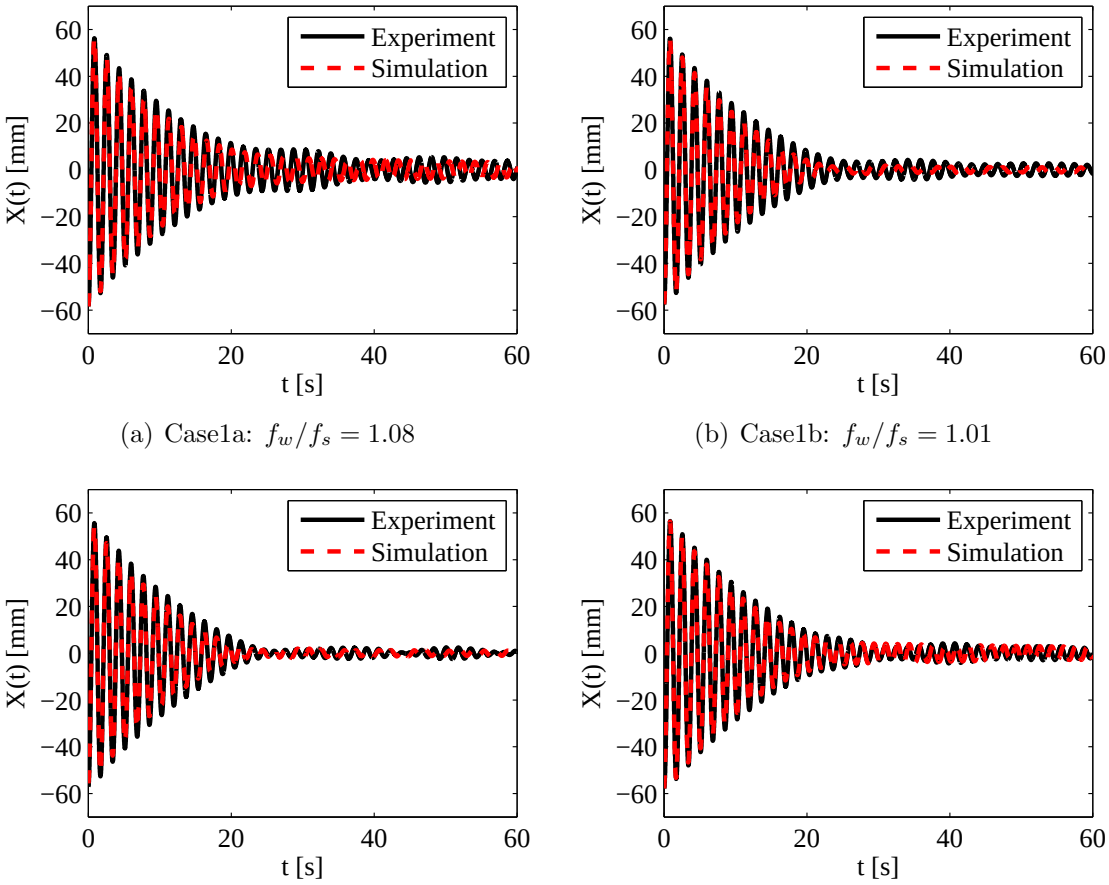

(a) Case1a: $f_w/f_s = 1.08$ (b) Case1b: $f_w/f_s = 1.01$

(c) Case1c: $f_w/f_s = 0.96$ (d) Case1d: $f_w/f_s = 0.90$

Figure 5.2: *Coupled free decay experiments Case1a-d.*

5.3 Free decay - results

For all eight cases given in table 5.1 the experimental and simulated free structural response $X(t)$ is shown in figure 5.2 and figure 5.3. Note from table 5.1 that the mass ratio for Case1 is approximately 2% and only around 0.4% for Case2. For Case1 in figure 5.2 the structural response and the decay is seen to be captured extremely well by the proposed interaction model for all four different water depths, i.e. four different frequency ratios. From a visual judgement Case1c seems to be the best configuration with a very fast decay. When the structural displacement reaches a certain low value a clear beating response appears. For low base amplitudes the surface profile changes from discontinuous to continuous and the internal fluid damping is decreased accordingly, resulting in a beating phenomenon well know from Tuned Mass Dampers with too low internal damping ratios.

For Case2 the mass ratio is roughly 4-5 times smaller and the damping effect therefor also much smaller. In figure 5.3 the structural response is shown and notice the time axis is started from $t = 60$ seconds. Obviously the decay is much less significant compared to Case1, but also the interaction model does not capture the response quite as good. The explanation could be the long simulation time compared to the previous case. Nonetheless

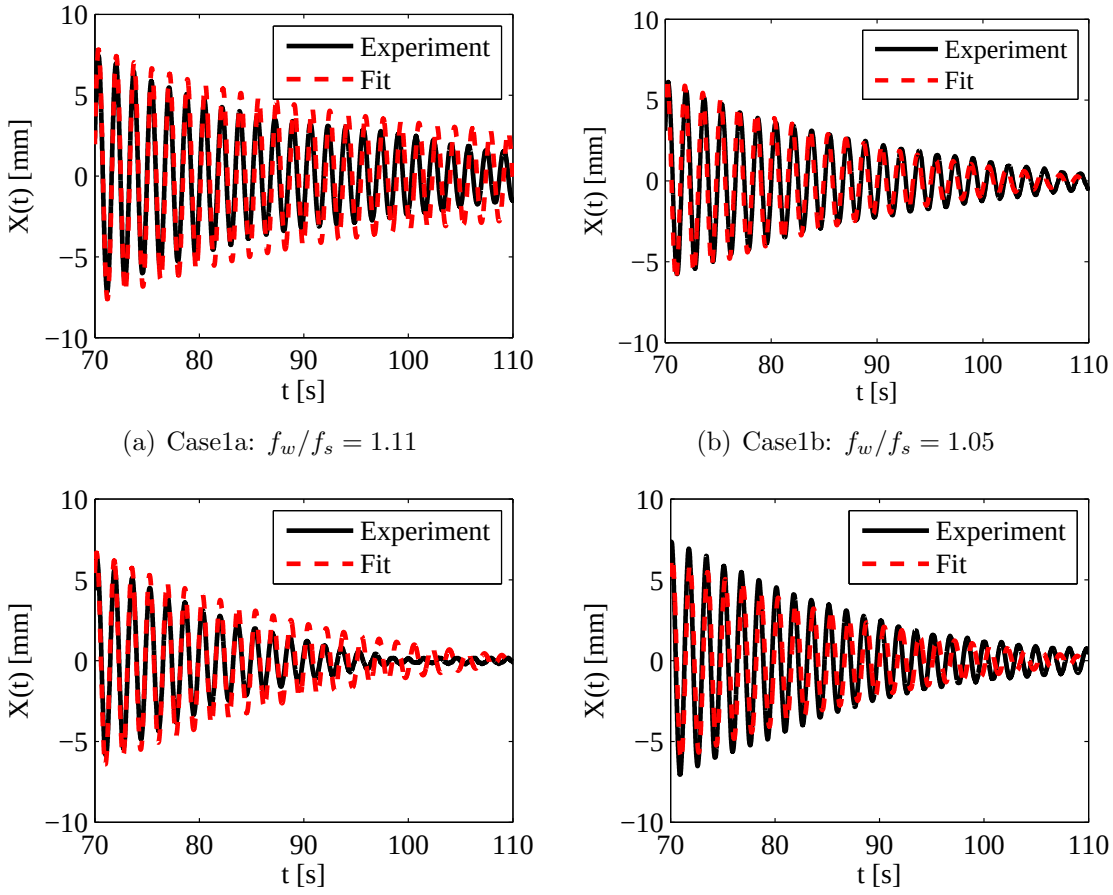

(a) Case1a: $f_w/f_s = 1.11$

(b) Case1b: $f_w/f_s = 1.05$

(c) Case1c: $f_w/f_s = 0.99$

(d) Case1d: $f_w/f_s = 0.92$

Figure 5.3: *Coupled free decay experiments Case2a-d.*

the agreement is still very convincing and certainly useful for predicting the increased structural damping of the coupled system.

Based on the structural time series the logarithmic decrement of the coupled TLD-structure displacement was defined as Krabbenhoft et al. (2010c)

$$\delta_{s+w} = \frac{1}{n} \ln \frac{X(t)}{X(t + nT_s)} \tag{5.3}$$

with T_s defined as the structural period $T_s = 1/f_s$. The factor n is use for smoothing the damping function. For Case1 and Case2 the logarithmic decrement for the coupled response is depicted in figure 5.4. The structural damping is shown by a solid red line and is seen to attain a rather constant value of $\delta_s \simeq 2.5\%$, with a small tendency to increase for decreasing structural amplitude, which is a bit unusual and could indicate that friction damping is present in the structural system. The total logarithmic damping is seen to be quite constant for both cases for high structural amplitudes and the value is more or less constant for the different depth ratios, i.e. tuning rations. TLDs are known by practitioners to be very robust in terms of frequency tuning, which the shown curves to some degree substantiate. The reason for the very robust behavior should most

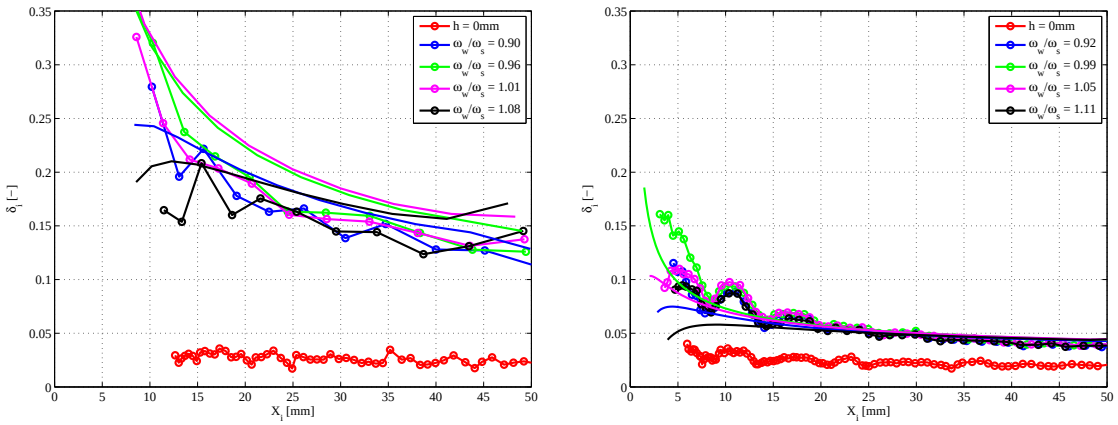

(a) Case1a-d (b) Case2a-d

Figure 5.4: *Experimental and simulated logarithmic decrements as function of structural displacements. The simulated curves are shown with full lines and the experimental results with marked lines. Each line color represents a different case.*

likely be found in the high internal liquid damping present for large base amplitudes. The drawback of a robust damper is a lack of efficiency. The increase in structural damping for Case1 is approximately a factor of 5-6 for high amplitudes while for Case2 the increase in the high amplitude range is a modest factor 2. Remember though that the mass ratio is 4-5 times lower for this case.

In the low amplitude range the damping is seen to increase dramatically for $f_w/f_s \simeq 1$, while the damping is almost constant for the depth ratios resulting in a frequency range far from 1.0. The explanation should once again be found in nature of the internal damping. For low structural amplitudes the internal fluid damping decreases and clearly approaches a more optimal value resulting in a better damping of the structure. How ever when the internal damping is reduces the frequency tuning, i.e. the ratio f_w/f_s becomes more important, analogous to the tuning of TMDs, and hence the modest increase in damping for the two depth ratios with poor frequency tuning. The interaction model captures the trend qualitatively but the values are not very exact. For this low amplitude range a more appropriate choice of sloshing model might be a Boussinesq type fluid model.

5.4 Forced response - results

Using the dampers to capture the transient response, as shown in Krabbenhoft et al. (2010c) both by a visual comparison of video recordings and simulated free liquid surface as well as structural response time series, must be considered as a more challenging test than a forced steady state response test case. Presented in figure 5.5 are experimental results from Sun Sun (1991) and simulated results from the proposed interaction model. The interaction model captures the magnitude of the structural amplitude well but there seems to be quite a significant frequency shift in the position of the maximum amplitude. Thus the simulation, for both cases, estimates the maximum vibration amplitude at a lower frequency ratio $\beta = f_e/f_s$, with f_e being the excitation frequency, than the exper-

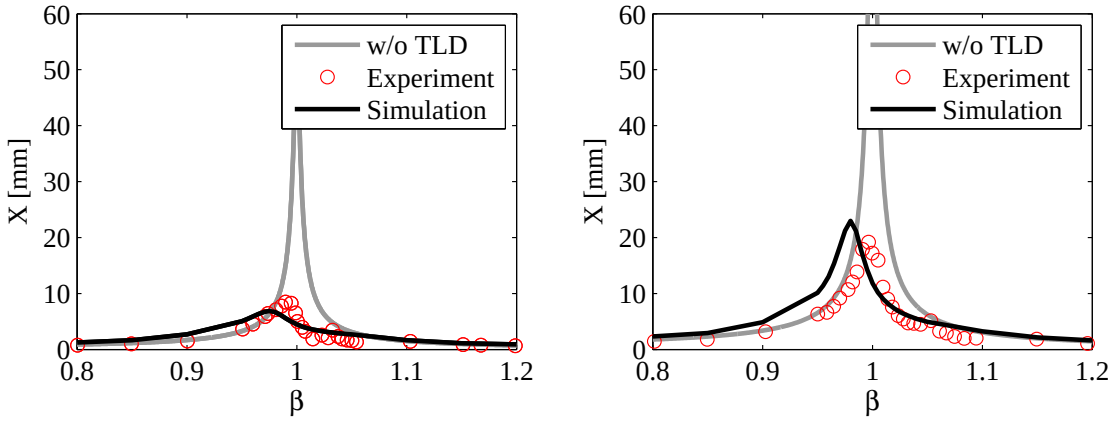

(a) $X_{\max} = 50$ mm (b) $X_{\max} = 100$ mm

Figure 5.5: *Frequency response curves for horizontal displacement of 1-DOF structure equipped with TLD. Experimental results taken from Sun et al. (1992)*

imental studies show. More experimental tests must be carried out, where the sloshing forces should be measured and compared to the simulated sloshing forces, in order to establish an explanation for this phenomenon.

5.5 Summary and conclusion

In chapter 4 an extensive experimental campaign was carried out in order to verify the proposed mathematical model. In all the experiments, and the following verification, the liquid tank, or TLD, was imposed a prescribed harmonic base motion and all the sloshing variables of interest were recorded and compared. In this chapter, instead of imposing a base motion, the sloshing model was coupled to an elastic structure, a simple linear SDOF system, and the interaction was studied. Based on the presented results an on the article Krabbenhoft et al. (2010c) the following conclusions can be drawn:

- The proposed interaction model is capable of reproducing the free decay of a structure coupled with a TLD. The frequency ratio of the TLD and structure was varied between $0.9 < f_w/f_S < 1.1$ and good agreement was found for all ratios.
- For large structural amplitudes the frequency ratio of the TLD and structure was found to be less important with respect to the total damping of the coupled system. For lower structural amplitudes the frequency ratio became important
- The TLD's that were tested worked better for low vibration amplitudes with a very high increase in total structural damping for low amplitudes compared to high amplitudes. This surely indicates that TLD's should be designed, if possible, to work at low amplitudes.
- For mass ratios as low as 0.4% the tested TLD's approximately double the logarithmic decrement from 2.5% to 5%. The value was constant for a very large amplitude range. This indicates that though the TLD may not be optimal tuned, analogous

to a detuned TMD, the TLD is extremely robust, and works in a large amplitude range in which the frequency tuning is not so important. Thus for the frequency range tested between $0.9 < f_w/f_S < 1.1$ the total logarithmic decrement was almost identical in the high amplitude range.

- A visual comparison in Krabbenhoft et al. (2010c) showed that the interaction model, and in particular the sloshing model, captures the free liquid surface well, even for transient experiments. This indicates that the model might be useful for studying impact type sloshing behavior,
- Results from two forced experiments performed by Sun in Sun (1991) showed that the interaction model can reproduce the magnitude of the structural frequency response curve very well, however with an error in the frequency location of the maximum structural response. More experimental data is needed for studying this problem further.

Chapter 6

Concluding remarks

The basic aim of this thesis was to establish a mathematical model for describing the interaction between a Tuned Liquid Damper and a structure. The road to this goal however turned out to be more crooked and hilly than expected. We chose to follow a road that gathered three of the main engineering disciplines namely mathematical modelling, numerical simulation and experimental verification as reflected in the subtitle of the present thesis.

Even though the goal throughout the study was to describe Tuned Liquid Dampers, the area of sloshing quite quickly became the center or rotation, with the simple reasoning that having established a model that could precisely and efficiently describe the sloshing forces the final coupling of this model to an elastic structure would be much less of a challenge, and thereby the initial problem of describing the interaction between a TLD and structure, would be virtually solved. For this reason a large part of the thesis has been devoted to studying liquid sloshing, which essentially is a study of the Navier-Stokes equations formulated in a non-inertial system, together with experimental work to understand and visually observe the *real* and *relevant* physics that any sound mathematical model must reproduce to an acceptable degree.

The thesis is finished with a conclusion, a discussion on the success in meeting the initial aim and suggestions to future work in this challenging and interesting area of research

6.1 Conclusion and discussion

- Starting from the Navier-Stokes equations the NSW equations including viscous effects were derived in a non-inertial coordinate system. Only the bulk viscous terms were retained in the solution. The effect of bottom friction in connection with numerical modelling of shallow water TLDs has not been performed using this approach in previous studies. In the work of Sun (1991) the effect of bottom friction and side wall friction was incorporated using results from classical studies Miles (1967) based on linear sloshing. The effect of bottom friction in connection with shallow water TLDs exposed to large base amplitudes has not been researched earlier to the authors knowledge. The study in Krabbenhoft et al. (2010a,b) showed that the effect of bottom friction can be neglected as long as the depth ratio h/L is

sufficiently large and when the material used for the tanks is smooth such as plastic, steel etc.

- The governing fluid equations for shallow water sloshing, the NSW equations, were analyzed by performing a nondimensionalization. The analysis revealed that for sloshing in a flat bottomed rectangular container the solution of the problem is defined by three parameters, namely a forcing term A/L, a frequency term $\beta = \Omega/\omega_w$ and a term concerned with the bottom friction. Although these dimensionless parameters have been used by previous researchers we have not seen a rigorous derivation or even argumentation for using them. This is done in Krabbenhoft et al. (2010a). The result from the nondimensionalization is important in connection with understanding the physics of the problem and certainly for designing TLDs. With respect to the latter point consider the following example. A TLD should always be designed such that the linear sloshing frequency is close to the structural frequency of interest i.e. $\omega_w \simeq \omega_s$. Now, designing a damper with a given frequency can be achieved by various choices of liquid depth h and tank length L, see (1.4). However from the analysis it was shown that A/L is the term defining the sloshing behavior and thus the damper dimension should be chosen not only based on the frequency but, very importantly, also based on the tank length. Another very important result from the analysis is the fact that the acceleration of the base motion, as one might suspect, is not the important term but in fact $A/L\beta^2$, i.e. the forcing ration multiplied with the frequency ratio squared is the governing term. This implies that for $\beta = 1$ and given a tank with a fixed length L, the fluid behavior will qualitatively behave in the same manner for a fixed base amplitude A. Consider for example increasing the fluid depth while still keeping $\beta = 1$ and the base amplitude fixed. This would result in an increased acceleration but the qualitatively behavior of the fluid would not change. This argumentation holds *only* as long as the depth enters as a pure scaling parameter as in the NSW equations. Thus, it is essential to study the effect of the h/L-ratio on the sloshing behavior.

- The derivation of the mathematical model was based on certain assumptions on the forcing ratio A/L and depth, or filling, ratio h/L. No information exists on the working range for the NSW equations in connection with modelling of sloshing in rectangular containers and the experimental and numerical work reported in Krabbenhoft et al. (2010a,b) is novel in this sense. Reed et. al. Reed et al. (1998) reported results from an experimental study followed by a rather perfunctory comparison study between experimental and numerical results. However based on the present rigorous work a working range for the application of the NSW equations in connection with sloshing has been established. It has been shown that choosing a depth ratio between $0.03 < h/L < 0.1$ combined with a forcing ratio of $0.015 < A/L < 0.1$ and a frequency range of $0.7 < \beta < 1.2$ results in good agreement between experimental and numerical results with respect to sloshing forces and dissipated energy. This information is imperative in connection with using the proposed model for simulating TLDs.

- The numerical solution of the NSW equations is a huge field of research with a

enormous amount of papers being published with new numerical schemes. For an engineer interested in simulating shallow water Tuned Liquid Dampers, and thus simulating the NSW equations, this research field may seem immense and very difficult to grasp. In the present research, therefor, a very large amount of work was dedicated to the numerical treatment of the fluid equations, for investigating and finding the simplest and most efficient way of solving the fluid equations for other researchers to use for studying TLDs. In Krabbenhoft et al. (2010a) a state of the art high order numerical method was compared to a simpler and easier implementable method, showing that the simpler method is adequate for solving the NSW equations in connection with sloshing. In several papers concerned with simulating sloshing behavior using the NSW equations, e.g. Reed et al. (1998); Armenio and Rocca (1996); Dillingham (1981) cumbersome, somewhat outdated and CPU expensive methods were used, making it difficult or impossible for engineers and researcher not experts in fluid dynamics, to use the proposed methods. The present study proposes a method that is clear, well documented and thus possible to implement without being an expert in computational fluid dynamics.

- The interaction of sloshing, described using the NSW equations and elastic structures has received very little attention in the research community as a whole. In connection with the design of TLDs there has been no significant attempts reported, and the work presented in Krabbenhoft et al. (2010c) is thus novel.

- The proposed interaction model is documented by free decay experiments with a visual analysis showing that the mathematical fluid model captures the transient fluid behavior very well. To the authors knowledge no numerical or experimental comparison studies exist in connection with this transient interaction. The results are convincing and indicate that the proposed model might be useful for studying impact dampers based on liquid sloshing. This result certainly meets a part of the initial aim of the present study as discussed earlier in this chapter.

- The interaction between the TLD and structure results in an increased damping of the coupled system. The free decay of the structural response for the coupled system is captured very well by the mathematical model.

- The total damping of the coupled system increases for decreased structural amplitudes. This effect is reproduced by the mathematical model.

- Experimental data from Sun (1991) was used to verify the model for the steady state interaction of a TLD and a structure with a harmonic load. The results from the analysis shows that the mathematical model captures the magnitude of the structural response. However, there is a shift in the simulated frequency at which the maximum structural response occurs.

6.2 Future work

6.2.1 Experiments

The test rig used in this study has room for improvements where the most obvious are the following

- In connection with interaction experiments an extensive study should be undertaken. This requires the generation of a reliable harmonic force with an adjustable frequency and load amplitude.
- Studying the interaction of shallow water TLDs and structures subject to random loading has not been studied in connection with shallow water TLDs. An experimental study would require the use of a random load generator.
- The unidirectional mode of the shaking table is secured by using primitive guiding wheels. The structural damping stems from this mechanism and should be improved, such that the structural damping can be adjusted more rigorously.
- All the experiments conducted in this research were unidirectional. Extension of the shaking table to a bidirectional table could be very interesting, and specially interesting in connection with interaction experiments.
- The effect of varying the fluid viscosity has not been tested experimentally. Studies by Sun Sun (1991) show that viscosity does have an effect on the liquid sloshing. In the derived equations it was assumed that the bulk viscosity could be neglected and that bottom friction was the only relevant contributor to energy dissipation, besides turbulence in the hydraulic jump. For a high viscous fluid the viscous term for the fluid bulk can most likely not be neglected. This will require a further study.

6.2.2 Mathematical models

The mathematical model derived and analyzed in this work should be further verified against numerical experiments. The error in the frequency shift in connection with the loaded interaction experiments should be further investigated.

Some point that have not been mentioned in this work and that could be researched in the future include

- The proposed model should be extended to 3D, enabling the simulation of 3D tanks of arbitrary geometry, and tested on more realistic structures and more realistic loading scenarios.
- The effect of a sloping bottom needs further attention. The point is interesting from a practical installation point of view where the mounting surface may be slightly inclined.
- In the field of naval engineering sloshing coupled to ships is simulated using different advanced methods. These methods should be studied as they might be useful for constructing simpler design models to be used by engineers.

Bibliography

Vincenzo Armenio and Michele La Rocca. On the analysis of sloshing of water in rectangular containers: numerical study and experimental validation. *Ocean Engineering*, 23 (8):705–739, 1996. ISSN 00298018.

H.F. Bauer. Stability boundaries of liquid-propelled space vehicles with sloshing. *AIAA Journal*, 1(7):1583–1589, 1963.

H.F. Bauer. Oscillations of immiscible liquids in a rectangular container: A new damper for excited structures. *Journal of Sound and Vibration*, 93(1):117–133, 1984. ISSN 0022460x.

M. Brocchini, R. Bernetti, A. Mancinelli, and G. Albertini. An efficient solver for nearshore flows based on the waf method. *Coastal Engineering*, 43(2):105–129, 2001. ISSN 03783839.

Casulli and Cheng. Semi-implicit finite difference methods for three-dimensional shallow water flow. *International Journal for Numerical Methods in Fluids*, 15(6):629–648, 1992. ISSN 02712091.

Casulli and Zanolli. Semi-implicit numerical modeling of nonhydrostatic free-surface flows for environmental problems. *Mathematical and Computer Modelling*, 36(9-10):1131–1149, 2002. ISSN 08957177.

V. Casulli. Numerical methods for free surface hydrodynamics. Lecture notes, 2007.

Piyawat Chaiseri, Yozo Fujino, Benito M. Pacheco, and Li Min Sun. Interaction of tuned liquid damper (tld) and structure. theory, experimental verification and application. *Doboku Gakkai Rombun-Hokokushu/Proceedings of the Japan Society of Civil Engineers*, (410):103–112, 1989. ISSN 02897806.

Jeff Dillingham. Motion studies of a vessel with water on deck. *Marine Technology*, 18 (1):38–50, 1981. ISSN 00253316.

F. Dodge. The new dynamic behavior of liquids in moving containers. Technical report, Southwest Research Institue, Texas, 2000.

Michael Dumbser, Cedric Enaux, and Eleuterio F. Toro. Finite volume schemes of very high order of accuracy for stiff hyperbolic balance laws. *Journal of Computational Physics*, 227(8):3971–4001, 2008. ISSN 00219991.

O. M. Faltinsen and A. N. Timokha. *Sloshing*. Cambridge Univ Press, 2009.

Odd M. Faltinsen, Olav F. Rognebakke, and Alexander N. Timokha. Resonant three-dimensional nonlinear sloshing in a square-base basin. *Journal of Fluid Mechanics*, (487):1–42, 2003. ISSN 00221120.

Odd M. Faltinsen, Olav F. Rognebakke, and Alexander N. Timokha. Resonant three-dimensional nonlinear sloshing in a square-base basin. part 2. effect of higher modes. *Journal of Fluid Mechanics*, 523:199–218, 2005. ISSN 00221120.

O.M. Faltinsen. A nonlinear theory of sloshing in rectangular tanks. *Journal of Ship Research*, 18:224–241, 1974.

O.M. Faltinsen, O.F. Rognebakke, I.A. Lukovsky, and A.N. Timokha. Multidimensional modal analysis of nonlinear sloshing in a rectangular tank with finite water depth. *Journal of Fluid Mechanics*, 407:201–234, 2000. ISSN 00221120.

H. Frahm. Device for damped vibrations of bodies, 1909.

Y. Fujino and L.M. Sun. Vibration control by multiple tuned liquid dampers (mtlds). *Journal of Structural Engineering*, 119(12):3482–3502, 1993. ISSN 07339445.

Yozo Fujino, Benito M. Pacheco, Piyawat Chaiseri, and Li Min Sun. Parametric studies on tuned liquid damper (tld) using circular containers by free-oscillation experiments. *Doboku Gakkai Rombun-Hokokushu/Proceedings of the Japan Society of Civil Engineers*, (398):177–187, 1988. ISSN 02897806.

Yozo Fujino, Limin Sun, Benito M. Pacheco, and Piyawat Chaiseri. Tuned liquid damper (tld) for suppressing horizontal motion of structures. *Journal of Engineering Mechanics*, 118(10):2017–2030, 1992. ISSN 07339399.

Gardarsson. Hysteresis in shallow water sloshing. *Journal of Engineering Mechanics*, 133: 1093–1100, 2007.

S. Gardarsson and Harry Yeh. Behavior of sloped-bottom tuned liquid dampers. *Journal of Engineering Mechanics*, 127(3):266–271, 2001. ISSN 07339399.

S. M. Gardarsson. *Shallow-Water Sloshing*. PhD thesis, University fo Washington, 1997.

EW Graham and AM Rodriguez. The characteristics of fuel motion which affect airplane dynamics. *Journal of Applied Mechanics-Transactions of the ASME*, 19:381–388, 1952.

Abramsom H.N. The dynamic behavior of liquids in moving containers. Technical report, NASA, Washington DC, 1966.

M. J. Hochrainer. Tuned liquid column damper for structural control. *Acta Mechanica*, 175(1-4):57–76, 2005. ISSN 00015970.

Changqing Hu and Chi-Wang Shu. Weighted essentially non-oscillatory schemes on triangular meshes. *Journal of Computational Physics*, 150(1):97–127, 1999. ISSN 00219991.

R.A. Ibrahim. *Liquid Sloshing Dynamics - Theory and Application*. Cambridge Univ Press, 2005.

Guang-Shan Jiang and Chi-Wang Shu. Efficient implementation of weighted eno schemes. *Journal of Computational Physics*, 126(1):202–228, 1996. ISSN 00219991.

A. Kareem. Reduction of wind induced motion utilizing a tuned sloshing damper. *Journal of Wind Engineering and Industrial Aerodynamics*, 36(1-3):725–737, 1990. ISSN 01676105.

A. Kareem and W.-J. Sun. Stochastic response of structures with fluid-containing appendages. *Journal of Sound and Vibration*, 119(3):389–408, 1987. ISSN 0022460x.

G.H. Keulegan. Energy dissipation in standing waves in rectangular basins. *Journal of Fluid Mechanics*, 6:33–50, 1959. Bestilt 24-2-2007.

C. G. Koh, S. Mahatma, and C. M. Wang. Reduction of structural vibrations by multiple-mode liquid dampers. *Engineering Structures*, 17(2):122–128, 1995. ISSN 01410296.

C.G. Koh, S. Mahatma, and C.M. Wang. Theoretical and experimental studies on rectangular liquid dampers under arbitrary excitations. *Earthquake Engineering and Structural Dynamics*, 23(1):17–31, 1994. ISSN 00988847.

J. Krabbenhoft, C. T. Georgakis, and (submitted). Shallow water sloshing. part i. theoretical and numerical background. *Engineering Structures*, 2010a. ISSN 01410296.

J. Krabbenhoft, C. T. Georgakis, and (submitted). Shallow water sloshing. part ii. experimemtal investigation and numerical verification. *Engineering Structures*, 2010b. ISSN 01410296.

J. Krabbenhoft, C. T. Georgakis, and (submitted). Interaction of shallow water tuned liquid damper and structure - theory and experimental varification. *Journal of Sound and Vibration*, 2010c. ISSN 0022460x.

B Le Méhauté. *An Introduction to Hydrodynamics & Water Waves*. Springer-Verlag, 1976.

T. G. Lepelletier and F. Raichlen. Nonlinear oscillation in rectangular tanks. *Journal of Engineering Mechanics*, 114(1):1–23, 1988. ISSN 07339399.

Randall J. LeVeque. *Finite Volume Methods for Hyperbolic Problems*. Cambridge University Press, 2002.

Xu-Dong Liu, Stanley Osher, and Tony Chan. Weighted essentially non-oscillatory schemes. *Journal of Computational Physics*, 115(1):200–212, 1994. ISSN 00219991.

P.A. Madsen, H.J. Simonsen, and Cun-Hong Pan. Numerical simulation of tidal bores and hydraulic jumps. *Coastal Engineering*, 52(5):409–433, 2005. ISSN 03783839.

Schäffer H. A. Madsen, Per A. A review of boussinesq-type equations for gravity waves. *Advances in Coastal and Ocean Engineering*, 5:1–94, 1999.

Adam Marsh, Mahesh Prakash, Eren Semercigil, and Ã–zden F. Turan. A numerical investigation of energy dissipation with a shallow depth sloshing absorber. *Applied Mathematical Modelling*, 34(10):2941–2957, 2010. ISSN 0307904x.

JW Miles. Surface-wave damping in closed basins. *Proceedings of the Royal Society of London Series A - Mathematical and Physical Sciences*, 297:459–, 1967. Bestilt 24-2-2007.

V. J. Modi, F. Welt, and M. L. Seto. Control of wind-induced instabilities through application of nutation dampers: a brief overview. *Engineering Structures*, 17(9):626–638, 1995. ISSN 01410296.

Vinod J. Modi and Mae L. Seto. Passive control of flow-induced oscillations using rectangular nutation dampers. *JVC/Journal of Vibration and Control*, 4(4):381–404, 1998. ISSN 10775463.

V.J. Modi and A. Akinturk. An efficient liquid sloshing damper for control of wind-induced instabilities. *Journal of Wind Engineering and Industrial Aerodynamics*, 90 (12-15):1907–1918, 2002. ISSN 01676105.

V.J. Modi and M.L. Seto. Suppression of flow-induced oscillations using sloshing liquid dampers: analysis and experiments. *Journal of Wind Engineering and Industrial Aerodynamics*, 67-68:611–625, 1997. ISSN 01676105.

V.J. Modi and F. Welt. Vibration control using nutation dampers. *International Conference on Flow Induced Vibrations*, pages 369–376, 1987.

Ockendon and Ockendon. Resonant surface waves. *Journal of Fluid Mechanics*, 59:397–413, 1973. ISSN 00221120.

Peregrine. Long waves on a beach. *Journal of Fluid Mechanics*, 27:815–827, 1967. ISSN 00221120.

Gray W. G. Pinder, F. G. *Finite Element Simulation in Surface and Subsurface Hydrology.* Academic Press, 1977.

Dorothy Reed, Jinkyu Yu, Harry Yeh, and Sigurdur Gardarsson. Investigation of tuned liquid dampers under large amplitude excitation. *Journal of Engineering Mechanics - Proceedings of the ASCE*, 124(4):405–413, 1998. ISSN 07339399.

Yu J.and Gardarsson S. Reed D. A., Yeh H. Experimental investigation of tuned liquid dampers. In *Proc. ASCE 1996 Int. Conf. on Natural Disaster Reduction*, 1996a.

Yu J.and Gardarsson S. Reed D. A., Yeh H. Performance of tuned liquid dampers for large amplitude excitation. In *Proc. 2nd Int. Workshop on Structural Control*, 1996b.

Bashir A. Sayar and J. R. Baumgarten. Linear ann nonlinear analysis of fluid slosh dampers. *AIAA Journal*, 20(11):1534–1538, 1982. ISSN 00011452.

M.L. Seto and V.J. Modi. Control of fluid-structure interaction instabilities using circular cylindrical nutation dampers. *International Journal of Offshore and Polar Engineering*, 7(3):174–180, 1997. ISSN 10535381.

L. Sun. *Semi-Analytical Modelling of Tuned Liquid Damper (TLD) with Emphasis on Damping of Liquid Sloshing*. PhD thesis, University of Tokyo, 1991.

Li Min Sun, Yozo Fujino, Benito M. Pacheco, and Masahiko Isobe. Nonlinear waves and dynamic pressures in rectangular tuned liquid damper (tld). simulation and experimental verification. *Doboku Gakkai Rombun-Hokokushu/Proceedings of the Japan Society of Civil Engineers*, (410):81–92, 1989. ISSN 02897806. hardcopy exists.

L.M. Sun and Y. Fujino. A semi-analytical model for tuned liquid damper (tld) with wave breaking. *Journal of Fluids and Structures*, 8(5):471–488, 1994. ISSN 08899746.

L.M. Sun, Y. Fujino, B.M. Pacheco, and P. Chaiseri. Modelling of tuned liquid damper (tld). *Journal of Wind Engineering and Industrial Aerodynamics*, 43(1-3):1883–1894, 1992. ISSN 01676105.

Jonsson I. G. Svendsen, I. A. *Hydrodynamics of Coastal Regions*. Den Private Ingeniørfond - Technical University of Denmark, 1994.

M. J. Tait. *The Performance of 1-D and 2-D Tuned Liquid Dampers*. PhD thesis, The University of Western Ontario, 2004.

M J Tait, N Isyumov, and A A El Damatty. Performance of tuned liquid dampers. *Journal of Engineering Mechanics - Proceedings of the ASCE*, 134(5):417, 2008. ISSN 07339399.

M.J. Tait, A.A. El Damatty, and N. Isyumov. The dynamic properties of a tuned liquid damper using an equivalent amplitude dependent tuned mass damper. *CSCE 30th Annual Conference Proceedings: 2002 Challenges Ahead - 4th Structural Specialty Conference, 4th Transportation Specialty Conference and 2nd material Specialty Conference and Proceedings, Annual Conference - Canadian Society for Civil Engineering*, 2002: 1995–2004, 2002. bestil 9.2.2007.

M.J. Tait, A.A. El Damatty, and N. Iayumov. Testing of tuned liquid damper with screens and development of equivalent tmd model. *Wind and Structures, An International Journal*, 7(4):215–234, 2004a. ISSN 12266116.

M.J. Tait, N. Isyumov, and A.A. El Damatty. The efficiency and robustness of a unidirectional tuned liquid damper and modelling with an equivalent tmd. *Wind and Structures, An International Journal*, 7(4):235–250, 2004b. ISSN 12266116.

M.J. Tait, A.A. El Damatty, and N. Isyumov. An investigation of tuned liquid dampers equipped with damping screens under 2d excitation. *Earthquake Engineering and Structural Dynamics*, 34(7):719–735, 2005a. ISSN 00988847.

M.J. Tait, A.A. El Damatty, N. Isyumov, and M.R. Siddique. Numerical flow models to simulate tuned liquid dampers (tld) with slat screens. *Journal of Fluids and Structures*, 20(8):1007–1023, 2005b. ISSN 08899746.

M.J. Tait, N. Isyumov, and A.A. El Damatty. Effectiveness of a 2d tld and its numerical modeling. *Journal of Structural Engineering*, 133(2):251–263, 2007. ISSN 07339445.

Y. Tamura, R. Kousaka, and V.J. Modi. Practical application of nutation damper for suppressing wind-induced vibrations of airport towers. *Journal of Wind Engineering and Industrial Aerodynamics*, 43(1-3):1919–1930, 1992. ISSN 01676105.

Yukio Tamura, Kunio Fujii, Tamio Ohtsuki, Toshihiro Wakahara, and Ryuichi Kohsaka. Effectiveness of tuned liquid dampers under wind excitation. *Engineering Structures*, 17(9):609–621, 1995. ISSN 01410296.

Yukio Tamura, Ryuichi Kohsaka, Osamu Nakamura, Koh-ichi Miyashita, and Vinod J. Modi. Wind-induced responses of an airport tower - efficiency of tuned liquid damper. *Journal of Wind Engineering and Industrial Aerodynamics*, 65(1-3):121–131, 1996. ISSN 01676105.

E. F. Toro. *Riemann Solvers And Numerical Methods For Fluid Dynamics: A Practical Introduction*. Springer, Apr 2009.

E. F. Toro. *Shock-capturing Methods For Free-surface Shallow Flows*. Wiley, April 2001.

WG Vandorn. Boundary dissipation of oscillatory waves. *Journal of fluid mechanics*, 24: 769–, 1966. Bestilet 24-2-2007.

C.B. Vreugdenhil. *Numerical Methods for Shallow-Water Flow*. Springer, 1994.

T. Wakahara, T. Ohyama, and K. Fujii. Suppression of wind-induced vibration of a tall building using tuned liquid damper. *Journal of Wind Engineering and Industrial Aerodynamics*, 43(1-3):1895–1906, 1992. ISSN 01676105.

Waterhouse. Resonant sloshing near a critical depth. *Journal of Fluid Mechanics*, 281: 313–318, 1994. ISSN 00221120.

P. Watts. The use of water chambers for reducing the rolling motion of ships at sea. *Trans. I.N.A.*, page 30, 1885.

F. Welt and J.V. Modi. Vibration damping through liquid sloshing, part 2. experimental results. *Journal of Vibration, Acoustics, Stress, and Reliability in Design*, 114(1):17–23, 1992a. ISSN 07393717.

F. Welt and V.J. Modi. Vibration damping through liquid sloshing, part i. a nonlinear analysis. *Journal of Vibration, Acoustics, Stress, and Reliability in Design*, 114(1): 10–16, 1992b. ISSN 07393717.

Swaroop K. Yalla and Ahsan Kareem. Optimum absorber parameters for tuned liquid column dampers. *Journal of Structural Engineering*, 126(8):906–915, 2000. ISSN 07339445.

J-K Yu, T Wakahara, and D A Reed. A non-linear numerical model of the tuned liquid damper. *Earthquake Engineering and Structural Dynamics*, 28(6):671–686, 1999. ISSN 00988847.

Appendix A

Experimental calibration

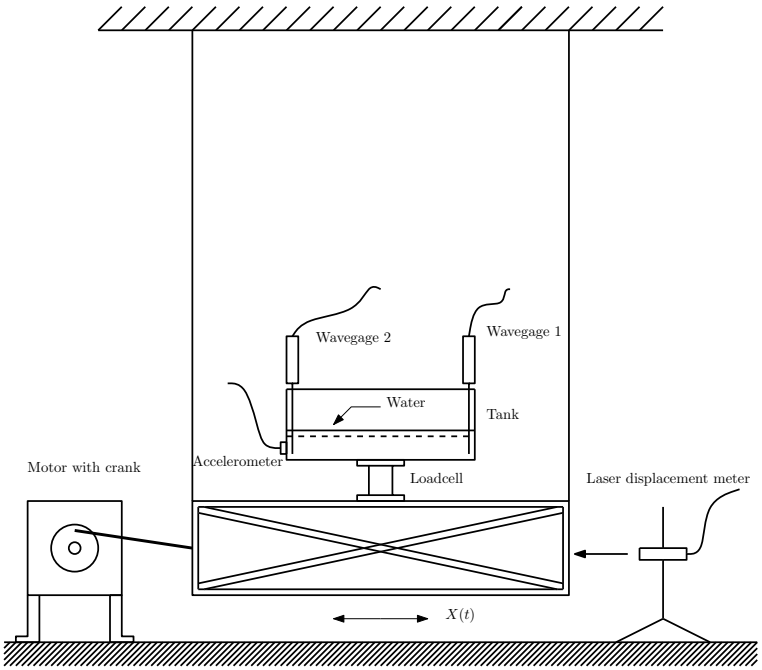

Figure A.1: *Experimental setup*

A.1 Experimental calibration procedure

In the experiments four different types of transducers are use: wave gages, a force transducer, an accelerometer and a displacement transducer. All transducers, except for the wave gages, are delivered with calibration constants, i.e. constants relating the measured voltage signal denoted $V_i^{\text{transducer}}$, where the lower index i indicates a discrete or sampled signal and the upper index refers to the specific transducer, with physical values. Thus

$$S_i^{\text{transducer}} = \frac{V_i^{\text{transducer}}}{K^{\text{transducer}}} \tag{A.1}$$

In the following the calibration constant are verified through a series of shaking table experiments collected in table A.1

Experiment i.d. [-]	A [mm]	f_e [Hz]	mass configuration [-]	m_{tot} [kg]
m01a05	5	0.4-1.2	11	15.045
m01a20	20	0.4-1.2	11	15.045
m01a60	60	0.4-1.2	11	15.045
m02a05	5	0.4-1.2	12	22.311
m02a20	20	0.4-1.2	12	22.311
m02a60	60	0.4-1.2	12	22.311
m03a60	60	0.4-1.2	13	0.0

Table A.1: *Measurement campaign. Calibration of FT and accelerometer.*

A.2 Calibration of accelerometer and laser displacement transducer (LDT)

The laser displacement transducer WayCON LAS-T-250A is delivered as calibrated and supplies a 0.10 voltage signal in the displacement range 50-300 mm, corresponding to a signal output of 25 mm/volt.

The accelerometer used in the test is of type B&K 4575 and has a calibration constant of 102.3 mv/ms^{-2}. The calibration constant is based on a calibration procedure from B&K in the frequency range from 1 to 200 Hz and thus the calibration constant may be different in the low frequency range 0.5-1.2 Hz where the majority of our experiments are carried out. A range of experiments are conducted to establish the amplitude relationship between the accelerometer and LDT. The shaking table is moved in the horizontal direction with an amplitude A and frequency Ω, thus the table displacement is approximately given by

$$X(t) = A\sin(\Omega t) \tag{A.2}$$

To establish the relation between the measured acceleration and displacement we choose to fit the measured displacement signal to the following function

$$\tilde{X}(t) = \tilde{A}\sin(\tilde{\Omega}t + \tilde{\phi}) \tag{A.3}$$

where the unknowns $\tilde{A}$, $\tilde{\Omega}$ and $\tilde{\phi}$ are found using a least square optimization procedure, thus a very good estimate of the table frequency and amplitude has been established. The frequency could of course also have been established using a Fourier transformation, however later on we will need the shown data fit. For every experiment id in table A.1 a total of nine experiments are performed varying the table frequency from 0.4 to 1.2Hz in steps of 0.1 Hz and keeping the table amplitude in a fixed position. The data processing shown in figure A.2 is performed for every one of the nine runs and based on the data the standard deviation of the voltage signal from the accelerometer and LDT is found and plotted as shown in figure A.3. A best straight line is estimated where the slope is an estimate of the calibration constant K^{acc}, using the following definition

$$K^{\text{acc}}[\text{V/ms}^{-2}] = \frac{\sigma_{V_i^{\text{acc}}}}{\tilde{\Omega}^2\sigma_{X_i}} \tag{A.4}$$

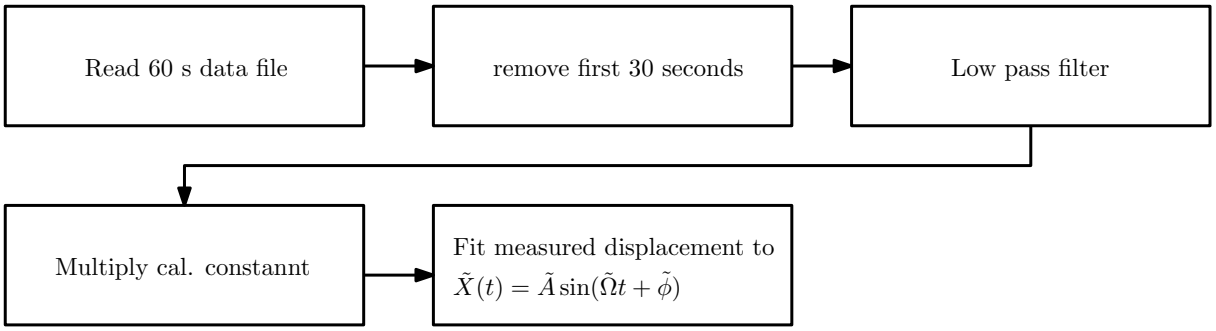

Figure A.2: *Fitting procedure*

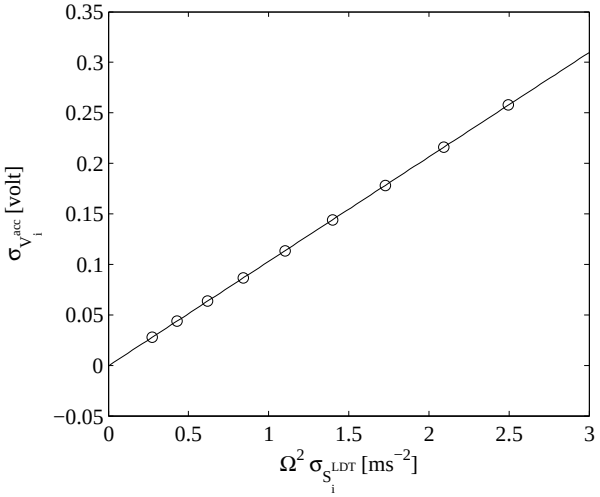

Figure A.3: *Best straight line fit through accelerometer and displacement data. The data is taken from experiment m02a60, see table A.1*

Experiment i.d. [-]	K^{acc} volt/ms^{-2}
m01a05	0.1030
m01a20	0.1035
m01a60	0.1040
m02a05	0.1028
m02a20	0.1037
m02a60	0.1041
m03a60	0.1034
$\frac{1}{N}\sum$	0.1035

Table A.2: *Computed slopes*

In table A.2 the computed slope is shown for all seven experiments. The calibration constant is close to constant for the different amplitudes. It is seen that the estimated calibration constant is close to the value supplied by B&K 4575 with a value of 0.1023

$\mathrm{V/ms^{-2}}$. This value is used in the experiments.

A.3 Calibration of Force Transducer (FT)

A vital part of the experimental setup is the Force Transducer (FT) used to measure the horizontal sloshing forces. The FT used in the experiments is of the type AMTI MC3-6-500 and is capable of measuring three force and three moment components.

The calibration is divided into a static part and a dynamic part. The purpose of a static calibration is solely to establish the static calibration constant while the dynamic calibration is twofold. First we need to determine the size of the inherent dead mass of the FT since this mass will give a contribution to the total inertia force. Secondly we need to determine the dynamic characteristics of the FT in the frequency area of interest.

A.3.1 Static calibration

The static calibration setup is depicted in figure A.4. A thin string is attached to the FT at at height h above the FT top plate, and is along a horizontal line drawn to and around a frictionless wheel where a mass tray is finally hung. By adding mass the gravity force F_g and thereby the horizontal force acting on the FT, can be varied. The calibration curve is shown in figure A.5 where the mean value of the voltage signal from the FT is shown as function of the applied force. The trend is very linear and the calibration constant is found as the slope of the shown line to

$$K^{\mathrm{FT}} = 0.0540 \frac{\mathrm{volt}}{\mathrm{N}} \tag{A.5}$$

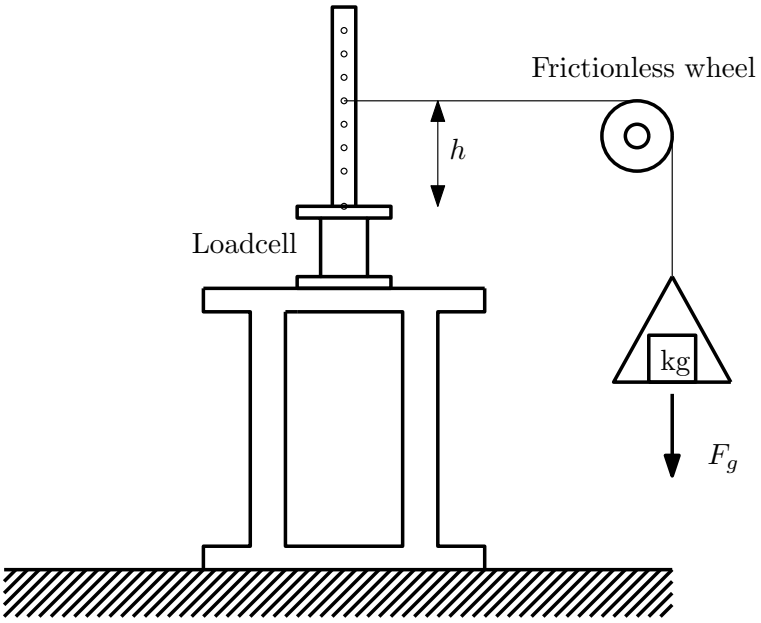

Figure A.4: *Static calibration of force transducer*

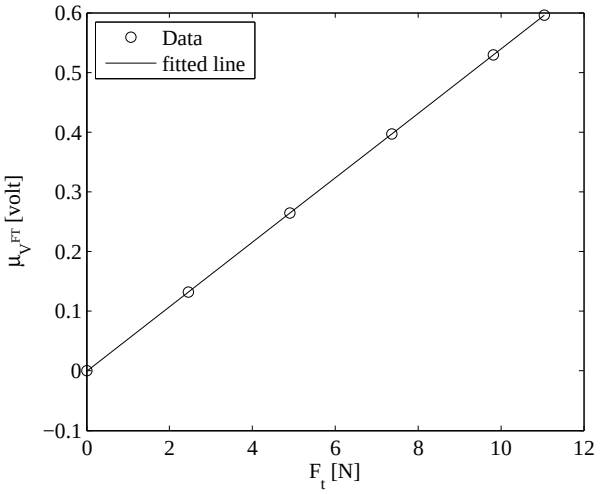

Figure A.5: *Static calibration of force transducer. In the figure $h = 0$ mm*

A.3.2 Dynamic calibration - inherent FT mass

To establish the inherent FT mass a number of shaking table experiments are conducted with no mass added to the FT. The experiment are identified as $m03a60$ in table A.1. In the experiments the amplitude of the table is set to a constant value of $A = 60$ mm and the frequency is varied from 0.4 Hz to 1.2 Hz in steps of 0.1 Hz. For each frequency value the standard deviation of the FT signal and acceleration signal is recorded and plotted as shown in figure A.6. Based on the following relation

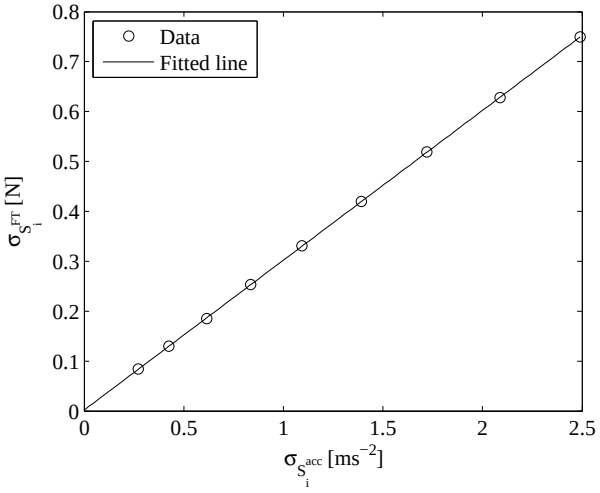

Figure A.6: *Dynamic calibration of FT. Inherent mass*

$$\sigma_{S_i^{\mathrm{FT}}} = m_{\mathrm{inh}} \sigma_{S_i^{\mathrm{acc}}} \tag{A.6}$$

the slope of the line in figure A.6 is a measure of the inherent FT mass $m_{mathrminh}$ and is found to

$$m_{\mathrm{inh}} = 0.290 \text{ kg} \tag{A.7}$$

A.3.3 Dynamic calibration - amplitude

The total horizontal inertia force acting on a force transducer loaded with a mass m and given a horizontal acceleration $\ddot{X}(t)$ is

$$F_I(t) = (m + m_{\text{inh}})\ddot{X}(t) = m_{\text{tot}}\ddot{X}(t) \tag{A.8}$$

In the previous section the calibration constant relating voltage output from the FT to force, K^{FT}, was found A.11 through a static calibration and also the calibration constant relating voltage output from the accelerometer to acceleration, K^{acc}, was established A.2. This enables us to compute the inertia force from either the FT or from the total mass and acceleration. The residual defined as

$$r_i = S_i^{\text{FT}} - m_{\text{tot}}S_i^{\text{acc}} \tag{A.9}$$

i.e. the difference between the force measured using the FT and the signal computed using measured acceleration and total mass, should be minimized, and theoretically equal to zero. However due to measurement noise, small phase lags between the different transducers, the residual will de different from zero. This is shown in figure A.7 where the force signals are shown to the left and the residual together with the FT signal to the right for different frequency values and a fixed amplitude of $A = 5$ mm. It is noticed that especially the low frequency case has a quite large residual signal. To improve this we try to use the displacement signal from the LDT and convert this into acceleration using the forcing frequency. As long as the forcing signal is narrow banded the error in the computed acceleration signal is very limited. In figure A.8 the force signals and residuals are again depicted nut now with a force based on the signal from the LDT. The residuals are reduced very much for the low frequency case while the effect is smaller for the higher frequencies.

To quantify the error connected with subtracting the two force signals we define the Noise to Signal Ratio, NSR, as the following

$$NSR = \frac{\sigma_{r_i}}{\sigma_{S_i^{\text{FT}}}} \tag{A.10}$$

In figure A.9 the Noise to Signal Ration has been plotted as function of the acceleration for mass configuration 1 and 2. In each figure the NSR has been computed using the accelerometer signal and the converted LDT signal. For all cases it is seen that the NSR for the converted LDT signal is well below 10% and for most cases around 5%. Even though the NSR is lower for the accelerometer based force in the acceleration range 0.5-3 ms^{-2} we find that using the converted LDT signal in general gives a more smooth signal, since of course spurious high acceleration peaks are not measured by the LDT, and therefor we use this approach for cases where the forcing frequency is narrow banded. For other cases the accelerometer based force will be used.

A.4 Calibration of wave gages

A wave gage is mounted in each end of the tanks and are not supplied with a calibration constant. The calibration routine is performed in the following way. The tank is placed

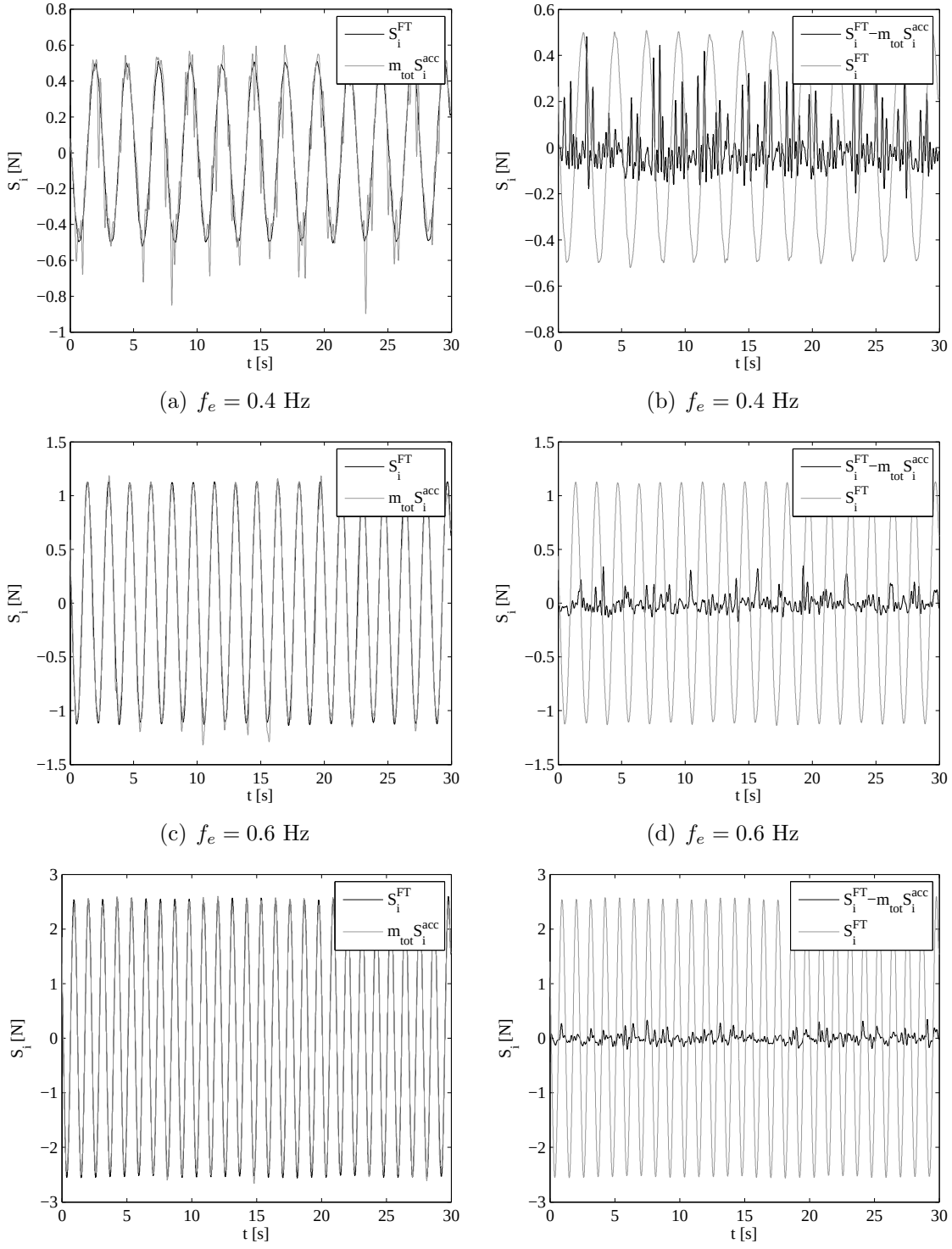

(a) $f_e = 0.4$ Hz (b) $f_e = 0.4$ Hz

(c) $f_e = 0.6$ Hz (d) $f_e = 0.6$ Hz

(e) $f_e = 0.9$ Hz (f) $f_e = 0.9$ Hz

Figure A.7: *Force measured by FT and force computed using measured acceleration S_i^{acc} and total mass m_{tot}.*

is placed on a horizontal plane with the wave gages in the working position. A fixed

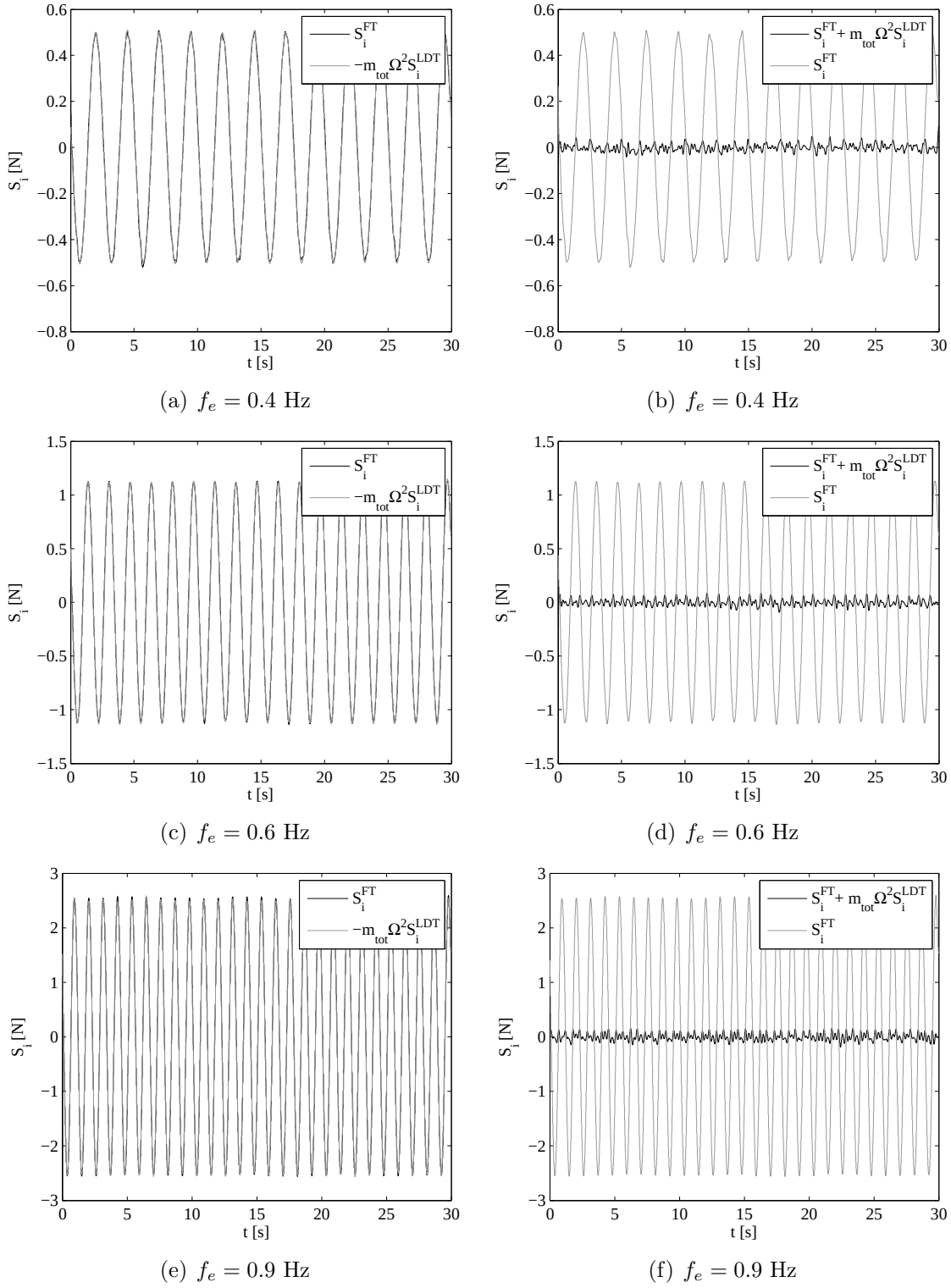

(a) $f_e = 0.4$ Hz (b) $f_e = 0.4$ Hz

(c) $f_e = 0.6$ Hz (d) $f_e = 0.6$ Hz

(e) $f_e = 0.9$ Hz (f) $f_e = 0.9$ Hz

Figure A.8: *Force measured by FT and force computed using measured displacement* S_i^{LDT}*, forcing frequency* Ω *and total mass* m_{tot}*.*

volume of water is measured on a scale and is poured into the tank. The undisturbed

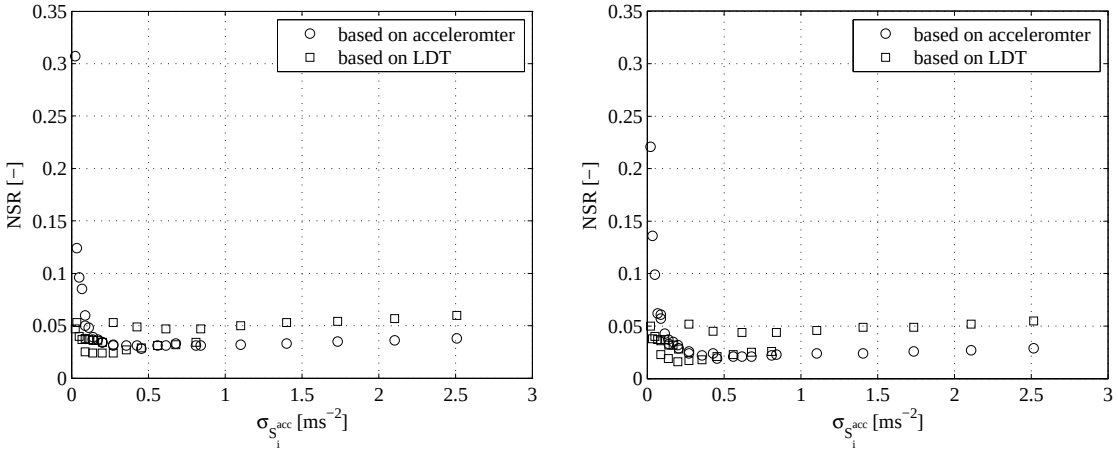

(a) Mass configuration 1 (b) Mass configuration 2

Figure A.9: *Noise to Signal Ratio, NSR, for mass configuration 1 and 2*

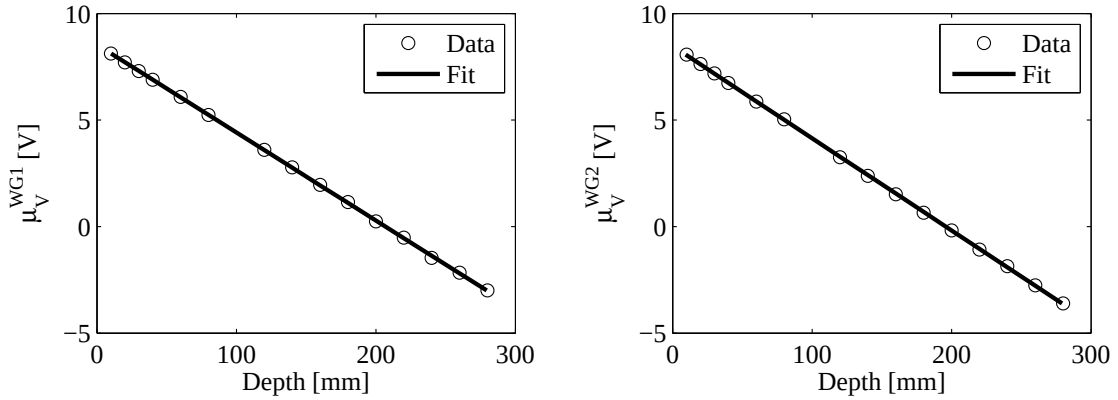

(a) Wave gage 1 (b) Wave gage 2

Figure A.10: *Wave gage calibration*

water depth is easily found using the dimensions of the tank together with the density of water $\rho = 1000\text{kg}$ and the mass of the mass. Using this routine compared to measuring the depth directly is much more precise. Of course the plane where the tank is mounted must be perfectly plane which is assured using a digital inclinometer. The results from the calibration are shown in figure A.10 and the calibration constants defined as the slopes of the best fitted straight lines are

$$K^{\text{WG1}} = -0.04130\frac{\text{volt}}{\text{mm}}, \quad K^{\text{WG2}} = -0.04327\frac{\text{volt}}{\text{mm}} \tag{A.11}$$

Appendix B

Frequency response curves

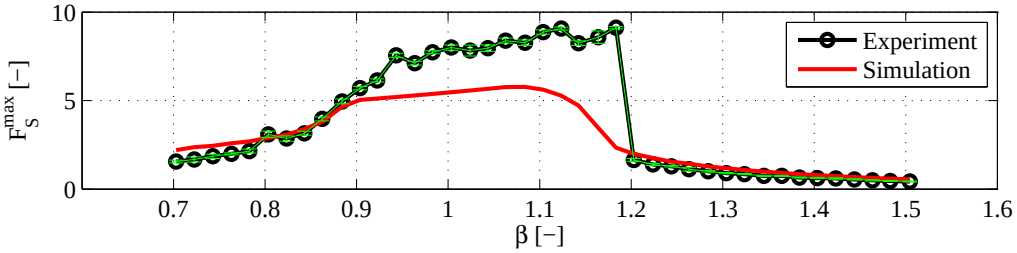

(a) $a = 5$ mm, $A/L = 0.009$

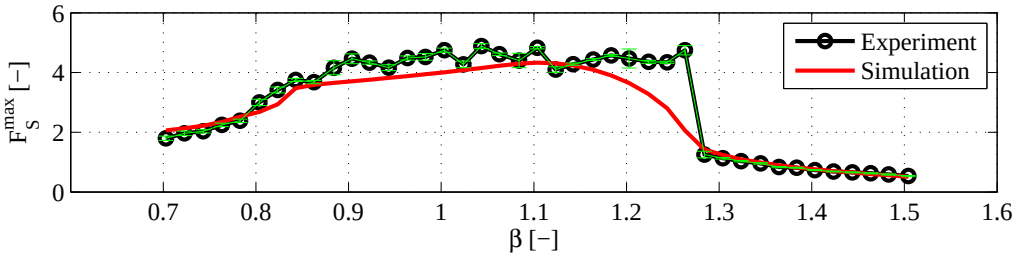

(b) $a = 10$ mm, $A/L = 0.017$

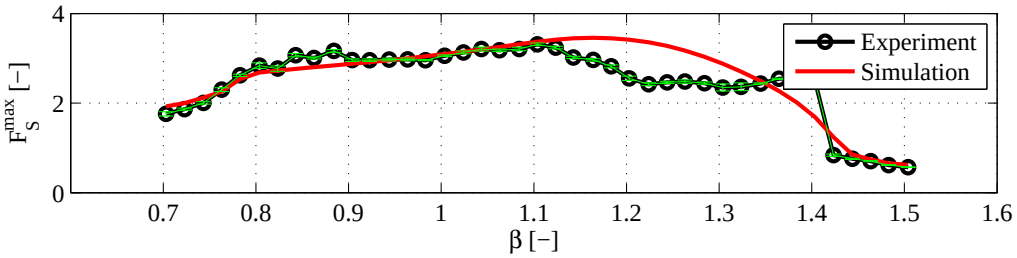

(c) $a = 20$ mm, $A/L = 0.034$

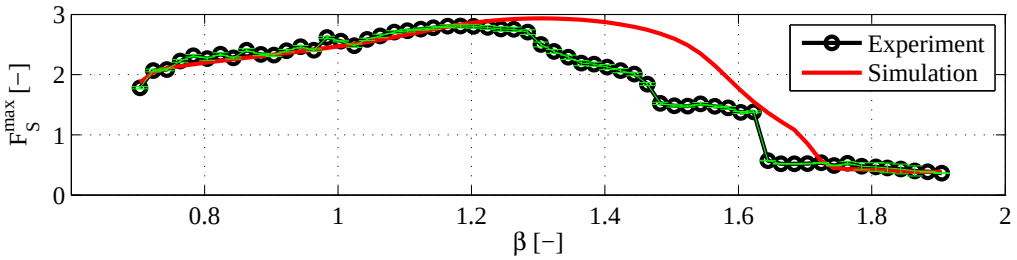

(d) $a = 40$ mm, $A/L = 0.068$

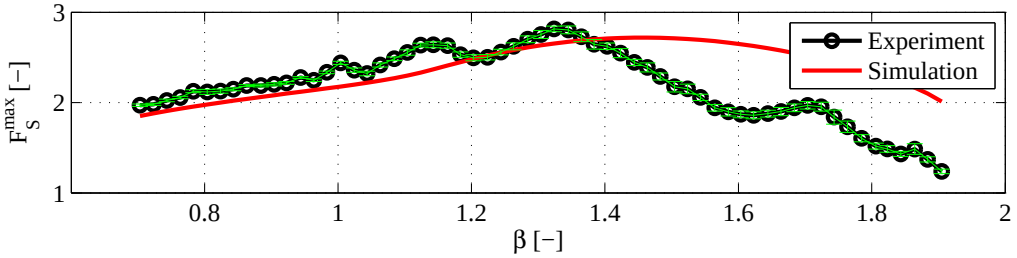

(e) $a = 60$ mm, $A/L = 0.101$

Figure B.1: *Frequency response curves for sloshing force. Water depth $h = 20$ mm corresponding to $h/L = 0.034$.*

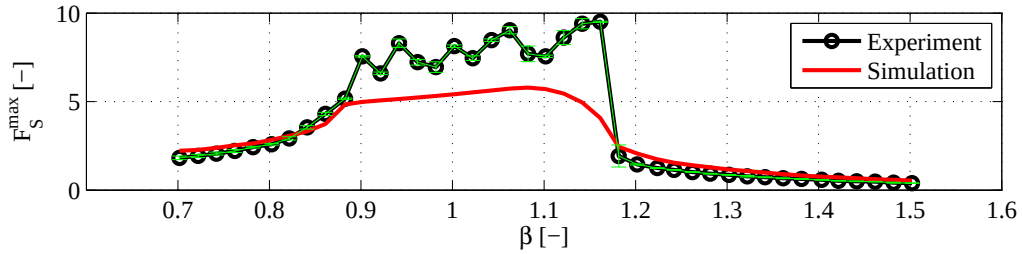

(a) $a = 5$ mm, $A/L = 0.009$

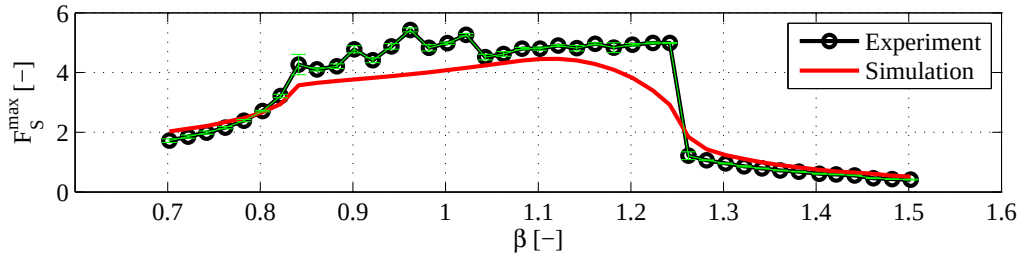

(b) $a = 10$ mm, $A/L = 0.017$

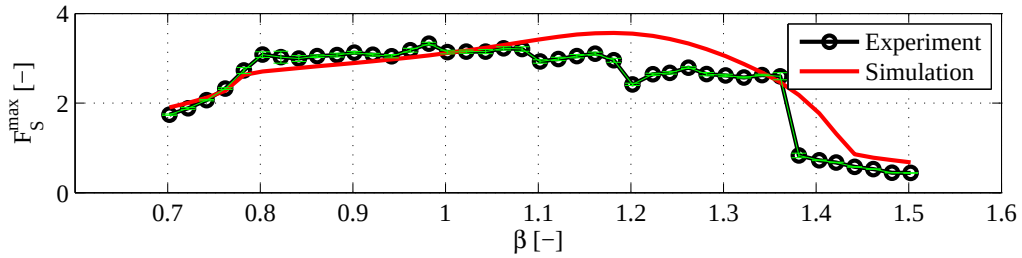

(c) $a = 20$ mm, $A/L = 0.034$

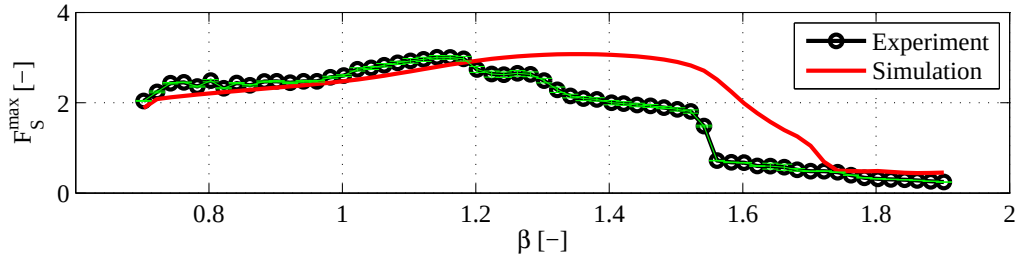

(d) $a = 40$ mm, $A/L = 0.068$

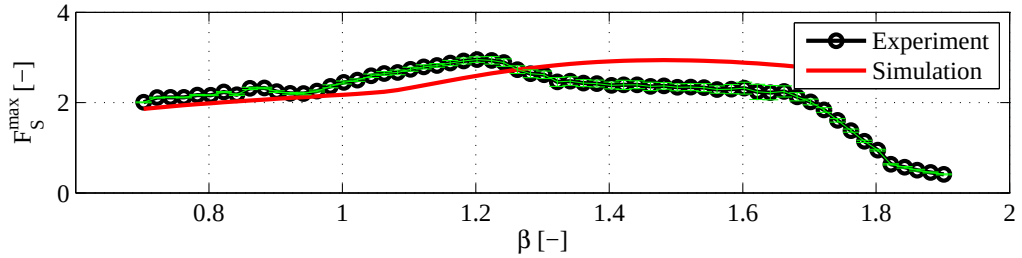

(e) $a = 60$ mm, $A/L = 0.101$

Figure B.2: *Frequency response curves for sloshing force. Water depth $h = 30$ mm corresponding to $h/L = 0.051$.*

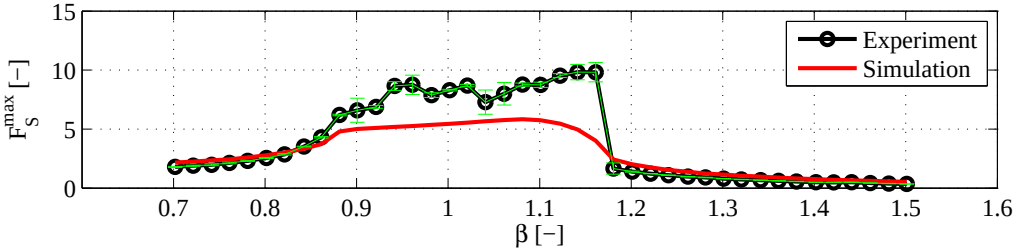

(a) $a = 5$ mm, $A/L = 0.009$

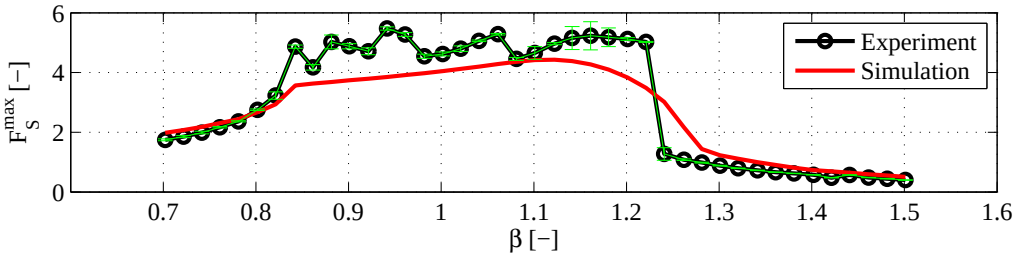

(b) $a = 10$ mm, $A/L = 0.017$

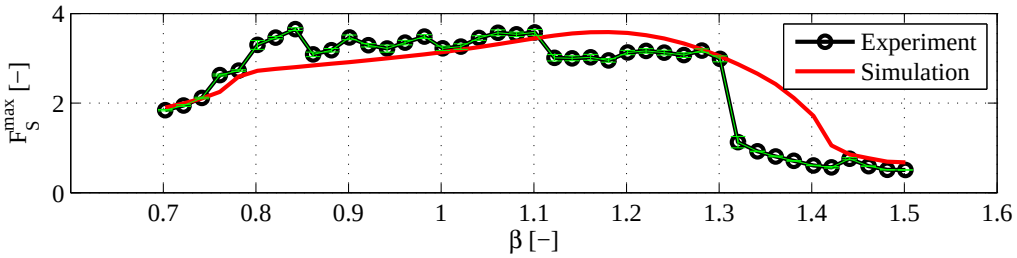

(c) $a = 20$ mm, $A/L = 0.034$

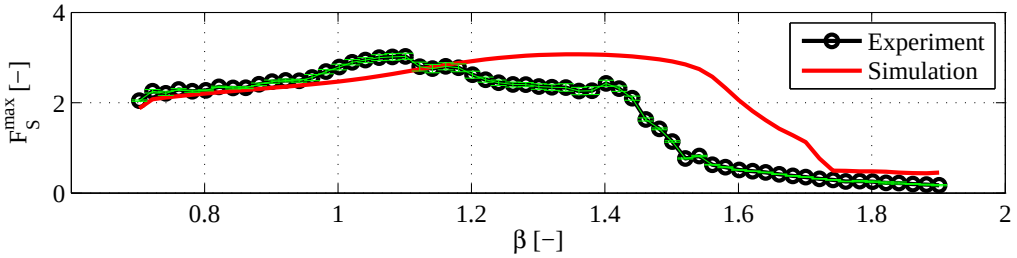

(d) $a = 40$ mm, $A/L = 0.068$

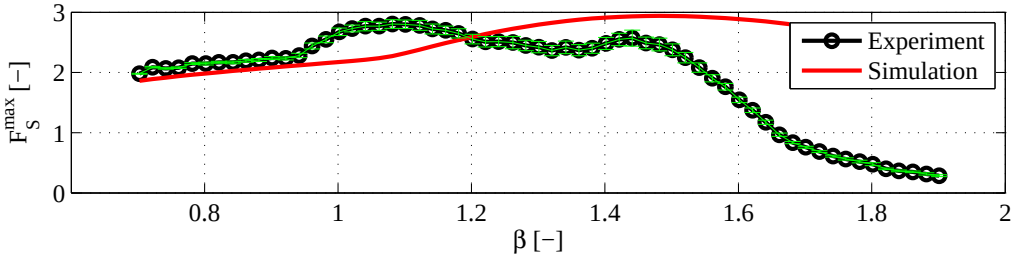

(e) $a = 60$ mm, $A/L = 0.101$

Figure B.3: *Frequency response curves for sloshing force. Water depth $h = 40$ mm corresponding to $h/L = 0.068$.*

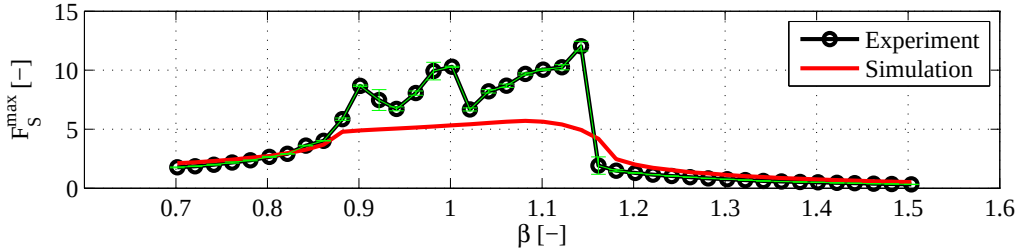

(a) $a = 5$ mm, $A/L = 0.009$

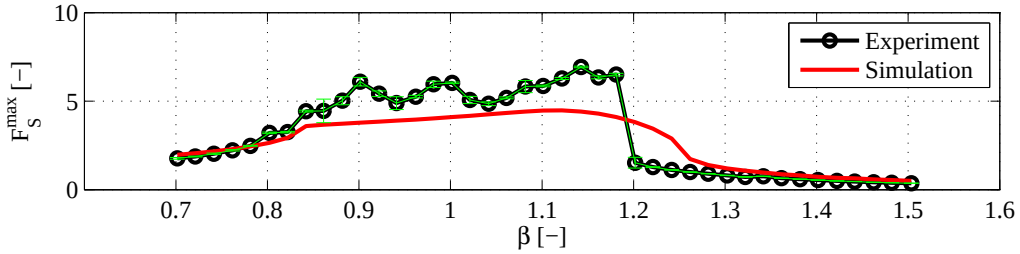

(b) $a = 10$ mm, $A/L = 0.017$

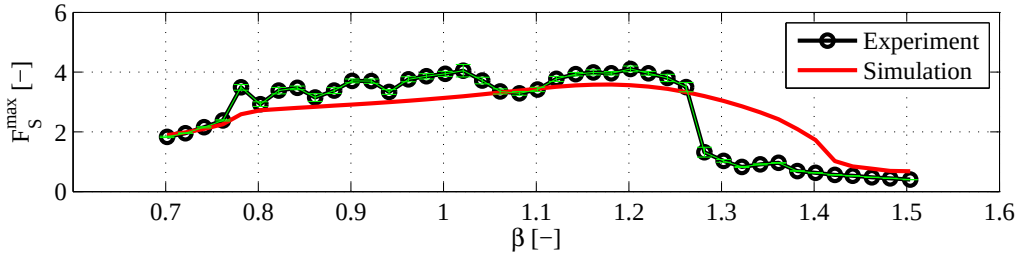

(c) $a = 20$ mm, $A/L = 0.034$

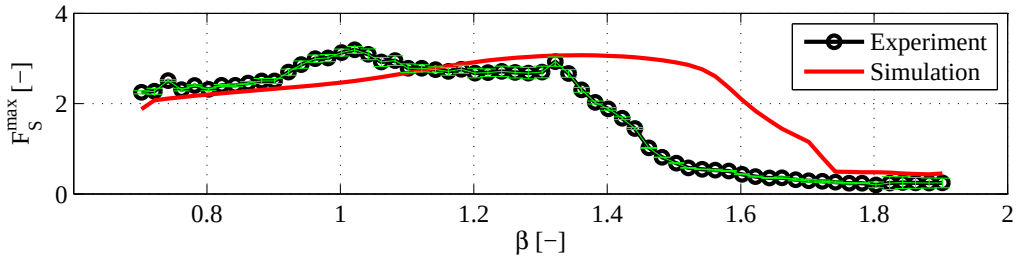

(d) $a = 40$ mm, $A/L = 0.068$

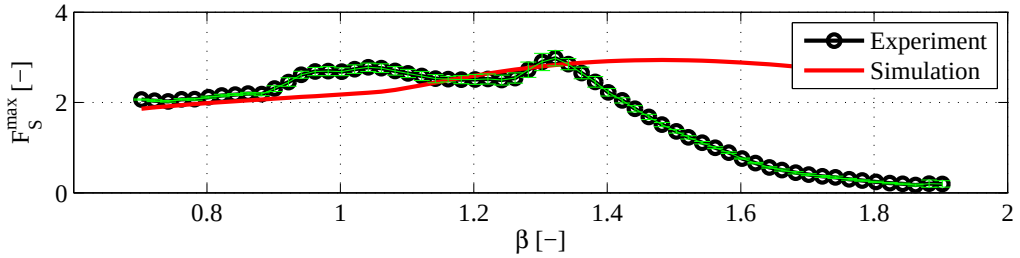

(e) $a = 60$ mm, $A/L = 0.101$

Figure B.4: *Frequency response curves for sloshing force. Water depth $h = 50$ mm corresponding to $h/L = 0.085$.*

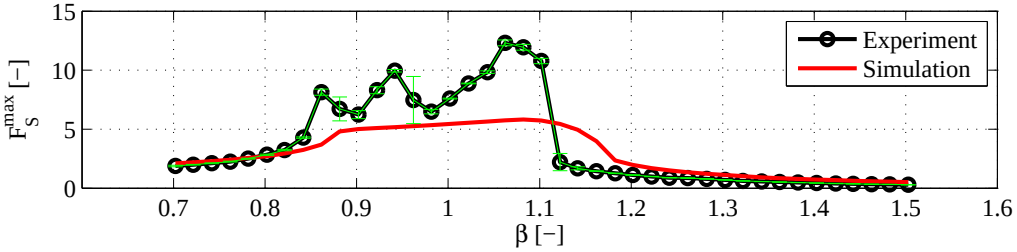

(a) $a = 5$ mm, $A/L = 0.009$

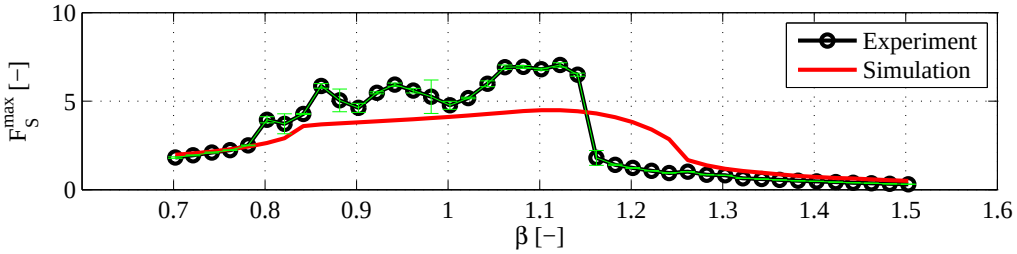

(b) $a = 10$ mm, $A/L = 0.017$

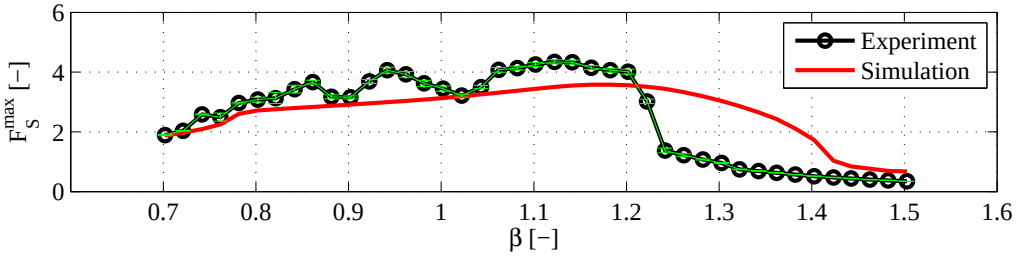

(c) $a = 20$ mm, $A/L = 0.034$

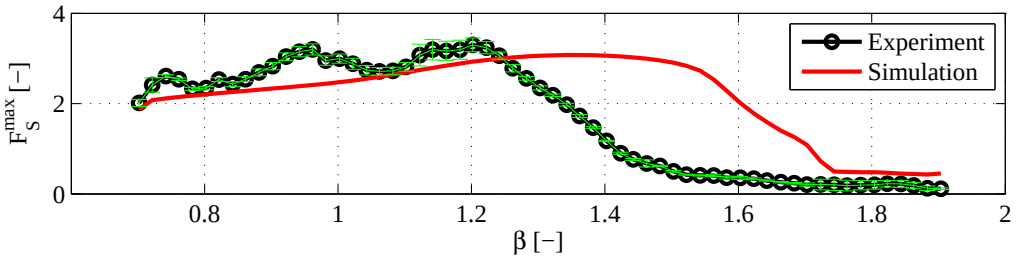

(d) $a = 40$ mm, $A/L = 0.068$

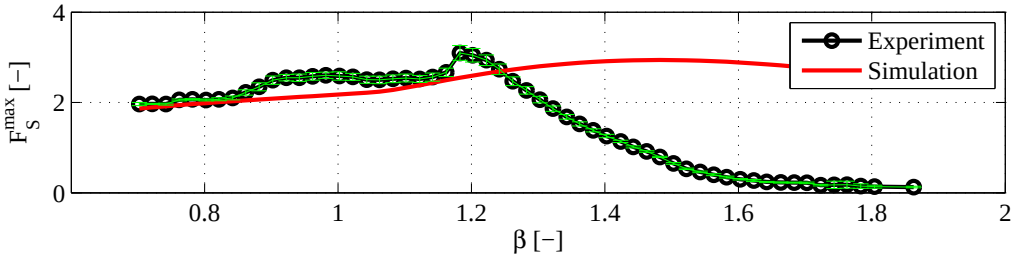

(e) $a = 60$ mm, $A/L = 0.101$

Figure B.5: *Frequency response curves for sloshing force. Water depth $h = 60$ mm corresponding to $h/L = 0.101$.*

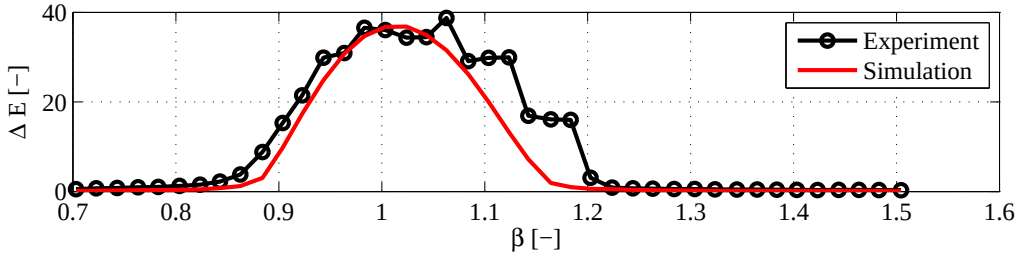

(a) $a = 5$ mm, $A/L = 0.009$

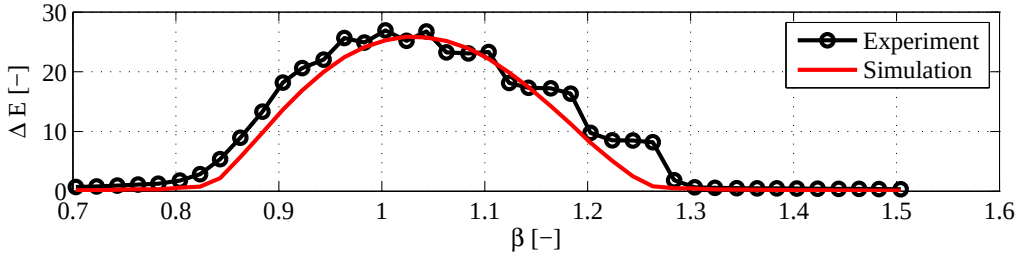

(b) $a = 10$ mm, $A/L = 0.017$

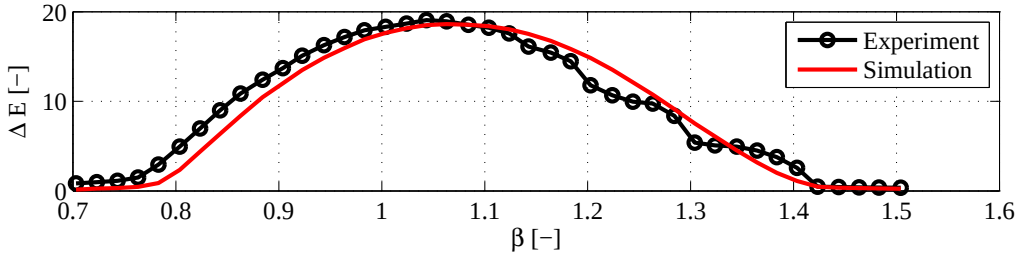

(c) $a = 20$ mm, $A/L = 0.034$

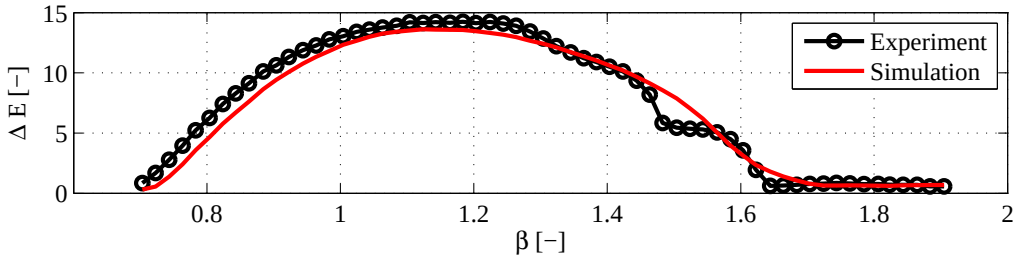

(d) $a = 40$ mm, $A/L = 0.068$

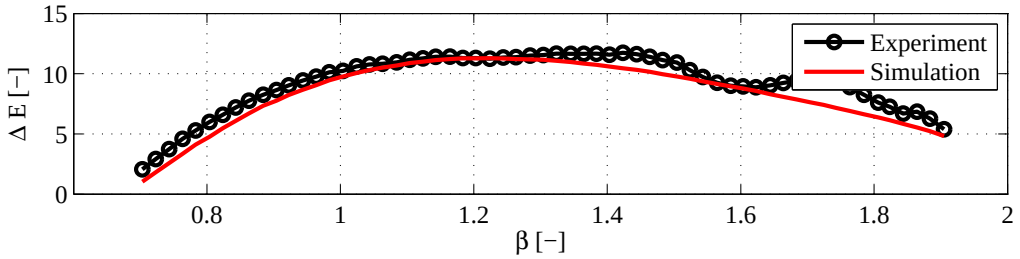

(e) $a = 60$ mm, $A/L = 0.101$

Figure B.6: *Frequency response curves for energy dissipation. Water depth $h = 20$ mm corresponding to $h/L = 0.034$.*

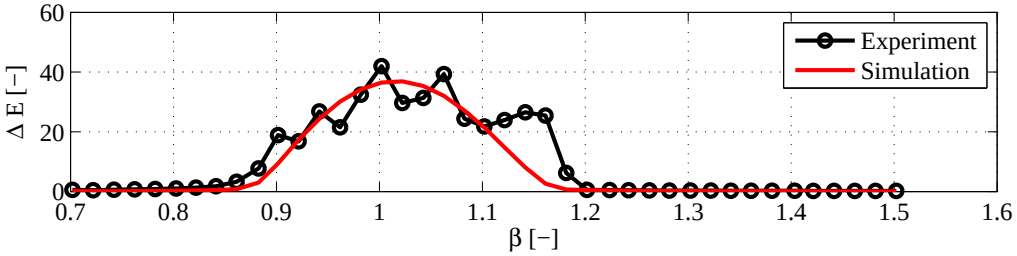

(a) $a = 5$ mm, $A/L = 0.009$

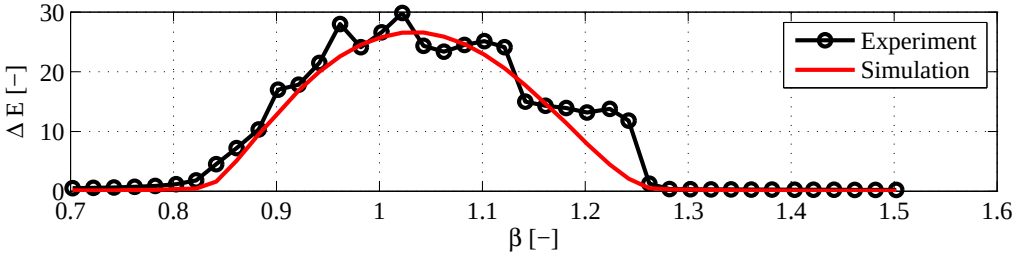

(b) $a = 10$ mm, $A/L = 0.017$

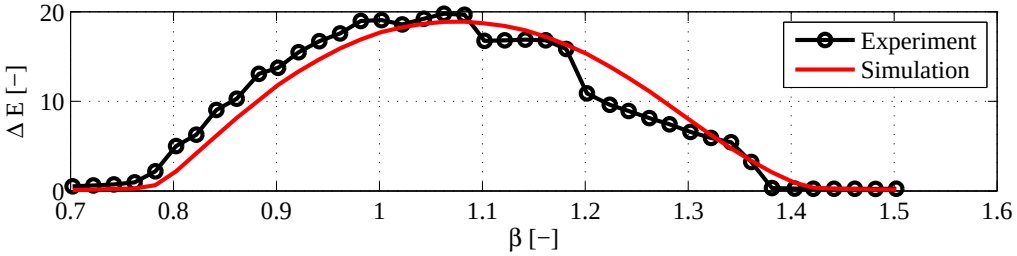

(c) $a = 20$ mm, $A/L = 0.034$

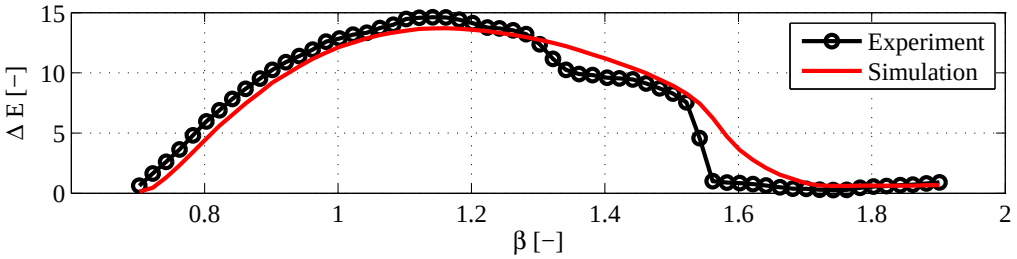

(d) $a = 40$ mm, $A/L = 0.068$

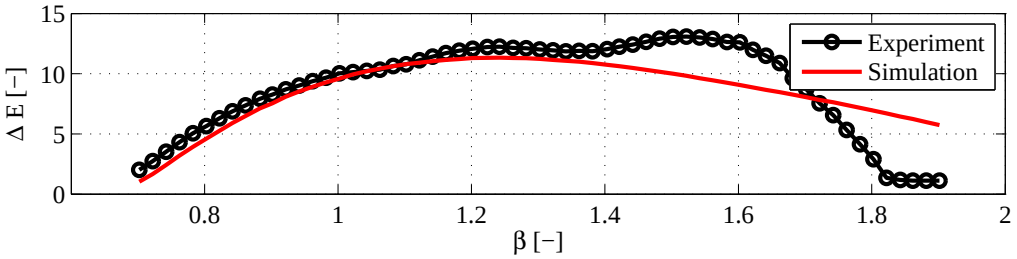

(e) $a = 60$ mm, $A/L = 0.101$

Figure B.7: *Frequency response curves for energy dissipation. Water depth $h = 30$ mm corresponding to $h/L = 0.051$.*

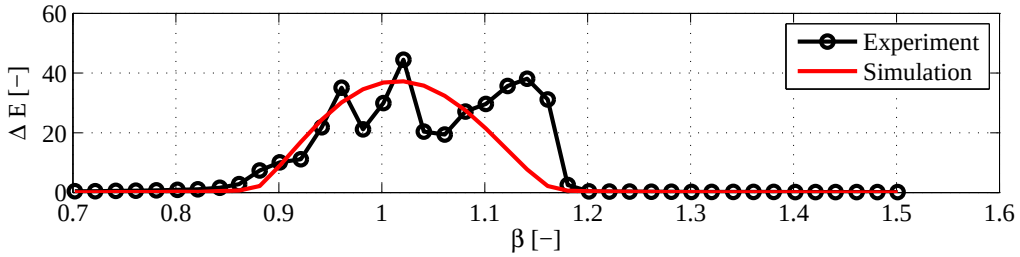

(a) $a = 5$ mm, $A/L = 0.009$

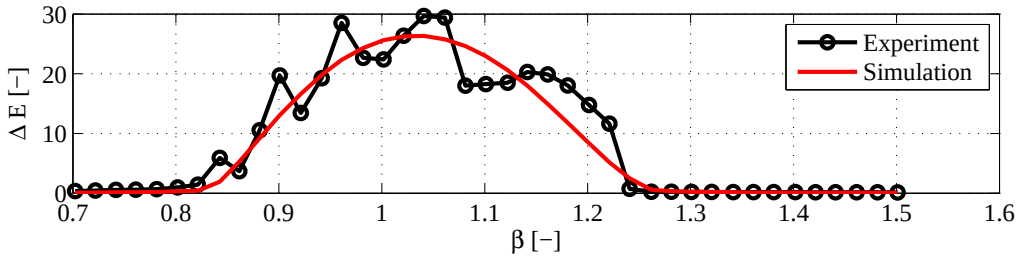

(b) $a = 10$ mm, $A/L = 0.017$

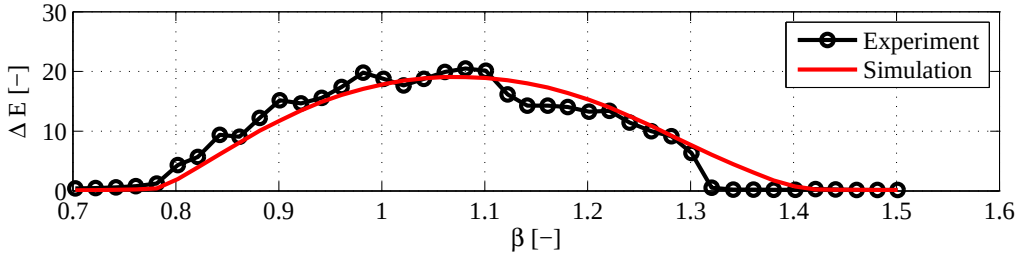

(c) $a = 20$ mm, $A/L = 0.034$

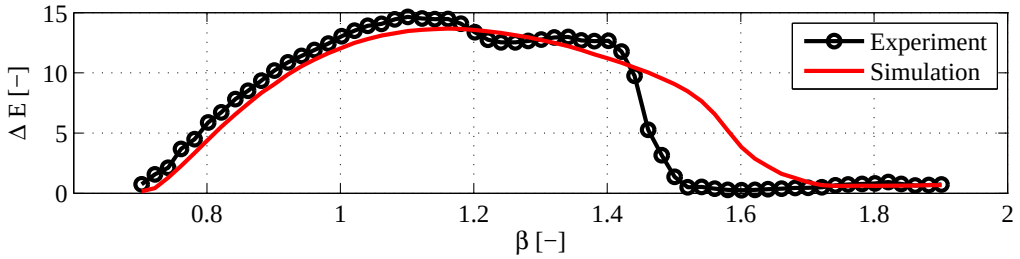

(d) $a = 40$ mm, $A/L = 0.068$

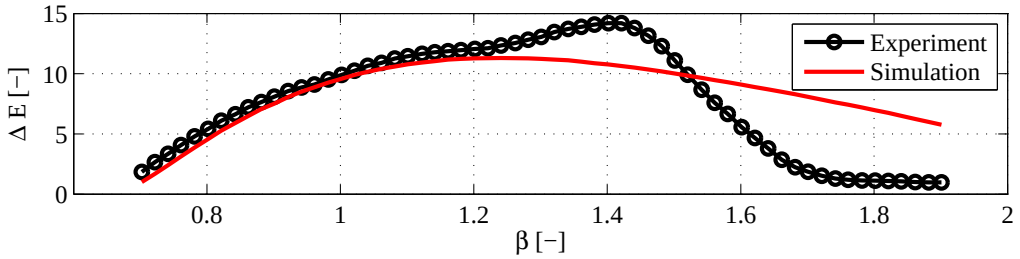

(e) $a = 60$ mm, $A/L = 0.101$

Figure B.8: *Frequency response curves for energy dissipation. Water depth $h = 40$ mm corresponding to $h/L = 0.068$.*

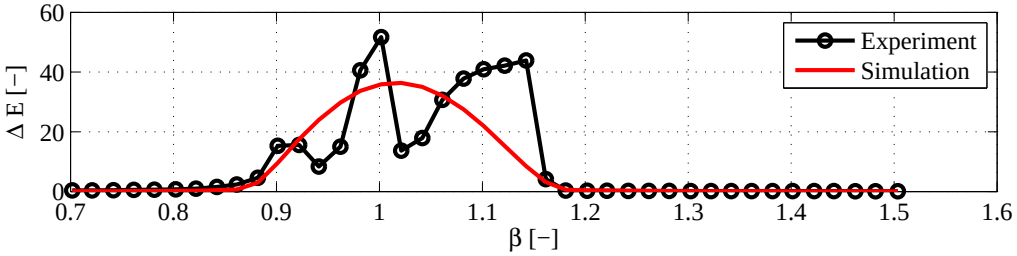

(a) $a = 5$ mm, $A/L = 0.009$

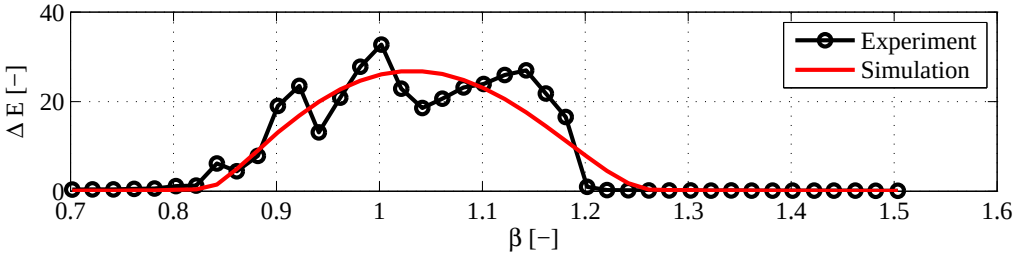

(b) $a = 10$ mm, $A/L = 0.017$

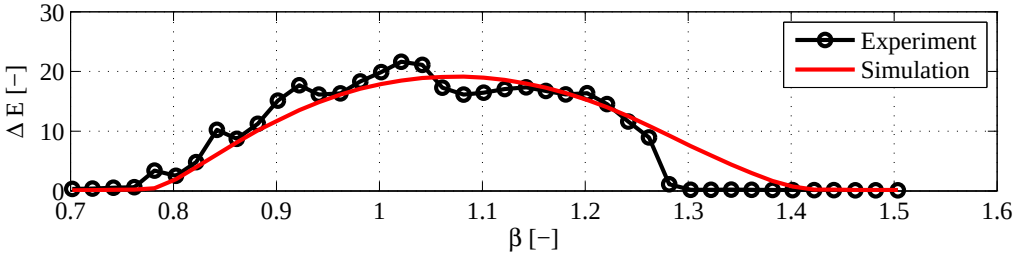

(c) $a = 20$ mm, $A/L = 0.034$

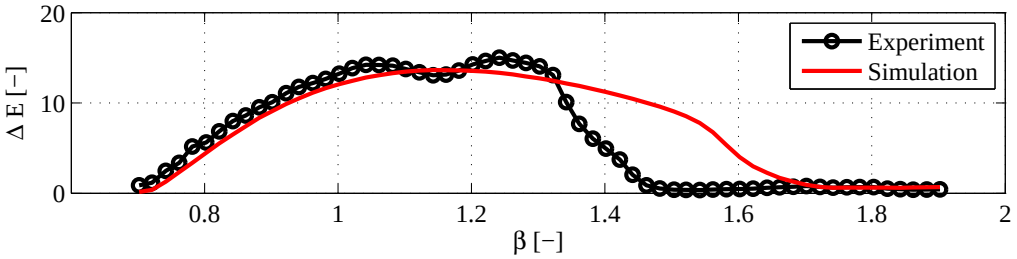

(d) $a = 40$ mm, $A/L = 0.068$

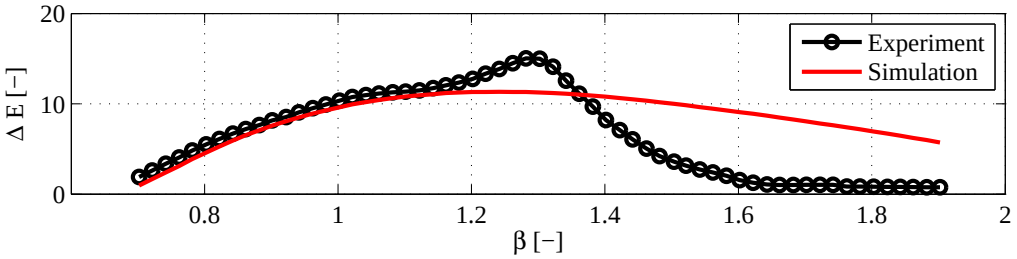

(e) $a = 60$ mm, $A/L = 0.101$

Figure B.9: *Frequency response curves for energy dissipation. Water depth $h = 50$ mm corresponding to $h/L = 0.085$.*

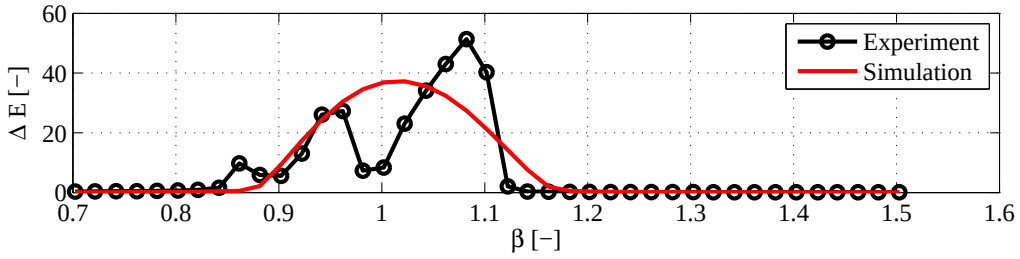

(a) $a = 5$ mm, $A/L = 0.009$

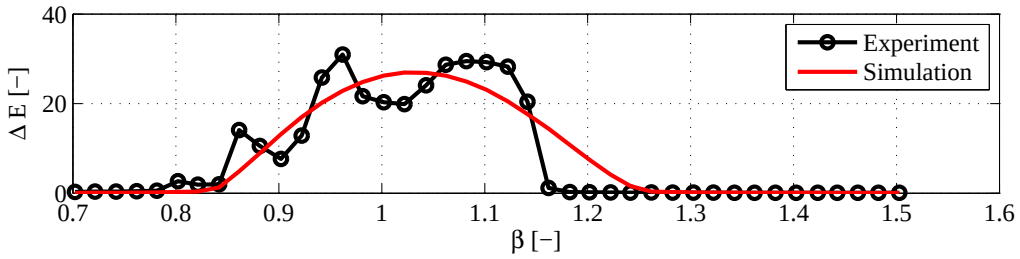

(b) $a = 10$ mm, $A/L = 0.017$

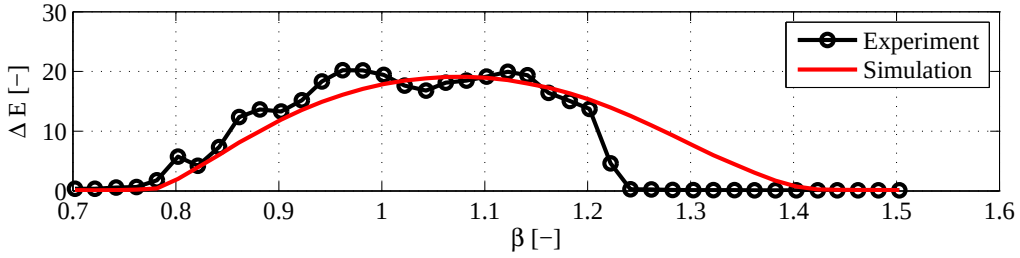

(c) $a = 20$ mm, $A/L = 0.034$

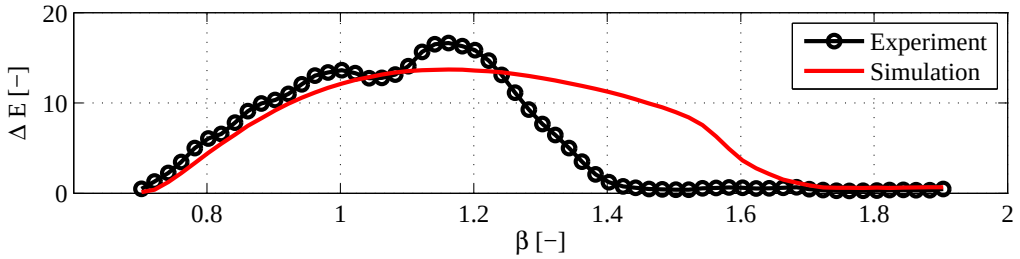

(d) $a = 40$ mm, $A/L = 0.068$

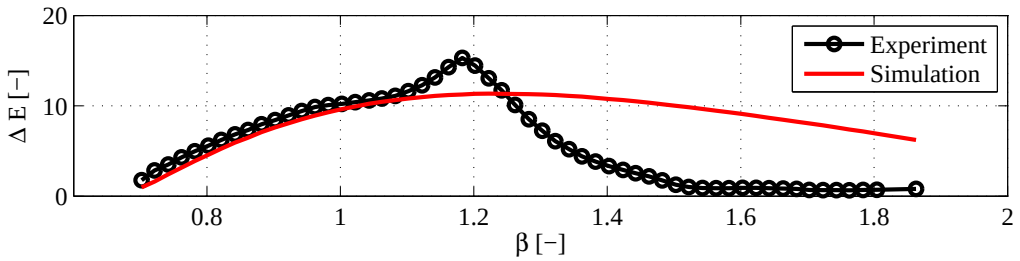

(e) $a = 60$ mm, $A/L = 0.101$

Figure B.10: *Frequency response curves for energy dissipation. Water depth $h = 60$ mm corresponding to $h/L = 0.101$.*

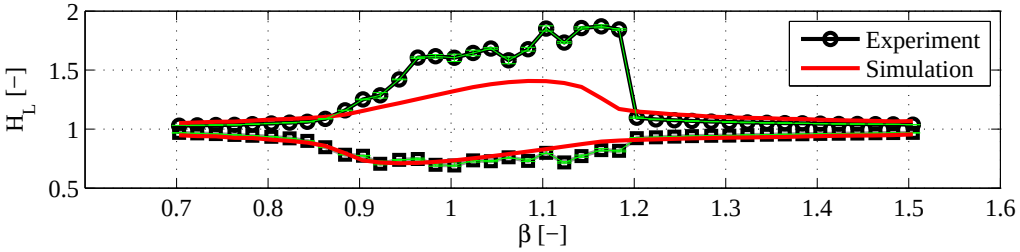

(a) $a = 5$ mm, $A/L = 0.009$

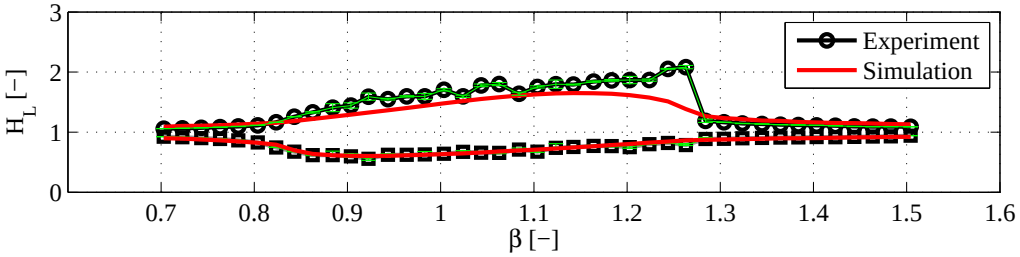

(b) $a = 10$ mm, $A/L = 0.017$

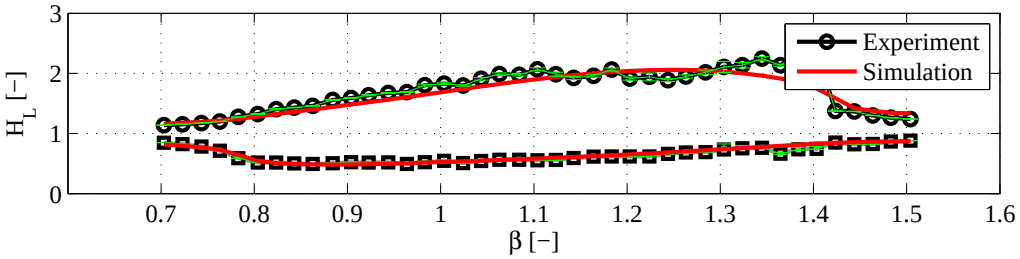

(c) $a = 20$ mm, $A/L = 0.034$

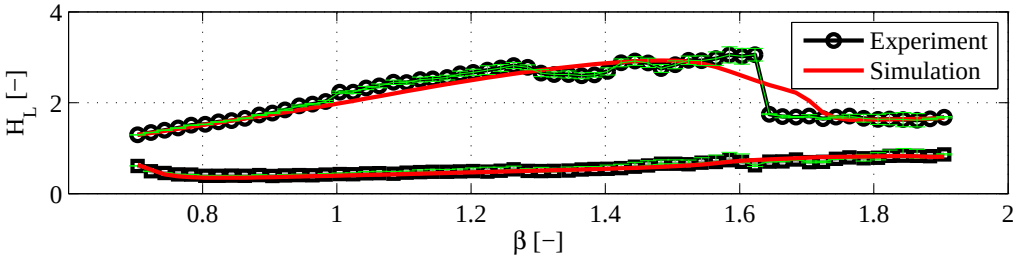

(d) $a = 40$ mm, $A/L = 0.068$

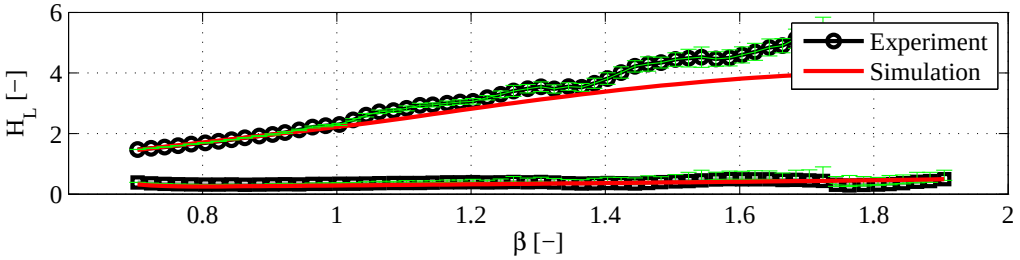

(e) $a = 60$ mm, $A/L = 0.101$

Figure B.11: *Frequency response curves for wave depth at left tank wall. Water depth $h = 20$ mm corresponding to $h/L = 0.034$.*

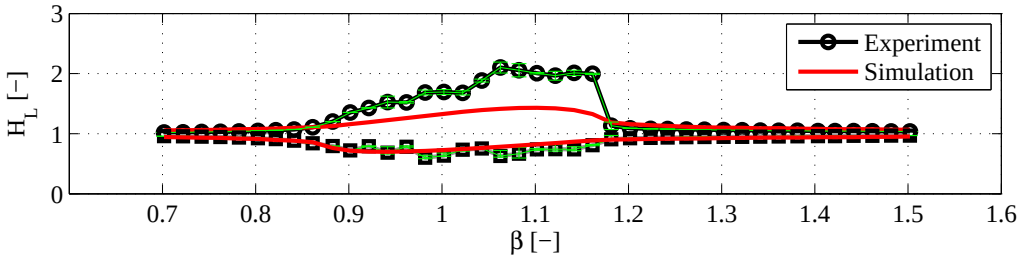

(a) $a = 5$ mm, $A/L = 0.009$

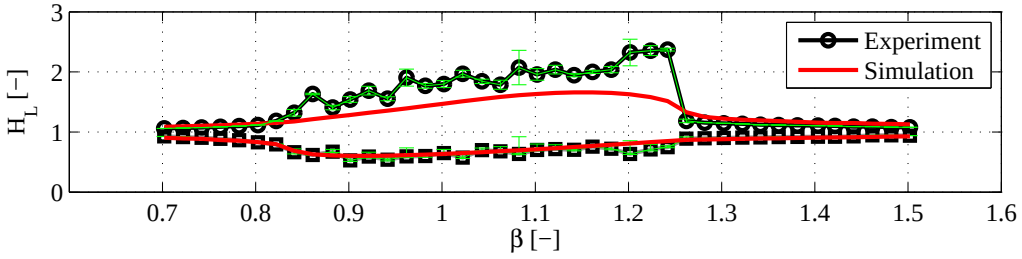

(b) $a = 10$ mm, $A/L = 0.017$

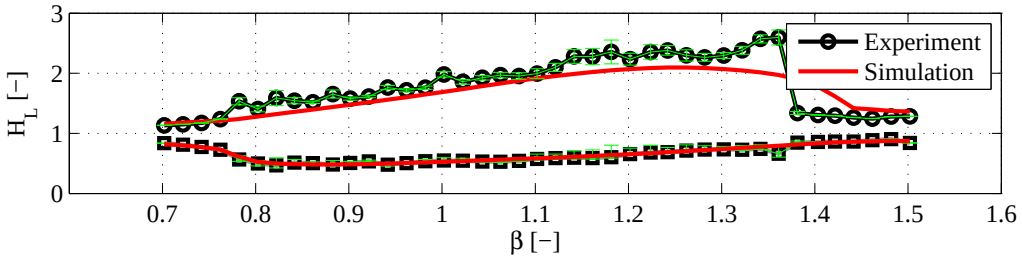

(c) $a = 20$ mm, $A/L = 0.034$

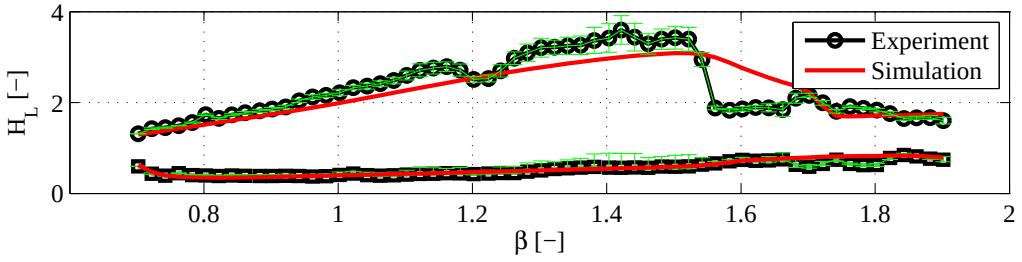

(d) $a = 40$ mm, $A/L = 0.068$

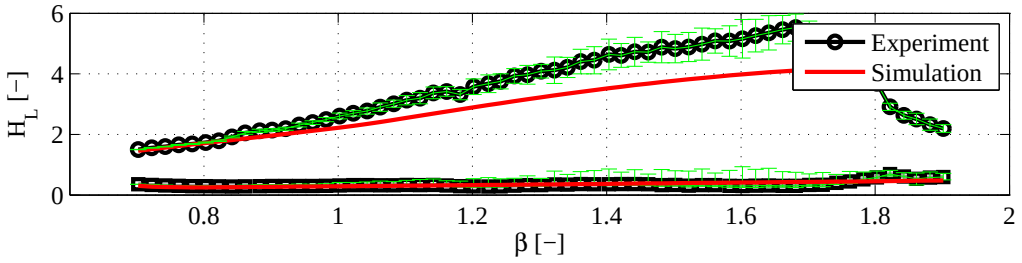

(e) $a = 60$ mm, $A/L = 0.101$

Figure B.12: *Frequency response curves for wave depth at left tank wall. Water depth $h = 30$ mm corresponding to $h/L = 0.051$.*

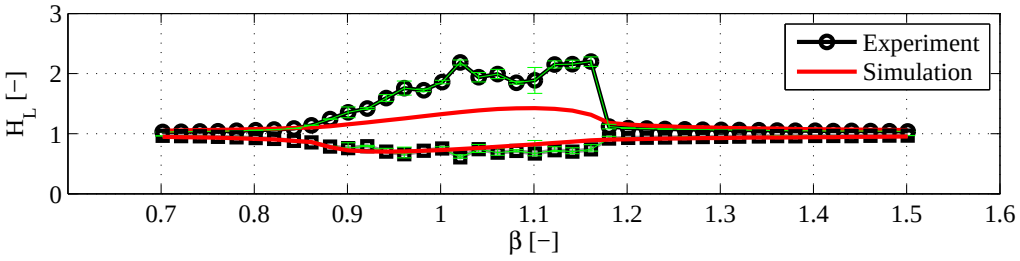

(a) $a = 5$ mm, $A/L = 0.009$

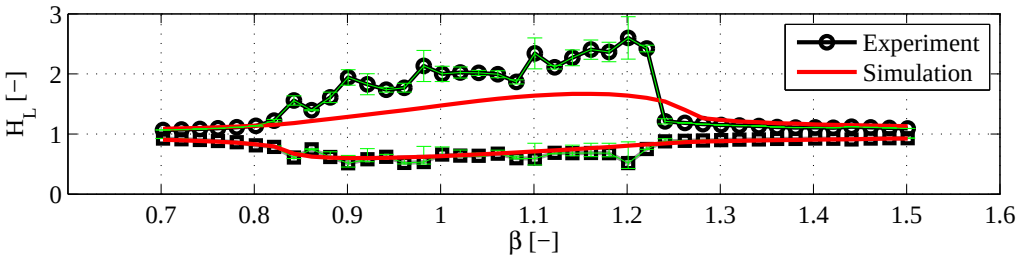

(b) $a = 10$ mm, $A/L = 0.017$

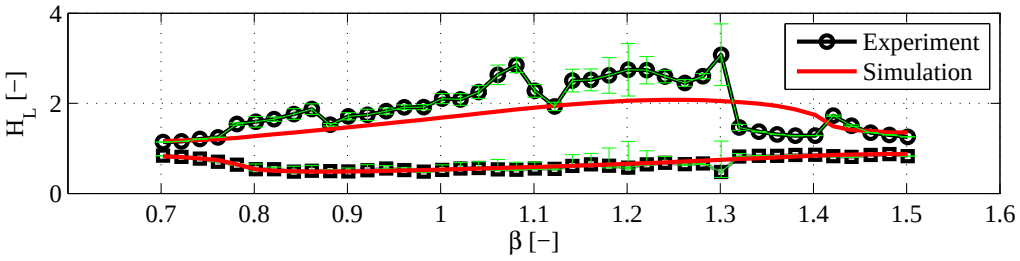

(c) $a = 20$ mm, $A/L = 0.034$

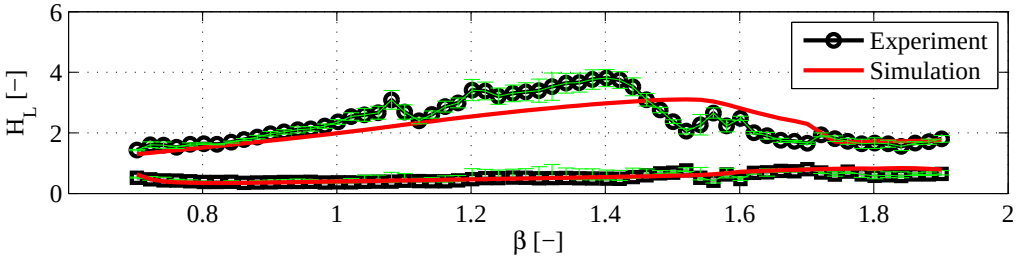

(d) $a = 40$ mm, $A/L = 0.068$

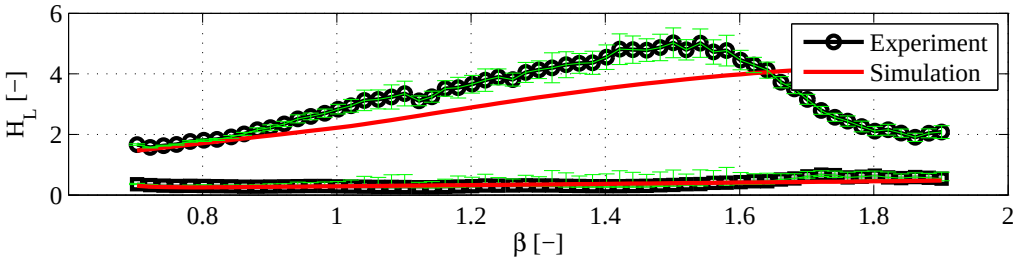

(e) $a = 60$ mm, $A/L = 0.101$

Figure B.13: *Frequency response curves for wave depth at left tank wall. Water depth $h = 40$ mm corresponding to $h/L = 0.068$.*

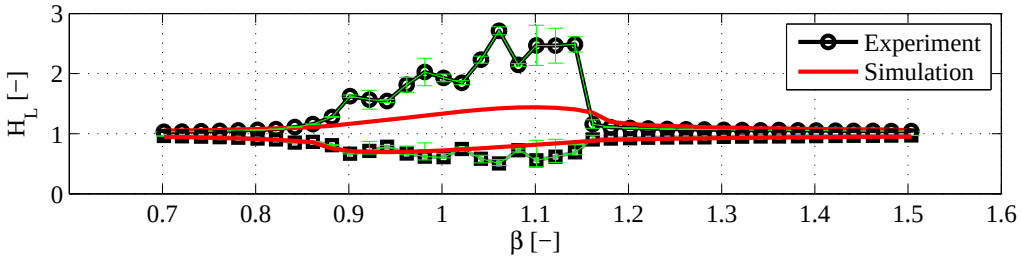

(a) $a = 5$ mm, $A/L = 0.009$

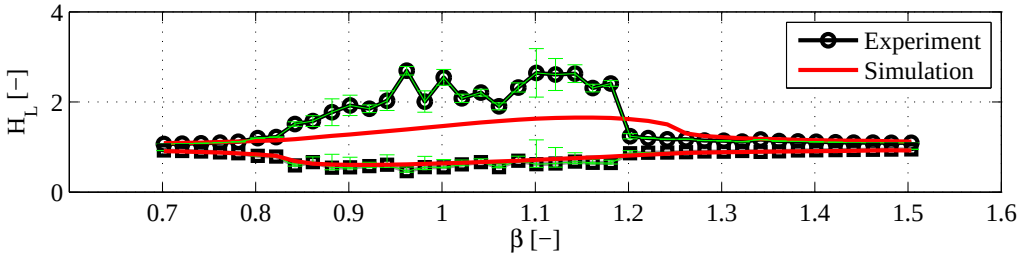

(b) $a = 10$ mm, $A/L = 0.017$

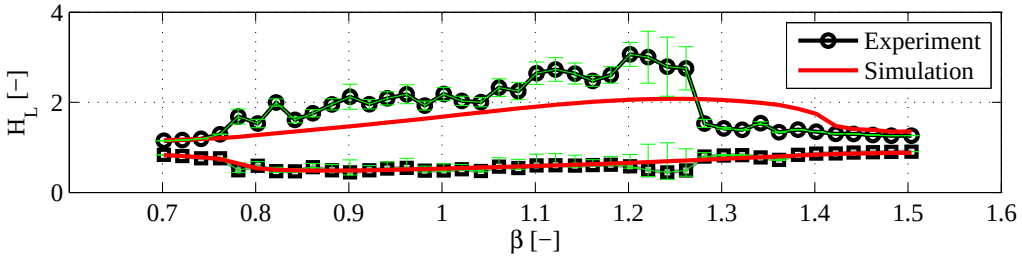

(c) $a = 20$ mm, $A/L = 0.034$

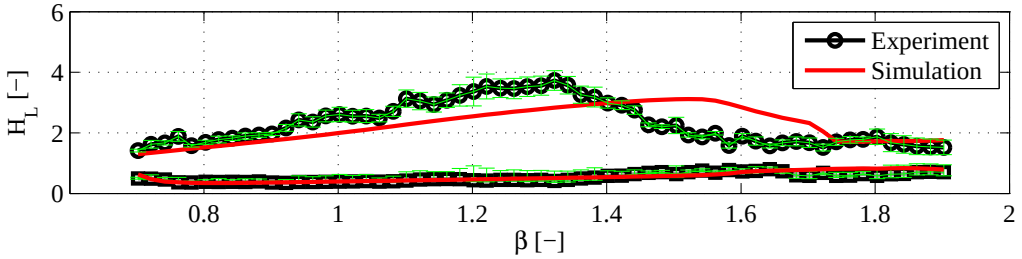

(d) $a = 40$ mm, $A/L = 0.068$

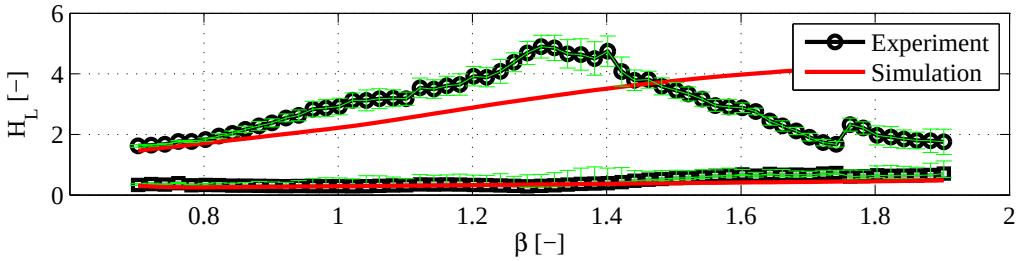

(e) $a = 60$ mm, $A/L = 0.101$

Figure B.14: *Frequency response curves for wave depth at left tank wall. Water depth $h = 50$ mm corresponding to $h/L = 0.085$.*

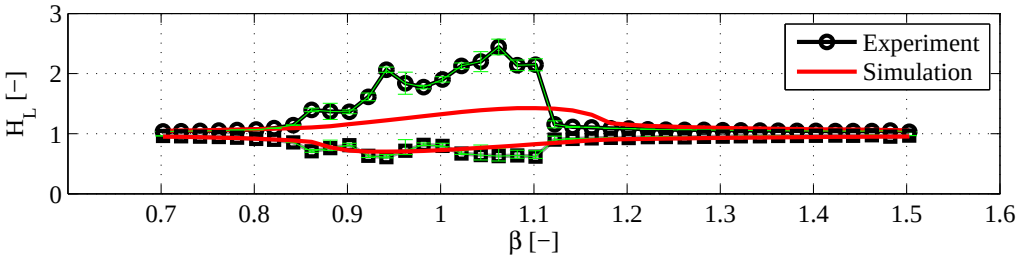

(a) $a = 5$ mm, $A/L = 0.009$

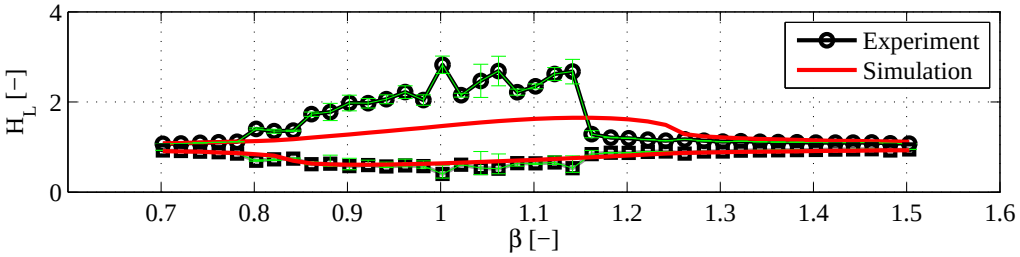

(b) $a = 10$ mm, $A/L = 0.017$

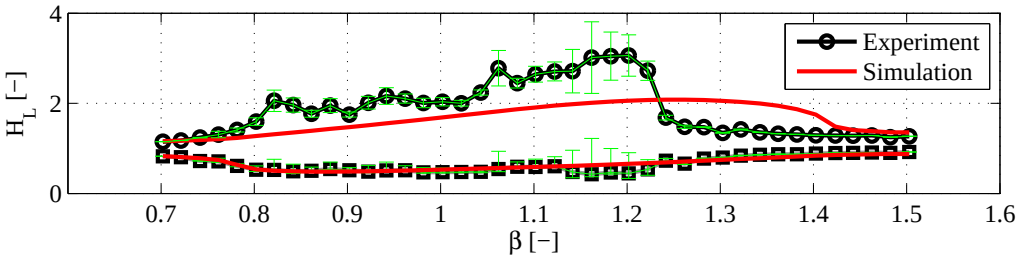

(c) $a = 20$ mm, $A/L = 0.034$

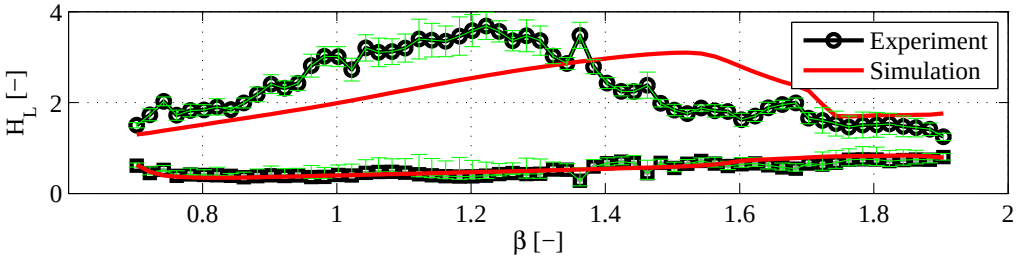

(d) $a = 40$ mm, $A/L = 0.068$

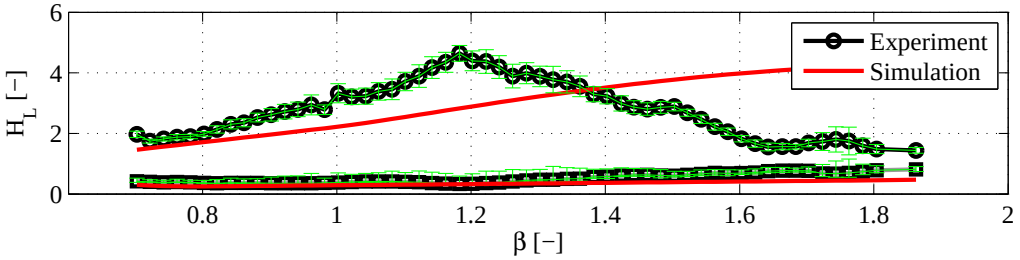

(e) $a = 60$ mm, $A/L = 0.101$

Figure B.15: *Frequency response curves for wave depth at left tank walln. Water depth $h = 60$ mm corresponding to $h/L = 0.101$.*

Part II

Appended papers

Paper I

"Shallow Water Sloshing. Part I. Theoretical and numerical background"

J. Krabbenhøft & C.T. Georgakis

Manuscript prepared for submission to: *Engineering Structures*

Shallow Water Sloshing. Part I. Theoretical and numerical background

J. Krabbenhøft*[,a], C.T. Georgakis[a]

[a]*Department of Civil Engineering, Technical University of Denmark, Building 118, Brovej, 2800 Kgs. Lyngby, Denmark*

Abstract

The nonlinear shallow water equations (NSW equations) describing fluid motion in a partially filled rectangular tank given a prescribed horizontal oscillatory base motion is investigated. The NSW equations, including contributions from friction and variable bottom topography, are derived. and a dimensional analysis, assuming a flat bottom, is carried out. This analysis results in three governing parameters: an amplitude parameter Λ, defining the ratio of base motion amplitude to tank length, a frequency parameter β, defining the ratio base motion frequency to linear shallow water sloshing frequency, and finally a friction parameter γ based on a Chezy type formulation. Neglecting friction, the behavior of the liquid sloshing at resonance is alone governed by the amplitude parameter Λ.

In order to solve the inhomogeneous set of hyperbolic partial differential equations (PDE) describing the liquid motion of two different algorithms are first tested intensively on problems with reference solutions and afterwards on a sloshing problem. The study shows that the simplest of the two methods is adequate for solving the governing set of hyperbolic PDEs. Also, in the numerical study the importance of using a consistent conserving formulation is illustrated, showing that a non-conserving formulation estimates an incorrect shock speed for a moving hydraulic jump when the jump is large.

A parameter study reveals that the system exhibits a hardening type behavior, especially with respect to the maximum wave height variation. The dimensionless sloshing force decreases with increasing base motion amplitude Λ indicating that the internal fluid dissipation increases with increasing Λ values. The work of the sloshing force per cycle follows the same behavior. Finally the effect of bottom friction on the solution is investigated, showing that for very shallow water tanks with a rough bottom the effect becomes significant, while for containers with smooth bottom the effect is negligible.

Key words: Nonlinear shallow water equation, sloshing, Tuned Liquid Damper, Energy dissipation

1. Introduction

Free surface oscillation of liquids in partially filled containers is of relevance in a large number of engineering disciplines. In naval engineering Liquid Nitrogen Gas (LNG) containers with

*Corresponding author

Email address: jkr@byg.dtu.dk (J. Krabbenhøft)

ballast tanks experience heave, pitch and roll motions due to wave loads on the ships. As a result, the containers must be designed to withstand the sloshing and slamming loads. In aerospace engineering, fuel containers must be analyzed and dimensioned such that the sloshing forces do not generate unwanted destabilizing feedback forces to the aircraft. Another unwanted effect of water sloshing is the destabilizing effect of green water on ship decks. This problem is especially relevant for stability of fishing vessels. Finally, Tuned Liquid Dampers (TLD) are used to limit unwanted structural vibrations in vibration sensitive structures such as high rise buildings, chimneys, telecommunication towers, and cables. In the present paper our focus is mainly on the description of TLDs. Although the theory presented is generally applicable, we limit ourselves to treating the case of horizontally oscillated rectangular containers. The analysis is further simplified by examining only the two-dimensional case, i.e. unidirectional container oscillations, and more importantly restricting the water to be shallow compared to the length of the container.

The mathematical description of sloshing is in general very complex and in its full form involves solving the full incompressible Navier-Stokes equations together with kinematic and dynamic free surface and bottom boundary conditions. More precisely the full three-dimensional problem consists of three equations for the conservation of momentum, one equation for the conservation of mass, a kinematic and dynamic equation for the free surface and finally a kinematic equation for the bottom topography. In some early analytical studies on fluid sloshing the full nonlinear set of equations were simplified by neglecting viscous effect and assuming irrotational flow (permitting the use of a potential formulation), linearizing the free surface condition and assuming flat-bottom containers. The resulting linear set of equations are know as the linear Euler equations. One of the earliest studies [1] solved the linear Euler equations in an oscillating rectangular flat bottomed container. Based on the results obtained an equivalent mechanical model of the fluid container was derived revealing that the so-called participating mass for a rectangular container oscillating in a horizontal direction attains a maximum value of approximate 81% of the total liquid mass. As the liquid depth to length ratio (h/L-ratio) increases the participating mass decreases. This early result has been utilized in several subsequent studies concerning the design of TLDs [2, 3]. For more complex geometry, e.g. for variable bottom topography, inclusion of baffles etc, it becomes difficult, or even impossible, to solve the linear Euler equations analytically and one must resolve to numerical methods. Some recent papers include [4, 5, 6] where the Finite Element Method has been used to handle more complex geometry and the case of baffled containers.

The linearized Euler equations, while possible to handle analytically and relatively easy to handle numerically, fail to give a description of the fluid behavior for forcing frequencies close to the natural sloshing frequencies. To analyze the resonance behavior of fluid sloshing a number of researchers have solved the full nonlinear set of equations for the 2D case [7, 8, 9, 10, 5] and for the 3D case [11, 12]. The simulations often agree qualitatively well with experimental results and handle extremely complex physical processes such as overturning and breaking waves, but the simulation time is often very long, spanning from hours [9] to days [11] or weeks [7]. The long simulation time together with an often complex numerical solution procedure, makes the approach far from obvious for simulating TLDs.

In the area of coastal hydrodynamics, concerned with the modelling of flows in for example rivers, channels, estuaries etc, shallow water approximations of the incompressible Navier-Stokes equations are often used. The most popular model equations for studying near-shore hydrodynamics [13], and in general free surfaces in shallow water flows, are the Nonlinear Shallow Water Equations (NSW equations) also known as the Saint-Venant equations together with a large class of so-called Boussinesq-type equations (BT equations). A comprehensive overview and review

of BT equations is given in [14]. In the shallow water models the momentum and mass conservation equations are depth-integrated resulting in a reduction of variables by one compared to the full problem described earlier. But more importantly, by substituting the nonlinear kinematic boundary condition into the depth integrated mass and momentum equations, the full nonlinear description of the surface is retained *exactly* leaving only, for the 3D case, two equations for the conservation of momentum and one equation for the conservation of mass. The variable describing the free surface enters into the mass conservation equation and thus requires no special treatment.

The price for performing the approximations is loss of a large part of the physics and thus the different approximate equations must be chosen and used with care such that they describe and represent the fundamental physical phenomena of interest. As a reward the equations can be solved extremely fast and very easily coupled to elastic structures to examine the fluid structure interaction relevant for for example TLDs.

The main difference between NSW and BT equations lie in their dispersion characteristics. The NSW equations are non-dispersive, i.e. waves propagate with a speed independent of its wave length, but are however capable of capturing very complex physical phenomena such as hydraulic jumps and bores, including the energy loss associated with these processes. The nature of the NSW equations result in development of bores given infinitely small and smooth initial conditions which is non-physical and thereby limits the use of the equations. The BT equations, on the other hand, include dispersion and are in general used to model long wavelength, small amplitude gravity waves [15]. The inclusion of dispersion in the BT equations results in a smooth surface profile and thus in order to include energy dissipation empirical terms must be added [13].

To date, most studies of liquid sloshing in partially filled containers have focused on the BT approach. An early paper by Chester and Bones [16], concerned with shallow water sloshing in horizontally excited rectangular containers, compared analytical expressions including dispersion to experimental results and found reasonable agreement. This study was based on a low excitation level of $A/L = 0.0013 - 0.0052$, A being the maximum amplitude of the base motion amplitude, and h/L-ratios between approximately 0.02 and 0.08. An often cited and somewhat classical numerical/experimental study of shallow water sloshing is [17] who solved the BT equations proposed by Peregrine [18] for a horizontally oscillating rectangular tank. The energy dissipation was modelled following the work of Miles [19]. The equations were solved using the FEM and good comparison was found between simulations and experiments. However, the base motion amplitude for the steady state experiments, $A/L \simeq 0.003$, was rather low. In [20] another set of BT equations, derived by Wei and Kirby [21], were solved for a rectangular container oscillating in both horizontal and vertical directions. Also here a good agreement between numerical and experimental results was found. A similar study using the same set of equations was performed later by Frandsen and co-workers also for low abse motion amplitudes [22]

Fewer studies have been carried out in connection with shallow water sloshing using the non-dispersive NSW equations. One of the earliest studies focusing on shallow water sloshing in rectangular tanks exposed to roll motion is reported in the paper by Verhagen and Wijngaarden [23]. An analytical expression derived from the linearized shallow water equations predicted infinite wave amplitudes in contradiction with the experiments where a bore was developed. Based on the 1D compressible Euler equations describing gas flow, an analytical expression was derived showing good agreement with the experimental results. Shallow water sloshing was studied numerically in [24] in connection with studies of vessels with water on deck. The NSW equations were here solved using the Random Choice Method together with a splitting scheme to handle the source terms generated by the moving frame of reference. In [25] roll motion

of a rectangular container was considered with depth ratios between $h/L = 0.05 - 0.20$. The authors concluded that the NSW equations could be used for depth ratios as high as $h/L = 0.15$ to provide fairly accurate results even for large excitation amplitudes.

In the context of Tuned Liquid Dampers, a model based on BT equations was used by Fujino and co-workers [26] to simulate sloshing in a rectangular container oscillating in a horizontal direction. The model was later modified with empirical functions to handle breaking waves [27]. In [28] Kaneko et. al. modelled Peregrines BT equations and included submerged nets in the formulation to simulate TLDs. The model was later used to analyze a TLD mounted on a bridge pylon. In [29] Reed and co-workers investigated rectangular containers with depth ratios between 0.029-0.079 exposed to horizontal base motion oscillations with amplitude ratios in the range $A/L = 0.03 - 0.068$. A single experiment with a h/L-ratio of 0.05 and $A/L = 0.03$ was compared to numerical simulations of the NSW equations showing good agreement.

Despite the many investigations of shallow water sloshing in rectangular containers, there is to the authors' knowledge, no comprehensive source of information regarding the application range of the NSW equations in connection with horizontally oscillating containers. It is essential for any practitioner wanting to use the NSW equations in a design situation that the working range of the equations are thoroughly established. Indeed, we must expect the NSW equations to break down for certain h/L-ratios but also for certain A/L-ratios. It is the main objective of this paper, together with an experimental companion paper, to investigate and establish a parameter range for which the NSW equations can be used to simulate sloshing in rectangular tanks oscillated in a horizontal direction. The chosen overall procedure is the following: first derive the the governing equations and find governing parameters. Next find a suitable numerical scheme to solve the equations. In this context suitable means simple, effective and precise. This is the subject matter of the present article. Next a range of experiments are performed, varying the governing parameters, and the experimental findings are compared to simulation results. This is the subject matter of the companion paper.

The present paper is laid out on the following form. First the 2D Euler equations for incompressible fluid are formulated in a non-inertial reference system, i.e. in a moving coordinate system. Based on these equations the depth averaged mass and momentum equations are derived for a tank with general bottom topography - the NSW equations. To establish governing system parameters the NSW-equations are nondimensionalized and the relevant dimensionless parameters are found. The NSW equations with source terms constitute a so-called System of Balance Laws which are not trivial to solve. We choose to solve the equations in a Finite Volume framework and implement two different schemes: A relative simple 1. order scheme and a more complicated 3. order scheme especially suited for handling System of Balance Laws. The schemes are first verified on different test cases and finally tested on a sloshing problem. Finally a full parameter study of the NSW equations is performed.

2. Nonlinear shallow water equations

In the following the nonlinear shallow water (NSW) equations, for a Newtonian fluid in a non-inertial frame are derived. The various simplifications performed in the derivation will be addressed and discussed. The derivation largely follows [30, 31] to whom the reader is referred to for further details.

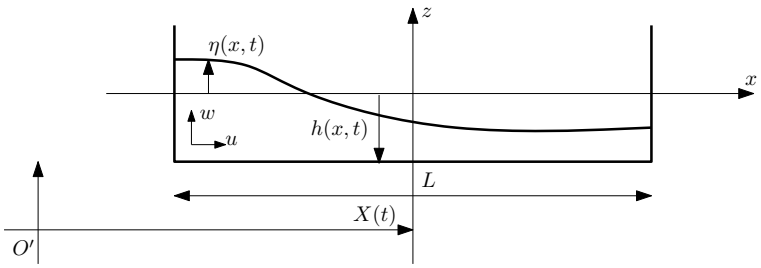

Figure 1: Sketch of rectangular TLD tank

2.1. Navier-Stokes equations

The governing equations describing two dimensional constant density flows of an incompressible fluid are the well known Navier-Stokes equations which express the conservation of momentum and mass:

$$u_t + (uu)_x + (uw)_z = -p_x/\rho + (\nu u_x)_x + (\nu u_z)_z - \ddot{X} \tag{1}$$

$$w_t + (wu)_x + (ww)_z = -p_z/\rho + (\nu w_x)_x + (\nu w_z)_z - g \tag{2}$$

$$u_x + w_z = 0 \tag{3}$$

In the above $u(x, z, t)$ and $w(x, z, t)$ are the velocity components in the x and z directions, t is the time, $p(x, z, t)$ is the pressure, g is the gravitational acceleration, $\ddot{X}$ is a function describing the acceleration of the inertial system in the x-direction and ν is a kinematic viscosity coefficient.

2.2. Boundary conditions for free surface flows

In the derivation of the NSW equations we place no restrictions on the vertical boundaries at $x = \pm L/2$, but instead consider the domain as having an infinitely horizontal extent. The boundary conditions at the vertical walls will be formulated for the final set of equations later. The vertical velocity of a point on a moving surface $z = F(x, t)$ can be expressed mathematically as

$$\frac{\mathrm{d}z}{\mathrm{d}t} = \frac{\partial F}{\partial t} + \frac{\partial F}{\partial x}\frac{\mathrm{d}x}{\mathrm{d}t}, \quad \text{at} \quad z = F(x, t) \tag{4}$$

For free surface flows the surface elevation is described by a variable $\eta(x, t)$ as shown in figure 2. Using (4), the kinematic boundary condition, expressing that water particles remain at the surface, is given by

$$w^s - \eta_t - u^s \eta_x = 0, \quad \text{at} \quad z = \eta(x, t) \tag{5}$$

where superscript s refers to the free surface. Equivalently, at the bottom the kinematic boundary condition, expressing that the velocity component perpendicular to the solid boundary vanishes, is given by

$$w^b + u^b h_x = 0, \quad \text{at} \quad z = -h(x) \tag{6}$$

where superscript b refers to the bottom and where it is assumed that the bottom topography is static, i.e. fixed in time.

Since viscous terms are included in the momentum equations, tangential stress boundary conditions need to be applied at the free surface and at the bottom-water interface. For the free surface, the tangential stress in the horizontal direction is zero which is formulated as [32]

$$(u_z - u_x\eta_x)|_{z=\eta} = 0 \tag{7}$$

$$\tag{8}$$

The tangential boundary condition at the bottom is given by specifying the bottom stress as follows

$$\nu(u_z + u_x h_x)|_{z=-h} = \gamma_B u^b \tag{9}$$

$$\tag{10}$$

where γ_B is a nonnegative bottom friction coefficient. The effect of bottom friction is an active research area which is still not fully understood and it is not within the scope of the present paper to include an in-depth study of the matter. However, simple semi-empirical formulas such as Chezy's law, have been successfully used in oscillating flows [13]. In the following we take γ_B as [33]

$$\gamma_B = C_\tau |u^b|, \qquad C_\tau = \frac{g}{M^2(h+\eta)^{\frac{1}{3}}} \tag{11}$$

where M is the Manning number with the dimension $\mathrm{m}^{1/3}/\mathrm{s}$ (the inverse of the also commonly used Manning's n) and g is the gravitational constant. The assumption in (9)-(11) that the bottom stress is proportional to the square of the horizontal velocity is valid only for stationary or near-stationary flows such as long period shallow water flows, where shear stress and horizontal fluid velocity are in phase [32]. More explicitly it can be shown that the in-phase approximation is valid as long as the relation $h^2/\nu < 0.1T$. An estimate of the eddy viscosity is $\nu \simeq 0.1\ \mathrm{m}^2/\mathrm{s}$ and $h_0 \simeq 0.1$ m giving a period $T > 1$ s which is valid for all our experiments. The friction coefficient (11) is seen to be inversely proportional to the total local water depth, and thus can be expected to have an increasing significance as the depth decreases.

The last boundary condition needed is the dynamic boundary condition at the surface specifying the excess pressure which we set to a constant:

$$p_e(x,t) = p_0 \tag{12}$$

2.3. Two-dimensional hydrostatic model

In flows where the horizontal length scales are large compared to the vertical scales one can assume that the vertical acceleration of the fluid, as well as the vertical viscosity forces are small when compared to the gravity acceleration and to the pressure gradient in the vertical direction [34]. Consequently, by neglecting the acceleration and viscous terms in the vertical momentum equation the following equation for pressure results

$$p_z = -\rho g \tag{13}$$

The pressure equation readily yields the pressure distribution in the depth by integration

$$p(x,z,t) = p_e(x,t) + \rho g\,(\eta(x,t) - z) \tag{14}$$

where $p_e(x,t) = p_0$ is the excess pressure. The pressure distribution is clearly seen to be hydrostatic which is a consequence of neglecting inertia and viscous forces in the vertical direction. Substituting the pressure expression (14) into the horizontal momentum equation yields the following two dimensional model equations

$$u_t + (uu)_x + (uw)_z = -g\eta_x + (\nu u_x)_x + (\nu u_z)_z - \ddot{X} \tag{15}$$

$$u_x + w_z = 0 \tag{16}$$

The above two equations contain three unknowns u, w and η, so in order to close the system an additional equation is needed which is the free surface boundary condition (5).

2.4. Depth integrated continuity equation

Integrating the continuity equation over the depth, i.e. from $-h$ to η, applying the Leibnitz rule on the first and second term while integrating the third term, and finally applying the boundary conditions (5)-(6) yields

$$\eta_t + \frac{\partial}{\partial x}\int_{-h}^{\eta} u dz = 0 \tag{17}$$

The above equation expresses the conservation of mass and is the fourth equation needed to close the system in (15). Denoting the total depth $H(x,t) = h(x) + \eta(x,t)$ and introducing the following notation for the averaged velocity in horizontal direction

$$U(x,t) = \frac{1}{H}\int_{-h}^{\eta} u(x,z,t) dz \tag{18}$$

the continuity equation (17) is rewritten as

$$H_t + (HU)_x = 0 \tag{19}$$

Here we have utilized that the bottom variation is not a function of time. Hence, η can be replaced by H under the time differentiation.

2.5. Depth integrated momentum equation

In the following the momentum equation (15) is integrated over the depth. Vertical integration of the left hand side of equation (15) yields

$$\text{LHS} = \frac{\partial}{\partial t}\int_{-h}^{\eta} u dz + \frac{\partial}{\partial x}\int_{-h}^{\eta} uu dz \tag{20}$$

$$-u^s[\eta_t + u^s\eta_x - w^s] + u^b[u^b(-h)_x - w^b] \tag{21}$$

where the terms in the brackets vanish due to the boundary conditions (5)-(6). By adding and subtracting $\frac{\partial}{\partial x}\int_{-h}^{\eta} U^2 dz$ to the above equations the following result is easily derived

$$\text{LHS} = (HU)_t + (HU^2)_x + \frac{\partial}{\partial x}\int_{-h}^{\eta}(u-U)^2 dz \tag{22}$$

Integration of the right hand side is done in two stages. First the pressure term and the forcing term are integrated and afterwards the viscous terms are treated. Integration of the pressure and forcing term is especially simple, the result being

$$\int_{-h}^{\eta} -g\eta_x - \ddot{X} dz = -Hg\eta_x - H\ddot{X} \tag{23}$$

Next, integrating the right hand side viscosity terms (RHS_τ) in the momentum equation over the depth and applying Leibnitz' rule yields

$$\mathrm{RHS}_\tau = \frac{\partial}{\partial x}\int_{-h}^{\eta} \nu u_x dz + \nu\left(u_x(-h)_x - u_z\right)|_{z=-h} - \nu\left(u_x\eta_x - u_z\right)|_{z=\eta} \tag{24}$$

Utilizing the tangential boundary conditions (7)-(9), adding and subtracting $\frac{\partial}{\partial x}\int_{-h}^{\eta} \nu U_x dz$ as well as $\gamma_b U$ yields

$$\mathrm{RHS}_\tau = \frac{\partial}{\partial x}\int_{-h}^{\eta} \nu U_x dz - \gamma_b U \tag{25}$$

$$+\frac{\partial}{\partial x}\int_{-h}^{\eta} \nu(u-U)_x dz - \gamma_b(u^b - U) \tag{26}$$

Lastly, by introducing the vertically averaged viscosity coefficient $\bar{\nu} = \frac{1}{H}\int_{-h}^{\eta} \nu dz$ and adding (23), the final right hand side expression is found as

$$\mathrm{RHS} = (\bar{\nu}HU_x)_x - \gamma_b U \tag{27}$$

$$+\frac{\partial}{\partial x}\int_{-h}^{\eta} \nu(u-U)_x dz - \gamma_b(u^b - U) - -gH\eta_x - H\ddot{X} \tag{28}$$

2.6. One-dimensional nonlinear shallow water model

In the above derivation the vertical viscosity term has been retained. However, using the same argumentation as earlier concerning horizontal and vertical scales, only the horizontal viscosity related to the bottom friction is retained in the following. To further reduce the equations it is assumed that the horizontal fluid velocity u is independent of z, i.e. constant across the depth. Thereby, the integrals in (22) and (27) cancel out and the final set of NSW equations can be stated as

$$H_t + (HU)_x = 0 \tag{29}$$

$$(HU)_t + (HU^2)_x = -gH\eta_x - \gamma_b U - H\ddot{X}(t) \tag{30}$$

2.7. Velocity and flux formulation

It is convenient to formulate the governing PDEs (29) in matrix notation. A set of hyperbolic inhomogeneous PDSs is commonly referred to as a system of balance laws (SBL) and takes the form

$$\mathbf{U}_t + \mathbf{F}(\mathbf{U})_x = \mathbf{S}(\mathbf{U}, x, t) \tag{31}$$

where the vector $\mathbf{U}$ is the vector of conserved variables, $\mathbf{F}$ is a flux function and $\mathbf{S}(\mathbf{U}, x, t)$ is the source term vector. The NSW equations (29) derived in the previous section can be formulated

in the general form (31) with two different sets of conserved variables. The flux formulation uses the water depth and momentum as conservative variables:

$$\mathbf{U} = \begin{pmatrix} H \\ HU \end{pmatrix}, \mathbf{F} = \begin{pmatrix} HU \\ HU^2 + \frac{1}{2}gH^2 \end{pmatrix}, \mathbf{S} = \begin{pmatrix} 0 \\ -gHh_x - \gamma_b U - H\ddot{X}(t) \end{pmatrix} \tag{32}$$

The velocity formulation uses the so-called primitive variables which are water depth and velocity and is easily derived by expanding derivatives in the momentum equation of (32) and utilizing the continuity equation in expanded form. The result is the following

$$\mathbf{U} = \begin{pmatrix} H \\ U \end{pmatrix}, \mathbf{F} = \begin{pmatrix} HU \\ \frac{1}{2}U^2 + gH \end{pmatrix}, \mathbf{S} = \begin{pmatrix} 0 \\ -gh_x - \gamma_b U - H\ddot{X}(t) \end{pmatrix} \tag{33}$$

The boundary and initial conditions for both formulations are given by

$$\begin{array}{lll} \text{I.C.} & : & H(x,0) = h(x),\ U(x,0) = 0 \\ \text{B.C.} & : & U(-L/2,t) = U(L/2,t) = 0 \end{array} \tag{34}$$

For smooth solutions the two formulations will give similar results. However, for flows where shocks or bores are generated the two formulations will yield different results which is a consequence of conserving velocity instead of momentum. In Section 5.1, this effect will be demonstrated numerically to underline the importance of using a correct formulation that conserves mass and momentum.

3. Governing parameters

It is convenient to rewrite the NSW equations on non-dimensional form to extract governing dimensionless parameters. In previous studies concerning TLDs the base motion amplitude to tank length ratio A/L has been used to characterize the dampers [29, 35]. However, these ratios have not been justified on theoretical grounds. In the following, this justification is provided. Moreover, it is shown that no other parameters for characterizing a TLD exists. In what follows all dimensional variables are starred unless otherwise stated.

3.1. Non-dimensionalization

In the following the bottom is assumed to be flat, i.e. $h = h_0$. The horizontal acceleration of the tank is given by

$$\ddot{X}^*(t^*) = -A^*\Omega^{*2}\sin(\Omega^* t^*) \tag{35}$$

The scaling parameters are chosen as follows:

$$x^* = x/k^*, t^* = t/\omega_w^*, H^* = Hh_0^*, U^* = \sqrt{gh_0^*}U \tag{36}$$

where $k^* = \pi/L^*$, L^* is the tank length, $\omega_w^* = k^*\sqrt{gh_0{}^*}$ is the lowest linear sloshing frequency of the water using a shallow water assumption, h_0^* is the *mean* still water level (in general $h = h(x)$), and g is the acceleration of gravity. The following identities are obtained using the chain rule and 36

$$\frac{\partial()}{\partial t^*} = \frac{\partial()}{\partial t}k^*\sqrt{gh_0^*} \qquad \frac{\partial()}{\partial x^*} = \frac{\partial()}{\partial x}k^* \tag{37}$$

Combining (35)-(37) with (32) the following non-dimensional set of mass and momentum conserving equations result:

$$\mathbf{U} = \begin{pmatrix} H \\ HU \end{pmatrix}, \mathbf{F} = \begin{pmatrix} HU \\ HU^2 + \frac{1}{2}H^2 \end{pmatrix}, \mathbf{S} = \begin{pmatrix} 0 \\ -\gamma \frac{|U|U}{H^{1/3}} + H\Lambda\Omega^2 \sin(\Omega t) \end{pmatrix} \tag{38}$$

$$\begin{array}{lll} \text{I.C.} & : & H(x,0) = 1,\ U(x,0) = 0 \\ \text{B.C.} & : & U(\frac{\pi}{2}, t) = U(\frac{\pi}{2}, t) = 0 \end{array} \tag{39}$$

with the dimensionless parameters

$$\beta = \frac{\Omega^*}{\omega_w^*} \qquad \Lambda = A^* k^* = \pi \frac{A^*}{L^*} \qquad \gamma = \frac{g}{\mu M^{*2} h_0^{*1/3}} \tag{40}$$

where the depth ratio μ has been defined as

$$\mu = h_0^* k^* = \pi \frac{h_0^*}{L^*} \tag{41}$$

The depth parameter is only relevant as long as the friction term is present. From the non-dimensionalization we can conclude that the sloshing problem in shallow water is governed solely by the three dimensionless parameters in (40): a frequency parameter β, an amplitude parameter Λ, and a friction parameter γ. It should be emphasized that the analysis is based on the NSW equations, and the parameters are as such only meaningful from a practical point of view as long as the NSW equations captures the relevant physics involved in the given problem.

The strength of the forcing term from the base motion of the tank is seen to be a product of the amplitude parameter Λ, as pointed out by previous researchers [29, 35], and the frequency ratio squared β^2. At resonance, which is the working area of interest, the forcing frequency is approximately equal to the linear sloshing frequency $\Omega^* \simeq \omega_w^*$ resulting in $\beta \simeq 1$, leaving as an approximation Λ as the only relevant parameter with respect to the forcing term. Furthermore, neglecting the bottom friction and sloping bottom, the depth, sloping and friction parameters vanish leaving Λ as the only relevant parameter. This is a very strong results and shows the motivation for establishing the parameter range for which the NSW equations are valid. Returning to the first term on the right side of (38), we see that the strength of the friction term depends, not surprisingly, on the inverse of the depth parameter μ. This is in agreement with e.g. [13], but also from a physical argumentation it seems reasonable based on the fact that the dissipating bottom boundary layer extends over a relatively larger part of the total water depth for shallow water.

3.2. Sloshing force and energy dissipation

The resultant hydrodynamic force acting on an accelerated fluid container consists of two contributions[36]: one contribution from the acceleration of the water treated as frozen, i.e. an inertial contribution F_{inertia}, and one contribution from the convective or dynamic part of the water F_{dyn}. The sum of the horizontal hydrodynamic forces is denoted the sloshing force, F_S,

$$F_S = F_{\text{inertia}} + F_{\text{dyn}} \tag{42}$$

For the shallow water case the sloshing force, i.e. the force containing both the inertial and dynamic contribution, is calculated using the hydrostatic pressure assumption as the difference between the integrated pressure on the right and left tank wall

$$F_S^* = \frac{1}{2}\rho^* g(H_R^{*2} - H_L^{*2}) \tag{43}$$

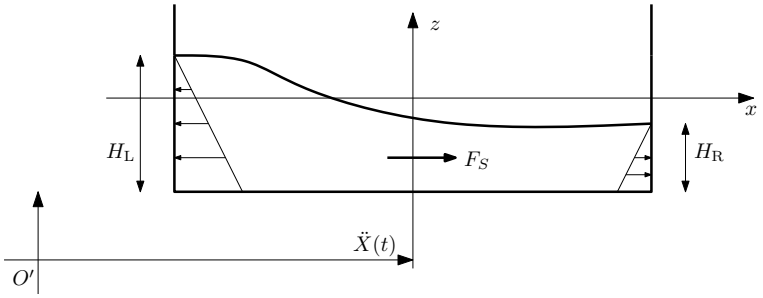

Figure 2: Definition of horizontal sloshing force F_S using a hydrostatic pressure assumption

The sloshing force is non-dimensionalized with the maximum inertial force of the water treated as a solid mass

$$F_S = \frac{F_S^*}{m_w^* A^* \Omega^{*2}} = \frac{1}{2\pi\Lambda\beta^2}(H_L^2 - H_R^2) \tag{44}$$

where m_w^* is the total mass of water per tank width. Another important quantity is the work done by the sloshing force per forcing period:

$$\Delta E^* = \int_T^* F_S^* dX^*(t^*) \tag{45}$$

In the context of TLDs, (45) is a measure of structural energy being dissipated per cycle by the sloshing force. In the following, therefore, we refer to ΔE^* as the dissipated energy per cycle. This is non-dimensionalized as follows

$$\Delta E = \frac{\Delta E^*}{\frac{1}{2} m_w^* (A^*\Omega^*)^2} = \frac{2}{\Lambda} \int_T F_S dX(t) \tag{46}$$

where the factor $\frac{1}{2} m_w^* (A^*\Omega^*)^2$ is a reference value.

4. Numerical scheme

The system of balance laws (SBL) expressed in (32) can be solved using any numerical method, the most popular choices being the finite element method [37], the finite difference method [34], and the finite volume method [38, 39]. In the current paper the finite volume method is chosen since this method is especially well suited for handling systems of conservation laws (SCL) and SBL as well as problems containing discontinuities such as shocks or bores.

It is well known that simple first-order Godunov upwind methods are quite diffusive, see e.g. [38], with the degree of numerical diffusion varying for different choice of numerical flux. However, due to this numerical diffusion, the methods are very stable and produce non-oscillatory solutions. In order to reduce the numerical diffusion, high order methods have been developed. The main drawback of such methods is that the lead to oscillatory solutions unless remedies are used, the implementation of which may be rather complex. When source terms are added to the SCL, the resulting SBL can be very challenging to solve depending on the characteristics of the

source term. However, regardless of the nature of the source term, developing and implementing high order methods for SBL is challenging. In the context of the current work we seek a numerical method that is capable of handling shocks, i.e. is shock preserving, together with handling source terms efficiently. Moreover, it is obviously desirable that the method be as simple as possible.

With these considerations in mind, two different schemes have been implemented, tested and compared in order to find the best suited scheme for our application. Both schemes guarantee conservation of mass and momentum. The first, and most simple, is a first order Godunov-type method using the Rusanov scheme [39]. Source terms are treated using a simple splitting procedure. The second, and certainly more complex, is a third order Godunov-type method, capable of efficiently handling shocks, and handling complex source terms of any order using the so-called ADER approach. Both methods are implemented in the framework of one-step finite volume methods.

It is well known that the first order Rusanov scheme, as well as other first order approximate Riemann solvers, have a large numerical dissipation. On the other hand they are relatively easy to implement. In general, higher order methods have lower numerical dissipation, but the tradeoff is a more complicated and CPU intensive scheme.

4.1. One-step finite volume methods

We consider hyperbolic SBLs for the vector of conserved quantities $\mathbf{U}$ on the following form

$$\begin{cases} \text{PDE}: & \mathbf{U}_t + \mathbf{F}(\mathbf{U})_x = \mathbf{S}(\mathbf{U}, x) \\ \text{IC}: & \mathbf{U}(x, 0) = \mathbf{U}_0(x) \end{cases} \tag{47}$$

The one-dimensional spatial domain $\Omega \in [0, L]$ is covered completely by N non-overlapping elements $Q_i =]x_{i-\frac{1}{2}}, x_{i+\frac{1}{2}}[$ with $\Delta x_i = x_{i+\frac{1}{2}} - x_{i-\frac{1}{2}}$ and the cell average of $\mathbf{U}_i$ within Q_i is defined at time t^n as

$$\mathbf{U}_i^n = \frac{1}{\Delta x_i} \int_{x_{i-\frac{1}{2}}}^{x_{i+\frac{1}{2}}} \mathbf{U}(x, t^n) dx \tag{48}$$

Integrating the governing systems of PDEs (47) over the space-time control volume $V_i = Q_i \times [t^n, t^{n+1}]$ the following integral form of the balance law is derived

$$\mathbf{U}_i^{n+1} = \mathbf{U}_i^n - \frac{\Delta t}{\Delta x_i} [\mathbf{F}_{i+\frac{1}{2}} - \mathbf{F}_{i-\frac{1}{2}}] + \Delta t \mathbf{S}_i \tag{49}$$

where

$$\mathbf{F}_{i+\frac{1}{2}} = \frac{1}{\Delta t} \int_{t^n}^{t^{n+1}} \mathbf{F}(\mathbf{U}(x_{i+\frac{1}{2}}, t)) dt \quad \text{and} \quad \mathbf{S}_i = \frac{1}{\Delta t} \frac{1}{\Delta x} \int_{t^n}^{t^{n+1}} \int_{x_{i-\frac{1}{2}}}^{x_{i+\frac{1}{2}}} \mathbf{S}(\mathbf{U}(x, t), t) dx dt \tag{50}$$

The scheme (49) is known as the one-step FV scheme and is exact given that the numerical fluxes and source term in (50) can be evaluated exactly.

4.2. First-order Godunov-type method

In the first-order method the solution is approximated by a piecewise constant solution for all discrete points in time. Thus, the solution given at each cell barycenter is a value for the average

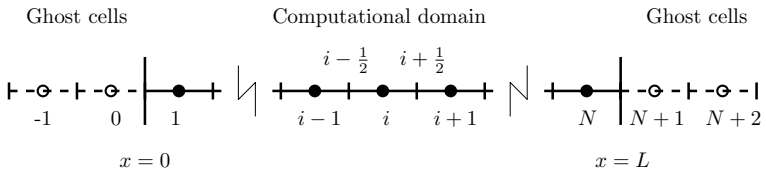

Figure 3: Computational domain

solution in the actual cell. In order to progress the solution in time from n to $n+1$ the flux function 50 must be evaluated at the cell intersections. This can done by considering each cell intersection as as an independent initial value problem, known as the Riemann problem:

$$\begin{aligned} &\text{PDE}: \quad \mathbf{U}_t + \mathbf{F}(\mathbf{U})_x = \mathbf{0} \\ &\text{IC}: \quad \mathbf{U}(x,0) = \begin{cases} \mathbf{U}_L & x < 0 \\ \mathbf{U}_R & x > 0 \end{cases} \end{aligned} \tag{51}$$

Numerical methods based on the exact solution of the Riemann problem, originally proposed by Godunov [40], are known as exact Riemann solvers, while methods which only use parts of the information concerning the wave propagation directions, are known as approximate Riemann solvers. We choose to use a simple approximate Riemann solver, namely the Rusanov scheme, with the following flux function:

$$\mathbf{F}^{Rus}_{i+\frac{1}{2}} = \frac{1}{2}(\mathbf{F}(\mathbf{U}^n_L) + \mathbf{F}(\mathbf{U}^n_R)) - \frac{1}{2}S^+\Delta t(\mathbf{U}^n_R - \mathbf{U}^n_L) \tag{52}$$

where

$$S^+ = \max\{|U_L| + a_L, |U_R| + a_R\}, a_L = \sqrt{gH_L} \tag{53}$$

The source term is treated using a simple splitting scheme, meaning that first the homogeneous SCL in (47) is advanced in time using (49), whereafter the temporary solution is used as an initial condition in a successive initial value problem. The scheme is written as

$$\left.\begin{aligned} &\text{PDE}: \quad \mathbf{U}_t + \mathbf{F}(\mathbf{U})_x = \mathbf{0} \\ &\text{IC}: \quad \mathbf{U}(x,t^n) = \mathbf{U}^n(x) \end{aligned}\right\} \rightarrow^{\Delta t} \mathbf{U}^* \tag{54}$$

and

$$\left.\begin{aligned} &\text{ODE}: \quad \frac{d}{dt}\mathbf{U} = \mathbf{S}(\mathbf{U}, x) \\ &\text{IC}: \quad \mathbf{U}^* \end{aligned}\right\} \rightarrow^{\Delta t} \mathbf{U}^{n+1} \tag{55}$$

The ODE in (55) can be solved using any conventional ODE solver. In the present work the ODE is simply integrated using a forward Euler method.

4.3. High order Godunov-type methods

We wish to construct a higher order method and still evolve the system using the one step FV scheme (49). Also, the method must be stable and non-oscillatory. Using the procedure known as the ADER approach [41] an FV scheme of arbitrary order can be constructed. The original ADER approach was recently extended by [42] to handle stiff source terms and will be used here. The ADER approach can be viewed as a three step method: First a reconstruction of the

averaged data is carried out using a WENO (weigthed essentially non-oscillatory) reconstruction technique [43]. This procedure guarantees a high-order non-oscillatory *spatial* representation of the state at time n. Secondly, the temporal evolution of the reconstruction is computed locally inside each cell using the governing PDE. The third and last step of the ADER approach consist of integrating the source in space and time and integrating the flux function in time at the element interfaces (50). For the evaluation of the flux at the interface the Rusanov flux (52) is used again. Finally, the solution is advanced using 49.

4.4. Time stepping restriction

In the update formula (49) certain restrictions must be placed on the size of the time step in order for the method to be stable. The value of the time step is dependent of the CFL condition which for the one dimensional shallow water equation can be stated as

$$\Delta t = \mathrm{CFL}\frac{\Delta x}{S^n_{\max}} \tag{56}$$

where $S^n_{\max}$ is the maximum propagation speed in absolute value in the differential equation. A practical choice of the maximum propagation speed is the following

$$S^n_{\max} = \max_i\{|U^n_i| + \sqrt{gH^n_i}\} \tag{57}$$

i.e. the maximum wave speed in the computational domain Ω. In the following we use CFL = 0.9 to satisfy the stability condition that CFL ≤ 1.

4.5. Boundary conditions

In the following, the treatment of periodic and solid wall boundary conditions are discussed. The first order method requires values from the neighboring cells on either side of cell i. Therefore, at each boundary and additional ghost cell is needed, the values of which are determined by application of a boundary condition. Periodic boundary conditions are modeled using the following relations

$$\begin{aligned} H_0 = H_m, U_0 = U_m \\ H_{m+1} = H_1, U_{m+1} = U_1 \end{aligned} \tag{58}$$

Solid wall boundary conditions are modeled using

$$\begin{aligned} H_0 = H_1, U_0 = -U_1 \\ H_{m+1} = H_m, U_{m+1} = -U_m \end{aligned} \tag{59}$$

For the third order scheme an additional ghost cell at each boundary is needed in order to carry out the WENO reconstruction. As an example, a periodic boundary condition applied at the left boundary is given by

$$\begin{aligned} H_0 = H_m, U_0 = U_m \\ H_{-1} = H_{m-1}, U_{-1} = U_{m-1} \end{aligned} \tag{60}$$

Table 1: Initial values used for the dam-break problem

H_L	U_L	H_R	U_R	x_c	t_{end}
$[m]$	$[m/s]$	$[m]$	$[m/s]$	$[m]$	$[s]$
1.0	0.0	0.5	0.0	0.5	0.1

5. Numerical convergence studies

To investigate the performance of the two proposed methods a numerical convergence study is carried out. First, the dam-break problem is solved. This is a standard benchmark test for numerical methods and is useful for validating the ability of the numerical methods to handle discontinuities and predict correct shock speeds. Next, the methods are tested on the nonlinear shallow water equations with source terms, i.e. on a system of balance laws, for which an exact reference solution is developed by construction. In general, the solution of SBLs is far from trivial it is imperative that the numerical scheme can handle source terms effectively. The last test case is a rectangular tank undergoing forced horizontal oscillations. The bottom friction and bottom slope are here neglected. In the study, the amplitude parameter Λ and frequency parameter β are varied while bottom friction is neglected ($\gamma = 0$). No analytical solutions exist for this test case and the purpose of the study is to compare the two different methods and estimate the necessary number of cells needed for the sloshing simulations.

5.1. Dam-break problem

The dam-break problem consists of an initial water level distribution with a discontinuity in depth at $x = x_c$ and zero initial velocity. The initial depth ratio, H_R/H_L between the right side, H_R, and the left side, H_L, of the dam determines the evolution of the flow for $t > 0$. This problem is the classical Riemann problem described earlier which can be solved exactly by implementing the procedure given in [39]. First, a grid convergence study using the flux formulation (32) is performed. Next, using a fixed mesh, the results produced by the fl;ux and velocity formulations are compared. For all the cases the computational domain is given by $\Omega = [0m, 50m]$, and the initial conditions are given in Table 1. For all the simulation the Courant number is chosen to CFL = 0.9. The computed total water depth is presented in 5.1 at time t=0.1 s together with the

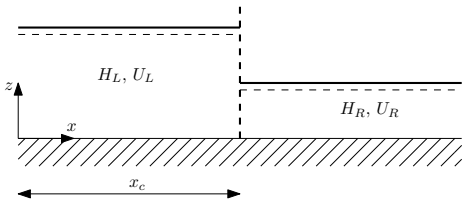

Figure 4: Dam-break problem. Initial depth profile at time $t = 0$

exact solution. The figures indicate that both solutions are converging to the analytical solution as the mesh is refined. To finally conclude that the methods are indeed converging we compute the L^1 norms at $t = t_{end}$ for the total depth variable H_i^n, where the L^1 norm is defined as

$$e(h) = \int_\Omega |w_h - u_e|^p d\Omega \tag{61}$$

Table 2: Convergence rates for dam-break problem

	First-order		Third-order	
M	L^1	k	L^1	k
25	2.34E-02		1.37E-02	
50	1.49E-02	0.7	4.98E-03	1.5
100	9.30E-03	0.7	2.68E-03	0.9
200	5.61E-03	0.7	1.36E-03	1.0
400	3.31E-03	0.8	6.15E-04	1.1

In the above w_h is the reconstructed numerical solution, which for a first-order method is a piecewise constant solution and for the third order-method is a polynomial. The exact solution is denoted by u_e and h is a measure of the mesh spacing. The error of a k-th order method then has the following asymptotic behavior

$$e(h) = C \cdot h^k \tag{62}$$

The results of the convergence rates and L^1 norms in Table 5.1 show that both method converge and with the third-order method being superior over the first-order method. The convergence rate is per definition defined for smooth problems which explains the low convergence rate of approximately 1 for the third-order method.

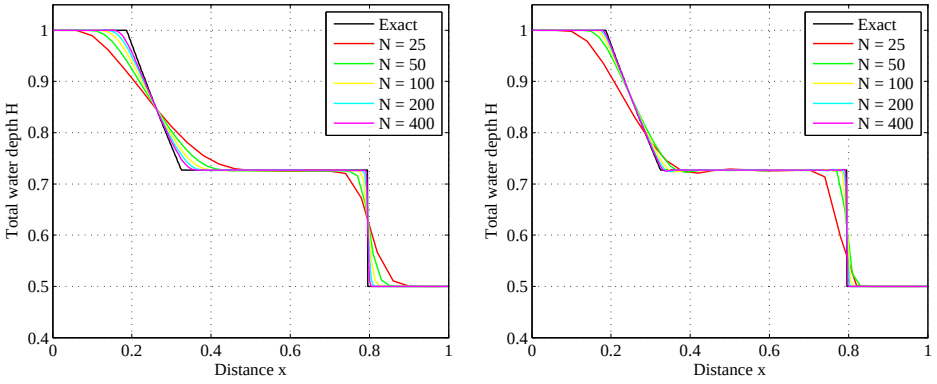

(a) First-order (b) Third-order

Figure 5: Dam-break problem grid convergence study for first-order and third-order methods

Finally, a computation comparing the flux formulation (32) and the velocity formulation (33) for two different initial conditions is performed. The first-order method is used with $M = 400$, CFL=0.9. The results in Figure 5.1 clearly show that the error associated with using the velocity formulation depends on the strength of the shock. Thus, for a relatively weak shock, $H_R/H_L = 0.5$, the solutions are close while using $H_R/H_L = 0.1$ as initial condition give rise to an incorrect shock speed when using the velocity formulation. The results underline the importance of using an appropriate formulation for the problem at hand.

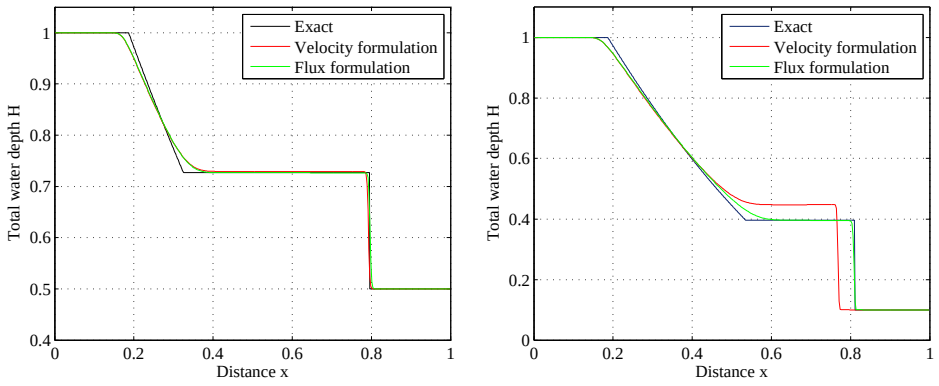

(a) $H_R/H_L = 0.5$ (b) $H_R/H_L = 0.1$

Figure 6: Dam-break problem using a momentum conserving and velocity conserving formulation.

5.2. *System of balance laws*

Consider the following system of balance laws

$$H_t + Q_x = S_1 \tag{63}$$

$$Q_t + (Q^2/H + \tfrac{1}{2}gH^2)_x = S_2 \tag{64}$$

with

$$S_1 = (H_e)_t + (Q_e)_x \tag{65}$$

$$S_2 = \nu\cos(\Omega t)(Q - Q_e) + (Q_e)_t + (Q_e^2/H_e + \tfrac{1}{2}gH_e^2)_x \tag{66}$$

By choosing any differentiable functions $H_e(x,t)$ and $Q_e(x,t)$ in (65) it is easily verified that $H = H_e$ and $Q = Q_e$ satisfies (63) for all times t, and hence an exact reference solution can been constructed and used for convergence studies. In the following we chose the reference solution given by

$$H_e = H_0 + A_H\sin(k_w x - \omega t) \quad , \quad Q_e(x,t) = Q_0 + A_Q\cos(k_w x - \omega t) \tag{67}$$

with the parameters: $H_0 = 4$, $A_H = 0.1$, $Q_0 = 6$, $A_Q = 0.3$, $k_w = \omega = 2\pi$ and $\Omega = 2\pi$. The parameter ν is varied. Our system (63) is solved on the domain $\Omega \in [0;1]$, with periodic boundary conditions. The Courant number is set to CFL = 0.9. The initial conditions are $H(x,0) = H_e(x,0)$ and $Q(x,0) = Q_e(x,0)$ and the solution is computed for one period, i.e. up to the final output time $t = 1.0$. It is clear from Table 3 that both methods are capable of treating source terms with a convergence rate somewhat below 1 for the first-order method, but for a very stable convergence rate of close to 3 for the third-order method. Also the L^1 norms show a much more precise result for the third-order method. The force factor ν has little influence on the results.

5.3. *Oscillating rectangular tank*

We now consider the system of balance laws together with the initial and boundary given in (38)-(39) describing horizontal oscillations of a rectangular tank. With length and water depth

Table 3: Convergence rates for $\nu = 1$ and $\nu = 3$.

	First-order $\nu = 1$		Third-order $\nu = 1$		First-order $\nu = 3$		Third-order $\nu = 3$	
M	L^1	k	L^1	k	L^1	k	L^1	k
8	7.65E-02		1.03E-02		1.35E-01		1.34E-02	
16	4.86E-02	0.7	1.80E-03	2.5	1.03E-01	0.4	2.29E-03	2.6
32	2.77E-02	0.8	2.40E-04	2.9	6.48E-02	0.7	3.07E-04	2.9
64	1.58E-02	0.8	3.03E-05	3.0	3.73E-02	0.8	3.89E-05	3.0
128	8.91E-03	0.8	3.80E-06	3.0	2.04E-02	0.9	4.90E-06	3.0

given in Table 5 the linear shallow water sloshing frequency is computed as $\omega_w^* = 2.8645$ rad/s, which is the value we choose for our forcing frequency Ω^*. The effect of bottom friction is neglected ($\gamma = 0.0$). In all the simulation the Courant number is chosen as $CFL = 0.9$ and the total simulation time is set to five periods. For both the first-order and third-order method a total of 128 cells is used in the simulations. In Figure 5.3 three graphs showing variation of wave height at the left tank wall, horizontal sloshing force and force-displacement elapse, are presented. The variation in the results are seen to be limited, indicating that the simple first-order method is adequate for describing the fluid sloshing behavior.

To establish a value for the number of cells needed in the sloshing simulations a grid convergence study is performed. The simulation time is as before set to five forcing periods and in the time window spanning from period 3 to 4 the maximum wave height, maximum sloshing force and the integral of the hysteresis loop, see e.g. Figure 7(b), is recorded. The results for different mesh sizes is given in Table 6 for the first-order and third-order method. It is clear from the results that both methods are convergent which has also been illustrated in Figure 5.3 where the energy ΔE is plotted as function of mesh density. The last column in Table 6 shows the difference between the energy dissipation estimated using a first and third-order method. When using more than 256 cells the difference between the two methods is less than or equal to 1%. Moreover, when comparing the dissipated energy for the first-order method using 128 cells to the third-order method using 1024 the difference is only 1.5% which for practical purposes is negligible. These observations indicate that using a first-order method for estimating sloshing behavior is sufficient.

5.4. Choice of numerical method

In the previous three sections the simple first-order method and highly accurate but complex third-order method have been tested on three cases. Both methods have shown to be capabile of

Table 4: Tank dimensions and forcing values.

L^*	h_0^*	A^*	$\Omega*$	g	Λ/π	β	γ
[m]	[m]	[m]	[rad/s]	m/s^2	[-]	[-]	[-]
0.590	0.0295	0.059	2.8645	9.81	0.1	1.0	0.0

Table 5: Parameters for sloshing simulation

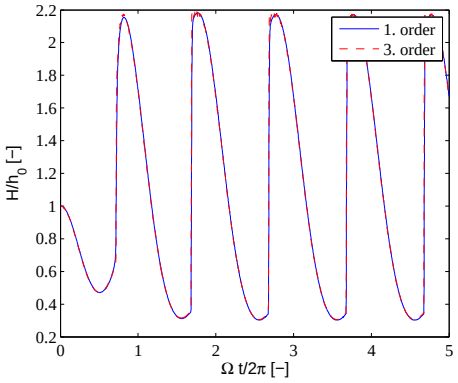

(a) Time variation of dimensionless total height

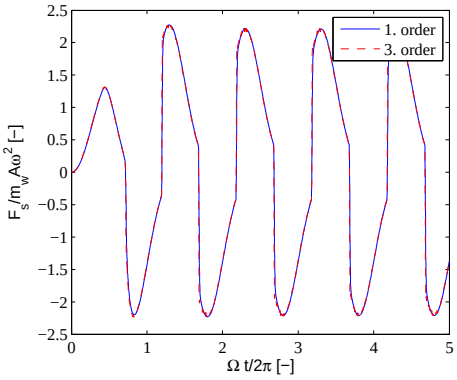

(b) Time variation of dimensionless shear force

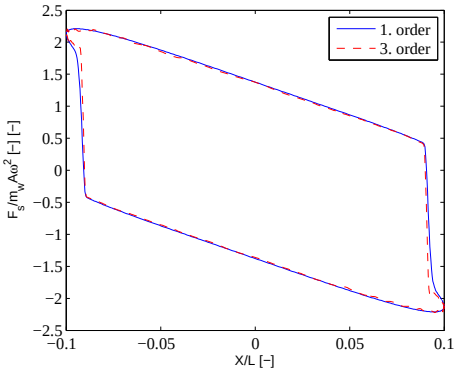

(c) Dimensionless hysteresis loop

Figure 7: Sloshing simulations using first-order and third-order methods

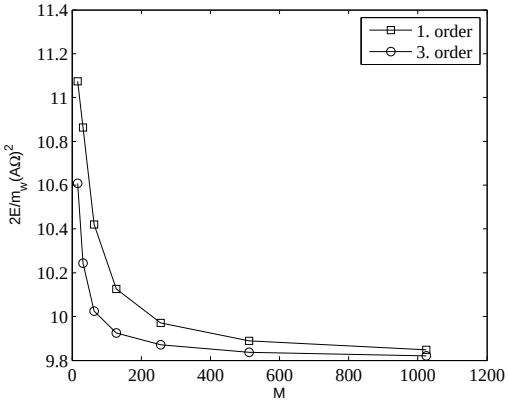

Figure 8: Convergence of dimensionless energy ΔE

Table 6: Sloshing results

	First-order			Third-order			
M	$H_L^{\max}$	$F_S^{\max}$	ΔE	$H_L^{\max}$	$F_S^{\max}$	ΔE	$\epsilon_{\Delta E}$
[-]	[-]	[-]	[-]	[-]	[-]	[-]	[%]
16	0.061294	2.0839	11.073	0.064596	2.286	10.608	4.4
32	0.063318	2.2171	10.863	0.06432	2.2694	10.244	6.0
64	0.063867	2.2628	10.421	0.064145	2.2674	10.025	4.0
128	0.064037	2.2741	10.127	0.064425	2.2784	9.9254	2.0
256	0.064055	2.2723	9.9702	0.064201	2.28	9.8711	1.0
512	0.064041	2.2696	9.8896	0.064139	2.2753	9.8365	0.5
1024	0.064032	2.2682	9.8485	0.064065	2.2704	9.8207	0.3

capturing shock and rare fraction waves as well as handling source terms. In general the third-order method gives smaller errors compared to the first-order method and for smooth problems also a high convergence rate of close to three. The price however is a more expensive algorithm computationally and, perhaps more importantly, a much more complicated implementation. In the final test case the two methods are compared for a sloshing simulation. For the specific case again the third-order methods converges faster than the first-order method but the difference in the simulation results are very small and therefore we choose the first-order methods using 256 cells for the following simulations.

6. Parameter study

Having established the governing NSW equations (38) describing fluid motion in a horizontal oscillating rectangular container, together with relevant dimensionless parameters (40), we want to perform a parameter study to determine how the individual parameters affect the solution. More precise we will be studying the effects of the amplitude parameter Λ together with the frequency parameter β. Moreover the effect of friction will also be investigated based on realistic friction parameters.

6.1. Sloshing response without friction

In the following the friction term is neglected, $\gamma = 0$, and only the influence of the amplitude and frequency parameters is studied. A total of 1320 simulations are performed, with $\Lambda/\pi = [0.005, 0.01, 0.025, 0.05, 0.075, 0.1$ and $\beta \in [0.6, 2.2]$. The domain is modeled using 256 cells and a Courant number of CFL $= 0.9$ is used in all runs. For each simulation a total of 30 periods are computed, and based on the last 10 periods the following steady state values are computed for each (Λ, β)-pair: the maximum and minimum total depth at the left container wall $H_L^{\max}$ and $H_L^{\min}$ respectively, the maximum horizontal sloshing force $F_S^{\max}$, and the dissipated energy per cycle ΔE. Figure 6.1, denoted the frequency-response curve what follows, shows the variation $H_L^{\max}$ as function of the frequency β. From this figure it is clear that the system exhibits a hardening type behavior in line with observations made in early works, e.g. [16]. In more recent studies [44, 29, 45] the same effect was reported and the hardening effect, which effectively is a consequence of the system responding more rapidly for increased forcing, can be

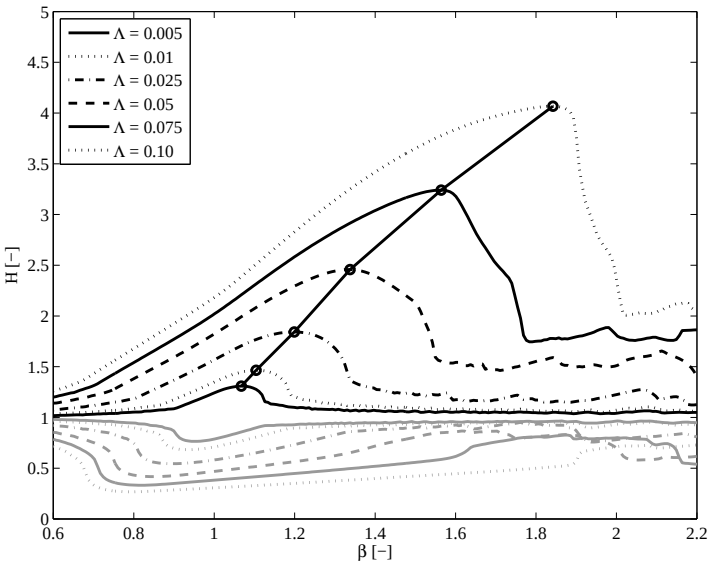

Figure 9: Frequency response curve for maximum and minimum steady state water water depth at left tank wall

explained by the fact that the propagation, or shock speed of a bore is a function on the water depth ratio to the left and right of the bore. More precisely, the propagation speed for a right facing shock, $H_L > H_R$, is given by [39]

$$S = U_R + \sqrt{\tfrac{1}{2} g \frac{H_L}{H_R}(H_L + H_R)} \tag{68}$$

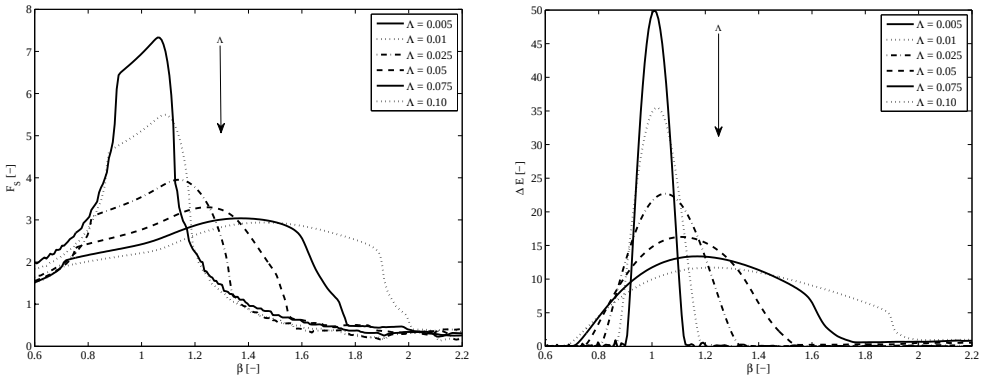

(a) Maximum horizontal sloshing force F_S

(b) Dissipated energy pr. cycle ΔE

Figure 10: Frequency response curves for F_S and ΔE

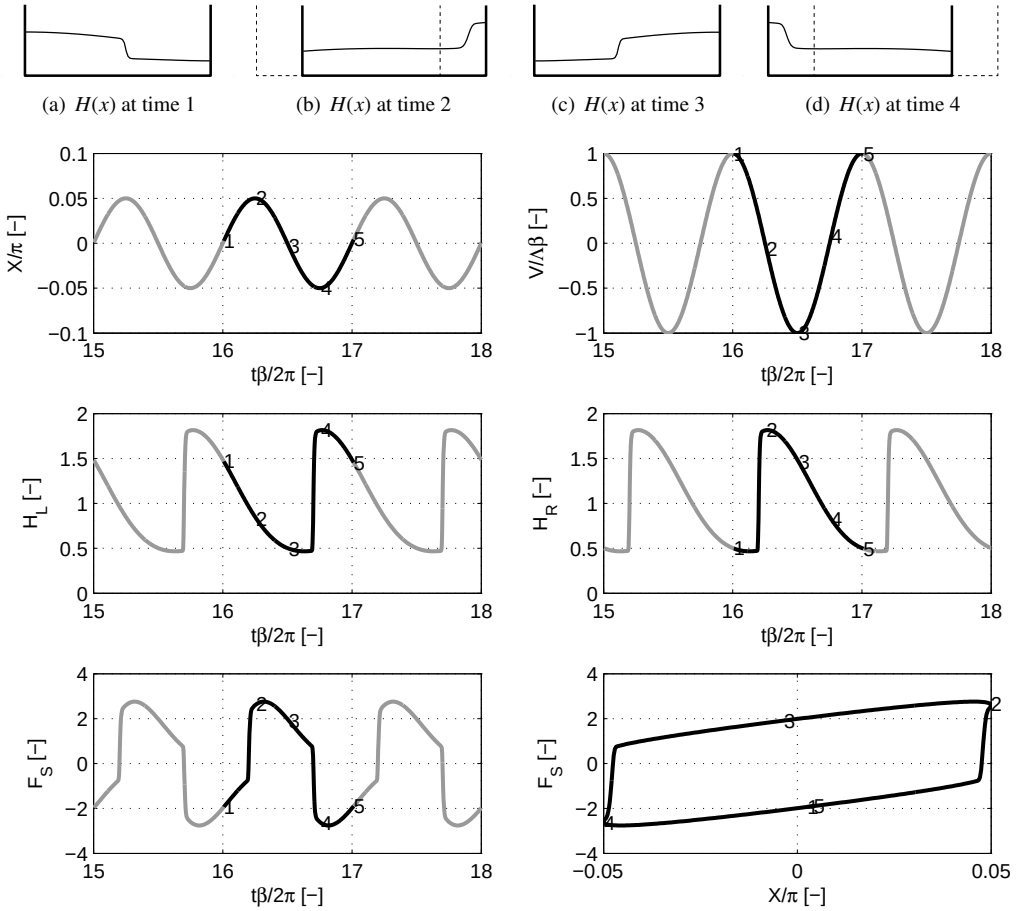

(a) $H(x)$ at time 1 (b) $H(x)$ at time 2 (c) $H(x)$ at time 3 (d) $H(x)$ at time 4

(e) Dimensionless hysteresis loop

Figure 11: A single period solution for $\Lambda\pi = 0.05$ and $\beta = 1.0$

Hence, for increased forcing, i.e. increased $\Lambda\beta^2$, the ratio H_L/H_R as well as U_R increases, resulting in a faster moving shock equivalent to a "stiffer" system. In Figure 6.1 a solid line has been drawn through each maximum of the frequency-response curves. This line, also known as the backbone curve, can be used to estimate the governing parameters in the Duffing equation [46].

Moving on to Figures 10(a)-10(b), which show frequency-response curves for the horizontal sloshing force and dissipated energy per cycle, the hardening effect is not as clear. From the energy curves in particular, the effect is only visible by an increase in the frequency location of the maxima while the elapse of the curves have no "leaning effect" and seem almost symmetric around their maxima. From the two figures it is also seen that the sloshing force and energy dissipation curves decrease in magnitude with increasing Λ values. This is not surprising since a stronger forcing term produces a stronger shock with an increase in *internal fluid* dissipation, reducing the force and energy dissipation (note again that the so-called energy dissipation is *not* the energy dissipated by the fluid internally but the work of the sloshing force with respect to the

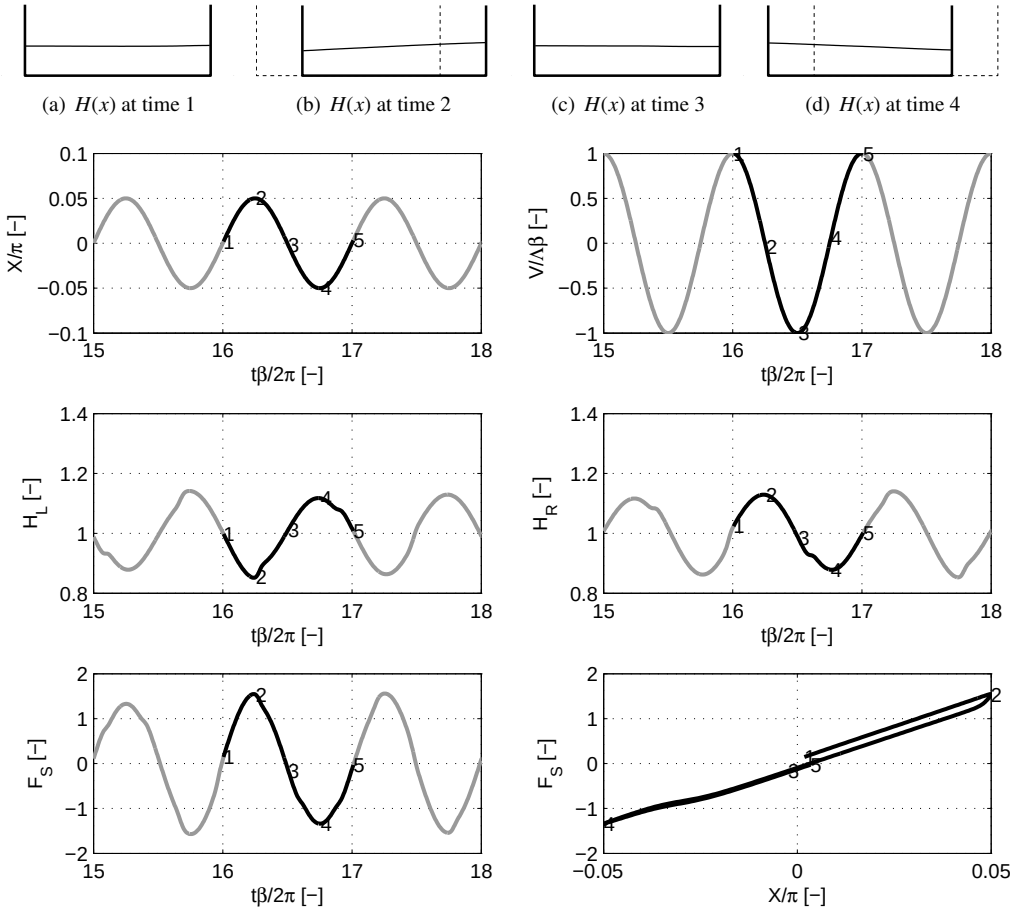

(a) $H(x)$ at time 1 (b) $H(x)$ at time 2 (c) $H(x)$ at time 3 (d) $H(x)$ at time 4

(e) Dimensionless hysteresis loop

Figure 12: A single period solution for $\Lambda/\pi = 0.05$ and $\beta = 0.6$

base motion, see (45)). Generally speaking, the situation is analogous to a simple base excited mass-spring-damper system with the damper having nonlinear amplitude dependent characteristics.

In Figures 11, 12 and 13 a detailed description of the sloshing behavior is illustrated for an amplitude ratio $\Lambda/\pi = 0.05$ and three different forcing ratios, $\beta = 1.0, 0.6, 1.4$, respectively. In the top row the water elevation is shown for four different time instances given in each of the six underlying figures. The initial tank position is shown in the figures with a dotted line. The two top curves show the base motion amplitude and velocity, respectively, using the sign convention from figure 2. The last four figures show the variation of water at the left and right wall, the variation of the sloshing force, defined positively to the right as shown in figure 2, and finally, a diagram showing the hysteresis loop. Is is clear from the figures that as the frequency ratio approaches unity the hysteresis curve opens up, corresponding to the sloshing force being in phase with the velocity, and energy is dissipated.

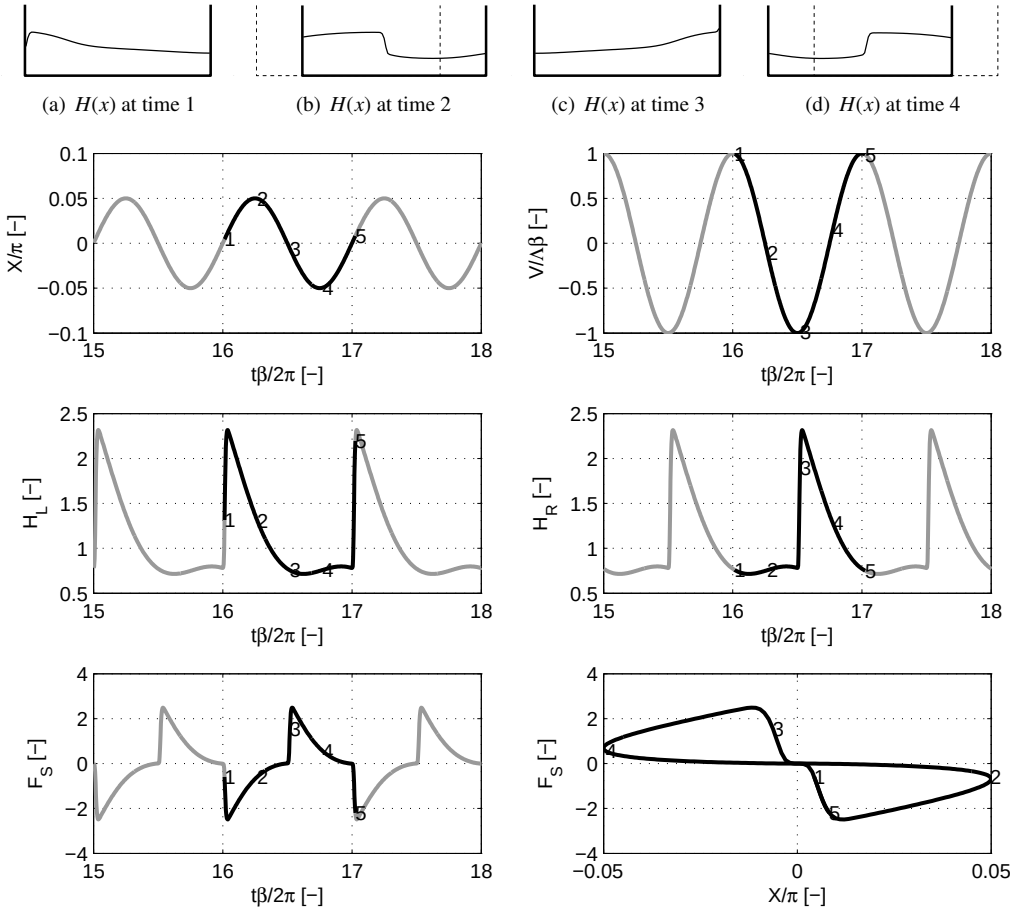

(a) $H(x)$ at time 1 (b) $H(x)$ at time 2 (c) $H(x)$ at time 3 (d) $H(x)$ at time 4

(e) Dimensionless hysteresis loop

Figure 13: A single period solution for $\Lambda/\pi = 0.05$ and $\beta = 1.4$

Table 7: Friction factor γ using $g = 9.81\text{m/s}^2$.

M^*	h_0^*	μ/π	γ
$[\text{m}^{1/3}/\text{s}]$	$[m]$	$[-]$	$[-]$
150	0.02	0.01	0.022
100	0.02	0.01	0.050
70	0.02	0.01	0.103

6.2. Effect of bottom friction

In the following the influence of friction is assessed, i.e we set $\gamma > 0$. For estimating the dimensionless friction parameter γ knowledge of realistic Manning numbers must be established. An extensive list of Manning numbers for a large variety of materials is contained in [47]. For smooth materials such as steel, plastic etc, a typical Manning number is $M \simeq 100$. In [48]

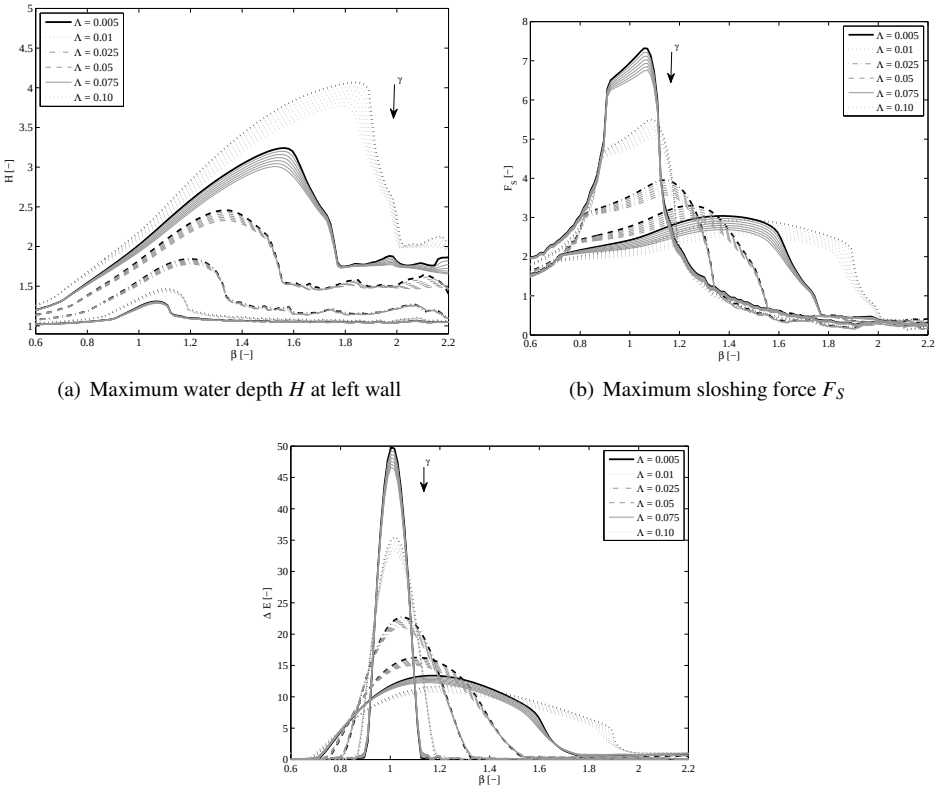

(a) Maximum water depth H at left wall

(b) Maximum sloshing force F_S

(c) Dissipated energy ΔE

Figure 14: Effect of Λ, β and γ. Friction parameters used are $\gamma = [0, 0.02, 0.04, 0.06, 0.08, 0.10, 0.12]$. The arrows indicates direction of rising γ-values.

Manning numbers for corrugated polyethylene pipes was reported to vary between 70 and 110. Much lower values have been reported though in different studies such as [33] where values of $M = 200 - 300$ were reported in connection with the modelling of tidal bores. There is clearly a large deviation in Manning numbers and also it should be stressed that the Manning numbers are based on a steady flow, which only approximately is valid for our case. In the present context though we are only interested in a qualitatively assessment of the friction term on the sloshing behavior and thus are satisfied with establishing a reasonably realistic level of the friction factor γ. In Table 7 three different friction factors have been computed using three different Manning numbers and estimates of the water depth and depth ratio, resulting in a friction factor in the range of $\gamma \simeq 0.02 - 0.10$. A lower water depth will result in a higher friction factor as will a lower depth ratio. However, the values used in Table 7 are very low and thus provide a rather conservative estimate.

Figure 11 shows the frequency response curves for maximum dimensionless water depth at left wall, $H_L^{\max}$, maximum sloshing force, $F_S^{\max}$, and dissipated energy per cycle, ΔE. In each graph the effect of varying the amplitude, Λ, and friction factor, γ, is illustrated. The case of

Table 8: Effect of γ and Λ on water depth $H_L^{\max}$

	$\Lambda/\pi[-]$					
$\gamma[-]$	0.005	0.01	0.025	0.05	0.075	0.1
0.00	1.00	1.00	1.00	1.00	1.00	1.00
0.02	1.00	1.00	0.99	0.99	0.99	0.99
0.04	0.99	0.99	0.99	0.98	0.98	0.98
0.06	0.99	0.99	0.98	0.97	0.96	0.96
0.08	0.99	0.98	0.98	0.96	0.95	0.95
0.10	0.98	0.98	0.97	0.96	0.94	0.94
0.12	0.98	0.98	0.96	0.95	0.93	0.93

Table 9: Effect of γ and Λ on sloshing force $F_S^{\max}$

	$\Lambda/\pi[-]$					
$\gamma[-]$	0.005	0.01	0.025	0.05	0.075	0.1
0.00	1.00	1.00	1.00	1.00	1.00	1.00
0.02	0.99	0.98	0.98	0.98	0.98	0.97
0.04	0.97	0.97	0.97	0.96	0.96	0.95
0.06	0.96	0.96	0.95	0.94	0.94	0.93
0.08	0.95	0.94	0.93	0.92	0.92	0.91
0.10	0.94	0.93	0.92	0.91	0.90	0.89
0.12	0.92	0.92	0.90	0.89	0.89	0.87

$\gamma = 0$ is represented by the dominant black curve while curves for variable γ are depicted as light grey. The friction factor is seen, not surprisingly, to have an effect on the maximum values of the curves while the overall shape of the frequency response curves are more or unless unaffected.

For each of the frequency response curves in 14, the maximum value has been found and are shown in Tables 8-10. These values have been normalized with results from the non-friction case. In general, the effect of the friction factor increases with higher Λ values, with the largest effect on sloshing force, and less effect on the water depth and energy dissipation. With the largest γ-value of 0.12, which is a very conservative estimate, the maximum value of the frequency response curves for the sloshing force is lowered some 8-13% and for the dissipated energy 5-9%. For a container with smooth bottom a more realistic γ-values is 0.02 which gives a reduction of the maximum values in the range of 1-3% and thus is of little practical importance.

7. Conclusions

In this work two dimensional nonlinear sloshing in a rectangular tank has been studied. Based on the assumption of an incompressible fluid, negligible viscous effects in the fluid bulk, and hydrostatic pressure assumptions, the governing set of nonlinear equations were derived - the so-called NSW equations including bottom friction. The set of equations were analyzed analytically and numerically and the following main conclusion can be drawn.

I. The behavior of fluid sloshing in a horizontally oscillated rectangular container described by the NSW equations is governed solely by three dimensionless parameters: an amplitude

Table 10: Effect of γ and Λ on dissipated energy ΔE

	$\Lambda/\pi[-]$					
$\gamma[-]$	0.005	0.01	0.025	0.05	0.075	0.1
0.00	1.00	1.00	1.00	1.00	1.00	1.00
0.02	0.99	0.99	0.99	0.99	0.98	0.98
0.04	0.98	0.98	0.97	0.97	0.97	0.97
0.06	0.97	0.97	0.96	0.96	0.96	0.95
0.08	0.96	0.95	0.95	0.95	0.94	0.94
0.10	0.95	0.94	0.94	0.93	0.93	0.92
0.12	0.94	0.93	0.93	0.92	0.92	0.91

parameter Λ, a frequency parameter β, and a friction parameter γ. The two first parameters are independent of the absolute liquid depth, while the friction parameter is dependent on the absolute water depth as well as on the depth ratio μ.

II. The governing system of balance laws describing sloshing can be effectively solved using a simple first-order finite volume method. Although such methods are renowned for excessive numerical dissipation, this source of dissipation is far outweighed by the physical dissipation occurring as a result of the development of bores.

III. Neglecting bottom friction, the liquid response at resonance, i.e. at $\beta = 1$, is governed solely by the amplitude parameter Λ.

IV. The response of the liquid is dependent of the friction factor for tanks with very shallow water and rough bottom conditions. For relatively smooth bottom conditions the effect of bottom friction is limited and will have little effect on the response.

V. The frequency response curves for maximum water depth, sloshing force, and dissipated energy all display a stiffening behavior meaning that the maximum values of the respective curves occur at increased β values for increased Λ values. The effect is most pronounced for the maximum water depth and less so for the dissipated energy. The effect is very important in the context of designing tuned liquid dampers as these will show a significant amplitude-dependent behavior.

References

[1] E. Graham, A. Rodriguez, The characteristics of fuel motion which affect airplane dynamics, Journal of Applied Mechanics-Transactions of the ASME 19 (1952) 381–388.

[2] A. Kareem, W.-J. Sun, Stochastic response of structures with fluid-containing appendages, Journal of Sound and Vibration 119 (3) (1987) 389–408.

[3] M. Tait, A. El Damatty, N. Iayumov, Testing of tuned liquid damper with screens and development of equivalent tmd model, Wind and Structures, An International Journal 7 (4) (2004) 215–234.

[4] J. R. CHO, H. W. LEE, K. W. KIM, Free vibration analysios of baffled liquid-storage tanks by the structural-acoustic finite element formulation, Journal of Sound and Vibration 258 (5) (2002) 847–866.

[5] J. Cho, H. Lee, S. Ha, Finite element analysis of resonant sloshing response in 2-d baffled tank, Journal of Sound and Vibration 288 (4) (2005) 829–845.

[6] K. Biswal, S. Bhattacharyya, P. Sinha, Dynamic characteristics of liquid filled rectangular tank with baffles, Journal of the Institution of Engineers (India): Civil Engineering Division 84 (2) (2003) 145–148.

[7] A. Marsh, M. Prakash, E. Semercigil, z. F. Turan, A numerical investigation of energy dissipation with a shallow depth sloshing absorber, Applied Mathematical Modelling 34 (10) (2010) 2941–2957.
[8] D. T. Valentine, Numerical investigation of two-dimensional sloshing: Nonlinear internal waves, Journal of Offshore Mechanics and Arctic Engineering 127 (4) (2005) 300–305.
[9] J. Frandsen, A. Borthwick, Simulation of sloshing motions in fixed and vertically excited containers using a 2-d inviscid s-transformed finite difference solver, Journal of Fluids and Structures 18 (2) (2003) 197–214.
[10] J. B. Frandsen, Sloshing motions in excited tanks, Journal of Computational Physics 196 (1) (2004) 53–87.
[11] M. Peric, T. Zorn, O. El Moctar, T. E. Schellin, Y.-S. Kim, Simulation of sloshing in lng-tanks, Journal of Offshore Mechanics and Arctic Engineering 131 (3) (2009) 1–11.
[12] D. Liu, P. Lin, A numerical study of three-dimensional liquid sloshing in tanks, Journal of Computational Physics 227 (8) (2008) 3921–3939.
[13] M. Brocchini, R. Bernetti, A. Mancinelli, G. Albertini, An efficient solver for nearshore flows based on the waf method, Coastal Engineering 43 (2) (2001) 105–129.
[14] S. H. A. Madsen, Per A., A review of boussinesq-type equations for gravity waves, Advances in Coastal and Ocean Engineering 5 (1999) 1–94.
[15] S.-M. J. Bristeau, M., Derivation of a non-hydrostatic shallow-water model; comparison with saint-venant and boussinesq systems., Discrete and Continuous Dynamical Systems 10 (2008) 759.
[16] W. Chester, J. A. Bones, Resonant oscillations of water waves. ii. experiment, Proceedings of the Royal Society of London. Series A, Mathematical and Physical Sciences 306 (1484) (1968) 23–39.
[17] T. G. Lepelletier, F. Raichlen, Nonlinear oscillation in rectangular tanks., Journal of Engineering Mechanics 114 (1) (1988) 1–23.
[18] Peregrine, Long waves on a beach, Journal of Fluid Mechanics 27 (1967) 815–827.
[19] J. Miles, Surface-wave damping in closed basins, Proceedings of the Royal Society of London Series A - Mathematical and Physical Sciences 297 (1967) 459–, bestilt 24-2-2007.
[20] Bredmose, Brocchini, Peregrine, Thais, Experimental investigation and numerical modelling of steep forced water waves, Journal of Fluid Mechanics 490 (2003) 217–249.
[21] G. Wei, J. T. Kirby, S. T. Grilli, R. Subramanya, A fully nonlinear boussinesq model for surface waves. part 1. highly nonlinear unsteady waves, Oceanographic Literature Review 43 (3) (1996) 216.
[22] M. Narayanaswamy, J. Frandsen, R. Dalrymple, Experimemtal and numerical investigation of forced oscillationsin rectangular tanks (2006) 1172–1183.
[23] J. Verhagen, L. van Wijngaarden, Non-linear oscillations of fluid in container, Journal of Fluid Mechanics 22 (Part 4) (1965) 737–751.
[24] J. Dillingham, Motion studies of a vessel with water on deck, Marine Technology 18 (1) (1981) 38–50.
[25] V. Armenio, M. L. Rocca, On the analysis of sloshing of water in rectangular containers: numerical study and experimental validation, Ocean Engineering 23 (8) (1996) 705–739.
[26] L. M. Sun, Y. Fujino, B. M. Pacheco, M. Isobe, Nonlinear waves and dynamic pressures in rectangular tuned liquid damper (tld). simulation and experimental verification, Doboku Gakkai Rombun-Hokokushu/Proceedings of the Japan Society of Civil Engineers (410) (1989) 81–92, hardcopy exists.
[27] L. Sun, Y. Fujino, B. Pacheco, P. Chaiseri, Modelling of tuned liquid damper (tld), Journal of Wind Engineering and Industrial Aerodynamics 43 (1-3) (1992) 1883–1894.
[28] S. Kaneko, M. Ishikawa, Modelling of tuned liquid damper with submerged nets, Fundamental Aspects of Fluid-Structure Interactions and American Society of Mechanical Engineers, Applied Mechanics Division, AMD 151 (1992) 185–203.
[29] D. Reed, J. Yu, H. Yeh, S. Gardarsson, Investigation of tuned liquid dampers under large amplitude excitation, Journal of Engineering Mechanics - Proceedings of the ASCE 124 (4) (1998) 405–413.
[30] V. Casulli, Numerical methods for free surface hydrodynamics, Lecture notes (2007).
[31] G. W. G. Pinder, F. G., Finite Element Simulation in Surface and Subsurface Hydrology, Academic Press, 1977.
[32] C. Vreugdenhil, Numerical Methods for Shallow-Water Flow, Springer, 1994.
[33] P. Madsen, H. Simonsen, C.-H. Pan, Numerical simulation of tidal bores and hydraulic jumps, Coastal Engineering 52 (5) (2005) 409–433.
[34] Casulli, Cheng, Semi-implicit finite difference methods for three-dimensional shallow water flow, International Journal for Numerical Methods in Fluids 15 (6) (1992) 629–648.
[35] J.-K. Yu, T. Wakahara, D. A. Reed, A non-linear numerical model of the tuned liquid damper, Earthquake Engineering and Structural Dynamics 28 (6) (1999) 671–686.
[36] C. W. Housner, Dynamic pressures on accelerated fluid containers, Bulletin of Seismological Society of America (1957) 15–35.
[37] T. R. L. N. P. Zienkiewicz, O. C., The Finite Element Method for Fluid Dynamics, A Butterworth-Heinemann Title, 2006.
[38] R. J. LeVeque, Finite Volume Methods for Hyperbolic Problems, Cambridge University Press, 2002.

[39] E. F. Toro, Shock-capturing Methods For Free-surface Shallow Flows, Wiley, April 2001.
[40] S. K. Godunov, A difference scheme for numerical solution of discontinuous solution of hydrodynamic equations, Math. Sbornik 47 (1959) 271–306.
[41] V. A. Titarev, E. F. Toro, Ader: Arbitrary high order godunov approach, Journal of Scientific Computing 17 (1-4) (2002) 609–618.
[42] M. Dumbser, C. Enaux, E. F. Toro, Finite volume schemes of very high order of accuracy for stiff hyperbolic balance laws, Journal of Computational Physics 227 (8) (2008) 3971–4001.
[43] X.-D. Liu, S. Osher, T. Chan, Weighted essentially non-oscillatory schemes, Journal of Computational Physics 115 (1) (1994) 200–212.
[44] S. M. Gardarsson, Shallow-water sloshing, Ph.D. thesis, University fo Washington (1997).
[45] Gardarsson, Hysteresis in shallow water sloshing, Journal of Engineering Mechanics 133 (2007) 1093–1100.
[46] A. H. Nayfeh, Nonlinear Oscillations, John Wiley & Sons, 1979.
[47] V. T. Chow, Open Channel Hydraulics, McGraw-Hill, Inc., 1959.
[48] S. Barfuss, J. P. Tullis, Friction factor test on high density polyethylene pipe. hydraulics report no. 208, Tech. rep., Utah Water Research Laboratory, Utah State University. Logan, Utah (1988).

Paper II

"Shallow Water Sloshing. Part II. Experimental investigation and numerical verification"

J. Krabbenhøft & C.T. Georgakis

Manuscript prepared for submission to: *Engineering Structures*

Shallow Water Sloshing. Part II. Experimental investigation and numerical verification

J. Krabbenhøft*[,a], C.T. Georgakis[a]

[a]*Department of Civils Engineering, Technical University of Denmark, Building 118, Brovej, 2800 Kgs. Lyngby, Denmark*

Abstract

The sloshing of water in a rectangular tank subjected to forced base motion is investigated experimentally and numerically with the aim of determining the range of applicability of the nonlinear shallow water equations derived and analyzed in Part I [1].

The experiments show that the depth ratio has a large influence on the fluid behavior in the range $0.03 < h/L < 0.1$, being in contradiction with the theoretical shallow water assumption. However, for the frequency range $0.7 < \beta < 1.1$ the experimental results show reasonable agreement with the NSW equations, dependent though on the base amplitude A/L and depth ratio h/L. Thus, for very shallow water, $h/L = 0.03$, the NSW equations provide a fair description of the fluid behavior for low base amplitudes of $A/L = 0.009$ while for $h/L > 0.07$ and $A/L = 0.009$ the agreement is poor. Increasing the base amplitude greatly improves the fluid description provided by the NSW equations, suggesting that the NSW equations could be used to model coupled tank-structure systems for a large range of depth and amplitude ranges.

Key words: Nonlinear shallow water equation, sloshing, Tuned Liquid Damper, Energy dissipation

1. Introduction

In Part I [1] a set of nonlinear, inhomogeneous PDEs describing sloshing of water in oscillating rectangular tanks were derived based on the full two-dimensional incompressible Navier-Stokes equations formulated in a translating coordinate system. The resulting set of equations, known as the nonlinear shallow water equations (NSW equations), were analyzed to determine governing parameters and numerically to study the effect of the derived parameters on the solution. The analysis revealed that shallow water sloshing described by the NSW equations are governed by three parameters: an amplitude parameter, Λ, defining the ratio of base motion amplitude to tank length, a frequency parameter, β, defining the ratio between the forcing frequency and shallow water frequency, and a friction parameter, γ, describing the effect of bottom friction. The purpose of this Part II is to describe experiments carried out in the Civil Engineering Laboratory at the Technical University of Denmark and to compare the findings with the numerical results from Part I.

*Corresponding author
Email address: jkr@byg.dtu.dk (J. Krabbenhøft)

Sloshing experiments in rectangular container with shallow water have been carried out by several researchers. Verhagen and Wijngaarden [2] and Armenio et. al [3] performed shallow water sloshing experiments in rectangular containers exposed to roll motions. An experimental study of horizontally oscillated containers, the focus of the present study, was performed by Reed et. al. [4] who concluded that bores or moving hydraulic shocks were formed and that the system exhibited a hardening type behavior. In the work by Reed et. al., which was primarily experimental, the authors compared a single experimental frequency response curve for a depth-length ratio of $h/L = 0.05$ and a base motion amplitude-length ratio of A/L=0.03 to a numerical simulation, showing promising results. In this study both the base amplitude as well as the depth ratio were expanded to $h/L = A/L = 0.1$ and compared to solutions of the NSW equations.

As mentioned earlier, and derived in detail in Part I of this paper, the general problem of shallow water sloshing with bottom friction is fully described by three dimensionless parameters. In the case where friction is neglected (and it was shown that this is a reasonable assumption), only two parameters are necessary. Finally, in the resonant case, $\beta \simeq 1$, a single parameter, namely the amplitude parameter Λ, remains. This effectively means that the problem must be analyzed for variable Λ and β. In the NSW equations the depth enters purely as a scaling parameter and thus has no effect on the qualitative behavior of the solution. This fact is very convenient since it simplifies the problem considerably, but entices one to pose the question: for which h/L values will the theory represent the actual physics? Moreover, for which combinations of Λ and β will the theory be adequate? These questions are the major motivation of the current work and is imperative when to the use the NSW equations for modeling sloshing, in the general case and in the context of tuned liquid dampers as is the focus of this work.

The paper is organized as follows. The theoretical results from the preceding Part I are first briefly summarized and the experimental program is then detailed. Next, results comparing experimental and numerical free surface profiles, time variation of water depth, sloshing force, and dissipated energy are presented. Finally, experimental and theoretical frequency-response curves are compared before conclusions are drawn.

2. Theoretical and numerical considerations

2.1. Governing fluid equations

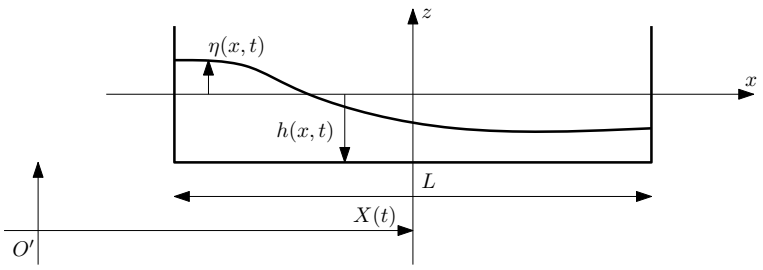

Figure 1: Sketch of rectangular TLD tank

The rigid rectangular container (figure 1), which has the length L, width W and still water depth h, is subjected to a horizontal base motion $X(t)$. It is convenient to refer the fluid motion to a moving coordinate system with origo attached to the middle of the tank at the free liquid

surface. Assuming an inviscid and incompressible fluid the equations describing the total water depth $H = H(x,t)$ and mean horizontal particle velocity $U = U(x,t)$ are the Nonlinear Shallow Water (NSW) equations:

$$\mathbf{U}_t + \mathbf{F}(\mathbf{U})_x = \mathbf{S}(\mathbf{U}, x, t) \tag{1}$$

with

$$\mathbf{U} = \begin{pmatrix} H \\ HU \end{pmatrix}, \mathbf{F} = \begin{pmatrix} HU \\ HU^2 + \frac{1}{2}gH^2 \end{pmatrix}, \mathbf{S} = \begin{pmatrix} 0 \\ -H\ddot{X}(t) \end{pmatrix} \tag{2}$$

It was shown in [1] that including bottom friction had little effect on the solution for smooth tanks and is left out here. The boundary conditions expressing solid end walls and initial conditions are

$$\begin{array}{lll} \text{I.C.} & : & H(x,0) = h,\ U(x,0) = 0 \\ \text{B.C.} & : & U(-L/2,t) = U(L/2,t) = 0 \end{array} \tag{3}$$

2.2. Base shear force due to liquid motion

Considering hydrostatic pressure and neglecting vertical acceleration effects as done in the derivation of the NSW equations the pressure can be expressed as

$$p(z) = \rho g(\eta - z) \tag{4}$$

The base shear force of the tank due to liquid motion is found as the difference of the integrated the pressure on either sides of tank, i.e.

$$F_S(t) = \tfrac{1}{2}\rho g(H_R^2 - H_L^2) \tag{5}$$

Here the friction of the side wall and bottom have been neglected.

2.3. Governing parameters

It was shown in the companion paper that the solution of the equations (2)-(3), for a harmonic base motion $X(t) = A\cos(\Omega t)$, is alone governed by the two dimensionless parameters

$$\beta = \frac{\Omega}{\omega_w} \qquad \Lambda = \pi\frac{A}{L} \tag{6}$$

with the linear shallow water frequency given by

$$\omega_w = k\sqrt{gh}, \qquad k = \pi/L \tag{7}$$

2.4. Numerical simulation method

The nonlinear inhomogeneous set of hyperbolic PDE's (2)-(3) are solved using a Finite Volume scheme described in detail in [1]. The computational domain $\Omega \in [-L/2, L/2]$ is partitioned into $N = 256$ non overlapping cells $\Omega = \bigcup_{i=1}^{256}$ where the solution is assumed constant in each cell. The solution is updated using a ones-step Finite Volume scheme

$$\mathbf{U}_i^{n+1} = \mathbf{U}_i^n - \frac{\Delta t}{\Delta x_i}[\mathbf{F}_{i+\frac{1}{2}} - \mathbf{F}_{i-\frac{1}{2}}] + \Delta t\mathbf{S}_i \tag{8}$$

where the numerical fluxes $F_{i\pm\frac{1}{2}}$ are evaluated using a Rusanov flux. As a time stepping restriction we use

$$\Delta t = 0.9\frac{\Delta x}{S^n_{\max}} \tag{9}$$

where the maximum wave speed in the computational domain is found suing the simple approximation

$$S^n_{\max} = \max_i\{|U^n_i| + \sqrt{gH^n_i}\} \tag{10}$$

3. Experimental setup

3.1. Experimental setup and apparatus

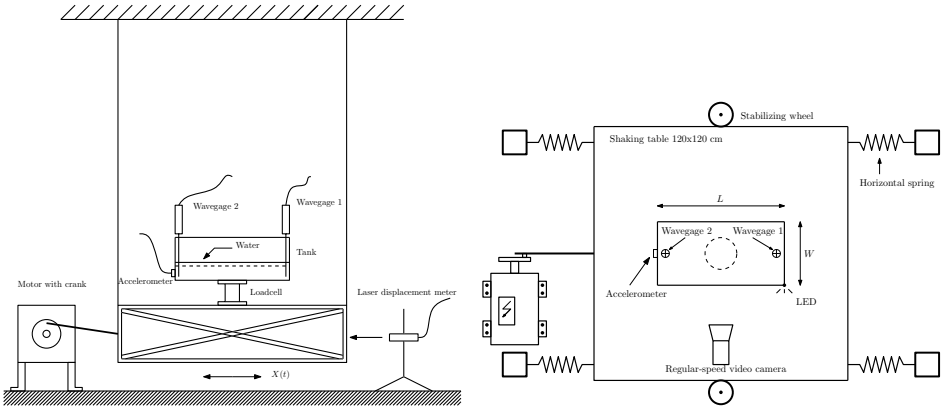

(a) Side view (b) Top view

Figure 2: Experimental setup viewed from the side and top.

A simple shaking table has been constructed in order to conduct an intense measurement campaign. A sketch of the shaking table in Figure 2(b) shows the construction principle of the test setup. A spacious steel frame, with a horizontal ground area of 120×120 cm covered with a 2 cm plywood plate, is suspended by four 300 cm steel cables. To ensure a uniaxial motion the steel cables have been installed with a slight inclination. Furthermore, guiding wheels have been mounted on the sides of the shaking table. Also, four horizontal springs laterally mounted between each corner of the shaking table and four vertical steel consoles ensure a stable motion. The test setup can be used both for simulating a flexible 1 degree of freedom system and for performing controlled sinusoidal base motion, the latter being of interest in the current context. A controlled base motion is generated by connecting a 120 cm long connector rod between the steel frame and motor shaft, i.e. a so-called crank mechanism is used. The motor used to drive the crank mechanism is a Lenze 9.2 kW servo controlled AC motor with a gearing of 1:23 securing a very high moment capacity, and with a maximum available frequency of 2.0 Hz. The excitation amplitude is varied by adjusting the connection eccentricity at the motor shaft, and the frequency varied by adjusting the rotational speed of the motor. In Figure 4 a typical measured displacement and acceleration time series is shown together with a best fit sine function, indicating a close to perfect sinusoidal signal. A rectangular tank with inner length

L = 590 mm, inner width W = 335 mm and a height of 300 mm, made of 10 mm acrylic plates, is used in all the experiments. An acrylic lid is fixed to the tank top where two wave gages made of steel wire are attached. Each wave gage is located 5 mm from the tank walls. The acrylic tank is placed on a load cell of type AMTI MC3-6-500 capable of measuring three force and three moment components. The horizonal base motion of the tank $X(t)$ is measured using a Laser Displacement Transducer (LDT) of type WayCON LAS-T-250A and the horizontal acceleration is measured using a variable capacitance accelerometer from Brüel and Kjær of the type B&K 4575 with a frequency range 0-300 Hz and 1000 mV/g sensitivity. All quantities are recorded using National Instruments hardware.

3.2. Presented variables and data treatment

Several dimensionless parameters are defined for presentation of the results. The base shear force measured by the force gauge in the x-direction, F_x, can be separated into three components: The inertial force due to the mass of the tank, wave gauges etc, F_{T}, the inertial force of the water treated as frozen liquid, F_{W}, and the dynamic force from the hydrodynamic pressure, F_{D}:

$$F_x(t) = F_{\mathrm{T}}(t) + F_{\mathrm{W}}(t) + F_{\mathrm{D}}(t) \tag{11}$$

We define the sloshing force as the sum of the inertial force of the "frozen" water and the hydrodynamic force, i.e.

$$F_S(t) = F_{\mathrm{W}}(t) + F_{\mathrm{D}}(t) \tag{12}$$

Combining (11) and (12) the sloshing force is evaluated as

$$F_S(t) = F_x(t) - F_{\mathrm{T}}(t) \tag{13}$$

Figure 3: Photographs of experimental setup.

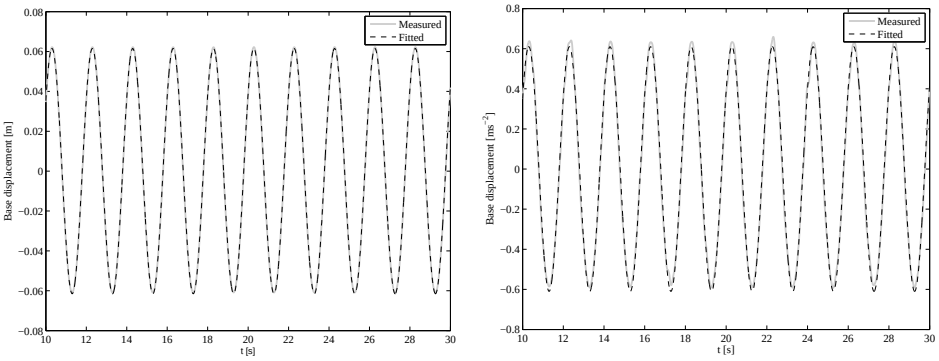

(a) Base motion displacement $X(t)$ (b) Base motion acceleration $\ddot{X}(t)$

Figure 4: Measured and fitted displacement and acceleration signals. The target amplitude and frequency are $A = 60$ mm and $\Omega = \pi$ rad/s, respectively.

The sloshing force is non-dimenzionalized using the maximum inertial force of the "frozen" liquid

$$F'_S(t) = \frac{F_S(t)}{m_w A\Omega^2} \tag{14}$$

where $m_w = hL\rho$. A TLD system subjected to a harmonic base motion defined by $X(t) = A\cos(\Omega t)$ will return a sloshing $F_S(t)$ which will produce an amount of mechanical work per cycle, on the base, given by

$$\Delta E = \int_t^{t+\frac{2\pi}{\Omega}} F_S(t)\mathrm{d}X(t) \tag{15}$$

Having two measured time series $F_S(t)$ and $X(t)$ it is straightforward to evaluate the latter integral in (15) using numerical integration. It is important to stress that the energy computed by (15) is not the energy dissipated *in* the fluid but the energy dissipated *by* the sloshing force. In the following we refer to (15) as the dissipated energy and put it on dimensionless form using the following relation

$$\Delta E' = \frac{\Delta E}{\frac{1}{2}m_w(\Omega A)^2} \tag{16}$$

i.e. the energy pr. cycle is divided by the mechanical energy of the "frozen" water. Finally, a wave gauge is located 5 mm from the left tank wall, Figure 2(b), to record the variation of the total water depth. The dimensionless water depth at the left wave gage is defined by

$$H' = \frac{H}{h} \tag{17}$$

The wave forms of the time histories vary significantly as either the excitation frequency β or the base amplitude A/L varies. For low base amplitudes and excitation frequencies below resonance the time histories of H and F_S are close to sinusoidal. Near resonance the time histories become non-sinusoidal and show traces of higher harmonic response due to the nonlinearity of the liquid motion. In Figure 5 a general harmonic signal y is shown, representing either H or F_S, with the excitation period indicated at the top. Based on the measured time series the local maximum and

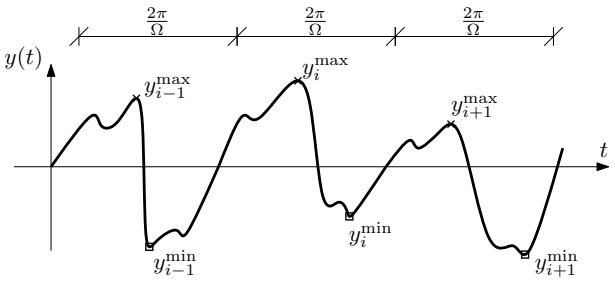

Figure 5: Definition of maximum and minimum values

minimum values inside equidistant time windows, defined by the forcing period, are found and the maximum value is defined as the mean value of N recorded local maximum values:

$$y^{\max} = \frac{1}{N} \sum_{i=1}^{N} y_i^{\max} \tag{18}$$

An equivalent definition applies to the minimum values.

3.3. Measurement campaign

The complete measurement campaign is given in Table 1. A total of 25 different $(h/L, A/L)$-configurations are tested, i.e. five different water depths and five different base motion amplitudes. For each combination of A/L and h/L we perform around 50 runs with the frequency parameter β varied between 0.7 to 1.5-1.9, depending on the amplitude of the base motion, in steps of 0.02. The experiments are performed by starting the motor with $\beta = 0.7$ and waiting until the liquid motion has reached a steady state which typically takes around 1-3 minutes. The data acquisition is started with a sampling frequency of 256 Hz and at the same instance a NI analog output module triggers a LED thereby synchronizing video recordings with the measured data. After 120 seconds the data is saved to a file and a new file is created while the base motion frequency is incremented with $\Delta\beta = 0.02$ over a 10 second period. This procedure is repeated until the base motion frequency has reached the final β value between 1.5-1.9. The raw data signals are processed by applying a low pass filter with a cut-off frequency defined by $\omega_c = 10\omega_w$,

File id	h	h/L	ω_w	f_w
[-]	[mm]	[-]	[rad/s]	[Hz]
h20a05 - h20a60	20	0.034	2.360	0.376
h30a05 - h30a60	30	0.051	2.890	0.460
h40a05 - h40a60	40	0.067	3.337	0.531
h50a05 - h50a60	50	0.085	3.731	0.594
h60a05 - h60a60	60	0.102	4.087	0.651

Table 1: Measurement campaign

A [mm]	5	10	20	40	60
$A/L[-]$	0.009	0.017	0.034	0.068	0.102

Table 2: Base motion amplitude A and amplitude parameter Λ/π

i.e. we include the first ten harmonics of the linear sloshing frequency in the analysis. The filtering is performed using a zero-phase forward and reverse technique assuring a precise zero phase distortion [5].

4. Numerical and experimental results

4.1. Free surface profiles – qualitatively analysis

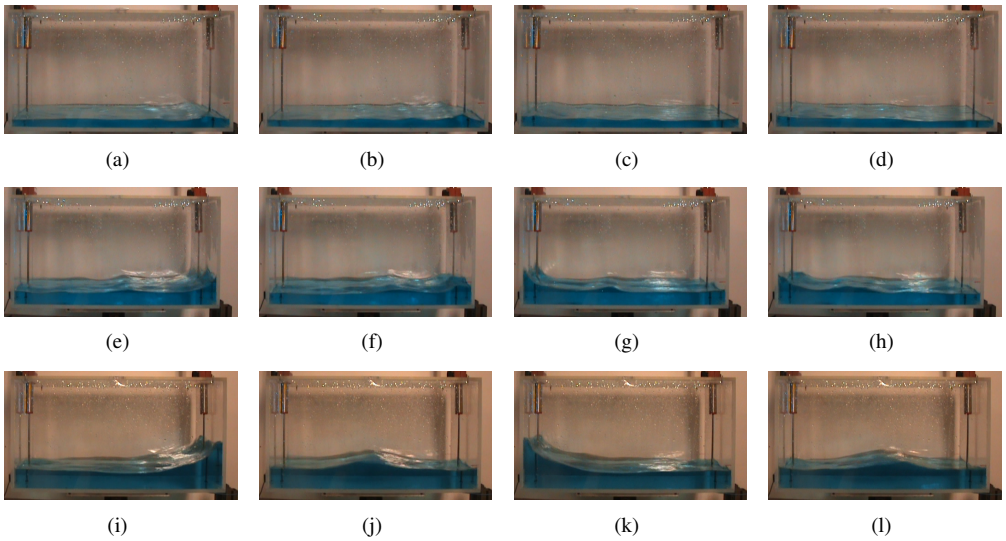

Figure 6: Surface profiles for fixed forcing frequency $\beta = 1.0$ and amplitude $A = 5$ mm corresponding to $A/L = 0.009$. Three different water depths are shown: (a)-(d) $h = 20$mm or $h/L = 0.034$, (e)-(h) $h = 40$mm or $h/L = 0.067$, (i)-(l) $h = 60$mm or $h/L = 0.10$. In the first photo (i.e. (a), (e) and (i)) the surface profile has a maximum value at the right tank wall and the waves then travel from right to left

From the extensive measurement campaign a very large amount of data was accumulated and thus we are forced to restrict the presentation to only a few specific tests. These are chosen to highlight important characteristic flow features.

For all the the test cases we used a regular-speed video camera (25 frames per second corresponding to $\Delta t = 1/25$=0.04 s) to record the water surface. Afterwards the recorded video was processed by extracting and editing relevant frames.

In figure 6-8 the effect of varying the amplitude ratio A/L and depth ratio h/L around the resonance condition $\beta = 1$, is illustrated. For a low amplitude ratio of $A/L = 0.009$, Figure 6, the water surface remains continuous, or close to continuous, for all of the three shown water depths. It is not too clear in the figure but actually an *increasing* number of higher harmonics is

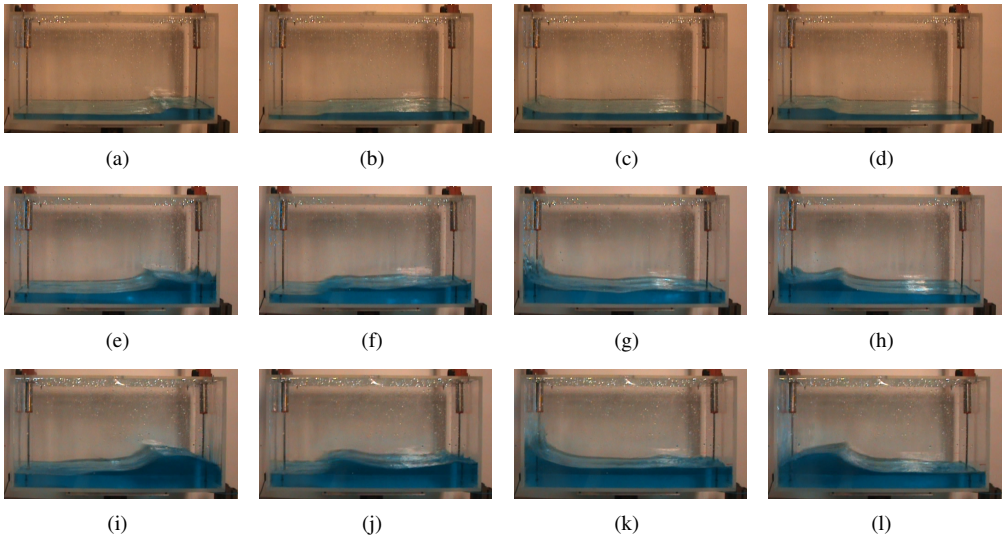

Figure 7: Surface profiles for fixed forcing frequency $\beta = 1.0$ and amplitude $A = 20$ mm corresponding to $A/L = 0.034$ =. Three different water depths are shown: (a)-(d) $h = 20$mm or $h/L = 0.034$, (e)-(h) $h = 40$mm or $h/L = 0.067$, (i)-(l) $h = 60$mm or $h/L = 0.10$. In the first picture (i.e. (a), (e) and (i)) the surface profile has a maximum value at the right tank wall and the waves then travel from right to left

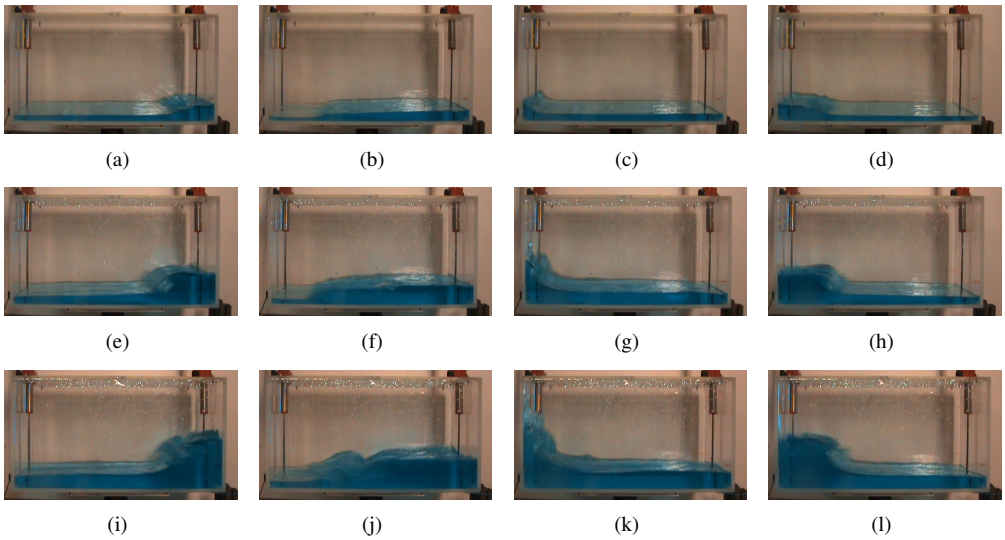

Figure 8: Surface profiles for fixed forcing frequency $\beta = 1.0$ and amplitude $A = 60$ mm corresponding to $A/L = 0.103$. Three different water depths are shown: (a)-(d) $h = 20$mm or $h/L = 0.034$, (e)-(h) $h = 40$mm or $h/L = 0.067$, (i)-(l) $h = 60$mm or $h/L = 0.10$. In the first picture (i.e. (a), (e) and (i)) the surface profile has a maximum value at the right tank wall and the waves then travel from right to left

observed in the surface profile for *decreasing* water depths. Clearly the non-dispersive shallow water theory based on the limiting value of $h/L \to 0$ will result in a single dominant wave traveling back and forth and is thus intuitively in contradiction with the experimental observations. However, dispersive models do in fact show an increasing number of higher harmonics in the solution for $h/L \to 0$ as reported in the analytical study by Ockendon et al. [6] and also address by Faltinsen et al. in [7]. For larger depth ratios the higher harmonics seem to disappear and for $h/L = 0.1$ a single solitary wave propagates back and forth. Increasing the amplitude ratio from 0.009 to 0.033, Figure 7, alters the surface profile significantly. Now the surface profile, for all water depths, develops a clear discontinuity with a front, or bore, traveling back and forth in the tank. As the front hits the tank wall a sheet film of water is driven up along the wall. This effect becomes more dominant for higher water depths and in Figure 7(k) the effect is clearly seen. Notice also the depression in the surface profiles in Figure 7, which is a consequence of water being displaced as the thin sheet film of water initially driven up later is accelerated downward as a falling jet [8]. For a further increase in the amplitude ratio to $A/L = 0.1$ the discontinuity in the surface profile appears sharper and an almost ideal bore propagates in the tank. As the depth increases, plunging breakers start appearing, Figure 8(e) or (i), which for the deepest water levels results in a depression in the surface profile close to the middle of the tank, Figure 6(j).

4.2. Time variation of water depth - end wall wave profiles

The dimensionless water depth at the left wall H'_L as function of time is presented in the following section. The experimental data is shown as a black solid line and the numerical simulations with a grey dashed line. For fixed β-values and variable water depths, i.e. column-wise, the results from the numerical simulations are identical since the water depth only enters the NSW equations as a scaling parameter. In this way the figures can be used to identify the valid working range for the NSW equations.

In Figure 9 the end wall wave profiles are shown for the lowest base motion amplitude of $A = 5$ mm corresponding to $A/L = 0.009$. The experimental end wall wave profiles for the off resonance situations $\beta = 0.8$ and $\beta = 1.2$ are seen to be quite similar for all three water depths and also the NSW equations gives a very good fit, whereas the resonance situation being the most relevant shows rather different wave profiles for variable water depths. As discussed earlier, the effect of increasing higher harmonics for lower water depths is clearly illustrated. For the lowest water depth $h = 20$ mm, corresponding to $h/L = 0.034$, the numerical solution captures quite well the overall trend of the end wall wave profile but because of its nondispersive character the higher harmonics are not represented in the solution. Increasing the water depth worsens the numerical solution and for $h = 60$ mm the numerical simulation underestimates the maximum end wall wave height but also far from captures the shape of the profile corresponding to the end wall water depth variation.

Increasing the base motion amplitude to $A = 20$ mm or A/L=0.034, Figure 10, dramatically improves the agreement between the experimental data and numerical simulations below and at resonance. The improvement is not too surprising bearing in mind the in Figure 7 showing the development of propagating bores in the tank. The agreement between the experimental data and simulation is again best for $h = 20$ mm and deteriorates for deeper water depths. In the end wall wave profile, for $h = 20$ mm and $\beta = 1.0$, the presence of the higher harmonics can be seen but the phases of the higher harmonics are organized in such a way that a saw-tooth shaped profile is formed. For deeper water depths, the higher harmonics again become more visible in the end wall wave profile. Notice the wave profile for $\beta = 1.2$ and $h = 40$ mm in Figure 10(f) showing a pattern with close to 50% higher water depths at every second period which is clearly

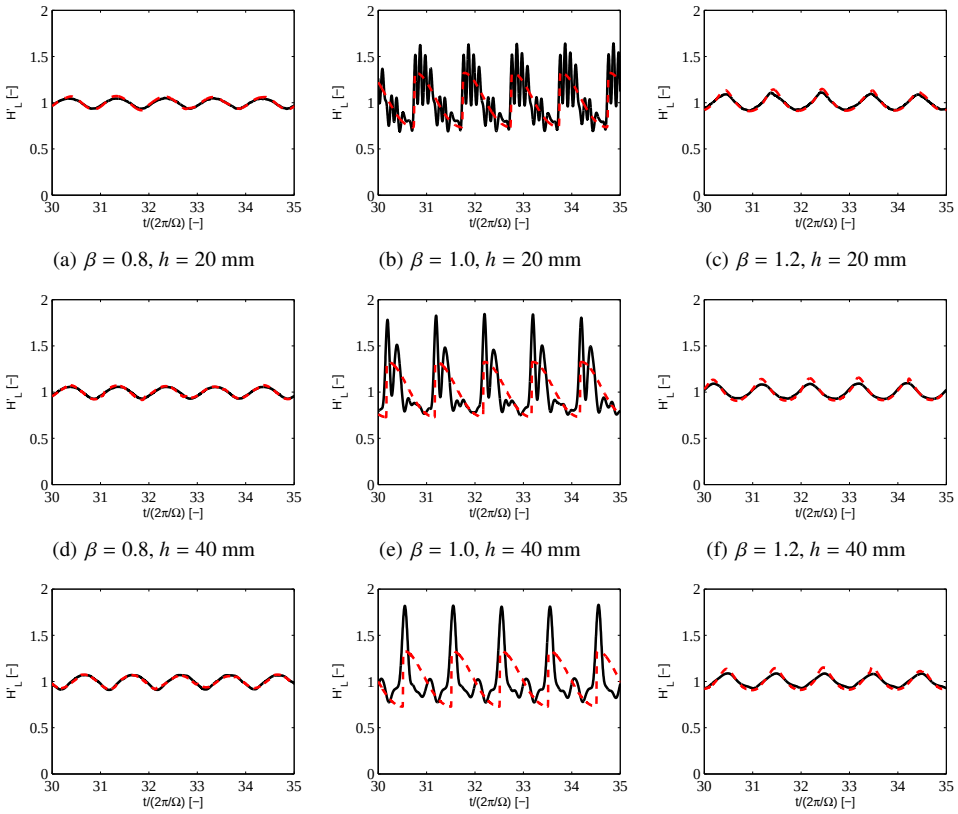

(a) $\beta = 0.8$, $h = 20$ mm (b) $\beta = 1.0$, $h = 20$ mm (c) $\beta = 1.2$, $h = 20$ mm

(d) $\beta = 0.8$, $h = 40$ mm (e) $\beta = 1.0$, $h = 40$ mm (f) $\beta = 1.2$, $h = 40$ mm

(g) $\beta = 0.8$, $h = 60$ mm (h) $\beta = 1.0$, $h = 60$ mm (i) $\beta = 1.2$, $h = 60$ mm

Figure 9: Time variation of total water depth at resonance and off-resonance with base motion amplitude $A = 5$ mm corresponding to $A/L = 0.009$. Experiments: ——, simulations: - - -.

not captured by the NSW equations. In general for $h > 40$ mm and $\beta = 1.2$ the end wall wave profile is captured rather poorly by the NSW equations.

When the base motion amplitude is further increased to $A = 60$ mm, figure 11, the characteristic saw-tooth shaped wave profiles are seen again. From the profiles in 11 the numerical data is seen to underestimate the wave height at the end wall quite significantly. It should be noticed that for large water depths and base motion amplitude a significant sheet of water is driven vertically up the end wall as the bore impacts, which affects the wave gauge placed 5 mm from the end wall.

4.3. Time variation of sloshing force and hysteresis loops

The ability of the numerical method to predict the free surface is relevant in connection with e.g. establishing a tank geometry with sufficient height to avoid a low ceiling blocking the water flow. However, the ability to predict the sloshing forces as well as the phase between the base motion and sloshing force is of far greater importance with respect to the design of e.g. tuned liquid dampers. The numerical method should obviously be able to predict the magnitude of

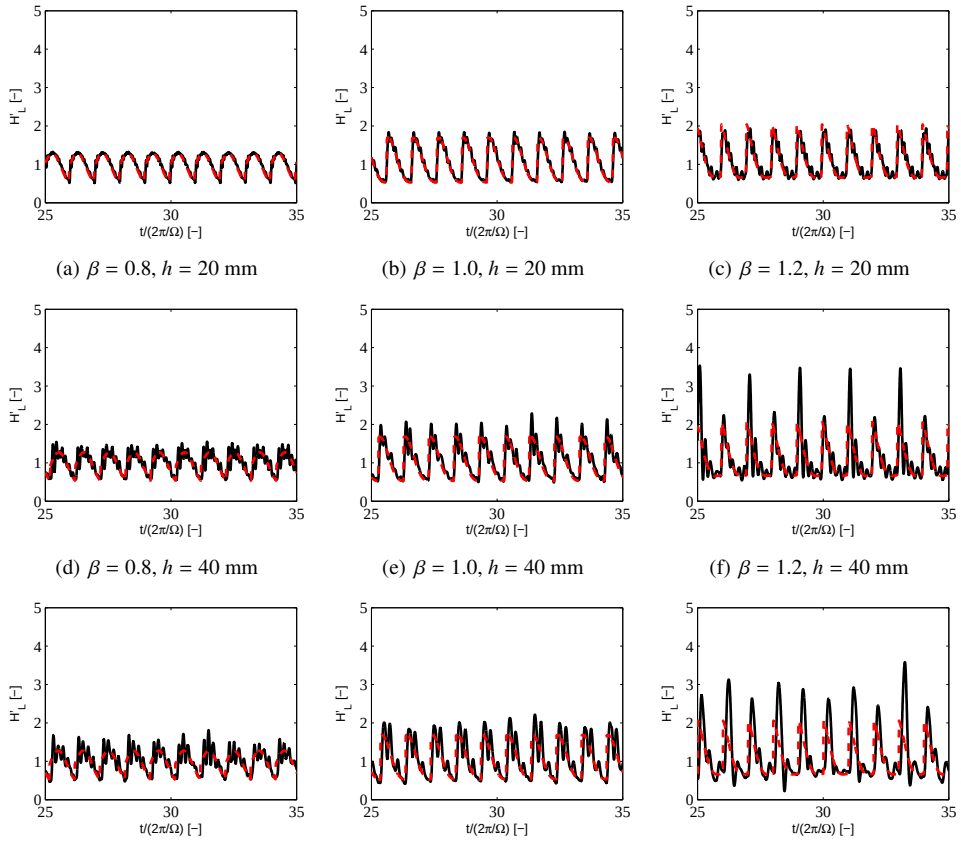

(a) $\beta = 0.8$, $h = 20$ mm (b) $\beta = 1.0$, $h = 20$ mm (c) $\beta = 1.2$, $h = 20$ mm

(d) $\beta = 0.8$, $h = 40$ mm (e) $\beta = 1.0$, $h = 40$ mm (f) $\beta = 1.2$, $h = 40$ mm

(g) $\beta = 0.8$, $h = 60$ mm (h) $\beta = 1.0$, $h = 60$ mm (i) $\beta = 1.2$, $h = 60$ mm

Figure 10: Time variation of total water depth at resonance and off-resonance with base motion amplitude $A = 20$ mm corresponding to $A/L = 0.034$. Experiments: ——, simulations: - - -.

the sloshing force, and since the amount of energy dissipated by the sloshing force is effectively evaluated as the area enclosed by the force-displacement hysteresis loops, capturing the phase between the sloshing force and base motion is equally important from a TLD-structure interaction point of view. As for the end wall wave profiles results for three different water depths and base amplitudes will be presented in the following. Slightly below resonance, $\beta = 0.9$, the numerical and experimental results are in general in good agreement, and for a fixed water depth of 40 mm hysteresis loops for three different base motion amplitudes are illustrated in Figure 12. Varying the water depth doesn't have a noticeable effect on the curves. The most interesting situation occurs at resonance and slightly above i.e. $\beta \geq 1$. For the resonance case, $\beta = 1$, and a low base amplitude of $A = 5$ mm, Figure 13, the sloshing force follows the same trend as the end wall wave profiles with increased oscillations for decreasing water depth, which is not surprising considering that the pressure in the shallow water limit is hydrostatic and thereby proportional to the surface elevation. For $h = 20$ mm the numerical method captures the overall trend of the sloshing force and the hysteresis loop is also captured even better. Notice in the hysteresis loop

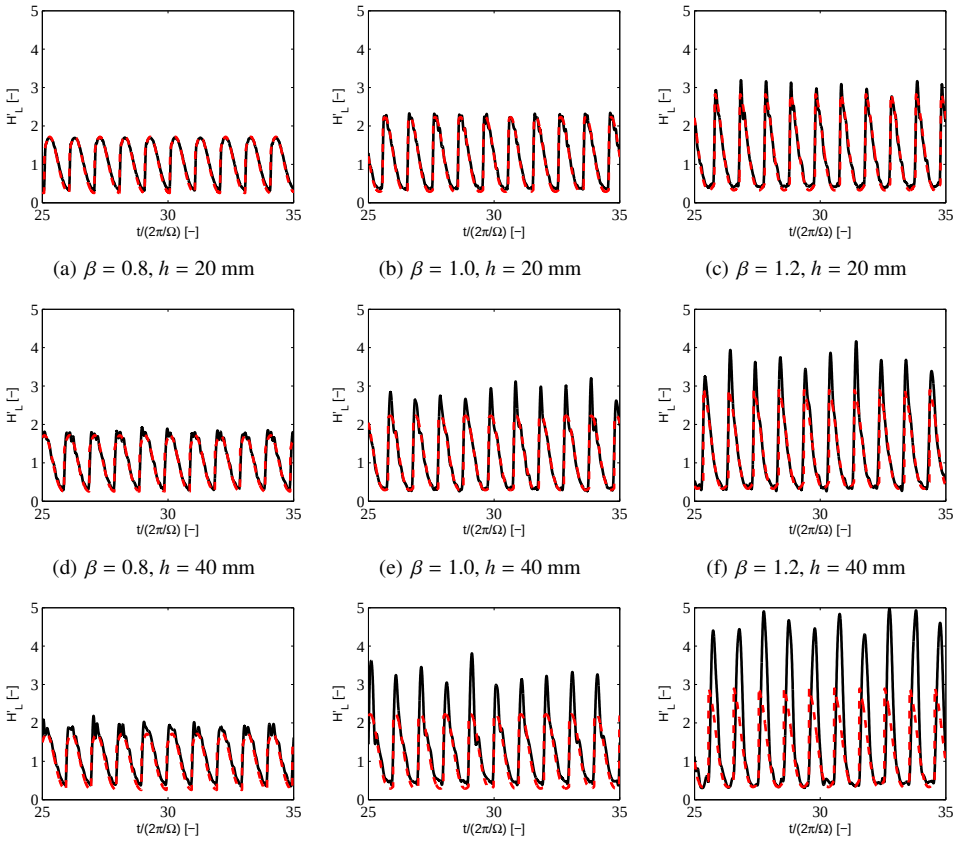

(a) $\beta = 0.8$, $h = 20$ mm (b) $\beta = 1.0$, $h = 20$ mm (c) $\beta = 1.2$, $h = 20$ mm

(d) $\beta = 0.8$, $h = 40$ mm (e) $\beta = 1.0$, $h = 40$ mm (f) $\beta = 1.2$, $h = 40$ mm

(g) $\beta = 0.8$, $h = 60$ mm (h) $\beta = 1.0$, $h = 60$ mm (i) $\beta = 1.2$, $h = 60$ mm

Figure 11: Time variation of total water depth at resonance and off-resonance with base motion amplitude $A = 60$ mm corresponding to $A/L = 0.103$. Experiments: ——, simulations: - - -.

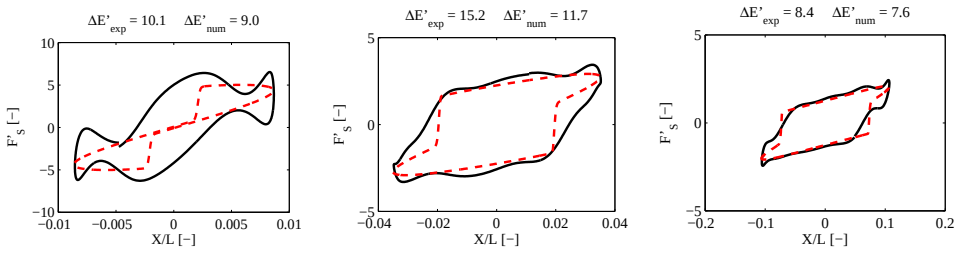

(a) $A = 5$mm (b) $A = 20$mm (c) $A = 60$ mm

Figure 12: Hysteresis loops for fixed values of $\beta = 0.9$, $h = 40$ mm and three different base motion amplitudes.Experiments: ——, simulations: - - -.

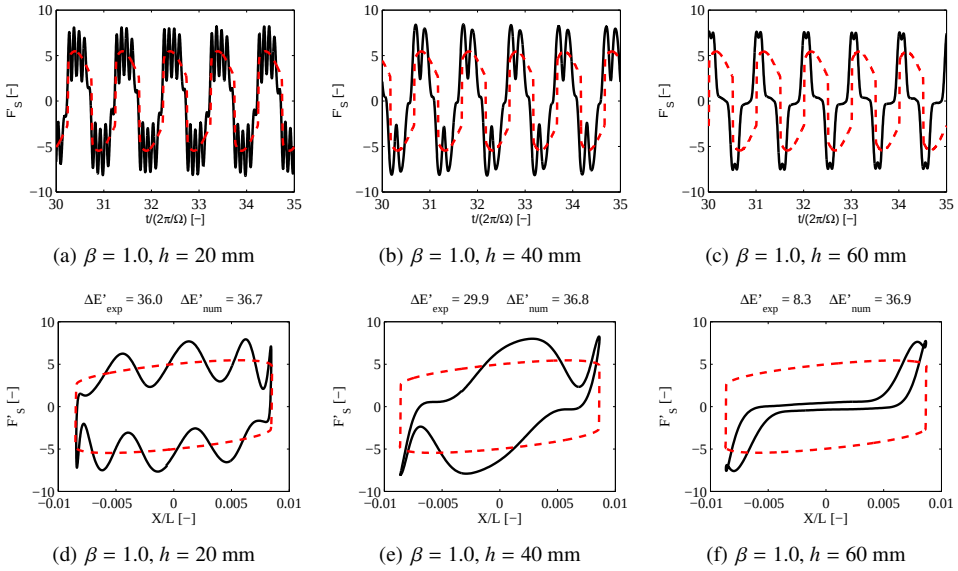

(a) $\beta = 1.0$, $h = 20$ mm (b) $\beta = 1.0$, $h = 40$ mm (c) $\beta = 1.0$, $h = 60$ mm

(d) $\beta = 1.0$, $h = 20$ mm (e) $\beta = 1.0$, $h = 40$ mm (f) $\beta = 1.0$, $h = 60$ mm

Figure 13: Time variation of sloshing force F'_S and hysteresis loops at resonance with base motion amplitude $A = 5$ mm corresponding to $A/L = 0.009$. Experiments: ——, simulations: – – –.

that the higher harmonics tend to cancel out when integrating the area. Indeed, for the shown curve the difference between the two areas is less than 2%. This result, which agrees with findings by Reed et al. [4], must be a consequence of fact that the sloshing forces generated by the higher wave harmonics tend to be in phase with the base displacement or base acceleration, thereby providing no contribution to the energy dissipation which by definition requires a force component in phase with the base velocity, (15). For $h = 40$ mm the NSW equations overestimate the dissipated energy by close to 20% and for $h = 60$ mm the energy is overestimated by more than a factor of four. For this case, the non-dispersive shallow water theory described by the NSW equations clearly becomes invalid and, based on the results in Figure 13, in seems reasonable to conclude that for water depths ratios $h/L > 0.05$ and base amplitudes $A/L < 0.01$ the NSW equations are not valid for the resonant case. To capture the liquid behavior more precisely one should include dispersion in the equations, using e.g. the classical Boussinesq approximation derived by Peregrine [9] and later used by several researchers for sloshing simulations, see e.g.[**?** 10, 11, 12].

Increasing the base amplitude to $A = 20$ mm, Figure 15, the sloshing force and hysteresis loops are captured almost perfectly near resonance, subfigures (a)-(f), and also relatively well above resonance, subfigures (g)-(l). For base amplitude of $A = 10$ mm the results are almost identical to those of Figure 15 and are not shown here. Again, it is noticed that in general an increased water depth deteriorates the agreement between the numerical and experimental results, and a water depth of 60 mm, corresponding to $h/L \simeq 0.1$, seems to be a fair suggestion for maximum depth ratio that can be accommodated by the NSW equations.

For a base amplitude of $A = 60$ mm, Figure 12, which must be regarded as a rather extreme condition, the NSW equations captures the sloshing force and hysteresis loops remarkably well. It must be emphasized that no empirical factors have been used to tune the governing equations or

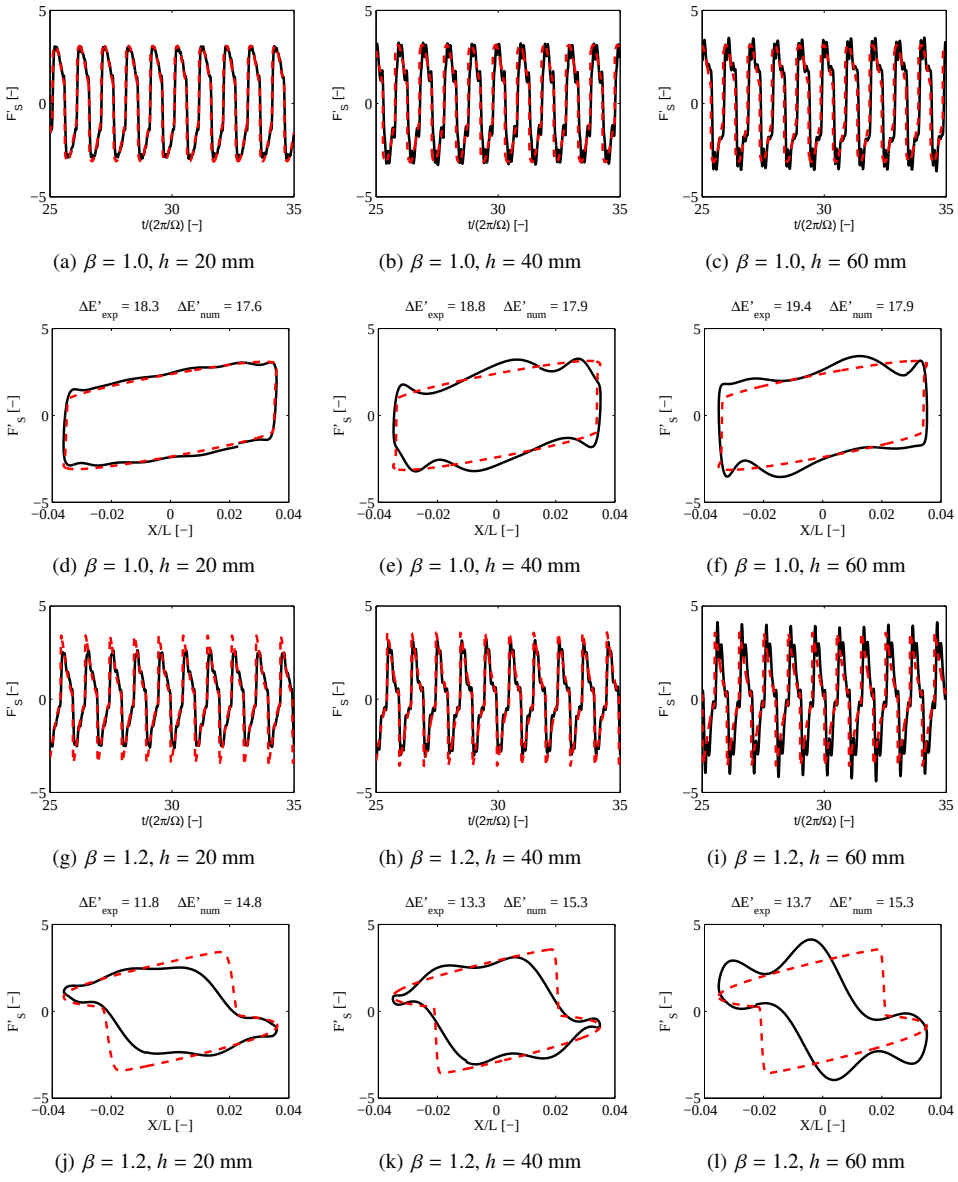

(a) $\beta = 1.0$, $h = 20$ mm (b) $\beta = 1.0$, $h = 40$ mm (c) $\beta = 1.0$, $h = 60$ mm

(d) $\beta = 1.0$, $h = 20$ mm (e) $\beta = 1.0$, $h = 40$ mm (f) $\beta = 1.0$, $h = 60$ mm

(g) $\beta = 1.2$, $h = 20$ mm (h) $\beta = 1.2$, $h = 40$ mm (i) $\beta = 1.2$, $h = 60$ mm

(j) $\beta = 1.2$, $h = 20$ mm (k) $\beta = 1.2$, $h = 40$ mm (l) $\beta = 1.2$, $h = 60$ mm

Figure 14: Time variation of sloshing force F'_S and hysteresis loops at resonance and off-resonance with base motion amplitude $A = 20$ mm corresponding to $A/L = 0.034$. Experiments: ——, simulations: - - -.

the numerical scheme. Considering the extreme complexity of the fluid pattern and the relatively simplicity of the NSW equations, the results must be regarded as very satisfactory. Again the depth ratio of $h/L \simeq 0.1$ seems to be a good choice for an upper limit.

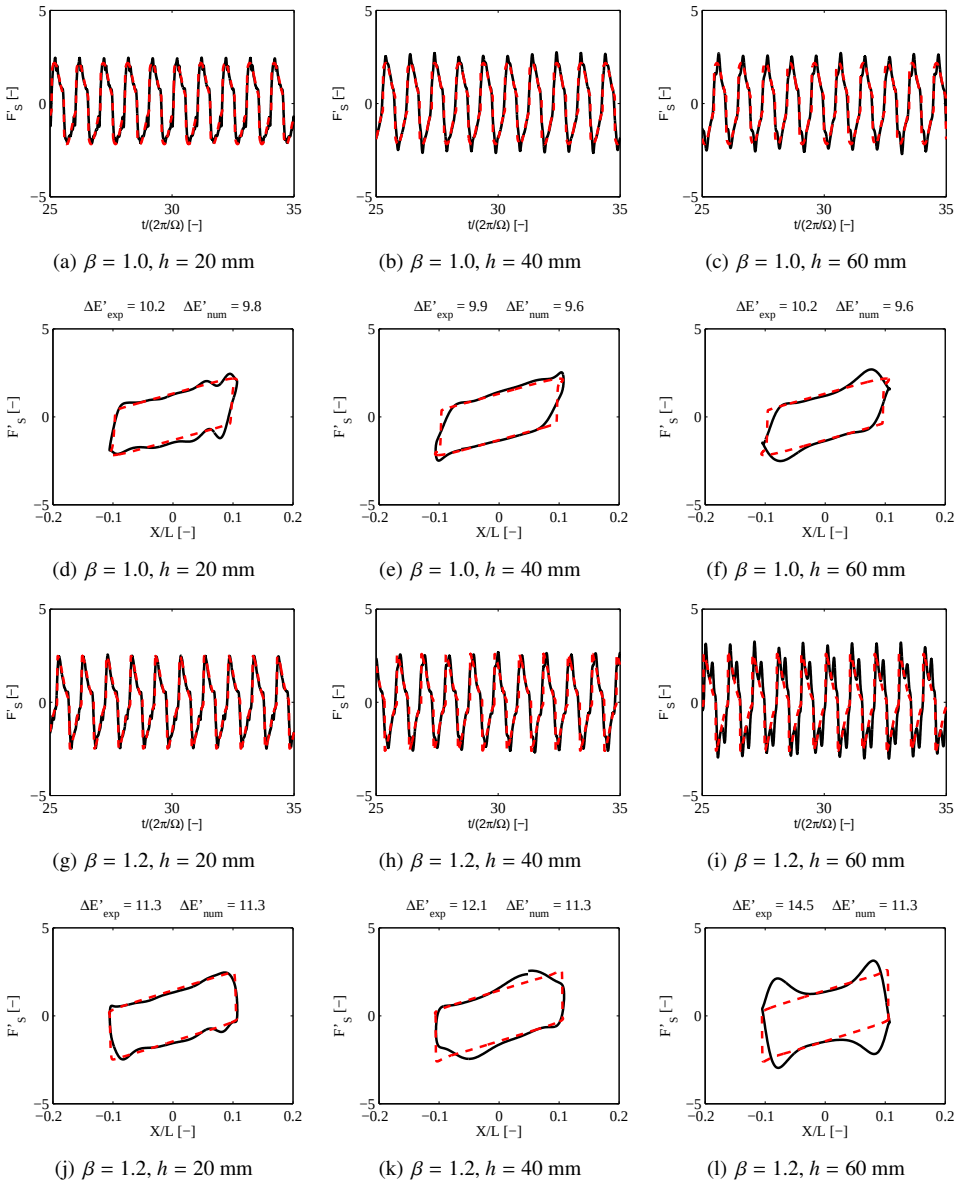

(a) $\beta = 1.0$, $h = 20$ mm (b) $\beta = 1.0$, $h = 40$ mm (c) $\beta = 1.0$, $h = 60$ mm

(d) $\beta = 1.0$, $h = 20$ mm (e) $\beta = 1.0$, $h = 40$ mm (f) $\beta = 1.0$, $h = 60$ mm

(g) $\beta = 1.2$, $h = 20$ mm (h) $\beta = 1.2$, $h = 40$ mm (i) $\beta = 1.2$, $h = 60$ mm

(j) $\beta = 1.2$, $h = 20$ mm (k) $\beta = 1.2$, $h = 40$ mm (l) $\beta = 1.2$, $h = 60$ mm

Figure 15: Time variation of sloshing force F'_S and hysteresis loops at resonance and off-resonance with base motion amplitude $A = 60$ mm corresponding to $A/L = 0.103$. Experiments: ——, simulations: - - -.

4.4. Frequency-response curves

The time histories presented previously, for a few discrete forcing frequencies, are supplemented in the following by frequency response curves for the three parameters: maximum and minimum total water depth at the left tank edge, maximum sloshing force and dissipated energy. The presented maximum and minimum total water depth and maximum sloshing force are com-

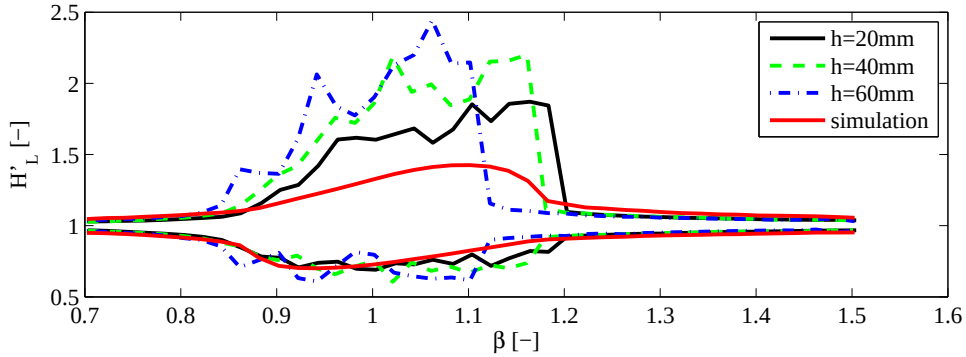

(a) A = 5 mm

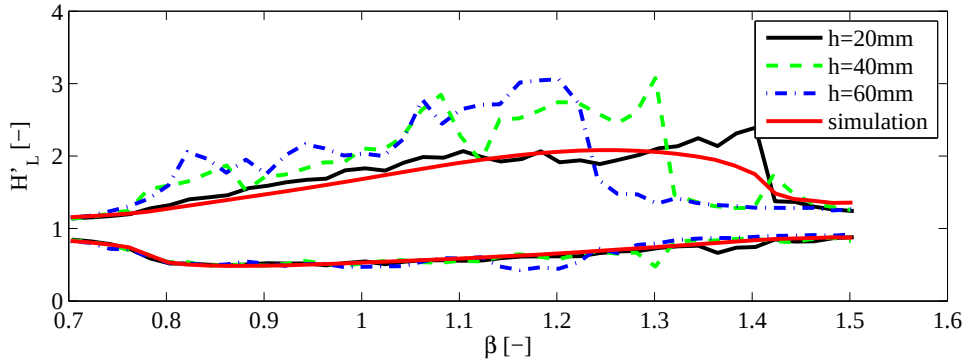

(b) A = 20 mm

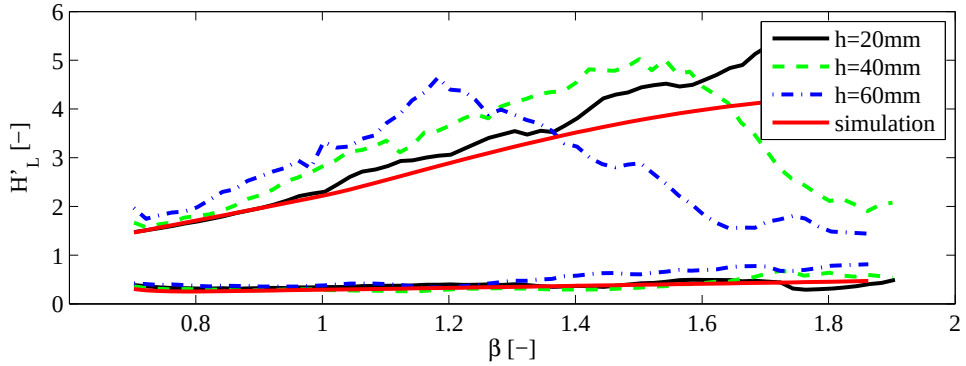

(c) A = 60 mm

Figure 16: Frequency response curves for maximum and minimum water depth at left wall.

puted according to (18) and the energy dissipation is computed as the average value of energy per cycle for a 60 second period. For each of the discussed parameters the frequency response curves are shown for three different water depths of h = 20,40 and 60 mm, and three different

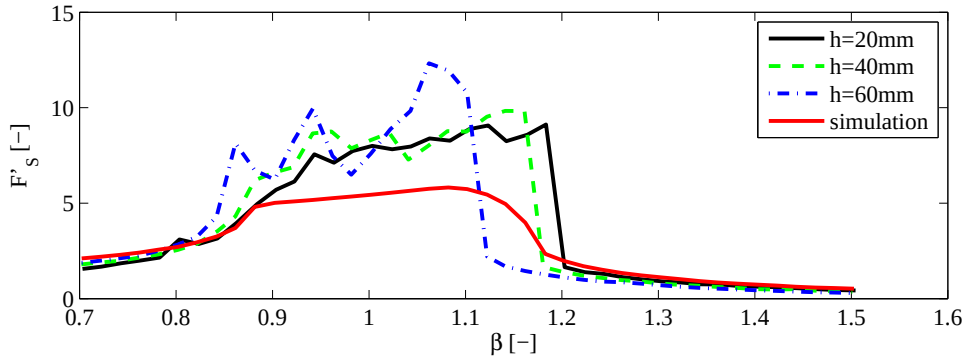

(a) A = 5 mm

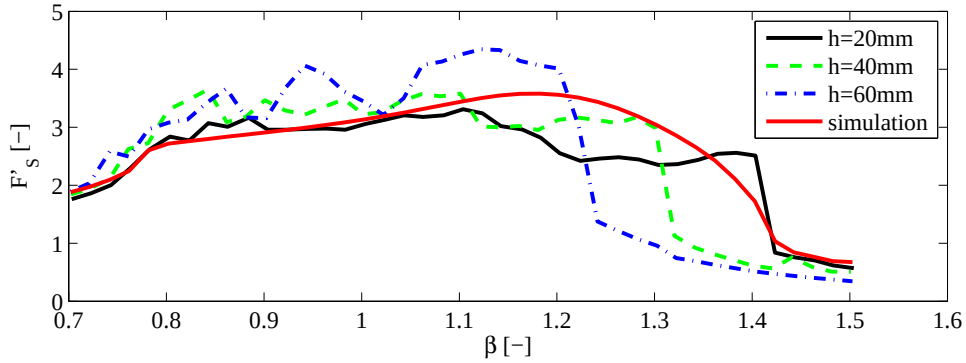

(b) A = 20 mm

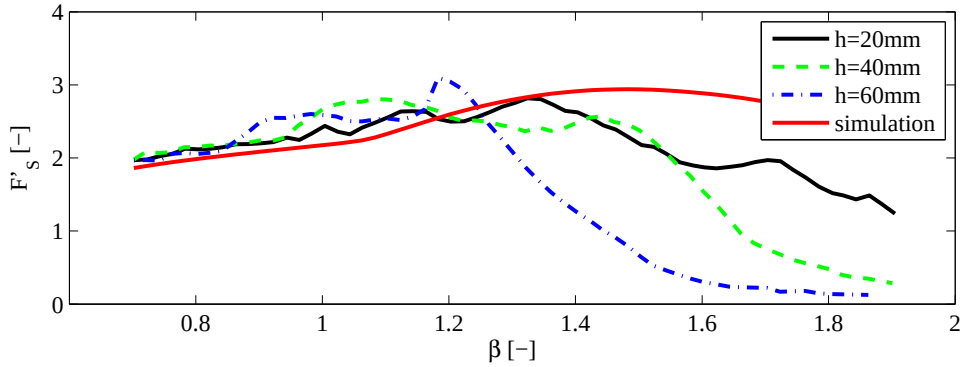

(c) A = 60 mm

Figure 17: Frequency response curves for maximum sloshing force.

base amplitudes A = 5, 20 and 60 mm, analogous to the results presented earlier.

The frequency response curves for maximum and minimum water depths are depicted in Figure 16. For each subfigure the experimental results are shown for the three different water depths

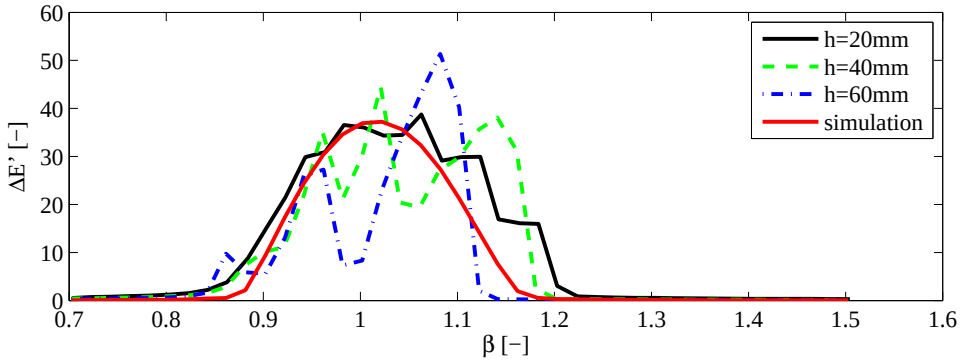

(a) A = 5 mm

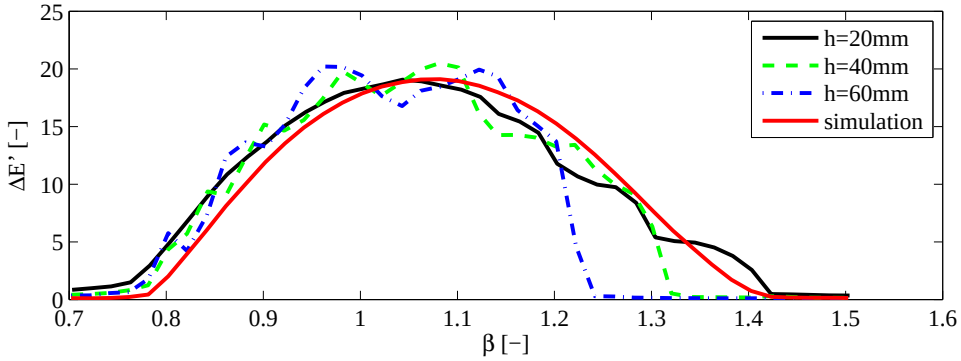

(b) A = 20 mm

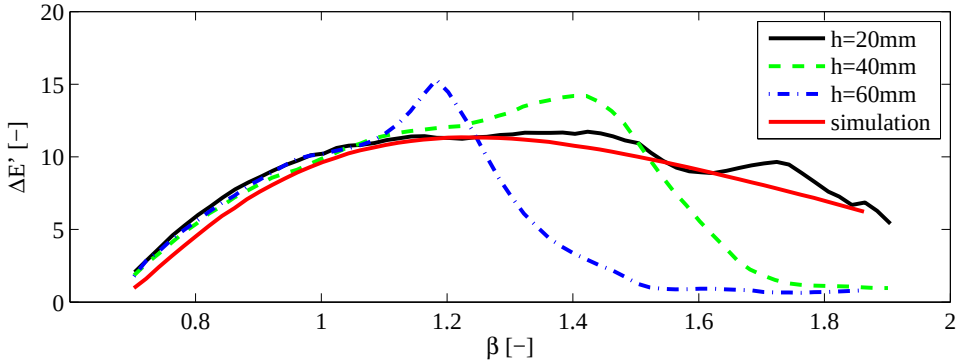

(c) A = 60 mm

Figure 18: Frequency response curves for dissipated energy pr. cycle.

as well as the numerical simulation, which as mentioned earlier is independent of the water depth. For the lowest base amplitude the numerical simulation, as expected from the previous time history analysis, gives a very poor fit. The amplitude is clearly underestimated and the

frequency response curve has a much smoother trend than the experimental curves which have a sharp drop as the frequency approaches a value clearly above the linear resonance value of $\beta = 1$. The frequency value at which the drop, or jump, depending on which side one views it, occurs is commonly called the jump frequency. Systems exhibiting jump frequencies higher than the linear natural frequency are of the so-called hardening type. It is interesting to note the effect of the water depth on the solution which shows a clear tendency of reducing the jump frequency. It is a well established result, see e.g. [13], that for a certain depth ratio of $h/L = 0.337$, know as the critical depth, the behavior changes from being a hardening type system to a softening type. So increasing the water depth further will result in the frequency response curve bending less to the right, becoming more symmetrical around $\beta = 1$, and at last bending left when exceeding the critical depth. Finally, it is seen that increasing the water depth in general leads to increased wave amplitudes. Increasing the base amplitude improves the performance of the NSW equations, which was also seen earlier, and for $h = 20$ mm and $A = 20$ mm the agreement between experiments and simulations is relatively good. However, notice that the error in the jump frequency worsens for this case. For a base amplitude of 60 mm the frequency response curves show an almost linear trend in the beginning, with the slope of the curves increasing for increasing water depths. The jump frequency is now no longer present and the curves show a more symmetric behavior, though with a maximum value at a frequency drastically above the linear sloshing frequency. The fact that the presence of a clear jump frequency cease to exist should most likely be found in the fact that the internal fluid damping increases for increasing base amplitudes, thereby smoothing the frequency response curves.

In Figure 17 the frequency response curves for the maximum sloshing force are presented. The curves show the same trend though with some clear differences. First of all, it seems that the effect of water depth on the experimental results are less distinct than for the maximum water depth for the frequency range $\beta < 1.1$. Secondly, the agreement between the numerical simulation and experiments is better, and especially in the frequency region $\beta < 1.1$ the agreement is quite good.

Finally, the frequency response curves for the energy dissipation are shown in figure 18. For $A = 5$ mm the frequency response curve is quite well reproduced by the numerical simulation for $h = 20$ mm, and reasonably well for $h = 40$ mm. For $h = 60$ mm the curve shows a very distinct drop near ? followed by a large peak near $\beta = 1$. For $A = 20$ mm and $\beta < 1.2$ the influence of the water depth on the results is limited and the frequency response curve is captured remarkably well by the numerical simulation. For $A = 60$ mm and the effect of the water depth becomes very apparent, with increasing agreement between simulation and experiments for decreasing water depth. Thus, for $h = 20$ mm energy dissipation is captured well in the entire range $0.7 < \beta < 1.9$. For increased water depth, the frequency range of acceptable agreement is narrowed down and for $h = 60$ mm the upper limit of the frequency range is approximately 1.1.

Comparing the frequency response curves of the three studied parameters it is clear that the amplitude of the curves are reduced for increased base amplitudes, which is naturally an effect of a rise in the internal fluid energy dissipation.

5. Concluding remarks

The liquid motion in a rectangular tank undergoing a horizontal harmonic base motions has been investigated both by experiment and by numerical analysis. Previous comparison studies by Reed et al. [4] between shallow water theory and experimental data consulted only a single base amplitude and depth ratio. In this study both the base amplitude as well as the depth ratio were

expanded to $h/L = A/L = 0.1$ and compared to solutions of the NSW equations. The following important novel conclusions can be drawn from the study

I The influence of the depth ratio h/L has a strong influence on the sloshing behavior in the region $0.3 < h/L < 0.1$. Thus, one need to exercise caution when applying the NSW equations in this region, and most certainly for $h/L > 0.1$.

II The valid working range for the NSW equations depends on the three parameters: β, h/L and A/L. For excitation frequencies in the range $0.7 < \beta < 1.1$, the energy dissipation $\Delta E'$ is captured remarkably well for $A/L > 0.03$. For $A/L < 0.03$ $\Delta E'$ is captured reasonably for $h/L < 0.05$. For $\beta > 1.1$ the energy dissipation is still captured well for low depth ratios and low amplitude ratios whereas for increased depths and amplitudes the upper limit of the valid frequency range is reduced. For the end wall wave profiles and sloshing force the same overall observations are made.

III For the parameter region $0.7 < \beta < 1.1$, $0.015 < A/L < 0.1$ and $0.03 < h/L < 0.1$ the dissipated energy ΔE is to a good approximation *independent* of the depth ratio h/L. This strongly indicates that the NSW equations can be used successfully for simulating tuned liquid dampers in this parameter region.

IV In the theoretical model the boundary layer is completely neglected indicating that this cannot be a major source of energy dissipation. For lower base amplitudes where hydraulic jumps are not formed the energy dissipation in the boundary layer may become important as suggested by e.g. Sun et al. [10].

V As the base amplitudes increase the strength of the hydraulic jump also increase. The energy dissipation across a moving hydraulic jump depends on the strength of the jump [14] which explains the reduced sloshing force F'_S and hence reduced $\Delta E'$ for increased base amplitudes.

The working range of the NSW equations has been established using forced base motion experiments. Instead of imposing the motion of tank it is more relevant from a practical point to analyze the coupled motion of the liquid and an external elastic structure. In future work this investigation will be undertaken in order to verify the presently estimated parameter region in connection with coupled tank-structure systems.

References

[1] J. Krabbenhoft, C. T. Georgakis, (submitted), Shallow water sloshing. part i. theoretical and numerical background, Engineering Structures.

[2] J. Verhagen, L. van Wijngaarden, Non-linear oscillations of fluid in container, Journal of Fluid Mechanics 22 (Part 4) (1965) 737–751.

[3] V. Armenio, M. L. Rocca, On the analysis of sloshing of water in rectangular containers: numerical study and experimental validation, Ocean Engineering 23 (8) (1996) 705–739.

[4] D. Reed, J. Yu, H. Yeh, S. Gardarsson, Investigation of tuned liquid dampers under large amplitude excitation, Journal of Engineering Mechanics - Proceedings of the ASCE 124 (4) (1998) 405–413.

[5] A. Oppenheim, R. Schafer, Discrete-Time Signal Processing, Prentice-Hall, 1989.

[6] Ockendon, Ockendon, Johnson, Resonant sloshing in shallow water, Journal of Fluid Mechanics 167 (1986) 465–479.

[7] Faltinsen, Timokha, Asymptotic modal approximation of nonlinear resonant sloshing in a rectangular tank with small fluid depth, Journal of Fluid Mechanics 470 (2002) 319–357.

[8] Bredmose, Brocchini, Peregrine, Thais, Experimental investigation and numerical modelling of steep forced water waves, Journal of Fluid Mechanics 490 (2003) 217–249.
[9] Peregrine, Long waves on a beach, Journal of Fluid Mechanics 27 (1967) 815–827.
[10] L. M. Sun, Y. Fujino, B. M. Pacheco, M. Isobe, Nonlinear waves and dynamic pressures in rectangular tuned liquid damper (tld). simulation and experimental verification, Doboku Gakkai Rombun-Hokokushu/Proceedings of the Japan Society of Civil Engineers (410) (1989) 81–92, hardcopy exists.
[11] S. Kaneko, O. Yoshida, Modeling of deepwater-type rectangular tuned liquid damper with submerged nets, Journal of Pressure Vessel Technology - Transactions of the ASME 121 (4) (1999) 413–422.
[12] M. Tait, A. El Damatty, N. Isyumov, M. Siddique, Numerical flow models to simulate tuned liquid dampers (tld) with slat screens, Journal of Fluids and Structures 20 (8) (2005) 1007–1023.
[13] O. Faltinsen, O. Rognebakke, I. Lukovsky, A. Timokha, Multidimensional modal analysis of nonlinear sloshing in a rectangular tank with finite water depth, Journal of Fluid Mechanics 407 (2000) 201–234.
[14] A. Ali, H. Kalisch, Energy balance for undular bores, Comptes rendus - Mecanique 338 (2) (2010) 67–70.

Paper III

"Interaction of Shallow Water Tuned Liquid Damper and Structure - theory and experimental verification"

J. Krabbenhøft & C.T. Georgakis

Manuscript prepared for submission to: *Journal of Wind Engineering and Industrial Aerodynamics*

Interaction of Shallow Water Tuned Liquid Damper and Structure - theory and experimental verification

J. Krabbenhøft*,[a], C.T. Georgakis[a]

[a] *Department of Civil Engineering, Technical University of Denmark, Building 118, Brovej, 2800 Kgs. Lyngby, Denmark*

Abstract

A mathematical model describing the interaction between a shallow water Tuned Liquid Damper (TLD) and a singe-degree-of-freedom (SDOF) structure is presented. The mathematical model of the TLD is based on the non-viscous Non Linear Shallow Water equations and the structure is modelled as a simple linear mass-spring system. Good agreement is found between simulations and experiments for the case of free decay. The mathematical model here captures the transient behavior of the fluid very well. The model is then verified against forced excitation tests showing that the magnitude of the frequency response function for the structural amplitude is reproduced.

Key words: Tuned Liquid Damper (TLD), Nonlinear Shallow Water (NSW) equations, transient response, steady state response.

1. Introduction

The application of vibration-control devices in civil engineering structures has become an accepted technology. One type of passive control device that has been used widely is the Tuned Liquid Damper [1, 2, 3, 4, 5, 6].

Vibration control devices utilizing hydrodynamic forces to produce a feedback force to the structure can roughly be divide into free surface dampers and liquid column dampers. The fluid behavior in the two are fundamentally different: in the free surface dampers the generated hydrodynamic forces are a result of the water sloshing which is a highly nonlinear and complex phenomenon, while the fluid behavior in the column dampers are much simpler to describe since the flow is internal and the free surface does not require any detailed description [7, 8]. For this reason liquid column dampers has received rather much attention in the last decade. The main advantage of the free surface dampers is clearly that these can be designed to work in several directions where the liquid column dampers are typically limited to working in one direction.

The class of free surface dampers can further be divided into two subclasses namely shallow water dampers and deep water dampers. The distinction between the two, as the

*Corresponding author
Email address: jkr@byg.dtu.dk (J. Krabbenhøft)

name indicates, relies on the ratio of the still water level h to the horizontal extension of the liquid container L, i.e. on the magnitude of h/L. The transition from one subclass to the other is not abrupt but rather gradual, and roughly one can use $h/L = 0.1$ as guiding transition value. In a recent paper [9] a theoretical model was compared to experimental results to establish a working range of h/L to use in a shallow water theory. The study showed that $h/L = 0.1$ seems to be an appropriate upper limit when applying nondispersive shallow water theory for modelling sloshing. The main difference in sloshing behavior of shallow and deep water dampers is found in the free surface. For shallow water dampers a moving hydraulic jump, a so called bore, is developed for quite low base amplitudes A. In a previous study [9] it was shown that for amplitude ratios as low as $A/L = 0.015$ a clear bore was formed near the linear sloshing frequency. Contrary to the discontinuous surface profile developed in shallow water dampers, the free surface in deep water dampers will have a tendency to remain continuous. This results in a much lower internal fluid dissipation, compared to the energy dissipation in a bore, and for this reason deep water dampers are often equipped with screens to increase the internal damping [10, 11, 12, 6].

The interaction of shallow water TLDs and structures has been investigated almost entirely for low amplitude vibrationd, i.e. for cases where the ratio A/L remains low. Thus in a paper by Tamura et. al. [1] the maximum used base amplitude was $A/L \simeq 0.007$, in Tamura et. al [2] dampers installed in the Airport Tower at the Tokyo International Airport experienced vibration levels of $A/L \simeq 0.002$ during a storm and in Fuji et. al. [3] dampers installed in the Airport Tower of Nagasaki Airport experienced vibrations levels of $A/L \simeq 0.003$. Sun et. al. [13] performed TLD-structure interaction experiments and found good agreement for $A/L = 0.008$. For higher base amplitudes they corrected their model using empirical expressions to include the high energy dissipation due to wave breaking and found reasonable agreement between experiments and their model for $A/L = 0.02 - 0.04$.

In the present work we focus on dampers subjected to base motion amplitudes of a significant magnitude, i.e. $A/L > 0.01$, where development of bores will most likely occur. A mathematical model that captures this behavior, without applying any empirical calibration factors, is the Nonlinear Shallow Water equations (NSW equations) analyzed in depth in [14, 9] using forced shaking table experiments. In this work the developed mathematical sloshing model will be coupled to an elastic structure to study the interaction behavior. Free decay and harmonic forcing will be investigated

First a TLD-structure interaction model is proposed and is verified through free decay as well as forced excitation experiments. This interaction model is relatively fast and precise and thus expected to be use full as an aid in designing shallow water TLDs.

2. Theoretical and numerical considerations

2.1. General description of TLD

Several different TLD geometries have been proposed in literature where the most popular are the annular tank proposed by Modi et. al. [15], circular [16] and rectangular [17]. Common for all the mentioned dampers is that the bottom is flat and horizontal. Sayer and Baumgarten investigated the interaction between a structure and spherical fluid container in [18, 19] and Gardarsson et. al. investigated the behavior of sloped-bottom TLDs in [20]. The price of working with more complex geometries is that the

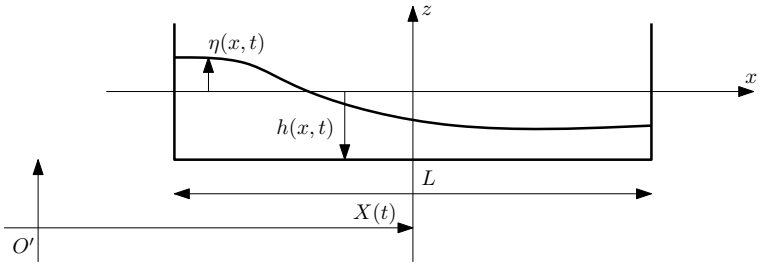

Figure 1: Sketch of flat bottomed rectangular TLD tank

already rather complex mathematical models become even more complex and using approximate shallow water models becomes very difficult. Thus in the present work a 2D rectangular tank with a flat bottom is used as shown in figure 1.

2.2. Governing fluid equations

The rigid rectangular container shown in figure 1, which has the length L, width W and still water depth h, is subjected to a horizontal base motion $X(t)$. It is convenient to refer the fluid motion to a moving coordinate system with origo fixed to the middle of the tank at the free liquid surface. Assuming an inviscid and incompressible fluid the equations describing the total water depth $H = h + \eta(x,t)$ and mean horizontal particle velocity $U = U(x,t)$ are the Nonlinear Shallow Water (NSW) equations [14]:

$$\mathbf{U}_t + \mathbf{F}(\mathbf{U})_x = \mathbf{S}(\mathbf{U}, x, t) \tag{1}$$

with

$$\mathbf{U} = \begin{pmatrix} H \\ HU \end{pmatrix}, \mathbf{F} = \begin{pmatrix} HU \\ HU^2 + \frac{1}{2}gH^2 \end{pmatrix}, \mathbf{S} = \begin{pmatrix} 0 \\ -H\ddot{X}(t) \end{pmatrix} \tag{2}$$

It was shown in [14] that including bottom friction had little effect on the solution for smooth tanks and is left out here. The boundary conditions expressing solid end walls, and initial conditions expressing quiescent fluid conditions are

$$\begin{array}{lcl} \text{B.C.} & : & U(-L/2,t) = U(L/2,t) = 0 \\ \text{I.C.} & : & H(x,0) = h,\ U(x,0) = 0 \end{array} \tag{3}$$

2.3. Base shear force due to liquid motion

Considering hydrostatic pressure and neglecting vertical acceleration effects as done in the derivation of the NSW equations the pressure can be expressed as

$$p(z) = \rho g(\eta - z) \tag{4}$$

The base shear force of the tank due to liquid motion is found as the difference of the integrated the pressure on either sides of tank, i.e.

$$F_S(t) = \tfrac{1}{2}\rho g W(H_R^2(t) - H_L^2(t)) \tag{5}$$

Here the friction on the side walls and bottom have been neglected.

2.4. Numerical solution of fluid equations

The nonlinear inhomogeneous set of hyperbolic PDE's (2)-(3) are solved using a Finite Volume scheme described in detail in [14]. The computational domain $\Omega \in [-L/2, L/2]$ is partitioned into I non overlapping cells $\Omega = \bigcup_{i=1}^{I}$ where the solution is assumed constant in each cell. The solution is updated in each time step using a ones-step Finite Volume scheme

$$\mathbf{U}_i^{n+1} = \mathbf{U}_i^n - \frac{\Delta t}{\Delta x_i}[\mathbf{F}_{i+\frac{1}{2}} - \mathbf{F}_{i-\frac{1}{2}}] + \Delta t \mathbf{S}_i \tag{6}$$

where the numerical fluxes $F_{i\pm\frac{1}{2}}$ are evaluated using a Rusanov flux [21]. As a time stepping restriction we use

$$\Delta t = 0.9\frac{\Delta x}{S_{\max}^n} \tag{7}$$

with the maximum wave speed in the computational domain evaluated using the simple approximation

$$S_{\max}^n = \max_i\{|U_i^n| + \sqrt{gH_i^n}\} \tag{8}$$

2.5. Interaction model

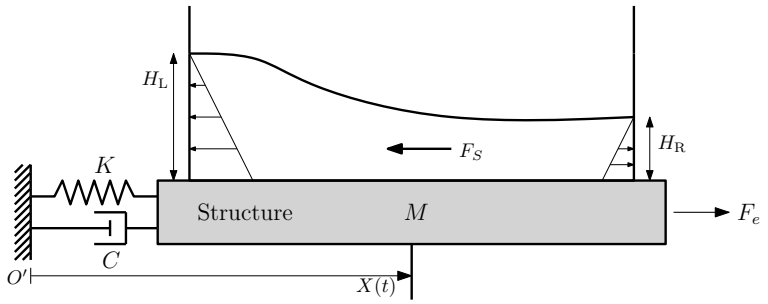

Figure 2: Coupling of TLD and simple SDOF structure.

The present TLD-structure interaction model is a single degree of freedom (SDOF) structure attached with a TLD as shown in figure 2. The structure is exerted by an external force denoted F_e and a horizontal feedback force from the liquid sloshing denoted F_S given in (5). The equation of motion describing the state of the structure is accordingly

$$M\ddot{X} + C\dot{X} + KX = F_e(t) + F_S(t) \tag{9}$$

where the structural mass, damping and stiffness are denoted with uppercase letters. The equation of motion (9) is expressed in the more practical form as

$$\ddot{X} + 2\zeta_s\omega_s\dot{X} + \omega_s^2 X = \frac{1}{M}(F_e(t) + F_S(t)) \tag{10}$$

where $\omega_s = (K/M)^{\frac{1}{2}}$ is the undamped angular frequency of the structure and $\zeta_s = C/(2M\omega_s)$ is the critical damping ratio of the structure. Introducing the state vector

Initialize $X^1 = X_0, V^1 = V_0, H^1 = H_0, U^1 = U_0$

for $n = 1 : N$

$\Delta t = 0.9\frac{\Delta x}{S^n_{\max}}$ using (7)-(8)

$F^n_S = \frac{1}{2}\rho g W((H^n_R)^2 - (H^n_L)^2)$

Find X^{n+1} and V^{n+1} given initial conditions X^n, V^n and F^n_S

$\ddot{X}^n = -2\zeta_s\omega_s\dot{X}^n - \omega_s^2 X^n + (F^n_e + F^n_S)/M$

$\mathbf{U}^{n+1}_i = \mathbf{U}^n_i - \frac{\Delta t}{\Delta x_i}[\mathbf{F}_{i+\frac{1}{2}} - \mathbf{F}_{i-\frac{1}{2}}] + \Delta t \mathbf{S}^n_i$

end

Table 1: Time-stepping algorithm for coupled system

$\mathbf{z}^{\mathrm{T}} = [X, V, \mathbf{U}]$, with $V = \dot{X}$ and $\mathbf{U}$ given in (1) the coupled TLD-structural system ca be expressed as

$$\dot{\mathbf{z}} = \mathbf{A}(\mathbf{z}) + \mathbf{F} \tag{11}$$

with

$$\mathbf{A}(\mathbf{z}) = \begin{bmatrix} V \\ -(2\zeta_s\omega_s v + \omega_s^2)/M \\ -\mathbf{F}(\mathbf{U})_x) \end{bmatrix} \quad , \quad \mathbf{F} = \begin{bmatrix} 0 \\ (F_e + F_S(H))/M \\ \mathbf{S}(H, \ddot{X}) \end{bmatrix} \tag{12}$$

The equations (11)-(12) describe the state of the coupled system and must be solved using a numerical integration scheme.

2.6. Solution strategy for coupled system

It would be possible to solve the coupled 1. order nonlinear system of ordinary differential equations directly using an ODE solver, e.g. a Runge-Kutta method. However, since we already have a stabile and robust scheme, namely (6), for solving the fluid equations, which by far is the most complex part of the coupled system, this strategy would be unwise, and instead we solve the fluid system and mechanical system with separate methods. For a mechanical system described by a linear 2. order ODE, as (10) with constant coefficients, the integration in time can be performed exact, assuming a piecewise linear forcing term [22]. A more general solution strategy, capable of handling nonlinear mechanical systems, is to use a high order explicit time integration scheme where some of the most popular are the 3. and 4. order Runge-Kutta methods [23]. In the present context we use a third order Runge-Kutta scheme. The structure of the complete time-stepping algorithm for the coupled TLD-structural system is indicated in table 1

Numerical simulations are always conducted under the condition that the water is initially at rest, i.e. $U^1_i = 0$ and $H^1_i = h$ for all i. The liquid domain in discretized using $I = 256$ elements and size of the time stepping increment is controlled using a Courant number of CFL = 0.9.

3. Experiments

The proposed fluid model (2) was investigated by experiments and numerical simulations in [14, 9]. In order to verify the proposed fluid model coupled with an elastic structure a number of free decay experiments were performed.

3.1. Experimental setup and apparatus

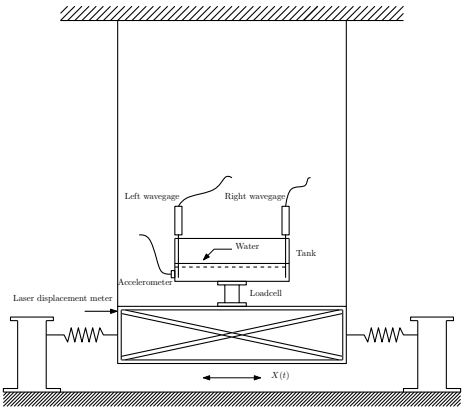

(a) Sketch of setup

(b) Photograph of setup

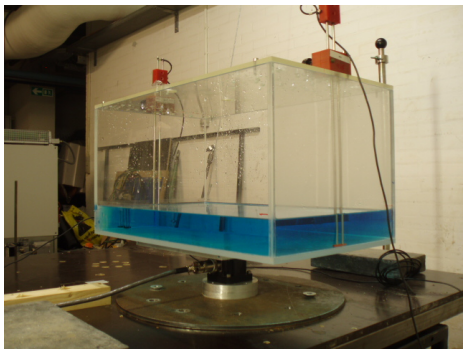

(c) Acrylic tank

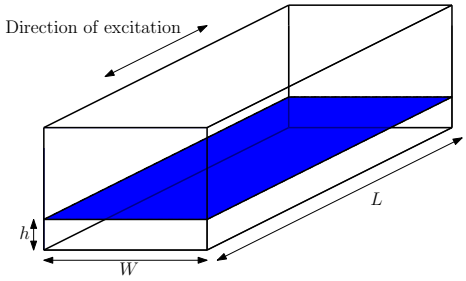

(d) Tank dimensions

Figure 3: Experimental setup.

A simple spring-pendulum shake table shown in figure 3 was constructed to perform the free decay experiments of the coupled TLD-structure system. The setup is a unidirectional single degree of freedom system with a horizontal vibration direction. The structural properties given by a mass M and stiffness K can easily be adjusted by adding or removing weights and by changing springs, respectively. Naturally this facilitates adjustments of the system frequency ω_s. No additional damping is added since the guide wheels provide a sufficient amount of structural damping. At one edge of the shake table a simple hook system was mounted permitting the table to be given a fixed initial displacement. The hook was in place until the water had come to rest, and was then released

by a applying an impulse force on the hook with a rubber hammer. This corresponds, as a good approximation, to structural initial conditions $[X(t=0), \dot{X}(t=0)] = [X_0, 0]$

Two different rectangular tanks were used in the experiments. One with horizontal inner dimensions $L \times W = 590 \times 335$ mm and the other with $L \times W = 400 \times 200$ mm. Both tanks had a height of 300 mm and were made of 10 mm acrylic plates. An acrylic lid was fixed to the tank tops where two wave gages made of steel wire were attached. Each wave gage is located 5 mm from the tank walls. The acrylic tank was placed on a load cell of type AMTI MC3-6-500 capable of measuring three force and three moment components. The horizonal base motion of the tank $X(t)$ was measured using a Laser Displacement Transducer (LDT) of type WayCON LAS-T-250A and the horizontal acceleration measured using a variable capacitance accelerometer from Brüel and Kjær of the type B&K 4575 with a frequency range 0-300 Hz and 1000 mV/g sensitivity. All quantities were recorded using National Instrument hardware.

3.2. Theoretical structural frequency

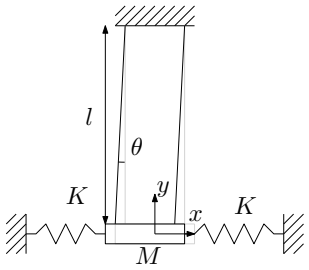

Figure 4: Spring-pendulum system.

It is convenient to use an energy principle to find the equation of motion for the spring-pendulum system. Lagrange's equation is given by

$$\frac{\mathrm{d}}{\mathrm{d}t}\left(\frac{\partial L}{\partial \dot{\theta}}\right) - \frac{\partial L}{\partial \theta}, \qquad L = T - V \tag{13}$$

Assuming small rotations, i.e. $X/L << 1$ and thereby $\theta << 1$, we approximate $sin\theta \simeq \theta$ and $\cos\theta \simeq 0$, resulting in a kinetic and potential energy of the system given by

$$T = \tfrac{1}{2} m (l\dot{\theta})^2 \tag{14}$$

$$V = 4\tfrac{1}{2} k (\theta l)^2 + mgl(1 - \cos\theta) \tag{15}$$

where $\cos\theta$ is retained in the potential energy equation in order for this term not to vanish when differentiated in Lagrange's equation. Inserting (14)-(15) into (13) gives the following result

$$\ddot{\theta} + \omega_s^2 \theta = 0, \qquad \omega_s = 4\frac{k}{m} + \sqrt{\frac{g}{l}} \tag{16}$$

In the analysis the mass is attached with four springs in total, two on each side, hence the constant value of four in the frequency expression (16)

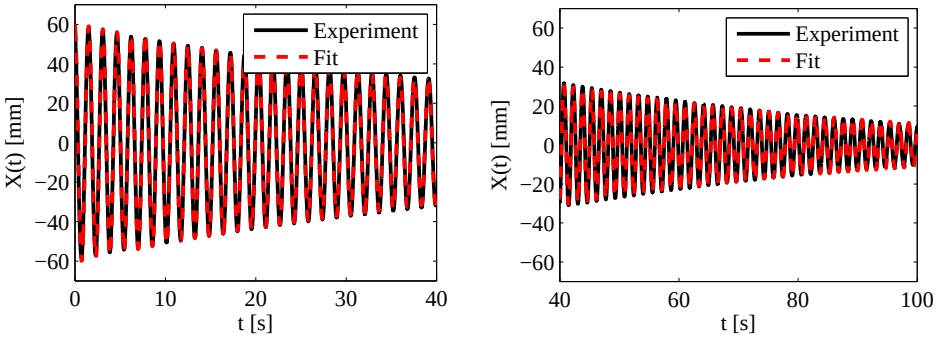

(a) High amplitude decay

(b) Low amplitude decay

Figure 5: Free decay experiments of shaking table for determining structural damping ζ_s and structural frequency ω_s.

3.3. Estimation of structural parameters

Even though the theoretical expression (16) should provide a very good estimate of the structural frequency, variations in the springs and uncertainties on the geometry, may result in a slightly different measured frequency. In order to determine the structural frequency and damping a range of free decay experiments were performed and the horizontal displacement of the structure was measured. Assuming the structural damping to be viscous the response can be described by

$$X(t) = Ae^{-\zeta_s \omega_s t} \sin(\phi + \omega_s t) \tag{17}$$

The values in (17) are found by fitting the expression to experimental decay records. A datafit for two different response histories is shown in figure 5 and it is clear that the viscous damping assumption is sufficiently precise for modelling the free decay. The damping and frequency are found to be almost independent of the amplitude and using $f_s = \omega_s/2\pi = 0.590$ Hz and $\zeta_s = 0.004$ provides a good fit of the measured data. The structural parameters are summarized in table 2

M [kg]	K [N/m]	l [m]	f_s^{theory} [Hz]	f_s [Hz]	ζ_s [-]
496.3	1260	2.5	0.596	0.590	0.004

Table 2: Structural parameters

4. Results

In order to verify the proposed coupled TLD-structure model first a number of coupled free decay experiments were performed. The purpose of the campaign is solely to verify the model and not to analyze the efficiency of the TLD. Next the TLD-structure model

Exp. name [-]	L [mm]	W [mm]	h [m]	m_w [kg]	h/L [-]	f_w [Hz]	f_w/f_s [-]	m_w/m_s [-]
Case1a	590	335	58	11.5	0.098	0.640	1.08	2.29
Case1b	590	335	50	9.88	0.085	0.594	1.01	1.98
Case1c	590	335	45	8.89	0.076	0.563	0.96	1.78
Case1d	590	335	40	7.91	0.068	0.531	0.90	1.58
Case2a	400	200	28	2.24	0.070	0.655	1.11	0.45
Case2b	400	200	25	1.98	0.062	0.617	1.05	0.40
Case2c	400	200	22	1.79	0.056	0.586	0.99	0.36
Case2d	400	200	19	1.54	0.048	0.543	0.92	0.31

Table 3: Different tank configurations for the free decay tests.

is tested on two forced excitation experiments with experimental results taken from [13].

4.1. Coupled free decay experiments

The two tanks were filled with four different water depths, given in table 3, in order to vary the sloshing frequency of the liquid. The sloshing frequency of the water is calculated using the dispersion relation for shallow water given by

$$f_w = \frac{\sqrt{gh}}{2L} \tag{18}$$

The tanks were mounted on the shaking table and the table was given an initial displacement of $X(t=0) \simeq 60$ mm. When the water in the tank had come to a rest the table was released.

It is interesting to study the transient behavior of the sloshing and to see how well the proposed interaction model captures this. In figure 6-7 a total of sixteen snapshots, taken from video recordings, are presented for different time instances normalized by the structural period $T = 1/f_s$. Seen from the video camera, the structure is initially displaced to the left. In each of the snapshots the simulated free surface is shown with a solid red line. The snapshots show that the model captures the location of the moving front very well and also the surface elevation at the two walls is captured remarkably well. It is clear from the pictures that the flow pattern is extremely complex and e.g. in picture 7(h) a spilling breaker is present which by the model is represented by a discontinuity in the surface. In fact for almost all the snapshots it is noticed that the front is represented by the model as moving front or hydraulic jump, i.e. a bore.

The motion of the table $X(t)$ for Case1a-d is shown in figure 8. Comparing to the free decay of the structure without TLD, figure 5, it is clear that the structure is far more damped with an attached TLD. For all the four tested cased the simulation captures the decay well, and for experiments as well as simulations, the case of $f_w/_s = 0.96$ is

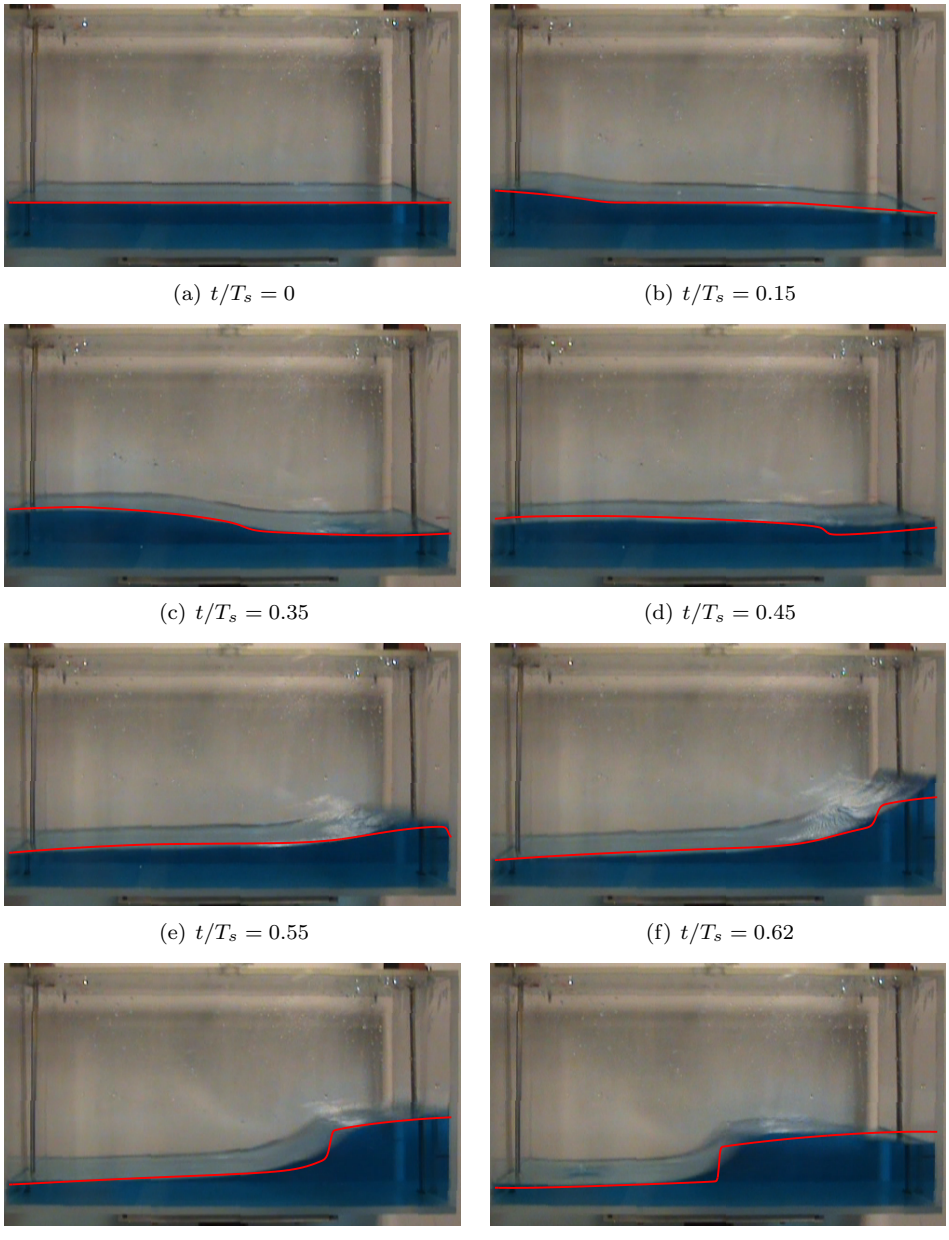

(a) $t/T_s = 0$ (b) $t/T_s = 0.15$

(c) $t/T_s = 0.35$ (d) $t/T_s = 0.45$

(e) $t/T_s = 0.55$ (f) $t/T_s = 0.62$

(g) $t/T_s = 0.69$ (h) $t/T_s = 0.80$

Figure 6: Snapshots in time window $0.0 \leq t/T_s \leq 0.80$. Case 1b

seen to be the best damped configuration. The logarithmic decrement of the coupled

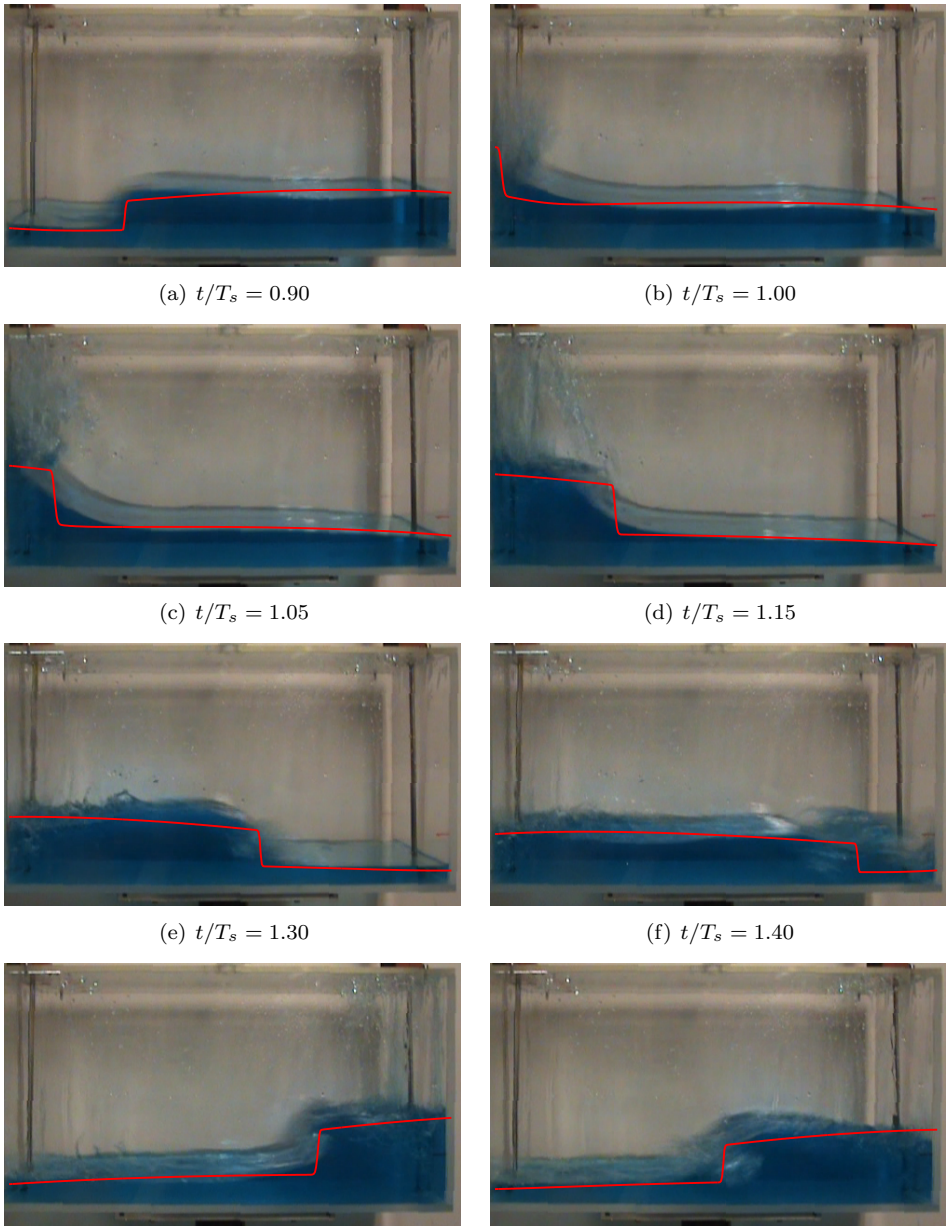

(a) $t/T_s = 0.90$ (b) $t/T_s = 1.00$

(c) $t/T_s = 1.05$ (d) $t/T_s = 1.15$

(e) $t/T_s = 1.30$ (f) $t/T_s = 1.40$

(g) $t/T_s = 1.65$ (h) $t/T_s = 1.75$

Figure 7: Snapshots in time window $0.90 \leq t/T_s \leq 1.75$. Case 1b

TLD-structural response is defined by

$$\delta_{s+w} = \frac{1}{n} \ln \frac{X(t)}{X(t + nT_s)} \tag{19}$$

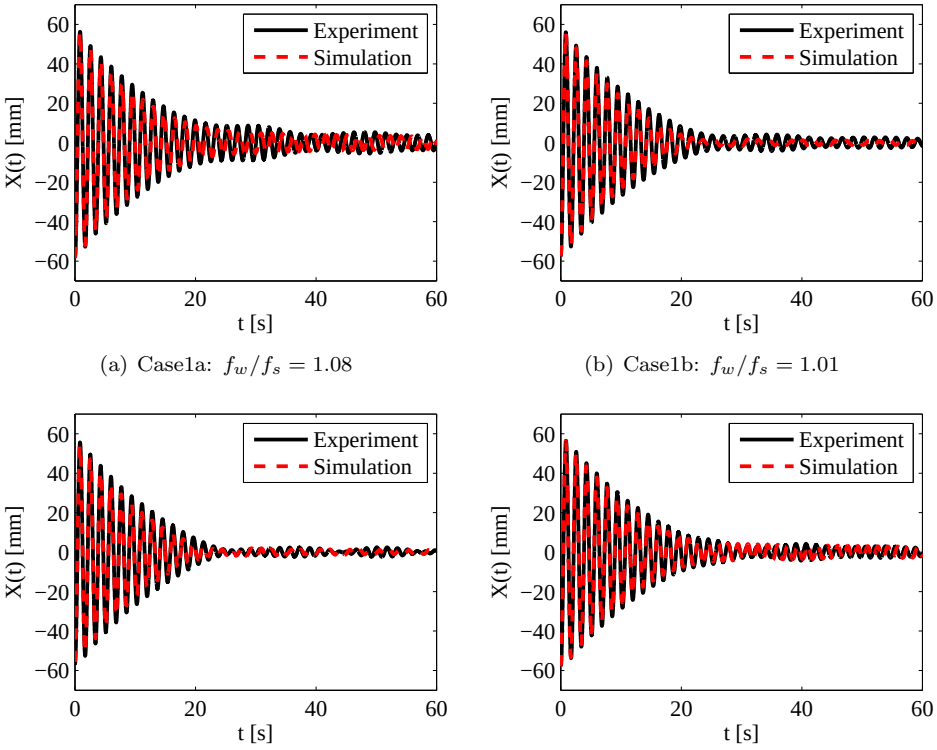

(a) Case1a: $f_w/f_s = 1.08$ (b) Case1b: $f_w/f_s = 1.01$

(c) Case1c: $f_w/f_s = 0.96$ (d) Case1d: $f_w/f_s = 0.90$

Figure 8: Coupled free decay experiments Case1a-d.

Using (19) it is possible to compute curves showing the damping, δ_{s+w}, as function of vibration amplitude $X(t)$. Using $n > 1$ seem to provide smoother curves and in figure 9 damping curves for case1 and case 2 are presented where $n = 4$ has been used. For both cases the measured structural damping is plotted with a solid red line showing aa almost constant structural damping value of $\delta_s = 2\pi\zeta_s \simeq 2.5\%$. For Case1a-d in 9(a) the damping is seen to be slightly overestimated by the simulation for all cases, how ever the trend is very well captured for all four cases. Thus for Case1b and Case1c the damping is seen to increase quite dramatically for decreasing structural amplitudes while case1a and case1d have a more moderate increase for lower structural amplitudes. For all cases the damping for high structural amplitudes is relatively constant with a value of $\delta_{s+w} \simeq 15\%$. Thus, by attaching a TLD to the structure the damping has been increased by around 12%. For Case2a-d the trend is quite similar and the simulation captures the damping δ_{s+w} extremely precise for large structural displacements.

4.2. Forced excitation experiments

In a paper by Sun et. al. [13] two coupled TLD-structure experiments were performed where wave breaking occurred in the TLD. A container with a length of 390 mm and width of 220 cm was filled with 30 mm of water corresponding to a sloshing frequency

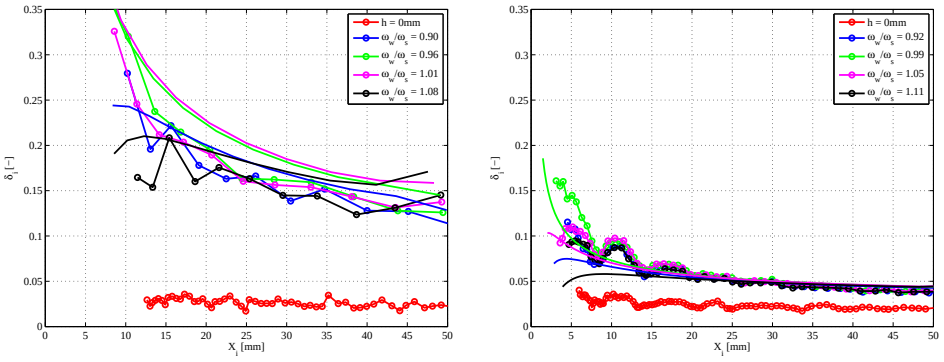

(a) Case1a-d (b) Case2a-d

Figure 9: Experimental and simulated logarithmic decrements as function of structural displacements. The simulated curves are shown with full lines and the experimental results with marked lines. Each line color represents a different case.

of $f_w = 0.696$ Hz. The mass ratio of TLD to structure was 1.05% and the structural frequency and damping of the structure was measured to $f_s = 0.689$ Hz and $\delta_s = 0.32$ %, respectively. Two different loading cases were considered: one where the structural response at resonance experienced a maximum value of $X_{\max} = 50$ mm and another with $X_{\max} = 100$ mm. The frequency ratio defined by

$$\beta = \frac{f_e}{f_w} \tag{20}$$

with f_e being the excitation frequency, was swept from 0.8 to 1.2. In figure 10 frequency response curves for the horizontal structural displacements are given for the two different loading cases. According to [13] breaking waves were clearly observed near resonance.

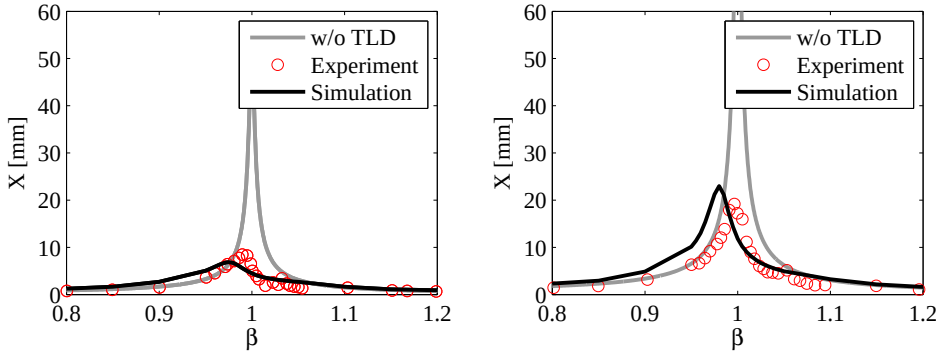

(a) $X_{\max} = 50$ mm (b) $X_{\max} = 100$ mm

Figure 10: Frequency response curves for horizontal displacement of SDOF structure equipped with TLD. Experimental results taken from [13]

For both cases the maximum structural response is captured very well by the proposed interaction model however there is a clear discrepancy between the simulated and experimental frequency ratio at which the maximum response occurs. The simulated curve peaks at a lower frequency than the experimental curve for both loading cases. However in the range $\beta > 1$ the agreement between experiment and simulation is satisfactory.

5. Concluding remarks

In the present study we have proposed a coupled TLD-structure model for estimating the response of structures equipped with TLDs. The study can be summarized as follows:

I An earlier proposed sloshing model based on the NSW equations is coupled to a simple 1-degree-of-freedom system and a simple explicit time-stepping algorithm for the coupled system is presented.

II Free decay experiments for coupled TLD-structure systems, with the structure given an initial displacement, show that the proposed model captures the transient behavior of the free water surface well and estimates the position of the wave front precisely.

III The total damping of the coupled system is estimated rather accurately by the model for structural amplitude above 10 mm. For lower structural amplitude larger deviation is found between experimental and simulated results. How ever qualitatively the model still performs well in this region.

IV Forced excitation experiments for a coupled TLD-structure system taken from [13] show that the model estimates the maximum value of the frequency response curve satisfactorily. The maximum value of the simulated frequency response curves has its maximum at a lower frequency value than the experimental curve.

As regards the last point further force excitation experiments should be conducted and the phase of the measured and simulated hydrodynamic fed back to the structure should be analyzed in order to establish an explanation of the found discrepancy. This will be performed in future work.

References

[1] Y. Tamura, R. Kousaka, V. Modi, Practical application of nutation damper for suppressing wind-induced vibrations of airport towers, Journal of Wind Engineering and Industrial Aerodynamics 43 (1-3) (1992) 1919–1930.

[2] Y. Tamura, R. Kohsaka, O. Nakamura, K.-i. Miyashita, V. J. Modi, Wind-induced responses of an airport tower - efficiency of tuned liquid damper, Journal of Wind Engineering and Industrial Aerodynamics 65 (1-3) (1996) 121–131.

[3] K. Fujii, Y. Tamura, T. Sato, T. Wakahara, Wind-induced vibration of tower and practical applications of tuned sloshing damper, Journal of Wind Engineering and Industrial Aerodynamics 33 (1-2) (1990) 263–272.

[4] T. Wakahara, T. Ohyama, K. Fujii, Suppression of wind-induced vibration of a tall building using tuned liquid damper, Journal of Wind Engineering and Industrial Aerodynamics 43 (1-3) (1992) 1895–1906.

[5] Y. Tamura, K. Fujii, T. Ohtsuki, T. Wakahara, R. Kohsaka, Effectiveness of tuned liquid dampers under wind excitation, Engineering Structures 17 (9) (1995) 609–621.

[6] C. Georgakis, H. Koss, W. De Toffol, Tuned liquid dampers for the new european court of justice, luxembourg, Structural Engineering International: Journal of the International Association for Bridge and Structural Engineering (IABSE) 15 (4) (2005) 228–231.
[7] S. K. Yalla, A. Kareem, Optimum absorber parameters for tuned liquid column dampers, Journal of Structural Engineering 126 (8) (2000) 906–915.
[8] M. J. Hochrainer, Tuned liquid column damper for structural control, Acta Mechanica 175 (1-4) (2005) 57–76.
[9] J. Krabbenhoft, C. T. Georgakis, (submitted), Shallow water sloshing. part ii. experimemtal investigation and numerical verification, Engineering Structures.
[10] T. Noji, H. Yoshida, E. Tatsumi, H. Kosaka, H. Hagiuda, Vibration control damper using sloshing of water, Structural Design, Analysis and Testing (1989) 1009–1018.
[11] S. Kaneko, O. Yoshida, Modeling of deepwater-type rectangular tuned liquid damper with submerged nets, Journal of Pressure Vessel Technology - Transactions of the ASME 121 (4) (1999) 413–422.
[12] M. Tait, A. El Damatty, N. Iayumov, Testing of tuned liquid damper with screens and development of equivalent tmd model, Wind and Structures, An International Journal 7 (4) (2004) 215–234.
[13] L. Sun, Y. Fujino, B. Pacheco, P. Chaiseri, Modelling of tuned liquid damper (tld), Journal of Wind Engineering and Industrial Aerodynamics 43 (1-3) (1992) 1883–1894.
[14] J. Krabbenhoft, C. T. Georgakis, (submitted), Shallow water sloshing. part i. theoretical and numerical background, Engineering Structures.
[15] V. Modi, F. Welt, Vibration control using nutation dampers, International Conference on Flow Induced Vibrations (1987) 369–376.
[16] Y. Fujino, B. M. Pacheco, P. Chaiseri, L. M. Sun, Parametric studies on tuned liquid damper (tld) using circular containers by free-oscillation experiments, Doboku Gakkai Rombun-Hokokushu/Proceedings of the Japan Society of Civil Engineers (398) (1988) 177–187.
[17] L. M. Sun, Y. Fujino, B. M. Pacheco, M. Isobe, Nonlinear waves and dynamic pressures in rectangular tuned liquid damper (tld). simulation and experimental verification, Doboku Gakkai Rombun-Hokokushu/Proceedings of the Japan Society of Civil Engineers (410) (1989) 81–92, hardcopy exists.
[18] B. A. Sayar, J. R. Baumgarten, Pendulum analogy for nonlinear fluid oscillations in spherical containers, Journal of Applied Mechanics, Transactions ASME 48 (4) (1981) 769–772.
[19] B. A. Sayar, J. R. Baumgarten, Linear ann nonlinear analysis of fluid slosh dampers, AIAA Journal 20 (11) (1982) 1534–1538.
[20] S. Gardarsson, H. Yeh, Behavior of sloped-bottom tuned liquid dampers., Journal of Engineering Mechanics 127 (3) (2001) 266–271.
[21] E. F. Toro, Shock-capturing Methods For Free-surface Shallow Flows, Wiley, April 2001.
[22] A. K. Chopra, Dynamics of Structures, Prentice Hall; 3 edition, 2006.
[23] W. E. Boyce, P. C. Deprima, Elementary Differential Equations and Boundary Value Problems, 4th. ed., Wiley, New York.

Paper IV

"Simulation of tuned liquid dampers using a momentum conserving nonlinear shallow water model: theory, computations and experimental verification"

J. Krabbenhøft & B. Lazarov

Published in: *Proceedings of the 3rd Int. Conf. on Structural Engineering, Mechanics and Computations, Cape Town, South Africa*

A study of rectangular tuned liquid damper using a momentum conserving formulation and experimental verification

J. Krabbenhøft
Department of Civil Engineering, BYG•DTU, Technical University of Denmark, Denmark
B. Lazarov
Department of Mechanical Engineering, MEK, Technical University of Denmark, Denmark

Keywords: Tuned Liquid Damper, Nonlinear shallow water, Flux formulation, Momentum conservation

ABSTRACT: Rectangular tanks filled with shallow liquid, also know as shallow-water type Tuned Liquid Dampers, have been investigated by several researchers. Common to the approaches is that an energy conserving form of the nonlinear shallow water equations is used for describing the sloshing motion. This form, also known as the velocity formulation, breaks down when discontinuities in the surface or waves are formed. In the current paper we use a formulation of the nonlinear shallow water equations based on momentum conservation instead. Using this approach the energy dissipation as a result of discontinuities is captured by the method. Numerical simulations and experimental results show surprisingly well agreement, taking the degree of nonlinearity in consideration, and that no calibration is performed of the numerical model.

1 INTRODUCTION

The idea of applying tuned liquid dampers (TLD) to reduce vibrations in civil engineering structures began in the mid-1980s. Because of its clearly economical benefits and high efficiency TLDs are increasingly being used as vibration absorbers to mitigate the dynamic response of structures. Unlike tuned mass dampers (TMD), which often respond in a purely linear manner, the behavior of TLDs is in general highly nonlinear due to the fluid motion. The aim of the dampers is of course the same, namely to transfer mechanical energy from the structure to the damper, thereby dissipating energy. In order for the damper to dissipate energy the damper must equipped with some sort of internal dissipation mechanisms. In a TMD the internal damping is often attained by adding e.g. a viscous damper to the damper mass. In a TLD the internal damping is attained directly through the fluid and thus is in general a very complex quantity to describe.

TLD's are often classified in two categories: shallow-water and deep-water type damper. The characterization is based on the ratio of the water depth to the horizontal dimension of the tank. In the limit of infinite small vibration amplitudes both types of dampers behave qualitatively identical and their behavior is well described by linear potential theory. However as the vibration amplitudes increase the behavior of the two dampers significantly changes and the same theory can no longer be applied to model both damper types.

In the case of a deep water-damper the free water surface at large vibration amplitudes becomes nonlinear but remains continuous. The energy dissipation in the fluid for this case stems primarily from the bottom friction and the free surface. Since these contributions are in general small, additional baffles and screens are often inserted in the fluid thereby increasing the internal energy dissipation.

In the case of shallow water type dampers the free surface at large vibration amplitudes no longer remains continuous. Due to nonlinearities a moving hydraulic jump or a shock wave is formed, also known as a bore, which is characterized as a wave with an almost vertical front. The generated bore is dominated by a large recirculating roller region from which turbulence originates and hence dissipates energy. The energy dissipated by the bore will generally be of such magnitude that no additional energy dissipating devices inside the bulk of the fluid is needed.

The motion of fluids in rigid containers has received considerable attention over the the last five or six decades due to its frequent application in many engineering disciplines. One of the first studies done (Graham and Rodriguez, 1952) was on the behavior

of fuel motion in tanks and was solved using linear potential theory and analogous mechanical models were derived. These analogous mechanical models have received much attention due to their simplicity and physical interpretation of mechanical quantities. A weakness however of the methods is their need to be calibrated up against experimental results.

Numerical modelling of shallow-water dampers have been done by several researchers (Sun et al., 1992; Sun and Fujino, 1994; Koh et al., 1994). For some reason though the majority of work done up to now has been based on an energy conserving form of the nonlinear shallow water equations also know as the velocity formulation. For base motions where no bore is developed the model works very well but as pointed out in (Sun and Fujino, 1994) even for relatively small base motions bores are developed and the velocity formulation is no longer valid. In order to capture the energy dissipation empirical constants are added to the equations, and thus the model needs calibration.

In this paper a momentum conserving form, also know as the flux formulation, is used instead. By conserving mass and momentum the equations are able to capture the energy loss occurring in the bore and hence calibration of the model can be avoided.

2 MODEL FOR LIQUID SLOSHING IN A TLD

The rigid rectangular TLD tank (Figure 1), which has the length $2a$, width b, and still water liquid depth h, is subjected to a horizontal base-motion x_s. It is convenient to refer the fluid motion to a moving coordinate system as the variables are measured relative to the moving frame. The local cartesian coordinate system (O, x, z) is thus attached to the tank at the center of the free liquid surface. The fluid is assumed inviscid, incompressible and initially irrotational. The equations describing liquid sloshing in the moving frame of reference are the continuity equation

$$\frac{\partial u}{\partial x} + \frac{\partial w}{\partial z} = 0 \tag{1}$$

and two-dimensional Euler equations

$$\begin{aligned} \frac{\partial u}{\partial t} + u\frac{\partial u}{\partial x} + w\frac{\partial u}{\partial z} + \frac{1}{\rho}\frac{\partial p}{\partial x} &= -\ddot{x}_s \\ \frac{\partial w}{\partial t} + u\frac{\partial w}{\partial x} + w\frac{\partial w}{\partial z} + \frac{1}{\rho}\frac{\partial p}{\partial z} &= g \end{aligned} \tag{2}$$

for $-h \le z \le \eta$. The kinematic boundary condition at the free surface is

$$w = \frac{\partial \eta}{\partial t} + u\frac{\partial \eta}{\partial x}, \quad \text{at} \quad z = \eta(x, t) \tag{3}$$

and at the bottom

$$w = -u\frac{\partial h}{\partial x}, \quad \text{at} \quad z = -h(x) \tag{4}$$

At the end walls the boundary conditions are

$$u(x = \pm a, t) = 0 \tag{5}$$

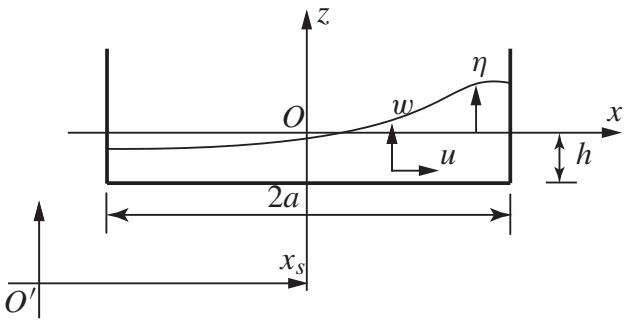

Figure 1. Sketch of a rectangular TLD tank.

2.1 *Vertical integration of continuity and Euler equations*

The depth integrated continuity equation is found by integrating the continuity equation (1) and utilizing (3) and (4):

$$\frac{\partial \eta}{\partial t} + \frac{\partial}{\partial x}\int_{-h}^{\eta} u dz = 0 \tag{6}$$

Integrating the horizontal momentum equation (2) and again utilizing (3) and (4) leads to:

$$\begin{aligned} \frac{\partial}{\partial t}\int_{-h}^{\eta} u dz + \frac{\partial}{\partial x}\int_{-h}^{\eta} u^2 dz + \frac{\partial}{\partial x}\int_{-h}^{\eta} \frac{p}{\rho} dz + \\ \frac{\partial h}{\partial x}\frac{1}{\rho}p(-h) + \ddot{x}_s(\eta + h) = 0 \end{aligned} \tag{7}$$

At last integration of the vertical vertical momentum equation is given by

$$\begin{aligned} \frac{1}{\rho}p(z) = g(\eta - z) + \frac{\partial}{\partial t}\int_{-h}^{\eta} w dz + \\ \frac{\partial}{\partial x}\int_{-h}^{\eta} uw dz - w^2(z) \end{aligned} \tag{8}$$

2.2 *Shallow water approximations*

In the following we assume that the vertical variation of the horizontal velocity component is negligible and that the flow can be approximated by a uniform velocity profile

$$u(z) \simeq U \equiv \frac{Q}{h + \eta}, \quad \text{where} \quad Q \equiv \int_{-h}^{\eta} u dz \tag{9}$$

Since the vertical flow velocity is significantly weaker than the horizontal one the pressure can be assumed hydrostatic, i.e. (8) is approximated by

$$\frac{1}{\rho}p(z) \simeq g(\eta - z) \tag{10}$$

2.3 *The flux formulation*

By inserting (9) and (10) into (7), the depth integrated horizontal momentum equation simplifies to

$$\frac{\partial Q}{\partial t} + \frac{\partial}{\partial x}\left(\frac{Q^2}{h+\eta}\right) + (h+\eta)\left(g\frac{\partial \eta}{\partial x} + \ddot{x}_s\right) = 0 \tag{11}$$

This should be combined with the depth integrated continuity equation

$$\frac{\partial \eta}{\partial t} + \frac{\partial Q}{\partial x} = 0 \tag{12}$$

and the boundary and initial conditions

$$\begin{array}{ll} \text{B.C.:} & Q(\pm a, t) = 0 \\ \text{I.C.:} & Q(x, 0) = Q_0(x),\ \eta(x, 0) = \eta_0(x) \end{array} \tag{13}$$

Following (Madsen et al., 2005) we emphasize that the governing equations (11)-(12) conserve depth integrated mass and momentum. This implies that continuous as well as discontinuous solutions are possible and as a very important and essential point: the energy dissipation associated with a discontinuity will be described by the equations.

By introducing the variable $d \equiv h + \eta(x, t)$ and the following operator

$$\frac{\partial \mathbf{F}}{\partial t} + \frac{\partial \mathbf{H}}{\partial x} + \mathbf{S} = \mathbf{0} \tag{14}$$

the flux formulation (11) and (12) can expressed as

$$\begin{aligned} \mathbf{F} &= \begin{bmatrix} d \\ Ud \end{bmatrix} \\ \mathbf{H} &= \begin{bmatrix} Ud \\ U^2 d + \frac{1}{2} g d^2 \end{bmatrix} \\ \mathbf{S} &= \begin{bmatrix} 0 \\ d\ddot{x}_s \end{bmatrix} \end{aligned} \tag{15}$$

This form will be used in the numerical solution procedure described next.

3 NUMERICAL SOLUTION PROCEDURE

The problem defined by equations (13)-(15) is discretized by using the Finite Volume method (FV) (LeVeque, 2002). The domain Ω is partitioned into N non-overlapping cells $\Omega = \bigcup_{k=1}^{N} \Omega_k$ and the solution within each cell is assumed to be constant. The differential equation is integrated over each cell

$$\int_{\Omega_k} \frac{\partial \mathbf{F}}{\partial t} + \frac{\partial \mathbf{H}}{\partial x} + \mathbf{S} \mathrm{d}\Omega = 0 \quad k = 1 \ldots N \tag{16}$$

The divergence theorem is applied on the second term of the above equation and (16) becomes

$$\int_{\Omega_k} \dot{\mathbf{F}} \mathrm{d}\Omega + [\mathbf{H}]_{x_{k-1}}^{x_k} + \int_{\Omega_k} \mathbf{S} \mathrm{d}\Omega = 0 \quad k = 1 \ldots N \tag{17}$$

The solution is approximated by a constant value inside each cell. The approximated flux $\mathbf{H}^h$ becomes discontinuous along the cell boundaries and has to be replaced by a suitable numerical flux $\mathbf{G}$ that depends on the values of the neighbor elements. The properties of the FV discretization depends on the choice of the numerical flux. Many suitable schemes have been utilized in practice (LeVeque, 2002) and in the present article we use the Roe numerical flux (Fagherazzi et al., 2004)

$$\mathbf{G}(i, j) = \frac{1}{2}\left(\mathbf{H}_i^h + \mathbf{H}_j^h\right) - \frac{1}{2}|\mathbf{A}|\left(\mathbf{F}_i^h - \mathbf{F}_j^h\right) \tag{18}$$

where the index i refers to the values computed inside the cell and the index j refer to the flux and the solution in the neighbor cell. The matrix $\mathbf{A}$ is computed as

$$\mathbf{A} = \begin{bmatrix} 0 & 1 \\ \bar{c}^2 - \bar{u}^2 & 2\bar{u} \end{bmatrix} \tag{19}$$

$$\bar{c} = \sqrt{\frac{1}{2}\left(c_i^2 + c_j^2\right)} \quad \bar{u} = \frac{c_i u_i + c_j u_j}{c_i + c_j} \quad c_i = \sqrt{g h_i} \tag{20}$$

The discretized equations becomes

$$\begin{aligned} & h_k \dot{\mathbf{F}}_k^h + \mathbf{G}(k, k+1) - \mathbf{G}(k, k-1) + h_k \mathbf{S}^h = 0 \\ & k = 1 \ldots N \end{aligned} \tag{21}$$

The equations are integrated in time using a standard 4th order Runge-Kutta solver.

4 EXPERIMENTAL SETUP AND PROCEDURE

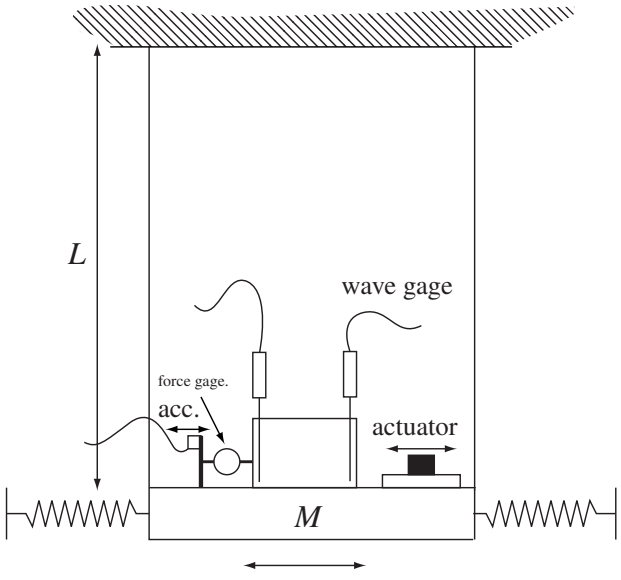

Figure 2. Sketch of the experimental setup.

A steel frame or table as shown schematically in figure 2 has been constructed in order to verify the results from the numerical simulations. The structure

consist of a steel frame with mass M being suspended by four cables with a length of $L = 3000$mm. In each corner of the frame a horizontal spring is mounted and by varying the spring stiffness and mass a large variety of structures, mainly low frequency ones, can be represented by the setup. In the current setup the mass of the structure is $M = 440$kg and the frequency is $\omega = 4.52$rad/s.

The TLD tank is placed on a frictionless support on top of the table making it possible to measure the total horizontal force using a force gage. The tank has a total inner length of $2a = 400$mm and a width of $b = 200$mm. The liquid depth is fixed to $h = 37$mm in all the experiments carried out. In the TLD tank two wave gages are placed, one at each end. The horizontal acceleration of the table is measured by an accelerometer. In order to excite the table an actuator is placed on the table, shown to the right of the TLD tank in figure 2, which supplies a horizontal force to the table at a chosen frequency. The data acquisition is done using LabVIEW.

The experiments are carried out in the following way: The actuator is programmed to deliver a sinusoidal force with a forcing frequency close to the natural frequency of the table and the TLD. After some time, typically around 30-60 seconds, a steady state motion of the liquid motion and table motion is reached and the acceleration, force and wave height is recorded for a period of 30s. By varying the forcing frequency the amplitude of the base excitation can be varied. The purpose of the experiments is not to determine the efficiency of the TLD but to get some records that can be verified by the numerical procedure.

5 VERIFICATION

To verify the experimental results we use the measured acceleration time series and apply these directly to the equations as $\ddot{x}_s$. The maximum horizontal amplitude of the table is estimated from the acceleration time series as

$$A = x_{\max} = \Omega^2 \ddot{x}_{s,\max} \tag{22}$$

where Ω is the frequency of the horizontal table motion. The fundamental natural frequency of the fluid based on linear potential theory is given by (Lamb, 1932)

$$\omega_f^2 = g \frac{\pi}{2a} \tanh\left(\frac{h\pi}{2a}\right) \tag{23}$$

which for our case gives $\omega_f = 4.67$rad/s. Based on the linear frequency the frequency ratio β is defined as

$$\beta = \frac{\Omega}{\omega_f} \tag{24}$$

5.1 *Wave height comparison*

The first method of verifying the numerical scheme is by comparing the measured wave height d at one of the end walls of the tank with the computed records. In

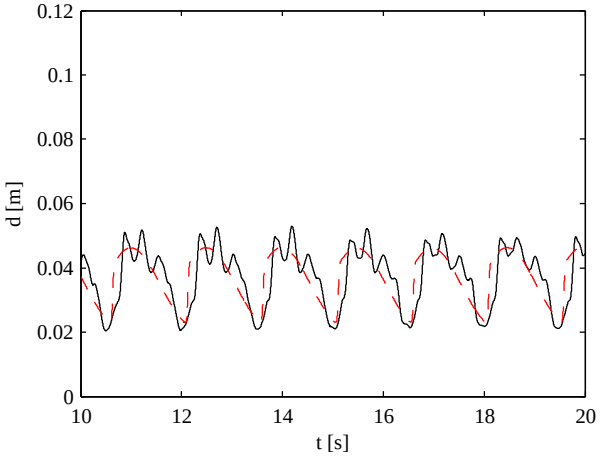

Figure 3. Free surface at $x = -0.2$m. $A/2a = 0.02$ and $\beta = 0.90$

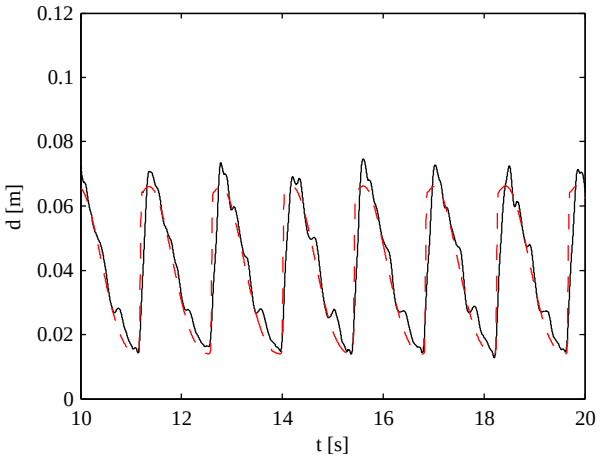

Figure 4. Free surface at $x = -0.2$m. $A/2a = 0.07$ and $\beta = 0.95$

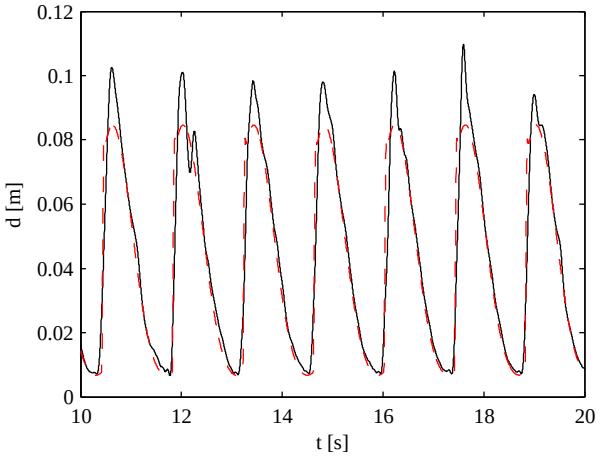

Figure 5. Free surface at $x = -0.2$m. $A/2a = 0.16$ and $\beta = 0.97$

all the following comparison plots the measured wave height is shown by a full curve while the computed wave heights are depicted by dashed curves.

It is clear from figure 3-6 that the equations describe the fluid motion remarkably well and it should be stressed that no calibration of the numerical model of any kind has been performed. The still water level is $h = 0.037$m and the nonlinearity of the problem is noticed by asymmetry of the free surface elevation; the

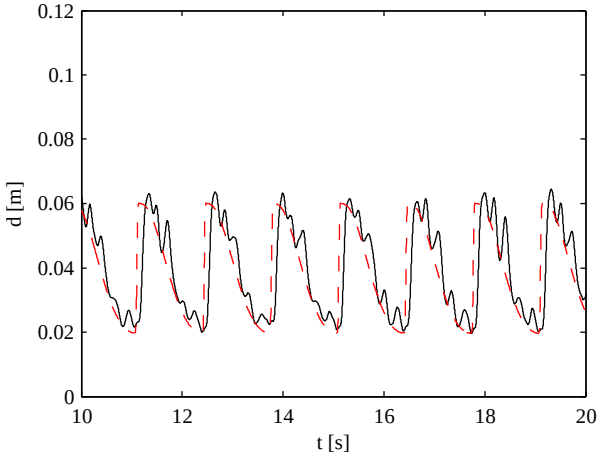

Figure 6. Free surface at $x = -0.2$m. $A/2a = 0.04$ and $\beta = 1.00$

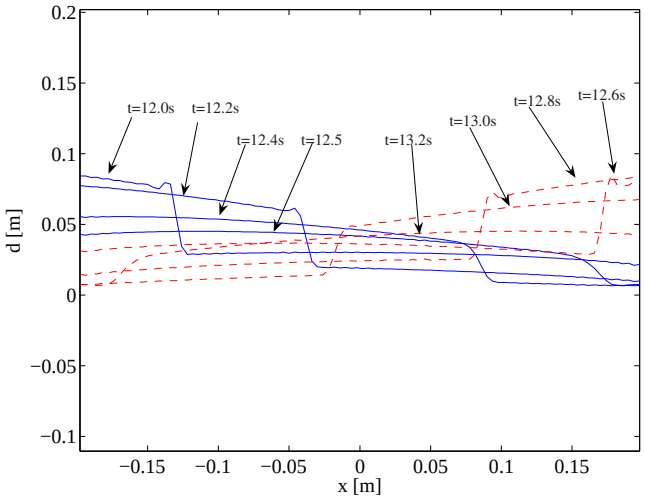

Figure 7. Surface profile for $A/2a = 0.16$ and $\beta = 0.97$ at eight different time instances. Full curve: Bore travelling from left to right. Dashed curve: Bore travelling from right to left.

free surface elevation in the upward direction is larger than in the downward direction. Computed surface profiles at eight different time instances in figure 7 also show the complexity of the problem.

It seems to be a general trend when studying the experimental data that higher harmonic components are superimposed on the bore. The numerical solution however does not capture this effects and the solution is instead more smooth. Also the numerical method very consistently underestimates the measured wave height. When performing the experiments it is visually observed that some splashing occurs when the bore hits the end walls, an effect which the numerical model is unable to capture.

As a last point it is noticed that the numerical model is able to capture the behavior of the fluid very well for base motions ranging from 2% to 16% of the tank length.

5.2 *Force comparison*

The second part that needs to be verified is the ability of the numerical model to capture the total horizontal force as a results of fluid sloshing. The total horizontal

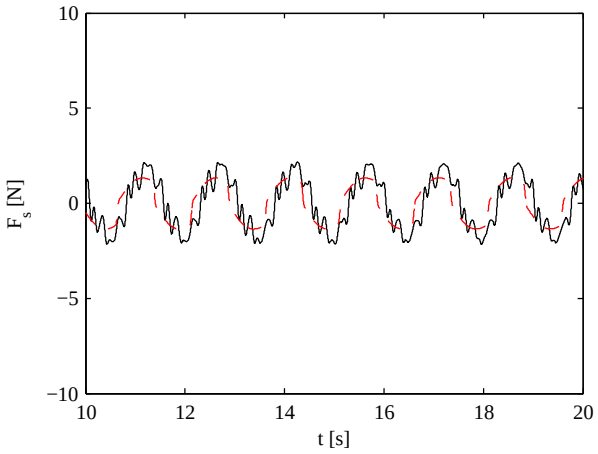

Figure 8. Total horizontal force F_s. $A/2a = 0.02$ and $\beta = 0.90$

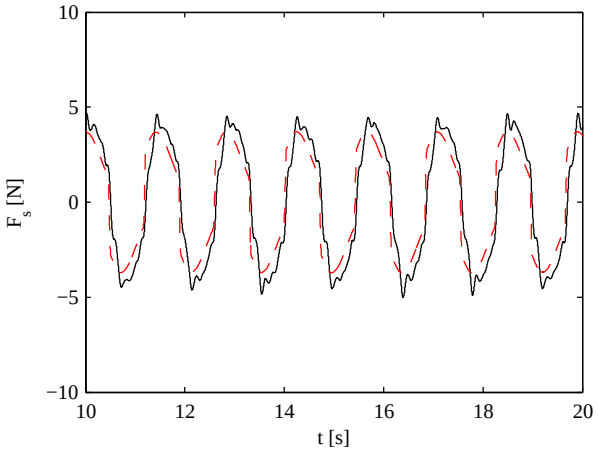

Figure 9. Total horizontal force F_s. $A/2a = 0.07$ and $\beta = 0.95$

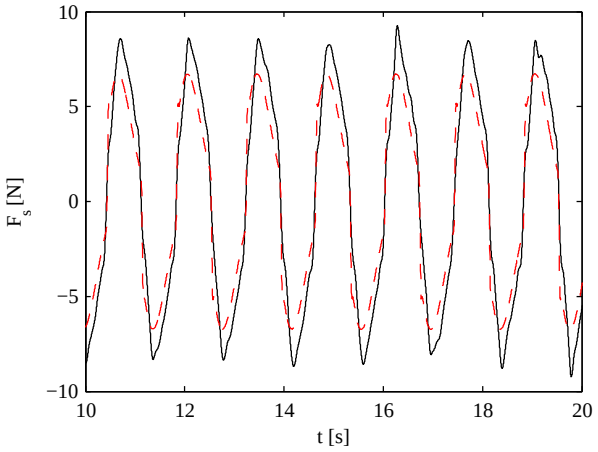

Figure 10. Total horizontal force F_s. $A/2a = 0.16$ and $\beta = 0.97$

force from the fluid motion is found by taking the difference of the integrated hydrostatic pressure (10) at both ends of the tank:

$$F_s = \frac{1}{2}\rho g b \left(d^2_{x=-a} - d^2_{x=+a}\right) \tag{25}$$

This force is compared with the horizontal force measured by the force gage, see figure 2. The comparison is presented in figures 8-11.

Again the numerical model is seen to capture the experimental data very well. As was also the case in the

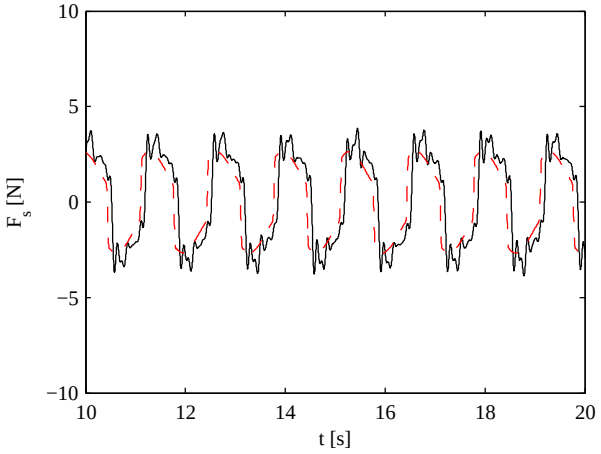

Figure 11. Total horizontal force F_s. $A/2a = 0.04$ and $\beta = 1.00$

previous section the measured force is underestimated by the numerical simulation.

6 DISCUSSION-CONCLUSION

The conclusions that can be drawn from the present study are summarized as follows:

(i) By numerically solving the nonlinear shallow water equations using a mass and momentum conserving form, the behavior of shallow water dampers can be described very well without having to introduce empirical constants describing the internal damping of the fluid. Both the wave height and sloshing force are captured very well by the numerical model.

(ii) The experiments show clearl traces of higher harmonic components which the numerical model is unable to capture. Instead the model seems to smooth out the solution.

(iii) The numerical method works well for different base motion amplitudes.

ACKNOWLEDGEMENTS

The authors would like to thank Uffe Lind from FORCE Technology, Lyngby, for providing wave gages and general assistance. The authors are grateful for informative discussions on hydrodynamics and wave theory with Associate Professor Harry Bingham and Professor Per Madsen of The Technical University of Denmark and for general discussions with Associate Professor Christos T. Georgakis. This research is financially supported by The Technical University of Denmark.

REFERENCES

Fagherazzi, S., Rasetarinera, P., Hussain, M. and Furbish, D. 2004, Numerical solution of the dam-break problem with a discontinuous galerkin method, *Journal of Hydraulic Engineering-ASCE* 130: 532–539.

Graham, E. and Rodriguez, A. 1952, The characteristics of fuel motion which affect airplane dynamics, *Journal of Applied Mechanics-Transactions of the ASME* 19: 381–388.

Koh, C., Mahatma, S. and Wang, C. 1994, Theoretical and experimental studies on rectangular liquid dampers under arbitrary excitations, *Earthquake Engineering and Structural Dynamics* 23: 17–31.

Lamb, S. H. 1932, Hydrodynamics, Cambridge University Press.

LeVeque, R. J. 2002, Finite Volume Methods for Hyperbolic Problems, Cambridge University Press.

Madsen, P., Simonsen, H. and Pan, C. 2005, Numerical simulation of tidal bores and hydraulic jumps, *Coastal Engineering* 52(5): 409–433.

Sun, L. and Fujino, Y. 1994, A semi-analytical model for tuned liquid damper (tld) with wave breaking, *Journal of Fluids and Structures* 8(5): 471–488.

Sun, L., Fujino, Y., Pacheco, B. and Chaiseri, P. 1992, Modelling of tuned liquid damper (tld), *Journal of Wind Engineering and Industrial Aerodynamics* 43(1-3): 1883–1894.

The application of vibration-control devices in civil engineering structures has become an accepted technology. One type of passive control device that has been widely used is the Tuned Liquid Damper (TLD). However, despite its frequent use the understanding of the interaction between TLD's and structures is by far fully understood. A mathematical model describing liquid sloshing in shallow water has been developed and validated by extensive experimental results. The mathematical sloshing model has further been coupled to an elastic structure to study the interaction effects of sloshing forces and structural response.

DTU Civil Engineering
Department of Civil Engineering
Technical University of Denmark

Brovej, Building 118
2800 Kgs. Lyngby
Telephone 45 25 17 00

www.byg.dtu.dk

ISBN: 9788778773142
ISSN: 1601-2917